Republic of Iraq
Ministry of Higher Education
and Scientific Research
University of Babylon
College of Engineering

SIMULATION AND TESTING OF A SOLAR ABSORPTION ASSISTED VENTILATION SYSTEM UNDER IRAQ CONDITIONS

A Dissertation Submitted to the

University of Babylon / College of Engineering

In Partial Fulfilment of the Requirements for the Degree of Doctor of Philosophy in Engineering/ Mechanical Engineering/Power

By

Ahmed Abbas Shahhath Daen

M.Sc. (Mech. Eng.)
2015

Supervised By:

Prof. Dr. Haroun A.K. Shahad *Prof. Dr.* Ala'a *Abbas Mahdi*

2022 A.D. 1443 A.H.

بسم الله الرحمن الرحيم

وَ جَعَلْنَا اللَّيْلَ وَ النَّهارَ آيَتَيْنِ فَمَحَوْنا آيَةَ اللَّيْلِ وَ
جَعَلْنا آيَةَ النَّهارِ مُبْصِرَةً لِتَبْتَغُوا فَضْلاً مِنْ
رَبِّكُمْ وَ لِتَعْلَمُوا عَدَدَ السِّنِينَ وَ الْحِسابَ وَ
كُلَّ شَيْءٍ فَصَّلْناهُ تَفْصِيلاً

صدق الله العلي العظيم

سورة الاسراء اية (12)

Supervisors Certification

We certify that this dissertation entitled **"Simulation and Testing of a Solar Absorption Assisted Ventilation System Under Iraq Weather "** has been prepared by ***"Ahmed A. Shahhath Al-Moselmawy"*** under our supervision at the Department of Mechanical Engineering, College of Engineering, University of Babylon as a partial fulfillment of the requirements for the Degree of Doctor of Philosophy in Mechanical Engineering/Power.

Signature:

Prof. Dr. Haroun A.K. Shahad

Department of Mechanical Engineering

College of Engineering

University of Babylon

Data: / / 2022

Signature:

Prof. Dr. Ala'a ***Abbas Mahdi***

Department of Mechanical Engineering

College of Engineering

University of Babylon

Data: / / 2022

Examining Committee Report

We certify that we have read this dissertation entitled **"Simulation and Testing of a Solar Absorption Assisted Ventilation System under Iraq Weather "** which has been prepared by **"Ahmed A. Shahhath Al-Moselmawy"** and as examining committee, examined the student in its contents. In our opinion, the dissertation is adequate for the debate the Partial Fulfilment of the requirements for the degree of Doctor of Philosophy in Power Engineering.

Signature:
Name: Prof. Dr. Haroun A.K. Shahad
Data: / / 2022
(Member and Supervisor)

Signature:
Name: Prof. Dr. Alaa Abbas Mahdi
Data: / / 2022
(Member and Supervisor)

Signature:
Name :Prof. Dr. Saba Y. Ahmed
Data: / / 2022
(Member)

Signature:
Name: Ass. Prof. Dr. Hameed K. Hamzah
Data: / / 2022
(Member)

Signature:
Name: Ass. Prof. Dr. Qusay R. AL-Amir
Data: / / 2022
(Member)

Signature:
Name: Ass. Prof. Dr. Nabeel A. Ghyadh
Data: / / 2022
(Member)

Signature:
Name: Prof. Dr. Ahmed Abed Mohmed
Data: / / 2022
(Chairman)

In view of the available recommendations, I forward this dissertation for the debate by the examination committee.

Signature:
Name: Ass. Prof. Dr. Samer Mohammed Abdulhaleem
Data: / / 2022
(Chairman of Mechanics Department)

Approval of the Dean of collage of Engineering/ University of Babylon.

Signature:
Name: Prof. Dr. Hatem Hadi Obeid
Data: / / 2022
(Dean of College of Engineering)

ACKNOWLEDGMENTS

Thanks to God the most Compassionate, the Merciful and my God bestow peace on Prophet Mohammed and all members of his family.

I would like to express my deep gratitude to my supervisors Prof. **Dr. Haroun A.K. Shahad** and **Prof. Dr. Ala'a Abbas Mahdi** who suggested this project and generously gave guidance throughout this work.

Many Thanks to the Department of Mechanical Engineering, College of Engineering at University of Babylon and Deanship for providing the requirements of research.

I would like to express my thanks and gratitude to **Prof. Dr. Dhurgam Abdulhassan** due to his assistance and his supporting situations for the return to study at the general admission channel.

I would like to express my deepest gratitude to staff of Post-Graduates studies laboratory in the Faculty of Engineering University of Babylon and in particular Mr. Hussein Hamza.

Many Thanks to all friends in working for all kinds of assistance in both of (Inspectorate Antiquities and Heritage of Gov. Najaf and Department of Tourism Board In Gov. Najaf).

Finally, special thanks and gratitude goes out to my family, my wife, my relatives and all friends for help, encouragement and various kinds of assistance, and to anyone who helped in one way or another in bringing out this work. My God bestow health and happiness to all of them.

Ahmed A. Shahhath Al-Moselmawy

Dedication

I'd like to dedicate my work for the
person who is my emblem….my father
The person who inspire me… my mother
God bless her tomb
My support…my brothers
My happiness… my sisters
My life… my wife
My daughter… Saja

Ahmed

Summary

The objectives of the present work is to design, fabricate and test a ventilation system powered by a solar absorption cooling system under Mid-Iraq climate conditions (Hilla city) with (32.4°latitude, 44.4° longitude) to ventilate an insulated office room using displacement ventilation. Moreover, a mathematical model has been developed for the solar collector loop and the solar absorption system loop, as well as simulating the tested ventilated room.

The solar absorption system consists of a parabolic trough solar collector (PTSC), storage tank, hot water pump, generator, condenser, two capillary tubes, evaporator, absorber, chemical water pump and heat exchanger. The ventilated office room has dimensions of ($2 \times 2 \times 2.5$m height) and is made of sandwich panel with thermal conductivity of 0.14 W/m.℃ and contains a thermal manikin with a total heat of 75 W, a computer with heat of 45W and lamp of 15W. There is a window in the north wall of the cooled room with a maximum heat gain of 31.26 W. The infiltration of the tested room is 0.5/h with total heat gain of 47.43W. The total required cooling load for the insulated office room is 300W. The (PTSC) collector has an aperture area of $2m^2$.

Acetone-water pair is used as a refrigerant-absorbent pair with solution mass of (12 kg). Three concentrations of acetone have been used in the present study which are (40%), (50%) and (60%) by mass.

The displacement ventilation has been performed by using a diffuser with dimensions of (0.3m width and 0.24m height) and velocity of supplied air of 0.3 m/s with volumetric air flow rate of 0.022 m^3/s. The supplied air to the evaporator is a mixture of 90% recirculated air from the room exit and 10% from the outdoor as a fresh air. The experimental work

was performed in the duration between May and July 2021 for the time between 9:00 AM and 3:00 PM, in outdoor weather conditions.

Two poles are used to measure the local temperature inside the cooled room. The first pole is located at (X=1m and Z=1m) at the line of diffuser and the person while the second pole is located at (X=1.25m and Z=1.5m) near the person.

The theoretical work has been performed by using three software's. The mathematical modelling of the absorption system was performed by using Engineering Equations Solver (EES software) by using energy and exergy balance for all the components of solar absorption system. Statistical Product and Service Solutions (SPSS software) was used to formulate a relationship between the mass of acetone vapor, generator temperature and the concentration of acetone in the solution. While the AirPak 3.0.16 software is used to simulate the cooled room using RNG K-ε model. The mesh of (1427500) nodes has been selected because it gave an accepted result.

The experimental results showed that, the maximum recorded required radiation was at 28-June of 2021 at (12:00 PM) with a value of 846 W/m^2 and maximum useful power, receiver surface temperature, storage temperature, generator temperature and collector efficiency of 1157W, 87.1℃, 78.5 ℃, 81.2 ◦C and 73.1% values respectively. The best results for solar absorption system were obtained at 7-July at acetone concentration of 60%. These results included air temperature difference across the evaporator, cooling effect, coefficient of performance, temperature of supplied air, overall coefficient of performance and daily efficiency with values of 14.1 ℃, 356 W, 0.76, 27.5 ℃, 0.2174 and 48.56% respectively. Moreover, the minimum measured temperature inside the tested room for that day is (34.4 ℃) at floor level and time of (11:00 AM)

while the minimum temperature at (28-June) at same time and location is (36.2 ℃); however, the minimum temperature at breathing level is at concentration of (60%) at (28-June) with value of (35.6 ℃) at time of (11:00 PM).

The best predicted results of the collector loop were obtained at 21-July with values for solar radiation, useful power, receiver surface temperature, generator temperature and collector efficiency of 1126 W/m^2, 1585 W, 96.32°C, 91°C and 79.2% respectively. The theoretical results for solar absorption system for 21-July at 01:00 PM and acetone concentration of 60% showed that, the air temperature difference across the evaporator, cooling effect, coefficient of performance, temperature of supplied air, daily coefficient of performance and overall coefficient of performance of 17.98 °C, 470 W, 0.4552, 13.22 °C 0.3387 and 0.2218 respectively. Moreover, the exergy destruction results for 21-July at 01:00 PM show that, the exergy destruction for collector, storage tank, generator, condenser, vapor throttling valve, evaporator, absorber, heat exchanger and solution throttling valve are (1358, 240, 663,135, 30, 116,517,675 and 769 W) respectively. The theoretical results for the cooled room showed that, the maximum values for air diffusion performance index(ADPI) and thermal ventilation effectiveness (ε_t) are at temperature of supplied air of 20 °C (temperature of design) with values of 70.92% and 1.402.

The comparison between theoretical and experimental results has been performed for 7-July by considering the heat gains from outside. The results showed an accepted agreement between the experimental and theoretical work at considering the outside heat gain.

Table of Contents

Title	Page No.
Abstract	I
Table of Contents	IV
Nomenclature	IX
Greek Letters	X
Sub-scripts	XI
Abbreviations	XII
CHAPTER ONE: Introduction	
1.1 Background	1
1.2 Solar Collectors	2
1.2.1 Parabolic Trough Solar Collector	3
1.3 Solar Absorption Cooling	4
1.4 Solar Assisted ventilation	6
1.5 Ventilation Systems	6
1.5.1 Displacement Ventilation (DV) System	7
1.6 Thermal Comfort Conditions and Its Parameters	9
1.7 Indoor Air Quality	9
1.8 Occupied Zone	10
1.9 Objectives of the Present Work	10
CHAPTER TWO: LITERATURE REVIEW	
2.1 Studies about the solar absorption cooling system	12
2.1.1 Experimental studies	12
2.1.2 Theoretical Studies	16
2.1.3 Experimental and Theoretical Studies	26
2.2 studies about the ventilation system	33
2.2.1 Theoretical Studies	33
2.3 Experimental and Theoretical Studies	34
2.5 Originality of the Present Work	36
CHAPTER THREE: EXPERIMENTAL APPARATUS AND PROCEDURE	
3.1 Components of the Solar Absorption Cooling System and the Tested Room	37
3.2 Design of the Insulated Tested Room	41

3.2.1 Cooling load calculations	43
3.2.2 Calculating supply temperature (T_s) and flowrate (V_{DV})	44
3.2.3 Supply air diffuser (DV)	46
3.2.4 The indoor room heat sources simulator	46
3.2.5 Description of the displacement ventilation system	48
3.3 Parabolic Trough Solar Collector Design	48
3.3.1 Reflector	48
3.3.2 Helical absorber tube	49
3.3.3 Support structure	49
3.3.4 The storage tank and hot water circulation	50
3.4 Absorption System Design	50
3.4.1 General assumptions of the absorption system	51
3.4.2 Design of generator	52
3.4.3 Design of condenser	57
3.4.4 Design of evaporator	59
3.4.5 Design of absorber	62
3.4.6 Solution heat exchanger design	64
3.4.7 Capillary tube design	66
3.4.8 Working fluid pair	68
3.5 Pumps	69
3.7 Temperature Measuring instrument	69
3.8 Experimental Procedures for the Absorption system and Room Test	70
3.9 Instruments Calibration	73
CHAPTER FOUR:THEORETICAL ANALYSIS	
4.1 Solar Angles	76
4.1.1 Latitude angle (ϕ)	77
4.1.2 Solar declination angle (δ)	77
4.1.3 Tilt angle (β)	77
4.1.4 Hour angle (ω)	78
4.1.5 Solar elevation (α)	78
4.1.6 Solar azimuth angle (γ_s)	79

4.1.7 Zenith angle(θ_z)	79
4.1.8 Angle of incidence(θ)	79
4.2 Direct Normal Radiation	79
4.3 Diffuse Radiation	80
4.4 Total Radiation	80
4.5 Solar Collector Loop	81
4.5.1 Parabolic trough solar collector (PTSC)	81
4.5.2 Calculation of thermal efficiency	81
4.5.3 Calculation of useful power	83
4.5.4 Heat balance of the tank	84
4.5.5 Exergy efficiency of the collector cycle	84
4.6 The Absorption Cycle	86
4.7 Quasi Steady State Model	88
4.7.1 Assumptions	88
4.7.2 Mass and energy analysis	88
4.8 Exergy Analysis of Solar Absorption Cycle	94
4.9 Thermodynamic Efficiency	98
4.10 The Engineering Equation Solver (EES) Software	99
4.11 Mathematical Formulation of Ventilation System	101
4.11.1 General governing conservation equations	101
4.12 Turbulence model	103
4.13 Computational Set and Numerical Scheme	104
4.13.1 General	104
4.13.2 Assumptions	104
4.13.3 Room geometry	105
4.13.4 Mesh generation	106
4.14 Verification Case	109
4.15 Numerical setup	110
4.15.1 Problem setup	111
4.15.2 Boundary conditions	112
4.16 Numerical solution procedure	113
4.16.1 Working fluid properties	113
4.16.2 Solution control	113
4.16.3 Convergence criteria	114
4.17 Prediction of Indoor Air Quality Parameters (IAQ)	117

4.17.1 Air mean age	117
4.17.2 Predicted percentage dissatisfied (PPD)	117
4.17.3 Predicted mean vote (PMV)	117
4.17.4 Air diffusion performance index (ADPI)	118
4.17.5 Thermal ventilation effectiveness	119
CHAPTER FIVE: RESULTS AND DISCUSSION	
5.1 Experimental Results	120
5.1.1 Collector loop and absorption loop results	121
5.1.1.1 Results of collector loop	121
5.1.1.2 Results of solar absorption system	127
5.1.2 Acetone Vapor mass flow rate empirical equation	137
5.1.2 Results of cooled space	138
5.2 Theoretical Results	142
5.2.1 Solar energy analysis	142
5.2.1.1 Results of solar collector	142
5.2.1.2 Results of solar absorption cooling system	146
5.2.1.3 Exergy analysis of collector loop	153
5.2.1.4 Exergy analysis of absorption system	154
5.2.1.5 Overall effecincy	159
5.2.2 Indoor air quality parameters	160
5.2.2.1 Air diffusion performance index (ADPI)	160
5.2.2.2 Thermal ventilation effectiveness (ε)	163
5.2.2.3 Temperature distribution	165
5.2.2.4 Velocity distribution	174
5.2.2.5 Mean age of air distribution	176
5.2.2.6 Predicted percentage dissatisfied (ppd) and predicted mean vote (pmv) distribution	179
5.3 Comparison Between the Experimental and Theoretical Results	181
CHAPTER SIX: CONCLUSIONS AND RECOMMENDATIONS	
6.1 Conclusions	186
6.2 Recommendations	188
REFERENCES	
References	189
APPENDICES	
Appendix (A):Tables	A-1
Appendix (B): Uncertainty Calculation of temperature.	B-1

Appendix (C): Comparison between experimental and theoretical work.	C-1
Appendix (D): Error Calculation.	D-1
Appendix (E): Published Papers	E-1

Nomenclature

Symbol	Description	Unit
A_c	Collector area	m^2
A_f	the floor area of room	m^2
AM	Air mass	…..
C	Optical concentration ratio	…..
CLTD	Cooling load temperature difference	℃
C_p	Specific heat	J/kg.ºC
EDT	effective draft temperature	℃
f	Darcy friction factor	…..
Gr	Grashof number	…..
h	Convection heat transfer coefficient	W/m^2. ºC
h_{fg}	Latent heat of evaporation	kJ/kg
HX	Heat exchanger effectiveness	…..
I_{dir}	Direct normal beam radiation	W/m^2
k	Thermal conductivity	W/m. ºC
L	Shell height	m
L_d	Thermal developing length	m
m	Mass	kg
Nu	Nusselt number	…..
P	pressure	N/m^2
Pr	Prandtl number	…..
$\dot{Q}$	Heat transfer rate	W
$\dot{q}_{ex}$	The heat gain from walls	W
$\dot{q}_{l}$	ceiling lighting heat source load	W
$\dot{q}_{oe}$	low level internal heat sources load	W
Ra	Rayleigh number	…..
Re	Reynolds number	…..
S	Solar irradiation	W/m^2
$S_{incident}$	direct normal incident solar irradiation per unit area	W/m^2
T	temperature	ºC
U	Total heat transfer coefficient.	W/m^2. ºC
U_o	Overall heat transfer coefficient	W/m^2. ºC
u_x	Velocity of supplied air in x-direction	m/s
V	Volume	m^3
V_{dv}	Volumetric flowrate	m^3/s
$\dot{V_{inf}}$	Infiltration volumetric flow rate	m^3/s
$\dot{W}_p$	Input power for pump	W
X	Acetone concentration	%

Greek Letters

Symbol	Description	Unit
α	Solar Elevation	degree
α_r	Absorptivity of receiver	…..
β	Tilt Angle	degree
γ_s	Solar Azimuth Angle	degree
δ	Solar Declination Angle	degree
ΔT	Temperature difference	℃
ΔT_{hf}	Temperature difference from head to foot level	℃
ε_a	Absorber tube emissivity	…..
ε_c	Effectiveness of contaminant removal	…..
ε_g	Glass envelope emissivity	…..
ε_t	Thermal ventilation effectiveness	…..
ζ	Thermal efficiency of collector	…..
η	Efficiency	…..
η_{ex}	exergy efficiency	…..
η_{sec}	Second law effeciency	…..
θ	Angle of incidence	degree
θ_z	Zenith Angle	degree
λ	Circulation ratio	…..
μ	Dynamic viscosity	kg/m.s
μ_t	Turbulent viscosity	$N.s/m^2$
ρ	Density	kg/m^3
σ	Stefan-Boltzmann constant	$W/m^2.K^4$
σ_{PTSC}	Effective transmissivity of PTSC	…..
τ	Time	s
τ_{cover}	Transmissivity of glass cover	…..
ϕ	Latitude Angle	degree
ψ	Ratio of obtained cooling effect to required cooling effect	…..
ω	Hour Angle	Degree

Subscripts

Symbol	Description
a	Absorber
av	Average
c	Condenser
dif	Diffused solar radiation
dir	Direct solar radiation
e	Evaporator
ex	External
g	Generator
hf	Head to foot level
HX	Heat exchanger
in	Inlet
Inf	Infiltration
l	Liquid
m	Mixing
out	Outlet
ov	Overall
r	Receiver
s	Supply
sp	Setup
ss	Strong solution
th	Thermal
v	Vapor
w	Water
ws	Weak solution

Abbreviations

Symbol	Description
ADPI	Air Diffusion Performance Index
ARs	Absorption Refrigerators
ASHRAE	American Society for Heating, Refrigeration, and Air Conditioning Engineers
CFD	Computational Fluid Dynamics
COP	Coefficient of Performance
CPC	Compound Parabolic Collector
CTC	Cylindrical Trough Collector
DV	Displacement Ventilation
EES	Engineering Equations Solver
ETC	Evacuated Tube Collector
FPC	Flat Plate Collector
HFC	Heliostat Field Collector
HVAC	Heating, Ventilating, and Air-Conditioning
IAQ	Indoor Air Quality
LEV	Local Exhaust Ventilation
LFR	Linear Fresnel Reflector
MV	Mixing Ventilation
PDR	Parabolic Dish Reflector
PMV	Predicted Mean Vote
PPD	Predicted Percentage Dissatisfied
PTC	Parabolic Trough Concentrator
PV	Personal Ventilation
SAC	Solar Absorption Cooling
SPSS	Statistical Product and Service Solutions

CHAPTER ONE

INTRODUCTION

CHAPTER ONE

INTRODUCTION

1.1 Background

The greatest benefit of solar energy in comparison to other kinds of energy is that it is clean and it is provided without any environmental pollution. It is also freely usable; merely it requires a collection system to harness it. The intermittent nature of its supply often makes it necessary to have a storage system. Nowadays, the conventional systems of collection and storing are highly expensive and not economic. To be more economically practical, the cost of collection and storing systems must be reduced. It should be mentioned that, the cost of material for a conventional collection and storing system is about 75% of the overall cost and so the reduction opportunity of the conventional system price seems not very bright, [1].

The climate of Iraq is hot, summer is dry, winter is cold, and the spring and autumn are warms, [2]. Iraq is one of the best locations on earth with sun-shine hours. Iraq has about 3000 annual sun-shine hours. Furthermore, Iraq has very long summer season, which lasts for about eight months when air conditioning is needed.

Due to this hot dry summer and cold winter, buildings in Iraq need cooling in summer and heating in winter. The climate is favorable for solar cooling, as the solar radiation is abundant and nearly in phase with the dry-bulb temperature. Iraq receives a high level of solar radiation: averages (7.56 kWh/m^2.day) in June and (5.02 kWh/m^2.day) annually, [3]. On the other hand, the impacts of a rare investment in the sector of power and tremendous rise in demand of electricity made a demand for reliable power. This, in turn, affected the using of the heating and cooling systems for buildings.

At summer, the cooling load is the greatest load on the electricity. Therefore, the solar energy can take the biggest influence to decrease it. The consumption of electricity for the system of cooling in the Arab countries, where the climate of hot desert prevails, takes about 70% of overall electricity consumption, [4].

Recently, the need for air conditioning and cooling has increased dramatically because of the population increase, increasing the standards of people living, as well as the great rise of the industrial plants. These have led to the spread of using systems of air conditioning utilizes compression technique. That caused a rapid rise of peak electricity need at summer that exceeded the limits of network capability and caused blackouts, [5].

1.2 Solar Collectors

There are two primary kinds of solar collectors: non-concentrating or stationary and concentrating. The non-concentrating collectors have the same area to intercept and absorb solar radiation, while a sun-tracking concentrating solar collectors usually have concave reflecting surfaces for intercepting and focusing the solar radiation to a smaller receiving area, thereby enhancing the radiation flux. There are several types of solar collectors available, [6]. Some of these collectors are:

1. Evacuated tube collector (ETC).
2. Flat plate collector (FPC).
3. Parabolic trough collector (PTC).
4. Compound parabolic collector (CPC).
5. Parabolic dish reflector (PDR).
6. Heliostat field collector (HFC).
7. Linear Fresnel reflector (LFR).
8. Cylindrical trough collector (CTC).

The parabolic trough collector (PTC) has a higher concentration ratio and it is also simple in setup, so it will be selected in this study.

1.2.1 Parabolic trough solar collector

The parabolic trough is a special kind of solar concentrators which has a cross sectional area such as a parabola in two dimensions and they are linear in the third direction. The parabolic shapes are extended linearly to construct a long reflector. The reflector shape concentrates sunlight along a line at the parabola focus. There is a heat receiver, normally a specially constructed pipe, which is located perfectly at this focus so that it can absorb the heat from the sun as shown in Fig. (1.1). The heat is transferred away by a fluid pumped through the pipe, [7].

Parabolic trough can effectively produce heat up to temperatures about (400 ℃). This collector is formed by a parabolic mirror and a metal black tube covered by a glass tube for reducing losses of heat to surroundings. This tube is extended along the mirror focal line, [8]. This kind of collectors will be used in the present work.

a- b-

Fig.(1.1) the parabolic trough solar collectors in two different tracking positions, [7].

1.3 Solar Absorption Cooling

Solar energy supplies cheap and clean energy for the applications of cooling all over the world. Absorption coolers may be operated using heat sources of low-quality such as solar energy or process waste heat. Alternating the commercially dominated vapor compression coolers with absorption refrigerators (ARs) reduces the consumption of electricity. Moreover, the main distinction between absorption and compression systems is the utilized working fluid. Compression systems mostly utilize chlorofluorocarbons (CFC) which are known that halogens causing ozone layers' depletion. The systems of absorption cooling are environmentally friendly because they utilize green natural materials such as ammonia, water, acetone etc. which are available and inexpensive, [8]. The solar absorption cooling system, thus, will be used in the present study.

Solar absorption cooling (SAC) utilizes harmless working fluids (refrigerants) such as water and ammonia to produce chilled fluid for the removal of heat through space-cooling, [9]. The coefficient of performance for the absorption system changes due to operating parameters, including change in temperature levels and load. The COP can be defined as: the heat extructed at lower temperature level to the provided heat flux, [10].

The typical (COP) of a single-effect solar absorption system is (0.5-0.8). The components of absorption systems are: generator, condenser, evaporator, and absorber. The working fluid is a mixture of a refrigerant and absorbent. A typical system is shown in Fig. (1.2). Heat (e.g., solar input) is transferred to vapourize the refrigerant from the solution entering the generator. The vapourized working fluid then passes through a condenser, and exit as a liquid. Heat is rejected at an intermediate temperature from the condensing process to a heat rejection water stream. The fluid then expands through a throttling valve to reduce the pressure, and enters an evaporator, where it removes heat from an incoming stream

to produce cooled air. This produces the useful cooling effect, as the cooled air is used for space-cooling in the distribution portion of the air conditioning system, [10].

The vapourized refrigerant is absorbed by a dilute solution within the absorber. The mixing heat and the latent heat of condensation resulting from the absorption process are extracted by a heat rejection medium, typically water. The absorbent, now rich in refrigerant (strong solution), is discharged through the heat exchanger to the generator, where it is heated above the boiling point of the solution, which causes the refrigerant to desorb. This heat is provided by the solar-heated fluid from the solar collectors. The absorbing solution, now with renewed absorbing capacity, returns to the absorber, while the vapourized refrigerant flows to the condenser, [10].

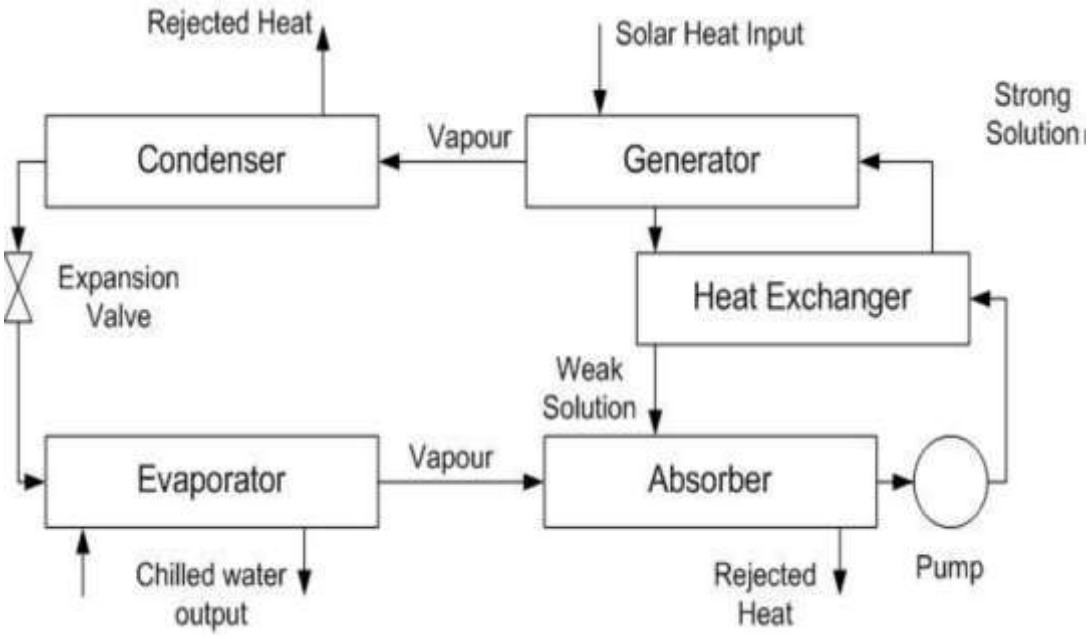

Fig. (1.2) schematic of a single-effect solar absorption chiller, [10].

1.4 Solar Assisted Ventilation

In Iraq, a great amount from the electricity is utilized for air conditioning at residential and commercial sectors, due to the higher temperature reached. Because the location of Iraq near the solar belts countries, the solar radiation levels and the need for air cooling in residential and commercial buildings reach peak level simultaneously, [11].

Solar-assisted ventilation systems reduce the maximum consumption of electricity. It has also less noise and it is free of vibration, because there is no a compressor. This makes it more reliable, and, thus, needs low maintenance and the consumption of its electricity is about four times less (21.8kW versus 5.5kW for 35kW of cooling) than that of an electric driven chiller with a mechanical compressor, [12]. Therefore, this system will be utilized in the present work.

Ventilation rate is one of the most significant parameters that affects the indoor air quality and consumption of energy for buildings, [13].

The ventilation process can be defined as the process of changing and replacing air (removing the old air and providing a fresh air instead). The ventilation controls and regulates the temperatures inside the rooms, in addition to eliminating unpleasant odors and harmful gases and controlling the level of humidity inside the building [14].

1.5 Ventilation Systems

Recently, different methods for ventilation systems design like the systems of displacement ventilation (DV), piston ventilation system, personal ventilation (PV) systems, local exhaust ventilation (LEV) and mixing ventilation (MV), as shown in Fig.(1.3), are utilized in a widespread case for providing an accepted indoor environment in

inhabited buildings and for enhancing the IAQ while decreasing the consumption of energy, [15]. The displacement ventilation (DV) system will be used in this work due to its high efficiency in comparison to other ventilation types.

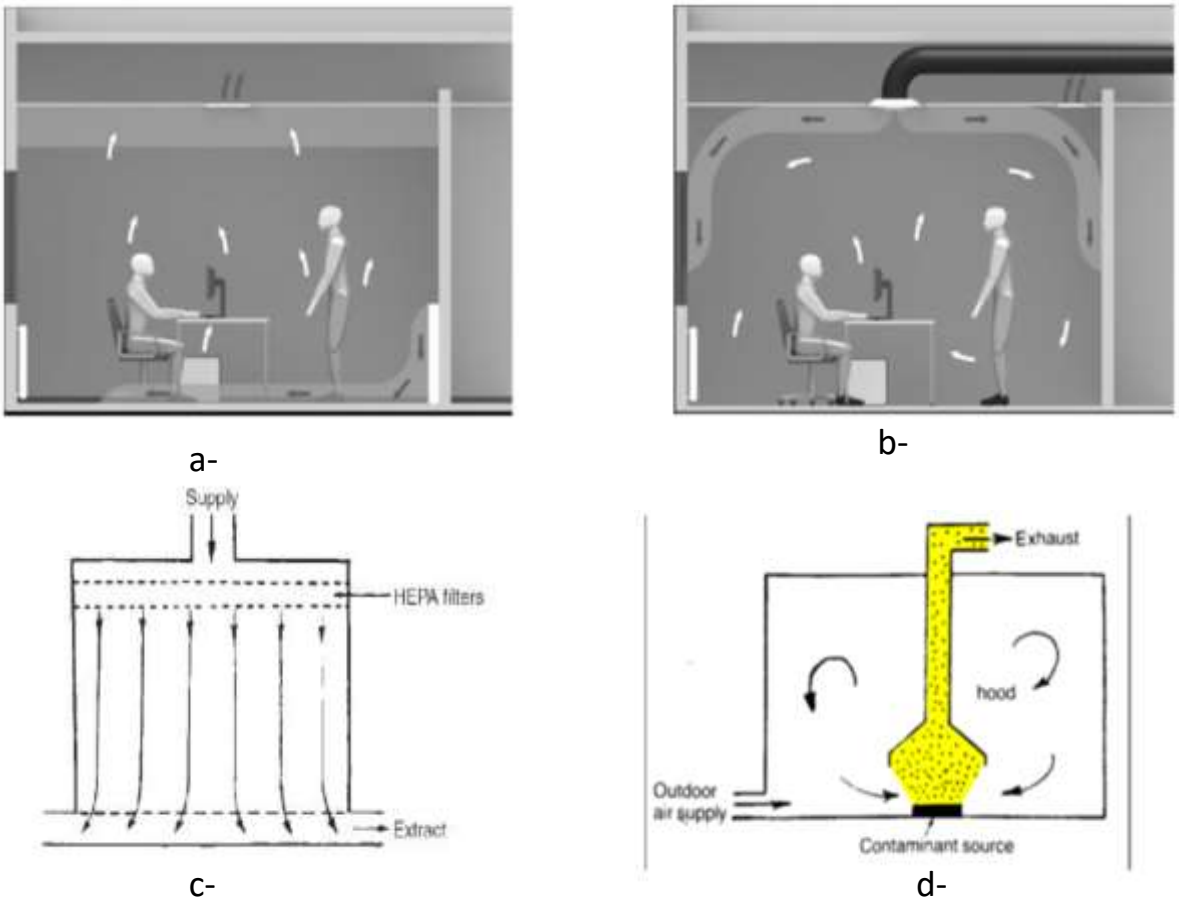

Fig.(1.3) types of ventilation systems. a-Displacement ventilation system. b- Mixing ventilation system. c- Piston ventilation system. d-Exhaust ventilation system, [12].

1.5.1 Displacement ventilation (DV) system

The cooled and fresh air in the system of displacement ventilation (DV) is normally provided at, or near to, floor level at lower velocity and the exit of air is located at ceiling level. The displacement system has been widely utilized in Scandinavian countries in recent times, [16]. At this system, the warm air moves towards the ceiling by natural convection due to its warming by contacting room heat sources such as people, equipment and lights. The temperatures of stratification and concentration of contaminant forms in the room, and the horizontal profile of temperature

are regular except for the regions close to the (DV) supply and sources of heat.

In (DV) system, the room is divided into two zones: the breathing zone from floor to head level, and the zone of contamination from head level to the ceiling as shown in Fig.(1.4). Recently, there is more attention for (DV) system in worldwide due to its capability to enhance the (IAQ) and give a comfortable environment in the room, [17]. The consumption of energy of (DV) system is 33% less than that of a comparable MV system, [18]. However, a draft risk because the difference in temperature between head and foot, and the distribution of movement contaminants are regarded to be the major drawbacks of this ventilation system type.

The objective of (DV) is to create conditions in the occupied zone close to the supply air conditions. However, care must be taken when the pollutants are generated from a large area source on the lower level such as from the floor, where the supply air may become contaminated before reaching the occupied zone, [19]. This type of ventilation will be considered in the present study.

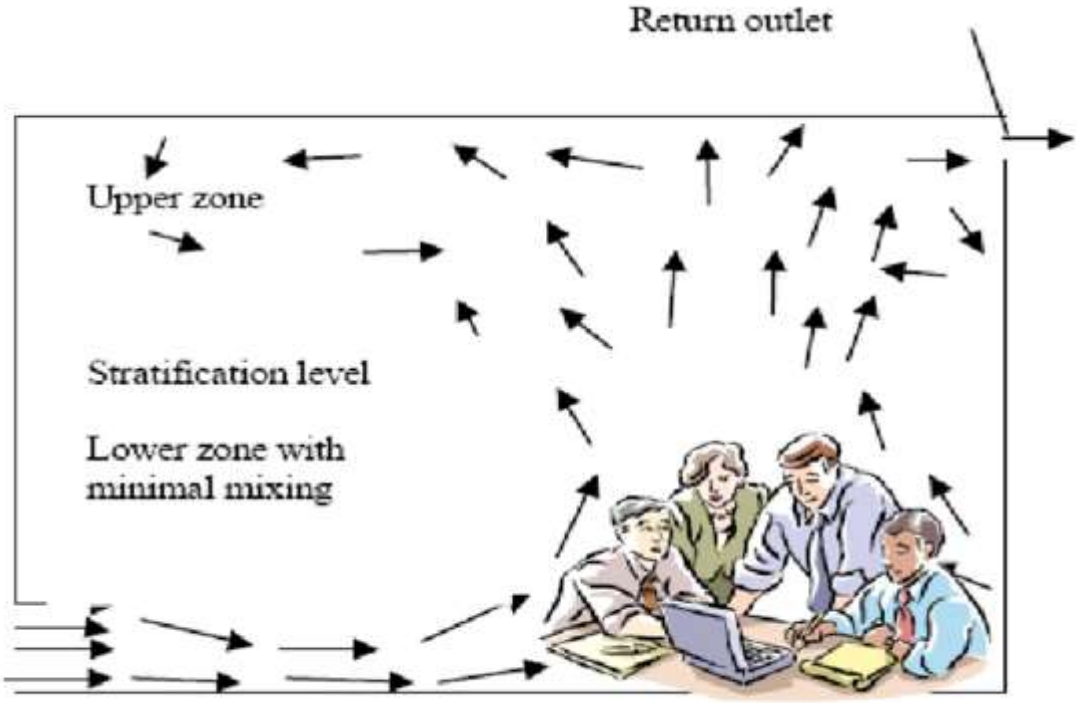

Fig. (1.4) typical room with displacement ventilation system, [17].

1.6 Thermal Comfort Conditions and Its Parameters

According to the utilization purposes, features of certain comfort condition, which can be considered as indicators of user's satisfaction in an environment, should be met on account of health and efficiency in a living space. Although a relative notion, some common conditions which are expected to be maintained in the environment according to the user's characteristics, [20].

Generally, the factors that affect the thermal comfort can be classified as personal and environmental factors. The ambient temperature, ambient relative humidity, speed of ambient air and average temperature are called environmental factors, while the personal factors are the person's metabolic activity rate and clothing, [21].

1.7 Indoor Air Quality

The sensible air quality is nearly corresponding to the pollution of indoor air and the rates of ventilation. The most pollutants found in the indoor air are organic (volatile organic compounds), inorganic (CO, CO_2, etc.) and environmental (tobacco smoke) and biological (fungi, mites, etc.). The pollutants come from different sources like outdoor air, the buildings fabric, furniture and human activities, [20]. The concentration of contaminant should be decreased to a minimum accepted value by supplying enough quantity of fresh air into the ventilated place for assuring occupants' health.

In the prediction of indoor air quality, many parameters must be studied such as the local ventilation effectiveness for the temperature distribution that describes the ventilation system ability to satisfy thermal comfort in a ventilated space.

The designers can use the concentration of CO_2as a best indicator. The peak allowed concentration of CO_2 in a room is about (1000) parts per million by volume (ppm) and the concentrations of CO_2 in the room greater

than (1000) ppm means a poor ventilation and greater levels of pollutants, [17].

The determining of time length where the supplied outdoor air remains in a room is useful, [17]. The local air age can be defined as the average time where the molecules of air remains at a special site in the room. This factor can be considered as a measure of air freshness: The "youngest" air is at the supply of air, whereas the "oldest" air may be at a zone of stagnation or at the exhausts.

1.8 Occupied Zone

The occupied zone is a space which occupants feel with an optimum climate with respect to indoor air quality and thermal comfort. Room area outside the occupied zone may have Areas of the room outside the occupied zone may have a compromised conditions, such as, great operative temperature, radiant temperature asymmetric, very high velocity of air and velocity gradient, [22]. These places may be near the inner boundaries or near the diffuser zone. Generally, the occupied zone can be defined as the place with 0.5-1.5 meter away from wall with windows, door, and radiator, and 0.25 – 0.75 m from external and internal walls. The height of occupied zone is about 1.1 m for seated person and 1.8 m for the standing person, [23].

1.9 Objectives of the Present Work

This work is comprised of both experimental and theoretical performance studies of a solar assisted ventilation system utilizing a new operating pair driven by solar energy under the Mid-Iraq climate conditions. The ventilation air flow rate is recognized as the main parameter for measuring the thermal comfort and indoor air quality. Therefore, the objectives of the present work are:

1- Fabricating and testing a solar assisted absorption cooling system with displacement ventilation operated with acetone-water pair and to test its performance under mid Iraq weather conditions.
2- Investigating the influence of many factors on output of a solar assisted absorption cooling system with displacement ventilation such as the effect of refrigerant mass flow rate, the concentration of refrigerant in the solution, the time, the day number, condenser temperature, velocity of supplied air and the location of air exit.
3- Obtaining the exergy analysis for the collector loop and the solar absorption cooling system.
4- Studying the effectiveness and performance of the displacement ventilation by calculating the air diffusion performance index, and heat removal effectiveness.
5- Predicting airflow motion and temperature distribution in the cooled space under Iraqi climate conditions using displacement ventilation system.
6- Calculating the efficiency of air exchange in a ventilated office room with a displacement ventilation system to reach an efficient air distribution system that provides a comfortable, healthy environment with less energy consumption under a hot climate.
7- Calculating other indoor air quality parameters such as the mean age of air, Predicted Percentage Dissatisfied (PPD) and Predicted Mean Vote (PMV) distribution in the tested room theoretically and how it changes with the solar radiation absorbed by the solar system and the concentration of acetone.
8- Comparing the experimental results with the numerically predicted results obtained by adopting appropriate turbulence model in a computational fluid dynamics (CFD) using AirPak software for improving air quality.

CHAPTER TWO

LITERATURE REVIEW

CHAPTER TWO

LITERATURE REVIEW

This chapter introduces the most significant and effective studies about the solar assisted absorption cooling system. The introduced studies are from different locations about world to see what are the difference in cooling load and the coefficient of performance around the world. It falls in two parts. The first part is the studies about the solar absorption cooling system and the second part are the studies about the ventilation system.

2.1 Studies about the solar absorption cooling system

It falls in three parts. The first part is the experimental studies and the second part is the theoretical studies, while the third part includes theoretical and experimental studies.

2.1.1 Experimental studies

Boonnasa and Namprakai, **(2010), [24],** conducted an experimental work on calculating the optimal potential for chilled water storage (CWS) and the related operating technique for air conditioning charges for different electricity tariffs. The capacity and peak demand of the mechanical chiller (MAC) could be reduced by more than 2 times and 31.2 % respectively. It could move power consumption by 35.7 % from the on-peak to the off-peak durations. The economic results revealed that the payback period(PB), the internal rate of return (IRR) and the net present value (NPV) were 10 y, 21% and 0.834 MUS$ relative to the new factory, with PB, IRR and NPV being 1.8 y, 66% and 1.28 MUS$ respectively.

Hamzah and Shahad, **(2012),[25],** modeled and manufactured an intermittent solar absorption cooling unit at Hillah city in Mid-Iraq. The solar absorption system was driven by a parabolic trough solar concentrator (PTSC) utilized as a solar rays mirror reflector with 2 m^2 aperture area. The aqua ammonia solution (NH_4OH) was utilized as a working fluid with various concentrations (25%, 30%, 35%, 40%). The peak pressure and temperature at generator were 12

bar and 120 ^{o}C respectively. The value of coefficient of performance (COP) between 0.01 and 0.09.

Mezher et al., (2014),[26], constructed, designed, and operated a solar absorption refrigeration system prototype using a flat plate collector due to its facility, cheapness and its efficiency. The methanol was used as a refrigerant to avoid global warming and greenhouse effect. The unit showed a (93.5 ^{o}C) peak generator temperature, on (July 18, 2013 at 2:30 pm), and the average generator temperature (T_{gavr}) was (74.7 °C), for that duration. The peak pressure (P_g) was (2.25 bar) on (July 19, 2013 at 2:00 pm). The tested system displayed a 0.15 ton cooling capacity with a (COP) of (0.48) and a minimum temperature of evaporator was (14.2 ^{o}C).

Widiharto et. al., (2015), [27], discussed the solar-absorption refrigeration unit modeling to replace traditional AC in seven lecture halls of the UGM department of Engineering Physics. The peak solar radiation was 4,802 kWh/m^2.day. The theoretical availability of solar energy from the NASA database was obtained utilizing homer by inputting latitude and altitude location of the department of Engineering Physics. The studied cooling load in the lecture halls was 15.63 kW. The average solar radiation absorbed by solar collector G_T was 4.802 kWh/m^2·day. The planned system's COP was around 0.84.

Ahmad et. al., (2016), [28], used a solar absorption system with three working fluids, namely water as an absorber, ammonia as a refrigerant and hydrogen as a pressure controlling gas. The installation and testing were carried out successfully and the vapor absorption system was used successfully utilizing hot water as a heat source from a 0.64m^2 solar collector. Mechanical improvements were done for the mini fridge for fitting the vapor absorption unit and the solar collector configuration have been conducted. 8 ℃ least cabin temperature has been investigated for a 40L mini fridge. The test circumstances were a sunny day, and the test time was 9 hours. The gained COP was 0.1675. The device tonnage was estimated as 0.0164TR.

Osman et. al., (2016), [29], modeled and fabricated a wr-lithium bromide (H_2O-LiBr) absorption refrigeration unit with a 1-TR capabilateity powered by solar power. A mathematical analysis of the absorption chilling loop was conducted for assessing the impact of different working circumstances on the thermal output. The outcomes of the experimental research, conducted in Khartoum city, revealed that the system COP of absorption refrigeration varied from 0.57 to 0.64, while the cooled water temperatures ranged mostly from 17 °C to 19.5 °C. Temperatures of condenser and absorber were below 45 °C, while the peak moving water temperature was 83 °C.

Gandhi et al., (2016), [30], attempted to estimate the cooling effect of the solar water heating unit and the vapor absorption cooling unit using a commercial flat plate collector of 100-liter storage tank in India. The solar water heating system consisted of an absorber plate on which the solar radiation dropped after passing through two 4 mm thick transparent covers with space 1.5 cm. They concluded that by using the vapor absorption refrigeration system, the solar flat plate water heater (SWH) could be used effectively in the summer to achieve refrigeration effect. The maximum temperature drop at the evaporator was 7 to 8 °C, while the system COP (Coefficient of Performance) was approximately 0.78 compared to the average COP system of 3.11 and the additional cooling cycle cost was very small.

Bux et al., (2017), [31], planned and tested an ecofriendly ammonia water vapor absorption cooling system of Solar Thermal Set Up. The system was designed and tested in Agnos College of Technology's Thermal Engineering Laboratory RKDF/ University Bhopal Madhya Pradesh for different operating conditions utilizing hot water as a heat source. The results showed that at using the vapor absorption cooling system, the solar flat plate collector water heater (SWH) could be used effectively in the summer to achieve cooling effect. The amount of cooling effect depended on the hot water temperature provided for the generator and the COP of system was approximately 0.78.

Chen et. al., (2017), [32], proposed a single-effect air-cooled absorption chiller with a 6 kW refrigeration power, and a solar cooling system. The air-cooled absorption chiller with single stage was manufactured and tested under a wide variety of steady state conditions as shown in Fig.(2.1). The chiller has been proven that it was effective for practical application without the risk of crystallization. The output of a solar air cooling system utilizing the proposed cooler was performed for residential refrigeration applications. The results explained that the absorption chiller tested could reach approximately 65 % of the building's overall refrigeration load with an overall COP of approximately 0.61. In addition, the solar air cooling system converted 28 % of the solar radiation to refrigeration energy.

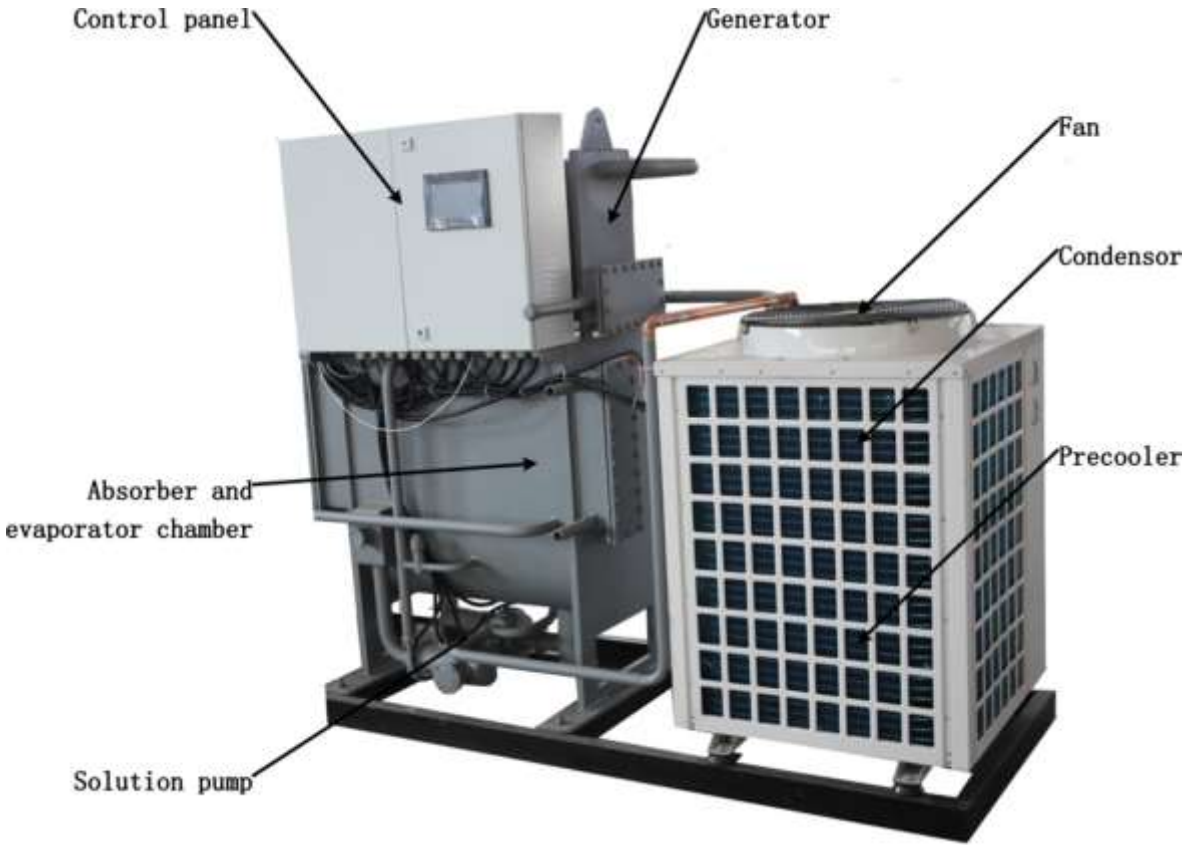

Fig.(2.1) prototype of the air-cooled absorption chiller, [32].

Reddy et. al., (2017), [33], configured a solar concentric dish collector with adjusted generator that refrigerates in vapor absorption device. An electrolux cooling system powered by three fluid systems, ammonia, water and hydrogen were used. Low-grade energy was used to drive this adapted device. The device was tested on sunny days. During sunny days the equipment was tested to provide

heat to the refrigeration system generator and the overall system was tested successfully. The lowest recorded temperature inside the 40L size mini fridge was 9 °C. The maximum coefficient of performance achieved was 0.172.

Huang et. al., (2019), [34], installed a solar refrigeration and heating unit with two heat pumps for air-source in Ningbo City, China, and has been in operation since 2018 with a chilling capacity of 35 Kw using LiBr-H_2O pair. The system was operated with two heat pumps with air-source, each with a refrigeration power of 23.8 kW and a 33 kW heating capability. They provided the operating outcomes and performance assessment of the system at the summer refrigeration and winter heating, moreover, during the typical summer day of 2018. It was found that the annual mean efficiency of collector was 44 % for refrigeration and 42 % for heating, and the absorption chiller mean COP was in the range of 0.68 and 0.76. With 56.6% average annual solar fraction for refrigeration and 62.5 % for heating. Annual energy savings was calculated as 41.1 % of the overall electricity consumption in buildings for refrigeration and heating.

Rahman et. al., (2020), [35], designed a solar absorption air cooling system operated under UAE climatic circumstances experimentally using lithium bromide-water pair as an operating fluid. Results showed that the system was capable of providing a required and uniform comfort temperatures at about 23°C inside the room. The COP of the system was evaluated to be 0.51. The outcomes explained that the new system was economically viable and environmentally friendly.

2.1.2 Theoretical studies

Grosu, (2014), [36], conducted an energy study of the absorption cooling unit by utilizing (lithium bromide-water) pair and solar energy as a source of heat. A simple refrigerator schematic and an improved one were compared utilizing Thermoptim and EES programs. There was an increment in the (COP) value from 0.69 to 0.8. Simulations were conducted for six condensation/absorption

temperature values ranging between 31 and 36 °C. The jump in these temperatures meant that the COP decreased from 0.8 to 0.56. The system analysis as a whole and of each portion showed a decrease in the system's exergetic efficiency from 0.27 to 0.18. An extensive exergy study of the absorber showed the real reasons of exergy destruction.

Fakhreddin, (2016), [37], planned a solar cooling system with a cold storage device for the Iraqi climate. Solar energy services have been evaluated and methods have been proposed to improve solar energy harvesting in the Iraqi environment using TRNSYS coupled with MATLAB software. The findings showed that the adoption of monthly average ideal tilt angle has led to an increase by almost 9% in the amount of solar energy produced. The optimum system proposed had an operating efficiency of 56%, a total rate of cost about US$ 4.19/hr, an annual CO_2 emission of 32199 kg with an annual total avoided CO_2 emission of 33.9% less than that of system without the use of a cold storage tank and a payback duration of 18.7 years. The payback was 9.3years, which is 50% less than the device without a cold storage container.

Cascetta et. al., (2017), [38], analyzed three various kinds of collectors (FPC, ETC and PTC) and two various chillers: single stage used with FPC and ETC collectors and (LiBr-H_2O) double stage for PTC collectors. The analysis was modeled by means of NEGST software (New Generation of Solar Thermal System) on a solar refrigeration and heating unit situated in Italy south. Thermal loads from people, PC, machines etc. have been evaluated by means of Energy Plus software. It was deduced that in the analysis of summer months, the PTC collectors have been more effective than the ETC and FPC collectors since the additional boiler did not operate during the months of summer, letting a minimum energy consumption for air cooling. In the winter study, collectors of ETC type were more effective than PTC and FPC, with a primary energy savings of 58 %.

Shirazi, (2017), [39], continually examined the matching of single-, double-and triple-stage absorption chillers with solar collectors using (LiBr-H_2O). The proposed systems had been modeled in (TRNSYS 17) software. They

observed that the triple-effect solar heating and cooling (SHC) cooler have a more power-efficient and good for the environment performance, led to around 47% and 62% decrease of the main power levels of consumption of the hotel and office buildings tests relative to the reference traditional systems and more than 75% funding would have been required to make sure that the suggested devices could accomplish a satisfying payback time (e.g. within 2 to 6 years). Parabolic tube collectors were proposed for such requirements and the chiller worked with COP of about 0.9-1.1 at an input temperature of ~168 °C, generating 6-7 kW of cooling.

Hui et. al., (2017), [40], conducted a study on the solar absorption refrigeration unit with the aid of Aspen Plus software. They proposed three pairs which are LiBr/H_2O, NH_3/H_2O and R134a/DMF. They found that when the temperature of condensing was 38 °C and the dilute solution concentration level was 54 % ~ 56 %, the low thermal solar collector could be chosen by the absorption cooling system of water-lithium bromide. The high/medium solar thermal collector was right for water-lithium bromide when the condenser temperature was greater than 42 °C. Only high/medium solar thermal collector could use the NH_3/H_2O unit. The R134a/DMF unit was suitable to the small solar thermal collector when the dwindled range was between 0.17 and 0.3. When the dwindled range was greater than 0.3, the R134a/DMF unit could choose a higher solar thermal collector.

Hussein, (2017), [41], developed and simulated the unit of absorption cooling using a solar receiver of flat-plate type with a mixture of (LiBr-H_2O) as an operating fluid using (TRNSYS and EES) software's. The weather conditions for the city of Erbil had been chosen for five proposed areas (140, 150, 160, 170 and 180 m^2). The effective field of the receiver of solar flat-plate has also been calculated and optimized for five proposed areas (140, 150, 160, 170 and 180 m^2). The results indicated tat the preferred form of the four absorption-chilling systems had a single effect, that had a COP of 80 % at a generator temperature of 81 °C. The outcomes also demonstrated that the optimal field of the receiver of solar flat-

plate was 160 m^2 that had accomplished the peak cooling and consuming capability of the generator (50 and 62.5 kW respectively).

Narayanan, (2017), [42], used solar thermal absorption refrigeration unit to power commercial/residences in India. A standard Indian commercial residences was used for simulation in TRNSYS. The simulation evaluated the feasibility and operating approach of the system, which was accompanied by a parametric test and an economic analysis of the model. Comparison to the cost of the conventional air conditioning system, that solar absorption refrigeration could take 13.6 years to pay off, and would take 15.5 years to pay back the cost of itself, and after all the additional money would be savings or income. Though the location selected for the test was one of the traditional tropical locations in India, that payback could differ with various locations, climate and refrigeration requirement.

Petela et. al., (2017), [43], noticed a compromise situation very likely exists between efficiency of collector and the (COP) of the absorption unit using the TRNSYS and EES software's. Through their theoretical analysis, they considered a solar chiller operated under a moderate climatic circumstances of Poland for representative days of three months during the cooling season. The simulation outcomes were compared with the reference case of fixed driving temperature. They noted through their computations that the refrigeration power output could be increased at different levels, more than 34 W per 1 m^2 of solar collector, by changing the driving temperature of the chiller during the cooling season.

Bellos et. Al., (2017), [44], presented an absorption cooler that was a single stage with a working pair of LiBr-H_2O combined with the evacuated tube collectors for cooling a building with a total area of 100 m^2. Ten regions were investigated and the evaluation was carried out with the open source software TRNSYS. According to the final outcome, Phoenix and Abu-Dhabi seem to be the most appropriate areas with a leveled cooling cost (LCOR) of 0.0611 € /kWh and 0.0667 € /kWh accordingly. The less appropriate sites are Rome and Istanbul

with 0.1897€/kWh and 0.1797€/kWh accordingly. In addition, locations with higher cooling loads and higher solar capacity have been described as the most appropriate areas for installation of solar air conditioning systems.

Xu & Wang, (2018), [45], investigated the choice of better chiller for solar absorption refrigeration units with CPC. They utilized LiBr-water absorption cooler included a chiller with single effect, an absorption chiller double effect and a novel chiller with variable effect. The unit of variable effect had high solar refrigeration fraction, low supplementary heat input and solar efficiency with high value. The unit of single stage had a medium solar fraction, high supplementary heat input and medium solar efficiency. The unit of double effect has a low solar refrigeration fraction, low supplementary heat input and solar efficiency with low value. The wider area of the solar collector raised the solar cooling proportion and decreased the supplementary heat supply.

Adibi, (2018), [46], used the renewable energy for refrigeration applications in the Middle East. The refrigeration load was estimated for big cities in the Middle East using the ammonia as shown in Fig.(2.2). Variations in temperature and refrigeration capacity were calculated in various months and hours of the day using EES software. The analysis indicated that the refrigeration capacity changed throughout the day. Interestingly, the findings revealed that the peak cooling power was similar to the peak refrigeration load of the building. The effect of the AARC heat exchanger efficiency was also explored. Results revealed that the (COP) and refrigeration power improved when the quality of the AARC heat exchanger improved.

Jing et. al., (2018), [47], adapted the match of solar cooling, i.e. solar/natural gas-driven absorption chiller (SNGDAC), solar vapor compression – absorption of integrated parallel configuration cooling system (SVCAIPCCS), and solar absorption-subcooled compression hybrid refrigeration system (SASCHRS). Building refrigeration was dependent on exergy economics. Three forms of construction refrigeration have been regarded: category 1 was a building of single-story, category 2 was the two-story and three-story constructions, and

category 3 was a building of multi-story. In addition, two cities from China, Guangzhou and Turpan, were taken into consideration. The flow rate of cost of the commodity was used as the main decision parameter. As a result, SNGDAC was regarded as an appropriate option for type 1 residences in Turpan due to its negligible consumption of natural gas and the lowest cost flow rate of product. SVCAIRSPC was more appropriate to type 2 building in Turpan due to its high actual absorption module refrigeration capability and lower fuel and product price flow rate. In addition, SASCHCS was the most comprehensive price-effectiveness, i.e., its energy depletion and product price flow rates were both the minimum if it is utilized in whole building types in Guangzhou or Class 3 buildings in Turpan.

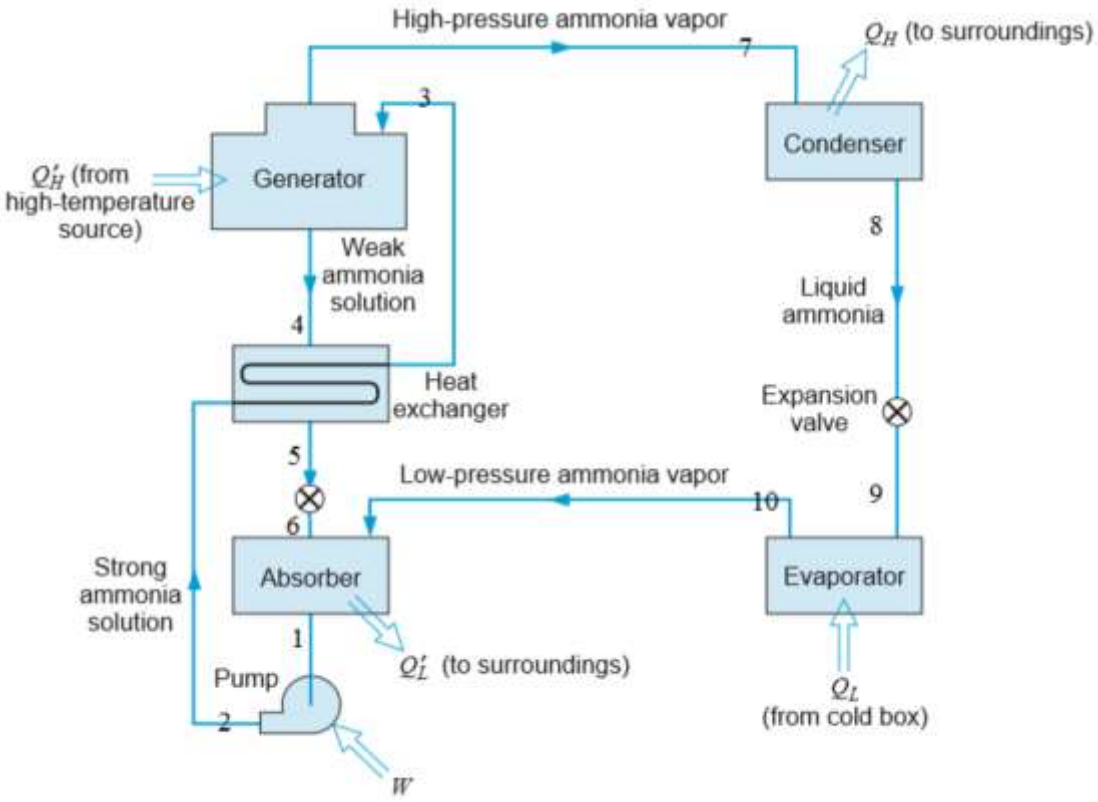

Fig.(2.2). the ammonia absorption refrigeration cycle, [46].

Dwivedi & Mishra, (2018), [48], improved the output of the system with half-effect by adding the Loop Heat Pipe (LHP) between the high absorber, high generator and the condenser (which had been eventually substituted by the LHP) for heat exchange with intra-cycle. The computations demonstrated that first law coefficient of performance (COPI) and second law coefficient of performance

(COPII) were enhanced by 64% and 27 %, respectively. The temperature of the LHP condenser T_{Cond} was also dependent on the temperature of the generator T_G. At higher T_G levels, the rise in COPII was greater than that in COPI. The mean heat leakage from the Q_{Leak} LHP was approximately 14.38 kW and the mean heat used by the Q_{Cond} LHP was determined to be 79.52 kW.

Kumar et. al., (2018), [49], provided a comparison and optimization between the single-effect LiCl-H_2O and LiBr-H_2O absorption refrigeration units incorporated with various types of solar collectors in Gujarat, India. An analysis of a 10 kW system at 7°C included four distinct solar collectors (flat-plate collectors (FPCs), parabolic trough collectors (PTCs), flat plate with compound parabolic reflectors (CPCs) and evacuated tube collectors (ETCs) connected to an adiabatic storage tank for supplying the LiCl-H_2O and LiBr-H_2O vapor absorption systems. With steady state conditions, a code was made in (EES) software and characteristics of each pair were taken from EES software. The study found the influence of heat source temperature on the quality aspects of the systems. Optimized temperature of heat source with regards to the energy and exergy features of the LiCl-H_2O pair was remarked to be lowest compared to the LiBr-H_2O pair for all types of collectors. Exergetic optimizing of each unit calculated the optimum required refrigeration collection area. Capital costs have been assessed at optimum collector areas. The differentiation between optimized devices defined that technology based on ETC was the most economical and, from an exergetic standpoint, PTC was recommended.

Arabkoohsar et al., (2018), [50], used absorption refrigerator that was solar assisted with systems of gas transmission. There were some expansion channels where the pressure of gas is significantly decreased. The drop in pressure causes the temperature to collapse in the gas stream. The Power Productive Gas Expansion Station (PPGES) was the latest design proposed for the channels where the device was configured with energy generation devices. They invested advantage of that drop in temperature for refrigeration production, which was suggested by combining the station with an absorption cooler. In that case,

the cooler could also meet the heating requirements of the expansion station. For assessing the suggested setup effectiveness, it was modeled for a case study in Denmark, i.e. Aarhus University (AU) hospital absorption cooler and Viborg gas station. The findings explained that an annual refrigeration output contribution of 27 % could be given by the expansion station. Moreover, there was a significant increase in the leveled energy cost (LCOE) of the case study in the use of the hybrid unit rather than the traditional chiller.

Uçkan et. al., (2019), [51], presented a solar-driven single-stage and used lithium bromide as an absorber and water as a refrigerant with a 35.17 kW refrigeration power theoretically using (TRNSYS) software. The system consisted of an evacuated tube solar collector using 95 m^2 aperture area. The collector slope was 30° with the horizon. The storage capacity of the hot water tank was 3 m^3. The unit cooled a ground area of 270 m^2. The outcome was that the COP of the chiller oscillated between 0.69 and 0.67 between 8:00 a.m. and 14:00 p.m. Afterwards, the COP of chiller gradually decreased from 14:00 to 18:00 between 0.69 and 0.57. The COP of the chiller was noticed to be 0.63. The optimization results of the unit revealed that the unit provided air conditioning for a construction of 270 m^2.

Pandya et. al., (2019), [52], compared the quality of the LiBr-H_2O and LiCl-H_2O double effect solar assisted vapor absorption refrigeration systems (VARS) combined with various solar collectors theoretically using EES software. The power capacity was 100 kW at 5°C temperature of evaporator and two temperatures of condensation 30°C and 40°C incorporated with the evacuated tube collector (ETC) and the parabolic trough collector (PTC). The impact of the temperature of the heat source on the thermodynamic and economic features of the devices has been shown. LiCl-H_2O VARS had been shown to have improved thermodynamic and economic quality in comparison to the LiBr-H_2O system. In addition, it was noticed that the appropriate mean typical collection area for the LiCl-H_2O pair was near to 1.25 m^2/kW, that was relatively low. The comparative evaluation showed that the ETC device was preferable from an economic point of

view and that the PTC device was suggested from a thermodynamic production standpoint.

Abdulateef et. al., (2019), [53], dealt with the theoretical analysis of a solar assisted refrigeration cooling system with MATLAB for investigating the irreversibility's of individual system elements and the system total entropy generation($\dot{S}_{tot}$). The outcomes showed that both ($\dot{S}_{tot}$) and (COP) were proportional to evaporator and generator temperatures and they inversely proportional to the absorber and condenser temperatures. Moreover, the greatest fraction of total destruction losses for the system was at the collector with fraction of (70%) and the next were the generator and absorber with the range of (6-14%). Therefore, these components needed more improvements in the aspects of design.

Nandi et. al., **(2019), [54],** analyzed a simple ammonia-water absorption system driven by solar power. The output of low power single-effect absorption refrigeration systems was, suitable for small building and residential applications. The major heat source was heat provided by solar collectors. Work had been carried out to check the coefficient of performance and circulation ratio using solar based system to observe the variables like flow rate and composition. The coefficient of performance was found to be 0.58.

Toprak et. al., **(2020), [55],** simulated the thermal performance of a building chilled for a time of 14 h/day using TRNSYS software. The unit utilized 1000 m^2 of parabolic trough solar collector with a cooling capacity of 1020 kW. The effect of cooled water storage (CWS) and refrigerating water storage (RWS) on the system output for various working hours per day under Izmir (Turkey) and Phoenix (USA) weather circumstances was analyzed. When the unit works for 14 h/day as the load for both systems and locations, the solar collector efficiency variation and the refrigeration load to the ratio of input heat remained less than 4% after the arrangements. From adding CWS to the reference system, a parametric study consisting of varying the unit working hours per day showed that a reduction of 34% of the needed refrigeration capacity of the unit. The power factor of the unit was increased from the reference value of 41% to 96%.

Abusaibaa et. al., (2020), [56], used a single acting solar absorption refrigeration system at climate of Najaf, Iraq. In the system model, a 105,6 kW single acting absorption coolers, was powered by evacuated tube collectors (ETC). TRNSYS (version 18) simulation was utilized to choose the different system factors and optimize them for increasing the efficiency of solar system. The computations developed a solar refrigeration model that simulated reality and was utilized considerably to cool service buildings. It was also found that the solar absorption loop decreases the annual electricity usage where the solar fraction was higher, up to 77% at Najaf, Iraq. Moreover, using solar power could give further profits for the governments as a reduction of CO_2 of 68.88 tons/ year.

Al-Falahi et. al., **(2020), [57],** investigated the output of energy of a solar assisted air-cooling device using absorption technique under Baghdad, Iraq weather conditions. The solar fraction and the thermal output of the solar air-cooling device were conducted for different summer months using (TRNSYS) software. The results discovered that the device working in August explained the best monthly mean solar fraction of (59.4%) and (COP) of (0.52) value because the higher solar radiation in this month. The seasonal efficiency of collector was 54% with 58% seasonal solar fraction and 0.44 absorption chiller COP.

Lamine et. al, (2020), **[58],** presented a thermodynamic of energy and exergy analysis for ammonia-water and ammonia-lithium nitrate absorption cooling coupled to flat plate collector with double glazing. The energy was stored in an adiabatic storage tank. The models were based on the first and second laws of thermodynamic using (FORTRAN) software for calculations. The outcomes indicated that ammonia-lithium nitrate loop gave better outputs than the ammonia-water cycle. Therefore, it could be used alternative to the ammonia-water loop. The exergy analysis showed that the system total exergy loss is associated strongly to the operating temperatures.

Chekir et. al., (2020), [59], simulated a solar absorption chiller using three operating mixtures: acetone/ propane, acetone/butane and acetone/iso-butane. The outcomes were compared with the water/ammonia mixture at the same

assumptions and operating conditions. The major benefits of the analyzed refrigerants were their similar refrigeration effect in comparison with ammonia with a COP of 0.58 to 0.63, and also, their low operating pressures. Although, the hydrocarbon mixture circulation ratio was higher in comparison with ammonia. Acetone/propane operating mixture was suitable for solar absorption air conditioners with some private precautions. The heat energy was supplied from evacuated tube solar collector with area of 90 m^2.

Tawalbeh et. al., (2020),[60], performed a parametric theoretical study of solar absorption cooling system with (LiBr-H_2O) operating pair using Engineering Equations Solver (EES) software to explain the effect of size of heat exchanger on the chiller coefficient of performance. It was found that the proposed system could work with optimum cooling power reaches to 16 kW and a high coefficient of performance about (0.7) while it was driven by a low grade energy. Moreover, increasing the mass flow rate of heat source had a considerably effect on both cooling power and COP at low values (< 10 kg/s) and not sensible effect at higher values (> 10 kg/s).

Souri et. al., (2020), [61], simulated a flat plate absorption cooling system using LiBr-H_2O mixture as an operating fluid at Tehran. The daily operation of the cooling system, showed that for the solar absorption cooling, there would be an optimum number of flat plate collectors which was 50. This number could give about 5 kW of cooling load a cooling load. It was found that the system COP was varying between 0.65 to 0.75 and it increased with increasing the evaporator temperature at constant generator temperature.

2.1.3 Experimental and theoretical studies

Rosiek & Batlles, (2011), [62], identified the quality of the air-conditioning device that is solar-assisted with two reservoirs mounted in the Research Center of Solar Energy (CIESOL) building using artificial neural network (ANN). The input`s weights were modified for producing an estimated output within specified errors. The device was mainly consisted of a solar

collector arrays, an absorption chiller that was driven by hot-water, a cooling tower, two hot storage tanks, a supplementary heater and two tanks for cold water. The outcomes indicated accurate estimates with a Root Mean Square Error (RMSE) less than 0.70 % and virtually zero variance, which could be regarded quite acceptable.

Gonzalez et al., (2012), [63], presented an adiabatic absorber flat-fan sheets which enables LiBr-H_2O air-cooled absorption machines in Madrid to operate far from crystallization limitations. A simulation model was performed in MatLab for the simulation of the system. A better agreement was observed between estimations and outcomes of experiments for most of the absorber's characteristic working variables. Lastly, it had been noted that the suggested absorber design allowed LiBr/H_2O air-cooled absorption devices to operate far from limitations of crystallization even at temperatures of the ambient of around 40°C.

Marc et al., (2012), [64], conducted a static modeling to evaluate chiller behavior with a 30 kW refrigeration power (EAW LB30 refrigerator using LiBr/H_2O solution pair. The results from experiments were analyzed and the steady-state chiller prototype and the identifying technique were established. The applied technique in this work used outcomes from experiments obtained in actual operation for creating a model which may be utilized for assessing the actual outputs of the installation in the design and the working phase. There was an agreement between the experimental results and the estimations guaranteed the model to be used not only for the design of the installation, but also for the monitoring and control of its performance.

Azhar & Siddiqui, (2013), [65], investigated and compared the vapor absorption loop single, double and triple effect by using LiBr-H_2O as an operating pair. Liquefied petroleum gas (LPG) and compressed natural gas (CNG) were chosen as the energy sources because the system with triple-effect need heat with quietly high temperatures. The experiment was conducted for various

temperatures of evaporator and condenser. The Peak COP of the collector with single effect loop was noted to be 0.7 to 0.86, and for double effect loop was 1.2 to 1.55, while it was found to be up to 2.16 in the triple effect loop. The improvement in the double effect loop COP reached 56-81% of that of the single effect loop, and for the triple effect was 103-152%. The operational cost of the double effect loop was between 57 and 68 % of the single effect loop, while for the triple effect loop, it was between 60 and 75 % of the double effect loop and between 40 and 45 % of the single effect loop.

Schwerdt et. al., (2014), [66], proved the operational feasibility of the AC system that was solar powered throughout a productive demonstration project of Fraunhofer UMSICHT, Germany and Assiut University at Egypt. It included the simulation of the system, design, installation and process of an optimized solar-powered residential cooling unit. The project was designed to test, control and assess the thermally controlled cooling process at the braving working circumstances of the Upper Nile Valley. It was demonstrated that the efficiency of chiller enhanced by 20-50 %, while the refrigeration power improved by about 15 %. Although the mounted cooling tower operated well under environmental conditions with lower relative humidity of ambient, the refrigeration capacity was just given by evaporation, thus consuming more than ~25 l/h (~300 l/d) of water.

Aman et. al., (2014), [67], proposed a solar absorption cooling system with 10 kW power capacity using ammonia-water pair. From the analysis, it was found that the most exergy loss which about (63%) occurred in the absorber and (13%) for the generator, while its value was (11%) for the condenser. It was seen that reducing absorber and condenser temperature to the ambient temperature did not considerably affect the system overall performance. Therefore, the absorption cooling system using water- ammonia and driven by solar collector with cooling of condenser and absorber by ambient temperature can be utilized for small-scale applications.

Sun et. al., (2015), [68], conducted and installed a refrigeration and heating system built on an absorption cooling that could be powered by both gas firing

and solar hot water. An energy mix for Net zero-energy building (nZEB) was evaluated from numerical simulations and in-field meteorological data. The unit was a hybrid capable of single-acting solar cooling and double-acting gas-fired cooling as well as their mixture. It operated in gas-fired configuration (dual-stage) when solar energy was not sufficient or the temperature of solar hot water was lower. The model and process plan was to utilize solar energy at first and gas fired as a replacement, so fossil energy savings were apparent. The gas/solar-driven absorption device could save gas usage of 49.7% compared to the gas-fired absorption system.

Zhai et. al., (2015), [69], built and mounted a mini-type solar absorption refrigeration unit which consisted of a single absorption cooler with 8 kW refrigeration power and a water storage tank with volume of 3 m^3 to store heat. The cooled water could be supplied either to the fan coils or to the radiant refrigeration panels which were mounted to meet the indoor thermal condition of the test area. It was noticed that the mean refrigeration output for the fan coil refrigeration mode was 3.62 kW during 8 hours of working under typical Shanghai weather conditions. With reference to the radiant refrigeration mode, a single fresh air unit was mounted to avoid the condensation of the cooling panels. In comparison to the experimental data of the fan coil refrigeration mode, the mean refrigeration output of the radiant refrigeration mode was 4.47 kW, which improved by 23.5 %.

Soussi et. al., (2017), [70], studied the estimation of a solar refrigeration system within an office building at Tunisia. The solar system consisted of solar collector of a linear parabolic trough type combined to 16 kW dual-stage lithium bromide absorption refrigerator with 126 m^2 building of laboratory. A dynamic model integrating the solar cooling unit using the TRNSYS software to evaluate the case study and enhance its performance. The results of the model revealed that the efficiency of the collectors ranged from 26–35 %, the coefficient of performance from 0.65 to 1.29, and the daily peak solar COP reached about 35 %. However, the solar unit was incapable to meet 32.3 % of the refrigeration

demands and the absorption chiller was turned on for only 53.8 % of its total working time. As a consequence, the chiller running time raised to 75.8 %, the cooling capacity improved by 75.6 %, the solar COP attained 57% and the fraction of solar was 87% on average. The estimated annual CO_2 emission avoided was 2947 kg.

Wang et. al., (2018), [71], suggested a dual stage LiBr – H_2O system of absorption refrigeration focused on the solar heat collector (PTC) parabolic trough. Thermodynamic prototypes, like PTC and absorption cooling, were built and confirmed by a comparison of computation outputs and findings from experiments. Subsequently, the effect of variable design specifications on thermodynamic efficiency was examined and addressed. The mathematical model of the absorption chiller driven by steam was conducted and simulated utilizing EES, and particularly, the thermal characteristics of the LiBr–H_2O solution were directly obtained from the EES software. The examination of the solar refrigeration system in the case study yielded a mean COP of the absorption cooling was around 1,195, and the system efficiency of solar refrigeration as a whole reached 61.98 % of solar energy using capacity.

Abdul Ameer and Shahad, (2018), [72], designed and built a two-dimensional compound, parabolic, concentrated solar collector for Iraqi climate. This compound parabolic concentrator was made of two parabolas of stainless steel with a concentration ratio of (5). The collector was examined during August, September and October. The results revealed that the peak measured temperature of hot water was (90 ^oC) at (0.0277 kg/s) mass flow rate and (94 ^oC) at (0.0377 kg/s) flow rate. It was found that a peak thermal efficiency was (67%) at (0.0277 kg/s) flow rate while it increased to about (69%) at (0.0377 kg/s) flow rate. The peak obtained theoretical thermal efficiency was (73%) at (0.0277 kg/s) flow rate and (75%) at (0.0377 kg/s) flow rate.

Abdul Ameer, (2018), [73], conducted an experimental and theoretical study for a solar-powered continuous flow absorption cooling unit using a compound parabolic concentrator (CPC) and two pairs of working fluids, LiBr-

H_2O and diethyl ether-ethanol. The simulation was performed using EES program. The results of the experiment revealed that the peak thermal efficiency achieved was approximately at 12:00 p.m. on 21st of each month from January to June about (0.48, 0.512, 0.57, 0.606, 0.618 and 0.67) respectively when the rate of flow was 0.0277 kg/s while the thermal efficiency was boosted to (0.5, 0.512, 0.58, 0.63, 0.637 and 0.69) when the water mass flow rate raised for 0.0377 kg/s. In addition, the hot water temperature was 98 °C and 94 °C at the two rates of mass flow, respectively. In the mathematical model, the thermal efficiency at 12:00 p.m. for the 21st of each month ranged from (0.67-0.73) for (0.0277 kg/s) flow rate with a (4.5) concentration ratio at the same climate conditions.

Nasruddin et al., (2019),[74], investigated a technique for prediction of the absorption chiller performance using solar collectors. Artificial Neural Network (ANN) was utilized based on data from experiments for predicting the solar absorption chiller performance at Universitas Indonesia. The Principle Component Analysis (PCA) was utilized for reducing the number of input parameters for performance predicting without sacrificing of the ANN's prediction accuracy, PCA identified the sensitive parameters from all input parameters. The presented combined model of ANN model and PCA (ANN+PCA) explained a better performance which had a comparable error with ANN model, specifically the configuration 9–6-2 (9 neurons, 6 inputs, 2 outputs) of the ANN +PCA model led to a COP root mean-square error of 0.0145.

Boero et. al., (2019), [75], made an assessment for the technical practice of a solar absorption cooling system at a small- scale application in an office building with a tropical climate in Ecuador at three cities numerically. The dynamic transient software TRANSYS was utilized for the modeling and simulation. The simulation was validated utilizing experimental data obtained from a real-life system with major elements: a vacuum tube collector with 12 m^2, $LiBr/H_2O$ absorption cooling system with power capacity of 4.5 kW, fan coil with 6 kW and sensible cold storage of 100 litre. The simulation outcomes showed a better agreement with the data from the experiments with 8.5% deviation. The

capacity of system predicted for the cities of Ecuador was as follows: a collector area of evacuated tube was 24 m^2, a heat exchanger with 20 kW, a single-effect LiBr/H2O with a power capacity of 15 kW, a cooling tower with 35 kW and 2 m^3 cold storage. It was found that the proposed system could investigate most of the demanded cooling load (Guayaquil and San Cristobal with 90%, Manta, considering a set point of 24℃ with 71%) of a typical single-story office building.

Qadeer et. al., **(2020), [76],** presented an experimental and theoretical study about a small-scale solar absorption refrigeration with 3.52 kW refrigeration power using LiBr/H_2O under the climate of Taxila, Pakistan. The theoretical model was applied to a flat-plate solar collectors for achieving the needed working mean temperature of 75°C. The mathematical analysis was obtained by applying the mass and energy balance for all system components by utilizing ESS software. The absorption system was driven by a solar collector for heating the water. It was found that the obtained peak mean system COP was 0.70, and 75 °C exit temperature of the solar collector.

Huirem et. al., (2020), [77], presented a steady-state model by using thermodynamic first and second laws for a single-effect solar absorption chiller with a cooling effect of 17.5kW. It was found that increasing generator temperature increases both of COP and exergetic coefficient of performance (ECOP). The rise of evaporator temperature from 1℃ to 7℃ increased the COP and decreases ECOP and total exergy destruction (TED), so the peak cooling capacity occured at the lower evaporator temperatures, since the maximum chilling potential was obtained at lower evaporator temperature. The optimum COP, ECOP and TED was 0.79, 0.448 and 0.821 kW respectively.

Ghayadh , (2020), [78], presented an experimental and theoretical study about a single effect solar absorption cooling system. The study was performed at middle of Iraq at Hilla city (32.4◦ latitude and 44.4◦ longitude). The solar system was driven by a parabolic trough solar collector (PTSC) with an aperture area of 2m^2.Two pairs of solutions were studied which are (methanol-water and acetone-zinc bromide). The first pair was studied using three concentrations of methanol

(40%, 50% and 60%) while the first pair studied using a concentration of 60%. It was found that the COP of the absorption system was in the range of 0.22 to 0.28 and the temperature drop across the evaporator was ranged from 9.8 ℃ to 15.8 ℃ for the methanol-water pair. While for acetone-zinc bromide, the maximum COP was 0.487 and the maximum temperature drop was 16℃. The theoretical study performed by using EES software. It was found that the theoretical study satisfied the experimental work.

2.2 studies about the ventilation system

2.2.1 Theoretical studies

Shbeeb A. A., (2020), [79], investigated the effect of combining the chilled ceiling with displacement ventilation system using one-way rectangular diffuser and semi-circular diffuser. The study was performed in Iraq (Hilla city) climate (hot and dry). The theoretical study was performed using (AIRPAK) software. The indoor air quality parameters were estimated numerically. Three tests were performed with different ratios of chilled ceiling load as (25%, 50% and 80%) in terms of the total cooling load required. The temperatures of air supply from diffuser are (19, 22, and 24.5 ^{o}C) at (0.045 m^3/s) flow rate of air while the temperatures of chilled ceiling are (21.5, 19 and 16 ^{o}C). It was found that the effect of diffuser shape on air age decreased with height and the maximum difference of mean age at height of (0.1 m) with value of (49 s) while its value is (11 s) at height of (2.25 m). The efficiency of air exchange for the CC/DV system at using semi-circular diffuser in the office space was greater by a mean value of 8.5% in comparison to the other case at the same conditions. The difference was reduced 3% at each increase in ratio of chilled ceiling cooling load.

Saheb et. al., (2021),[80] investigated the improvement of the inhaled indoor air quality using two types of ventilation systems (displacement and mixing ventilation) as well as a personal ventilation system. The study was carried out for an office room subjected to Iraqi climate weather conditions. The theoretical study was performed using (AirPak 3.0.16) software. Two cases were

performed. The first case used (personal and mixing) with temperature of supplied air from (21 to 23 °C), while at the second case used (displacement and mixing ventilation) with temperature of supplied air from (18 to 20 °C). The velocity of air at both cases is 0.6 m/s. It was found that there was a positive effect for using the personal ventilation at both cases. The values of air diffusion performance index (ADPI) and thermal ventilation effectiveness (ε_t) were (74.361 and 1.549) respectively for the first case, while their values were (68.321 and 1.71) respectively for the second case.

2.2.2 Experimental and theoretical studies

Muna, (2017), [81], studied the displacement ventilation using three different diffuser types to get the indoor air quality parameters theoretically and experimentally. Experimental work and (CFD) modeling were conducted for comparing the indoor air quality and thermal performance between three types of air supply diffusers (three directions-squared diffusers, semi-circular diffuser and two parts of one direction-squared diffuser). The experimental work was conducted for investigation of how the use of the three various arrangements would affect the thermal space inside the tested room with dimensions of (4×3.2×4) m. (ANSYS Fluent-14) was used to simulate the complex flow with buoyant inside the models rooms. It was found that the three direction-squared diffuser was the better kind in comparison to the other two kinds since it investigated (ADPI) of (66.76 %) and (ε_t) of (1.82) respectively, and the semi-circular kind gave (62.3) % and (1.55) respectively. In addition to, the measured relative humidity gave about converged values for all the three types.

Lastovets et al., (2019), [82], conducted a dynamic model for the DV temperature gradients and investigated the influence of thermal mass on the temperature stratification. The model was validated with the experimental work data of the lecture room using displacement ventilation. The outcomes showed that the model showed a better robustness for the thermal output prediction at different operating circumstances by picking up the dynamic characteristics of the building system accurately. Moreover, the heat loads time schedules were taken

into account in the model. The two-capacity prototype can predict the gradient of temperature for the indoor air in the dynamic circumferential by picking up the dynamic characteristics of the building system accurately. The model could be utilized for the DV design at various dynamic circumstances.

Shi et al., (2019), [83], conducted and analyzed a full-scale chamber using displacement ventilation and passive chilled beams (PCBs) to get information about the velocity of air flow, temperature and concentration of contaminants numerically and experimentally. It was found that PCBs were perfectly effective for decreasing the temperature gradient towards DV. However, the chilled beam produces a chilly descending plane which make a zone with high draft. Moreover, the draft extent may be corresponding to the cooling load removed by the PCBs. These descending air jet created by the PCBs might upset the stratification of contaminant and increase the mean age of air in the considered zone.

Cetin et. al., (2020), [84], investigated the characteristics of dispersion and deposition of various particle diameters (0.5-5-10 μm) for a displacement ventilated and floor heated environment, experimentally and numerically. The experimental results were utilized for validation of simulation outputs obtained via Eulerian-Lagrangian technique. Three shapes of various outlet opening and particle source heights were considered. The results were compared in terms of air change efficiency (ACE), average concentration of the room and the breathing height, contaminant removal effectiveness (CRE) and deposition fraction. It was discovered that the distribution of contaminant was highly related to the configuration of outlet opening and the position of particle source.

Mahdi et. al., (2021),[85] investigated the effect of adding the personal ventilation with the displacement ventilation on heat removal as well as the thermal comfort. The experiments were carried out on an insulated room with dimensions of (3 × 1.75 × 3) m. The experimental results were used for validation of the CFD simulation to predict indoor airflows using the RNG k- ε model. The temperature of supplied air from displacement ventilation was 18 °C with mean air velocity of 0.25 m/s, while the flow rates for personal ventilation were 5 l/s

and 10 l/s with a temperature close to where the air was draw (at height of 0.4 m). It was found that adding the personal ventilation improved the indoor air quality and thermal comfort. The flow rate of 10 l/s gave better efficiency for the device with regard to the air diffusion performance index (ADPI) and the thermal ventilation effectiveness (ε_t) with values of 71% and 1.8 respectively.

2.3 Originality of the Present Work

The design and performance of a combined solar absorption cooling system with ventilation system in an insulated office room under Iraqi climate would be designed, fabricated and tested as a new ventilation system under different conditions. This research investigates the effect of many parameters on performance of ventilation air flow and so the air quality as follows:

1- The effect of refrigerant mass flow rate, the fraction of refrigerant in the solution and the time.
2- There is no study conjugates the solar absorption system with displacement ventilation. So, this system will be performed in this study.
3- The pair of acetone-water did not used previously in the solar absorption system. So, this pair will be used to study its performance under Mid-Iraq climate.
4- Finding a correlation for the vaporized fraction of acetone as a function of generator temperature and the acetone fraction in the mixture using SPSS program.
5- Performing the exergy analysis of the absorption system and collector.
6- Enhancing the air exchange efficiency for a ventilated office room by using the displacement ventilation with solar absorption cooling system.
7- Studying the capability of this system to present acceptable thermal conditions in occupant zone.
8- Evaluation performance of this system under severe hot weather Iraqi climate (during summer season).

CHAPTER THREE

EXPERIMENTAL SET UP AND DESIGN CALCULATIONS

CHAPTER THREE
EXPERIMENTAL SET UP AND DESIGN CALCULATIONS

The design and manufacturing of a solar absorption system driven by a parabolic trough solar collector (PTSC) to ventilate an insulated room will be explained in the current chapter. It consists of a detailed analysis for all the system components individually and how the system operates to study the air flow and temperature distribution by displacement ventilation system. The testing of the system and ventilated room was performed at University of Babylon, Babylon province, Iraq (latitude of 32.46 °N and longitude of 44.42°E). The acetone-water pair is selected and tested as an operating working fluids under Iraqi climate. The outdoor and indoor design that is used in this study are based on Iraqi blog for cooling at Hilla city.

3.1 Components of the Solar Absorption Cooling System and the Tested Room

The sizes and dimensions of the various elements of the system are designed according to the required cooling load and the thermodynamic properties of used fluid pair. The system consists of two parts, the first part includes the components of the solar collector and solar absorption cooling system which includes:

A. Storage tank
B. Water pump
C. Parabolic trough solar collector
D. Generator
E. Condenser
F. Capillary tube

G. Evaporator
H. Absorber
I. Chemical pump
J. Heat exchanger
K. Water pump for cooling of condenser and absorber

The second part consists of the components of the insulated cooled room which includes:

A. Insulated Room
B. Rectangular diffuser
C. Manikin
D. Lamps
E. Three air ducts
F. Two Poles
G. Table

The aim of the current work is to ventilate an insulated room with a heat gain consisting of a one person, one computer, one lamp, infiltration and heat gain from the window. The system is operated by a solar absorption cooling system. A continual solar absorption cooling system is designed and constructed to perform this purpose. Acetone-water pair is used in the solar absorption cooling system. The acetone is used as a refrigerant while the water as an absorbent. The solar absorption ventilation system components will be explained in the following subsection. The system is shown schematically in Fig. (3.1), and the system photograph is shown in Fig. (3.2).

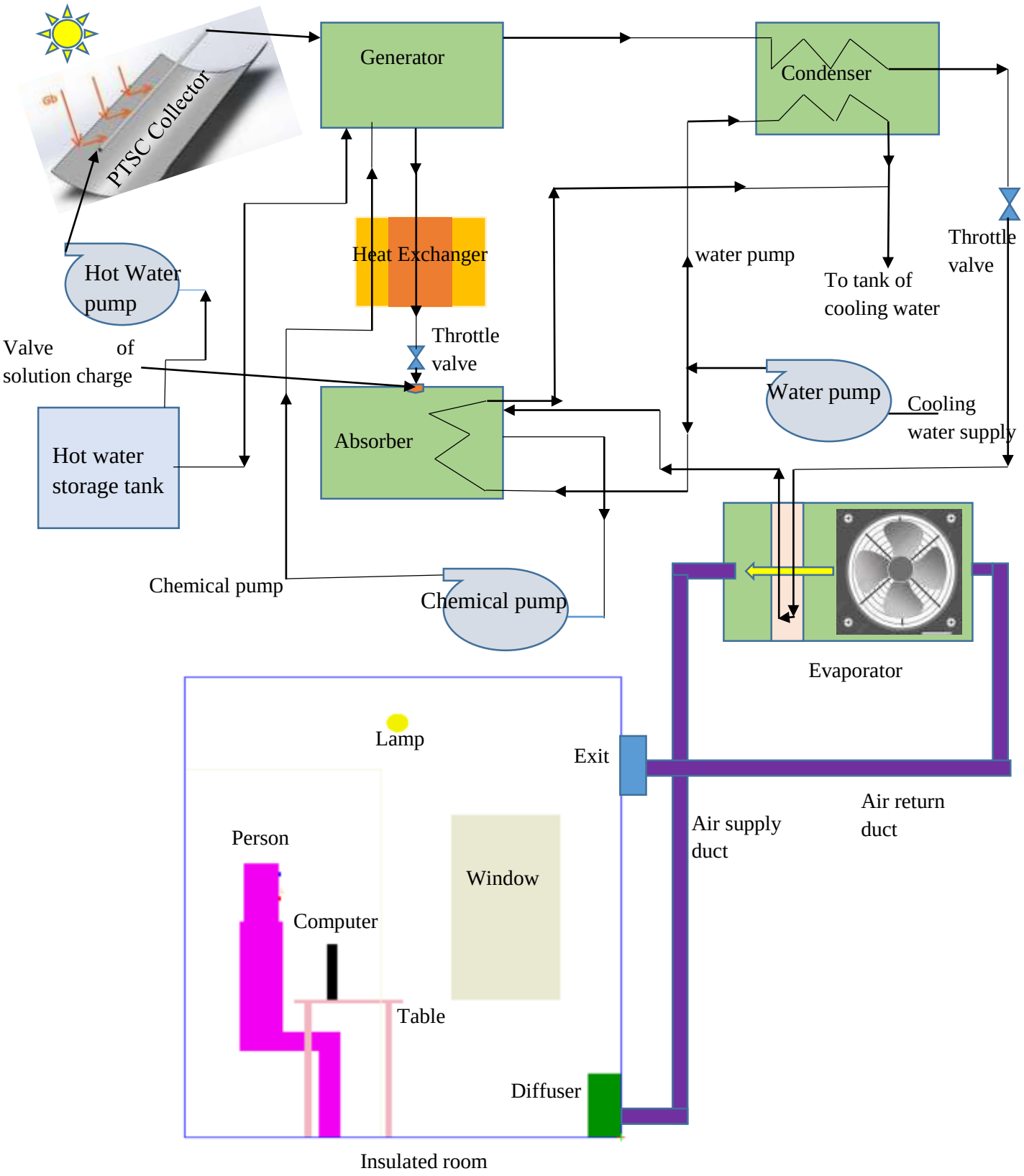

Fig. (3.1) schematic diagram of the solar system and the insulated room.

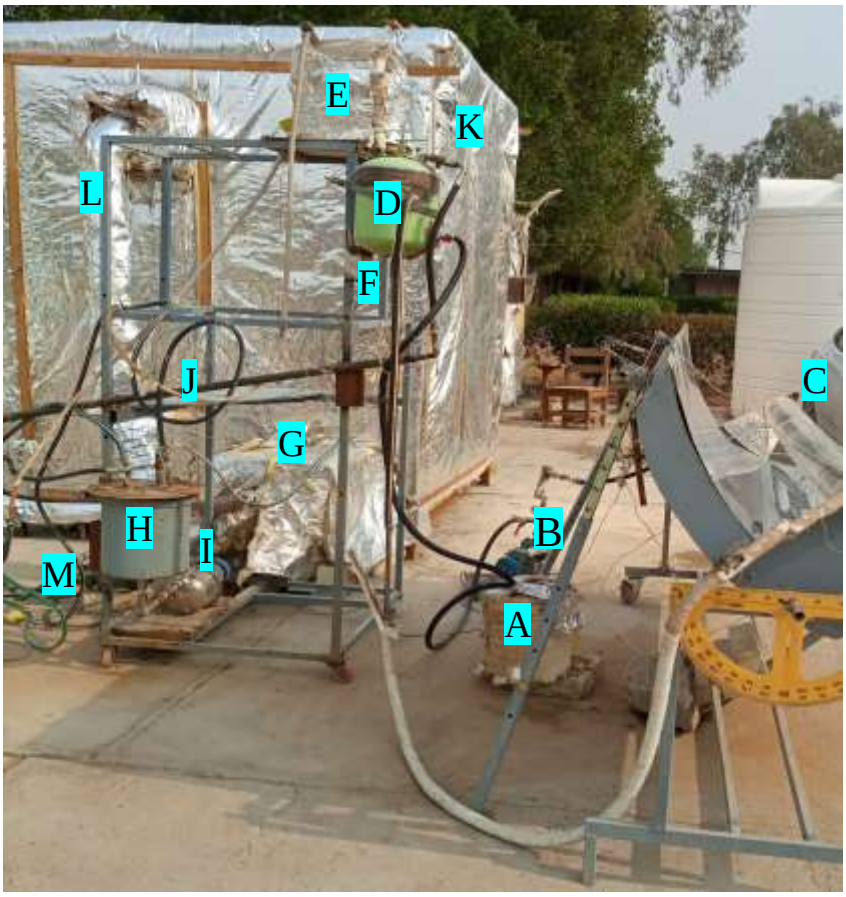

A-Storage tank
B-Water Pump
C- Parabolic trough solar collector
D-Generator
E- Condenser
F- Capillary tube
G- Evaporator
H- Absorber
I-Chemical pump
J- Heat exchanger
K-The insulated room
L- Insulated air duct
M- Water pump for cooling of condenser and absorber.

Fig. (3.2) photo of the solar system and the ventilated test chamber.

The design calculation is based on the following assumptions:

1. The heat gain comes from (window, infiltration, one person, one lamp and one computer) with total required cooling load of 300 W.
2. The system operates under quasi steady state
3. Generator and evaporator are adiabatic.
4. The refrigerant is considered to be in the saturated vapor state at the evaporator exit and generator exit.
5. The refrigerant is considered to be in the saturated liquid state at the condenser exit.
6. The temperature of the condenser (T_c) is assumed as (40 °C), which is a suitable temperature for the external sink to the condenser.
7. The evaporator temperature (T_e) is assumed as (6°C), which is a suitable temperature when using acetone as a refrigerant.
8. The pump work is negligible.
9. There is no pressure drop in the pipes.
10. Generator and condenser are assumed as same pressure and equal to high pressure of the system.
11. Evaporator and absorber are assumed as same pressure and equal to low pressure of the system.
12. The effectiveness of heat exchanger is 0.65.
13. The fluid temperature is constant inside that components.
14. The room and air ducts are insulated totally from the surrounding.
15. The infiltration from the surrounding is (0.5) room volume per hour.

3.2 Design of the Insulated Tested Room

The dimensions of the test room are (2× 2 × 2.5) m. The inlet air supply is situated at the west wall while the exit grill is at the same wall located in the center where its center below the roof of a distance (0.5 m). One occupant, one electric lamp and one computer and the heat gain from

window are used as heat sources. Fig. (3.3) shows a schematic representation of the test room. Table (3.1) provides a complete description of the setup and the various objects locations. Properties of human body are expressed by a seated manikin. Manikin height is (1.1 m), and area of surface is (1.65 m^2), [86]. A lamp is placed below the manikin to generate heat of (75W). Fig.(3.4) shows the locations of the contents of the tested room and the measuring devices.

table (3.1) ventilated room configuration

Item	**Location m**			**Size m**			**Heat**,[87] **W**
	X	**Y**	**Z**	Δx	Δy	Δz	
Room	0	0	0	2	2	2.5	-
Diffuser	0	0	0.85	0.1	0.25	0.3	-
Exhaust grille	0	1.955	0.85	0	0.19	0.3	-
Person	1.45	0	0.825	0.35	1.2	0.35	75
Computer	0.85	0.75	0.825	0.35	0.3	0.35	45
Lump	0.97	2.22	0	0.06	0.06	0.08	15
Table	0.9	0.7	0.6	0.5	0.05	0.8	0

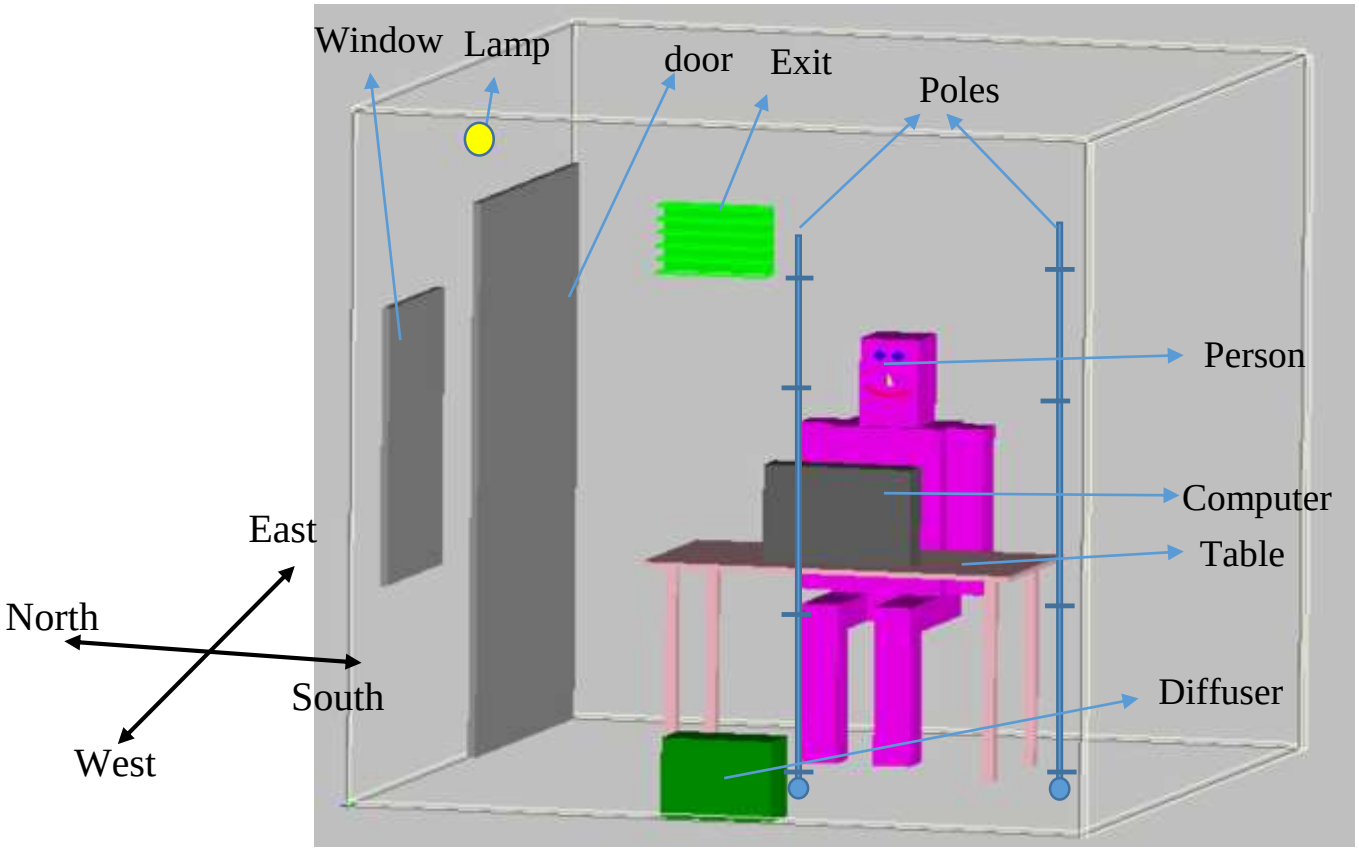

Fig. (3.3) schematic diagram of the tested office room.

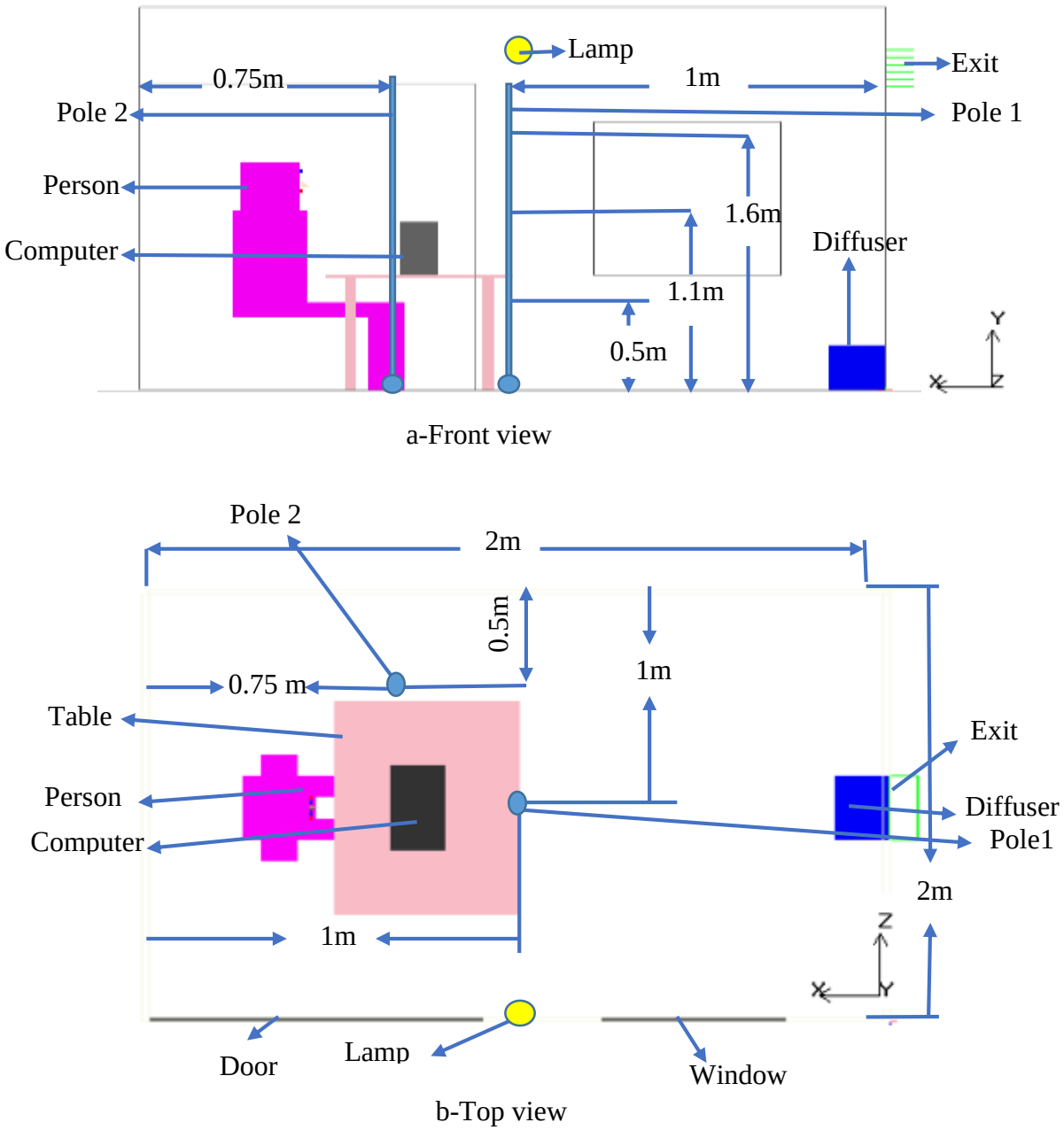

Fig. 3.4 locations of the contents of the tested room and the measuring devices.

3.2.1 Cooling load calculations

To calculate the supply temperature (T_s) and air flow rate (Q_{DV}), the cooling load must be estimated from the following equations as, [87]:

$\dot{Q}$= U*A*$CLTD_c$ …(3.1)

$$\frac{1}{U} = \frac{1}{h_{out}} + \frac{x_1}{K_1} + \cdots + \frac{x_n}{K_n} + \frac{1}{h_{in}} \quad \ldots(3.2)$$

$CLTD_c$ = CLTD+(25.5-T_R)+(T_o-29.4) …(3.3)

Where:

T_R is the indoor design temperature assumed 25 °C.

T_o is the outside environmental temperature assumed 50 °C.

The window consists of two layer of reflective glass of (6 mm) thickness with conductivity of (0.83 Btu/h.ft^2 °F), [88], and a cavity of air with 8 mm thickness.

Infiltration cooling load can be found from the equation:

$\dot{Q}_{inf}$=1.22*$\dot{V} * \Delta T$ …(3.4)

For infiltration of 0.5/h

$$\dot{V}_{inf} = \frac{1}{2} * \frac{v}{3600}$$

Cooling of air inside room for one hour and initial temperature of (35 °C) is found as:

$$\dot{Q}=\frac{m*cp*\Delta T}{t}=\frac{\rho*V*cp*\Delta T}{t} \quad \ldots(3.5)$$

Table (3.2) heat gain of cooled room

No.	Item	Power (W)
1	Window	31.26
2	Infiltration cooling load	47.43
3	Cooling of air inside room	33
4	Human cooling load	75
5	Computer cooling load	45
6	Lighting cooling load	15
	Total	246.7

3.2.2 Calculating supply temperature (T_s) and flowrate ($\dot{V}_{dv}$)

The required air flow rate for cooling load, [89], is:

$$\dot{V}_{dv} = \frac{0.295\dot{q}_{oe}+0.132\dot{q}_{l}+0.185\dot{q}_{ex}}{\rho cp\Delta T_{hf}} \quad \ldots(3.6)$$

Where,

$\dot{V}_{dv}$ = required air flow rate to meet the sensible cooling load in system, [l/s]

$\dot{q}_{oe}$=75+45=120 W

$\dot{q}_{l}$= 15 W

$\dot{q}_{ex}$=31.26+47.43+33=111.7 W.

$$q\dot{d}v = \dot{q}_{oe}+\dot{q}_{l}+\dot{q}_{ex} \quad \ldots(3.7)$$

$\dot{V}_{dv}$=0.022 m^3/s =22 l/s

Equation (3.6) is used to predict temperature of supplied air (T_s) during the experiments, [23].

$$T_s = T_{dr} - \Delta T_{hf} - \frac{A_f \times \dot{Q}_{dv}}{0.584 \times V_{dv}^2 + 1.2 \times A_f \times V_{dv}} \quad \ldots(3.8)$$

Where,

T_{dr}= dry bulb temperature, (°C)

$\dot{Q}_{dv}$= total heat transfer rate, (W)

A_f = the floor area of room (m^2)

T_s=20.79 °C

$$Q_s = \rho * \dot{V} * cp * (T_e - T_s) \quad \ldots(3.9)$$

Where, T_e is the temperature of room exit.

For T_s=20 °C, the flow rate must be corrected, so it will become:

$\dot{V}$= 0.02183 m^3/s

The heat balance for mixing (90%) of recirculated air and (10%) from the ambient will be:

$\dot{m}_m C_P T_m = \dot{m}_1 C_P T_1 + \dot{m}_2 C_P T_2$ …(3.10)

$T_m = \frac{\dot{m}_1}{\dot{m}_m} T_1 + \frac{\dot{m}_2}{\dot{m}_m} T_2$ …(3.11)

Where; $\frac{\dot{m}_1}{\dot{m}_m}$ =0.9 and $\frac{\dot{m}_2}{\dot{m}_m}$ =0.1

$T_m = 0.9 * T_e + 0.1 * T_o$ …(3.12)

$Q_s = \rho * \dot{V}_{dv} * cp * (T_m - T_s)$ …(3.13)

Q_s = 300 W

The air exchange per hour can be found as:

$ACH = \frac{\dot{V}_{dv} \times 3600}{V}$ …(3.14)

ACH= $\frac{0.02183 * 3600}{10}$ = 7.86/h

The value of (ACH) is within the acceptable range, [87].

3.2.3 Supply air diffuser (DV)

The air supply unit is basically fabricated as a perforated displacement device. There are certain objectives that must be met in displacement ventilation such as silent operation, less velocity, thermal comfort and less noisy diffuser. The area of diffuser can be found using equation (3.16), with assuming air velocity of (0.3) m/s, then the supply air unit dimensions are (0.3m*0.25 m) as seen in Fig. (3.5).

$\dot{V}_{dv} = u_x * A_d$ …(3.15)

Where $\dot{V}_{dv}$ is the air flow rate across the diffuser, u_x is the exit air velocity from the diffuser in the x-direction and A_d is the area of diffuser.

Fig. (3.5) one-way rectangular Supply air diffuser.

3.2.4 The indoor room heat sources simulator

The heat sources in the tested ventilated room are explained as follows:

1- Thermal manikin: The temperature of surface of the thermal manikin is controlled to remain as the same temperature reached by the body of human by locating a source of heat with power of (75 W) inside the manikin, and its height from the floor is (1.1 m) at the situation of the sitting, as explained in Fig. (3.6).

2- Computer: by fabricating a wooden box of (0.3×0.3×0.3) m^3 dimensions that includes a source of heat with capacity of (45 W) which is the same power generated by the computer, as displayed in Fig.(3.7).

3- Light: fluorescent lamp with power of (15 W) is located (0.25 m) below the ceiling in the middle of the room northern wall.

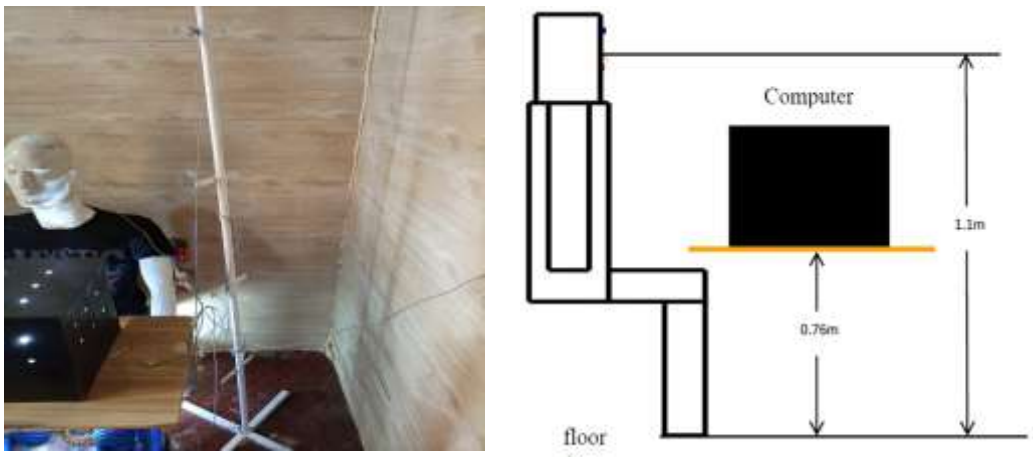

a-photo of thermal manikin b-schematic diagram of person

Fig. 3.6 thermal manikin in the experimental work.

3.2.5 Description of the displacement ventilation system

The displacement ventilation system (DV) in the present work was designed by installing an air diffuser of (30*25 cm) dimensions located near the floor level of the tested ventilated room. Air at velocity of (0.3 m/s) supplied by the diffuser. The diffuser is located on the same side of the air exit.

The diffuser is constructed of the aluminum metal of (4mm) thickness. The exit cross section of the diffuser is made of small circular holes with 1.6 cm diameter made by (CNC) machine. The air exit is situated below the ceiling (0.5 m) and its area is (0.3×0.2).

3.3 Parabolic Trough Solar Collector Loop Design

The parabolic trough collector (PTSC) system is a reflecting surface in the form of a parabola. The collector components are (i) a parabolic cross-sectional cylindrical concentrator (reflector), (ii) helical absorber (receiver) tube made of copper coated with a selective coating, (iii) a glass cylindrical cover enveloping the helical coil receiver and (iii) Support structure.

The solar irradiations incident on the reflecting surface is collected and reflected along the parabola focal line where a heat transfer liquid is flowing in the helical receiver tube. The heat is absorbed by the liquid. The collector loop consists of the following parts:

3.3.1 Reflector

The purpose of the reflector is to reflect and concentrate the incoming direct radiation to the focal line. The reflector in the shape of parabolas is made of stainless steel sheets. So, the dimension of the (PTSC) aperture is about (1.05m) width and length (2 m). The cylindrical parabolic reflector concentrates all the falling solar irradiation on a metallic tubular located along the (PTSC) focal line, [78].

3.3.2 Helical absorber tube

It acts as a receiver and transporter of the energy which is being concentrated at focal line of the reflecting surface. The receiver consists of mainly two components which are the helical coil receiver and the tubular concentric glass cover. The assembly is fixed along the focal line of the collector. The coil is manufactured of a copper tube with (12.7 mm) OD. and (1 mm) thickness. The coil is coated by heat resistant black paint and inserted into the glass cover tube. In some high-performance collectors, helical coil receiver is coated with selective paint and space between the tube and glass cover is evacuated. The concentric glass cover helps in reducing radiation and convection losses, [78].

Table 3.2 Dimensions of the helical coil receiver

O.D of evacuated tube 15 cm	12.7 mm
O.D of the helical tube (dt)	12.7 mm
Length of the helical tube (Lt)	19.15 m
thickness of the tube	1 mm
O.D of the coil (Dcoil)	63.4 mm

Length of the coil (Lcoil)	1.55 m

3.3.3 Support structure

It is a mechanical frame which gives the required support to sustain the weight and provide robustness against wind loads [90].

The optical performance is dependent on various factors, such as fault tracking, geometric error and surface shortcomings. Fig. (3.8) displays a cross section of both a receiver and a reflector that was designed by Nabeel Ghyadh, [78].

3.3.4 Storage tank and hot water circulation

The storage tank is used to store the hot water in the collector loop. The capacity of the storage tank is (12 liters) of water. The water enters to the helical coil receiver in the parabolic trough collector from the storage tank and exits from the helical coil receiver to generator and return to the storage tank with flow rate of (1.5 l/min). The tank is fabricated from steel and thermally insulated to reduce heat loss.

3.4 Absorption System Design

The thermodynamic design of acetone-water absorption cooling system assumes a steady-state operation. The required system cooling load is assumed to be (0.3 kW). The rates of heat added to or rejected from each component of system are found from equations of mass and energy balances. The heat transfer areas are determined from a suitable correlations of heat transfer coefficients. Fig.(3.9) shows a schematic diagram of the solar absorption cooling system.

The lower temperatures of condenser and absorber raise cycle efficiency and should be selected as low as possible. However, they are more or less fixed by the availability of cooling water.

The system pump work is neglected since it is very small in (COP) and performance calculations.

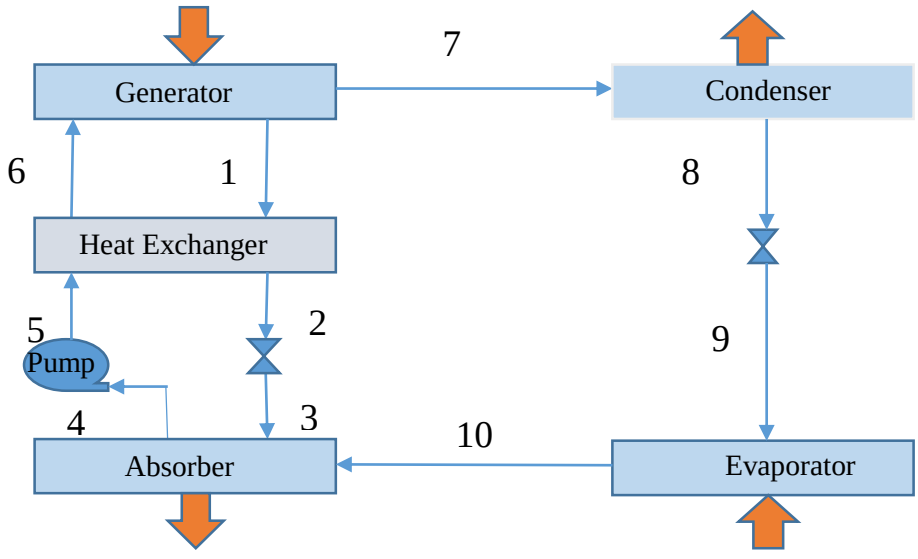

Fig.(3.9) schematic diagram of solar absorption cooling system.

3.4.1 General assumptions of the absorption system

Several assumptions must be considered to design the solar absorption system such as:

1. generator temperature is 80 °C.
2. condenser and absorber temperatures are 40 °C.
3. evaporator temperature is 6 °C.
4. the heat exchanger effectiveness is 0.65.

The saturation pressure of acetone vapor at (6 °C) equals (12.8 kPa). Considering a slight pressure differential between evaporator and absorber of (0.15 kPa), the pressure in the absorber will be (12.65 kPa). In the condenser, the saturation pressure of acetone vapor at (40 °C) is (56.53 kPa). Considering a small pressure differential of (3%),[73], between the condenser and the generator so the generator pressure will be (58.226 kPa).

With refrigerant mass flow rate ($\dot{m}_r$=0.0006224 kg/s), the strong solution mass flow rate is ($\dot{m}_{ss}$=0.01 kg/s) and weak solution mass flow rate is ($\dot{m}_{ws}$) of (0.009378 kg/s) value.

From above assumptions, the following parameters are obtained:

$\dot{Q}_G$= 0.7065 kW

$\dot{Q}_a$ = 0.6518 kW

$\dot{Q}_C$ = 0.3547 kW

3.4.2 Design of generator

The absorption cooling system generator unit is generally of the submerged form. It is a shell and coil heat exchanger. The hot water from the collector flows within the pipes, and the mixture pair (working fluid) in the shell as shown in Fig. (3.10). Table (3.2) shows the data of inlet and exit of the generator, while

Table (3.3) shows the properties of hot water and the water – acetone mixture properties at the generator.

Fig. (3.10) coils,[78].

Table (3.2). inlet and exit data to the generator.

$\dot{Q}_g$	$T_{hw,i}$	$T_{hw,o}$	T_{ws}	T_{ss}	T_g	$\dot{m}_{ws}$	$\dot{m}_{ss}$	X_{ws}	X_{ss}	T_{av}
kw	°C	°C	°C	°C	°C	kg/s	kg/s	%	%	°C
0.7065	90	84	75	52.2	80	0.00938	0.01	0.4668	50	87

Table (3.3) properties of hot water and Acetone - water solution

Properties of hot water at 87 °C, [91]		
ρ_w	kg/m^3	966.96
μ_w	kg/m.s	0.0003236
k_w	W/m.K	0.674
cp_w	kJ/kg.K	4.203

h_{fg}	kJ/kg	2289

Properties of acetone-water solution at 50% and 80°C,[91]		
ρ	kg/m^3	488.5
μ	kg/m.s	0.0001934
k	W/m.K	0.3342
c_p	kJ/kg.K	2.874

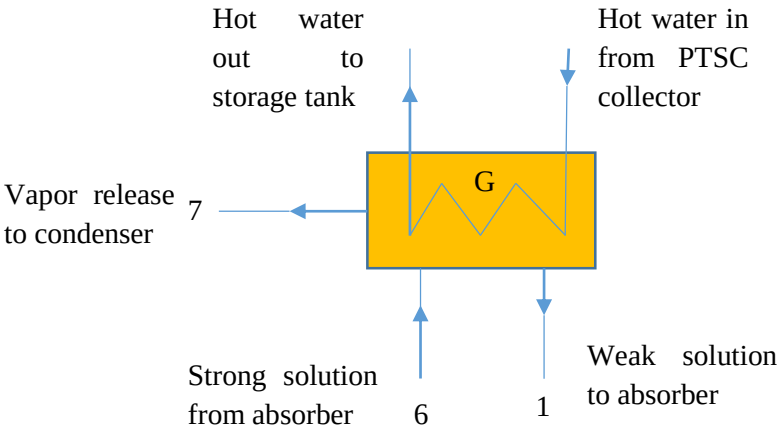

The prantdl number of hot water is :

$$Pr_w = \frac{\mu_w Cp_w}{k_w} = 2.018 \quad \text{...(3.16)}$$

For the hot water flowing into the coil, the inner heat transfer coefficient (h_i) is evaluated first. The hot water mass flow rate inside coil is assumed to be (1.5 L/min or 0.025 kg/s).

The Reynolds number can be evaluated as follows:

$$Re = \frac{4\dot{m}_w}{\mu_w \pi D_i} = 8201 \quad \text{...(3.17)}$$

Where (D_i) is the inside diameter of tubes. The dimensions of the copper tube are as follows; dimensions inside diameter are (D_i=12.7 mm), outside diameter are (D_o=13.4 mm) and thickness (0.7 mm). Since, the flow

is turbulent, the Nusselt number for fluids flowing inside the tubes of helical coil is, [92]

$$Nu = 0.021 * Re^{0.85} * Pr^{0.4} \left(\frac{r_i}{R}\right) \quad ...(3.18)$$

Where (r_i) , (R) are inner radius of tube and radius of coil respectively.

$$Nu = \frac{D_i h_i}{k_w} \quad ...(3.19)$$

$$h_i = 2994.6 \ \frac{W}{m^2 \ ℃}$$

The outside heat transfer coefficient (h_o) can be evaluated from the correlation of ref. [93] which is used for estimation of heat transfer by combined boiling and evaporation of falling liquid films on horizontal tubes. The average heat transfer coefficient over the tube circumferential length (L) is

$$h_o = h_b + h_d * \frac{L_d}{L} + h_c * \left(1 - \frac{L_d}{L}\right) \quad ...(3.20)$$

Where:

h_b :is the nucleate boiling heat transfer coefficient,

h_d: the mean heat transfer coefficient in the thermal developing region where the fluid is being superheated.

h_c; the convective heat transfer coefficient due to evaporation of liquid films at the vapor-liquid interface.

L: shell height.

L_d :the thermal developing length .

h_d is given by

$$h_d = \frac{3}{8} * CP * \frac{\Gamma}{L_d} \quad ...(3.21)$$

Where

$$\Gamma = \frac{\dot{m}}{2 * L_{tube}} \quad ...(3.22)$$

L_{tube}=0.3 m

$$V=\frac{\pi}{4} d^2 l \quad \ldots(3.23)$$

$$d=\sqrt{\frac{4V}{\pi\, l}} \quad \ldots(3.24)$$

d=0.226 m.

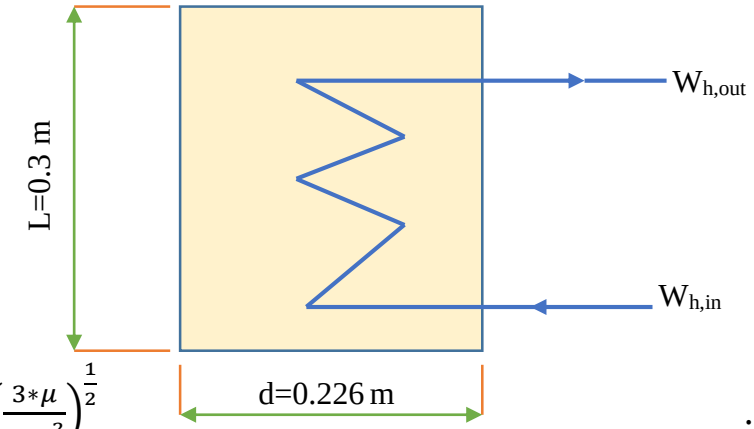

$$L_d = \frac{\Gamma^{\frac{4}{3}}}{4*\pi*\rho*\alpha} * \left(\frac{3*\mu}{g*\rho^2}\right)^{\frac{1}{2}} \quad \ldots(3.25)$$

α:is the thermal diffusivity of the solution

h_c: is found as follows

1-Laminer flow

$$h_c = 0.821 * \left(\frac{v^2}{k^3*g}\right)^{-0.33} \left(\frac{4*\Gamma}{\mu}\right)^{-0.22} \quad \ldots(3.26)$$

2-Turbulent flow

$$h_c = 0.0038 * \left(\frac{\mu^2}{k^3*g}\right)^{0.33} * \left(\frac{4*\Gamma}{\mu}\right)^{0.4} * \left(\frac{v}{\alpha}\right)^{0.65} \quad \ldots(3.27)$$

ν: is the kinematic viscosity. Therefore, Eq. (3.21) is rewritten as

$$h_o = h_d * \frac{L_d}{L} + h_c * \left(1 - \frac{L_d}{L}\right) \quad \ldots(3.28)$$

Shell height is 0.30 m.

$$\Gamma = \frac{\dot{m}_{ss}}{2*L_{tube}} = 0.01667 \ \frac{\text{kg}}{\text{m}*\text{s}} \quad \ldots(3.29)$$

$$\alpha_{ss} = \frac{k_{ss}}{\rho_{ss}*cp_{ss}} = \ 2.407 \ * 10^{-7} \ \frac{\text{m}^2}{\text{s}} \quad \ldots(3.30)$$

$L_d = 4.953*10^{-4}$ m

$h_d = 709053$ W/m^2 °C

The transition point from Eqs. (3.26 and 3.27) in calculating (h_c), [94]:

$$\left(\frac{4*\Gamma}{\mu}\right)_{tr} = 5800 * \left(\frac{\nu}{\alpha}\right)^{-1.06} = 973.2 \quad \ldots(3.31)$$

In this design,

$$\left(\frac{4 * \Gamma}{\mu}\right) = 344.8 \quad \text{laminar}$$

So the correlation for the laminar Eq. (3.26), may be utilized to give

h_c =3869.7 W/m^2 °C

The external heat transfer coefficient is evaluated from Eq. (3.28).

h_o= 3923.4 W/m^2.°C

The overall heat transfer coefficient (U_o) depend on the tubes outside area is, [95]**:**

$$U_o = \left[\left(\frac{D_o}{D_i * h_i}\right) + \left(\frac{D_o}{D_i}\right) * f_o + \left(\frac{1}{h_o}\right) + \left(\frac{D_o}{2*k} * ln\left(\frac{D_o}{D_i}\right)\right)\right]^{-1} \quad \ldots(3.32)$$

Where

$f_\circ$: the fouling factor for the hot water side at (75 °C) equal (0.0002 m^2*K/W), [73].

k: the copper tubes thermal conductivity. For copper tubes (k=390 W/m. K), [96].

$$U_o = 846.731 \frac{W}{m^2 * °C}$$

The logarithmic mean temperature difference (LMTD) is

$$LMTD = \frac{(T_g - T_{hot,o}) - (T_g - T_{hot,i})}{\ln\left(\frac{T_g - T_{hot,o}}{T_g - T_{hot,i}}\right)} = 12.33\ °C \quad \ldots(3.33)$$

$$Q_g = U_o * A_o * LMTD_c \quad \ldots(3.34)$$

Assume $LMTD_c$=0.99*LMTD …(3.35)

$A_o = \pi * d_o * l$ …(3.36)

l= A_o / л d_0 , l= 1.528 m

The characteristic of coil ;

Length of tube= 1.528 m

For a turn length of 0.5 m

$\pi \times D$=0.5 …(3.37)

Coil diameter is 15.9 cm.

Number of turns = 4

Pitch=15 mm

Coil height=n*d+(n-1)*p …(3.38)

H=4*14.1+2*15=86.4 mm

H=8.64 cm.

3.4.3 Design of condenser

The configuration of the condenser device is shell and coil. The acetone vapor flows inside the coil tube, and the cooling water in the shell. Table (3.4) explains the data of inlet and exit of the condenser, while Table (3.5) shows the properties of cooling water and acetone at the condenser.

Table (3.4) input and output data to the condenser.

Q_c	$T_{cw,i}$	$T_{cw,o}$	T_c	m_r	T_{av}
kW	°C	°C	°C	kg/s	°C
0.3553	30	35	40	0.0006224	32.5

Table (3.5). the properties of cooling water and acetone.

Properties of cooling water at 32.5°C, [91]		
ρ_w	kg/m^3	995.024
μ_w	kg/m.s	0.0007566
k_w	W/m.K	0.6205
Pr_w	--	5.1
cp_w	kJ/kg.K	4.183

Properties of Acetone at 40 °C, [91]		
ρ_l	kg/m^3	767.7
μ	kg/m.s	0.0002707
c_p	kJ/kg.K	2.182
h_{fg}	kJ/kg	515
ρ_v at P=56.53 kPa	kg/m^3	1.116

The outer heat transfer coefficient for a helical coil can be evaluated from the following equation, [92]:

$$\left(\frac{h_o * d_o}{k}\right) = 2.0487\, Ra^{0.1768} \quad \text{...(3.39)}$$

For $2 \times 10^6 \leq$ Ra $\geq 3 \times 10^9$

$$Gr = \frac{g*\beta*(T_w - T_\infty)*d_o^3}{\left(\frac{\mu}{\rho}\right)^2} \quad ...(3.40)$$

Assume the $T_{wall} = 38°C$ and $T_{av} = 32.5°C$

$$T_f = \frac{T_{wall} + T_{av}}{2} = 35.25°C$$

$$\beta = \frac{1}{T_f + 273} = 3.2441 * 10^{-3} K^{-1} \quad ...(3.41)$$

$$Gr = 726962.416$$

Ra=Gr*Pr=726962.416*5.1=3707508 …(3.42)

$$h_o = 1346.35 \ \frac{W}{m^2.°C}$$

The inside heat transfer coefficient for two phase flow is, [73]:

$$h_i = 0.725 * \left[\frac{\rho_l * g * h_{fg} * k^3 * (\rho_l - \rho_v)}{\mu * d_i * \Delta T}\right]^{\frac{1}{4}} \quad ...(3.43)$$

$$\Delta T = T_c - T_{wall} = 40 - 38 = 2°C$$

$$h_i = 2183.58 \ \frac{W}{m^2 * °C}$$

$$U_o = \left[\left(\frac{D_o}{D_i * h_i}\right) + \left(\frac{D_o}{D_i}\right) * f_o + \left(\frac{1}{h_o}\right) + \left(\frac{D_o}{2*k} * ln\left(\frac{D_o}{D_i}\right)\right)\right]^{-1} \quad ...(3.32)$$

$$U_o = 728.68 \ \frac{W}{m^2 * °C}$$

The log mean temperature difference can be found as:

$$LMTD = \frac{(T_c - T_{cw,o}) - (T_c - T_{cw,i})}{\ln\left(\frac{T_c - T_{cw,o}}{T_c - T_{cw,i}}\right)} \quad ...(3.44)$$

To account for perpendicular flow, the correction factor is (0.99), so that, [90]:

If we assume, $LMTD_c = (0.99) \times LMTD$

Then, $LMTD_c = 7.141$

$$Q_c = U_o * A_o * LMTD_c \quad \ldots(3.45)$$

$A_o = \pi d_o l$, $l = A / \pi d_o$, $l = 1.623$ m ≈ 2

The characteristic of coil ;

Length of coil = 1.623 m ≈ 2

Number of turn = 4

Coil height(H)=4*14.1+3*15=101 mm=10.1 cm

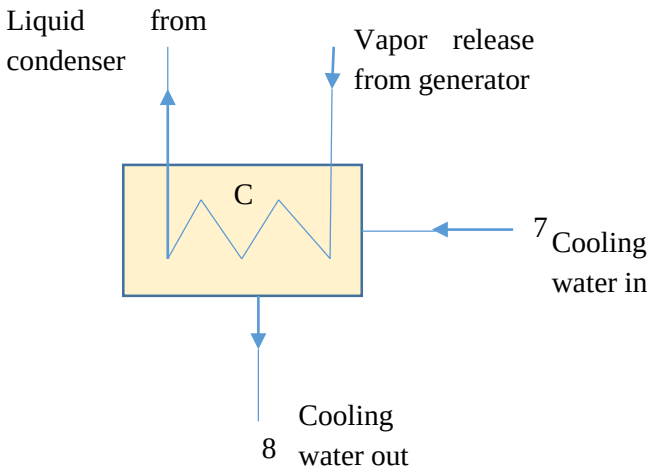

3.4.4 Design of evaporator

The evaporator is a cross flow fan and radiator heat exchanger. The acetone flows inside the radiator and the air to be cooled flows over and through the radiator. The supplied air to the fan consists of (90% of recirculated air and 10% of ambient air). Table (3.6) explains the data of inlet and exit prop pplied to the evaporator, while table (3.7) shows the aceton erties at their film temperatures. Fig. (3.11) shows the evap ents that are a fan, condenser and a wood case.

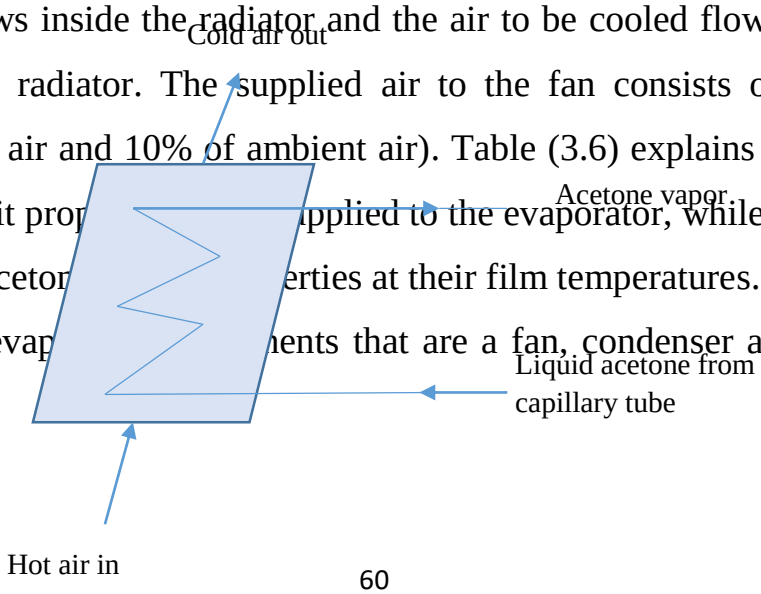

Fig. (3.11) photos of the evaporator.

Table (3.6) inlet and exit data to the evaporator.

Q_e	$T_{a,i}$	$T_{a,e}$	T_e	m_r	T_{av}
kW	°C	°C	°C	kg/s	°C
0.3	31.37	20	6	0.0006224	25.69

Inner diameter=0.012 m.

Outer diameter=0.0134 m.

The evaporator pressure is 12.8 kPa which is the saturation pressure of the acetone at (T=6 °C).

Gravitational acceleration (g=9.81 m/s^2).

Table (3.7). acetone and air properties at their film temperature, [91].

	μ (kg/m.s)	ρ_v (kg/m^3)	ρ_L (kg/m^3)	k (W/m.K)	pr	h_{fg} (kj/kg)

Acetone	0.0003703	0.194	805.7	0.1671	-	534
Air	0.00001852	1.181	-	0.02556	0.7302	-

From the information mentioned above, the inner heat transfer coefficient would be

$$h_i=0.725\left[\frac{\rho_l\times g\times h_{fg}\times k^3\times(\rho_l-\rho_v)}{\mu\times d_i\times\Delta T}\right]^{\frac{1}{4}}=\frac{2179.632W}{m^2.K} \quad \ldots(3.46)$$

The outer heat transfer coefficient is calculated using Churchill and Bernstein equation, [97]. The recommended equation is for all Re Pr≥ 0.2 has the shape.

$$Nu=0.3+\frac{0.62\times Re^{\frac{1}{2}}\times Pr^{\frac{1}{3}}}{\left(1+\left(\frac{0.4}{Pr}\right)^{\frac{2}{3}}\right)^{\frac{1}{4}}}\left(1+\left(\frac{Re}{282000}\right)^{\frac{5}{8}}\right)^{\frac{4}{5}} \quad \ldots(3.47)$$

Nu=1412.68

$$Nu=\frac{h_o d_i}{k} \quad \ldots(3.48)$$

h_o=97.86 W/m^2. K

The overall coefficient of heat transfer (U_o) depend on the outside area of the tubes is, [96]:

$$U_o=\left[\left(\frac{d_o}{d_i h_i}\right)+\left(\frac{d_o}{d_i}\right)f_o+\left(\frac{1}{h_o}\right)+\left(\frac{d_o}{2k}\ln\left(\frac{d_o}{d_i}\right)\right)\right]^{-1} \quad \ldots(3.32)$$

Where

f is the fouling factor for the hot air side at (50°C) equal to (0.0002 m^2*K/W).

U_o = 82.15 W/m^2. K

$$\Delta T_{Lm}=\frac{(T_{h\,in}-T_{c\,out})-(T_{h\,out}-T_{c\,in})}{ln\left(\frac{T_{h\,in}-T_{c\,out}}{T_{h\,out}-T_{c\,in}}\right)} \quad \ldots(3.49)$$

LMTD = ΔT_{Lm}=19.12 °C

$LMTD_c$=0.99*LMTD=18.93°C

$$Q_e = U_o * A_e * LMTD_c \quad \ldots(3.50)$$

A_e= 0.1929 m^2, required surface area of radiator.

If the area is rectangular without two surfaces and neglecting the fins with width of 30 cm, the height will be

$h= A_e /(2*w)$ …(3.51)

h= 0.1929/(2*0.3)=0.322

h=0.33 m.

3.4.5 Design of absorber

The absorber is of shell and coil type. The dropping film form used the flow of the solution through the pipes and the cooling water within the pipes. Table (3.8) explains the data of inlet and exit of the absorber, while table (3.9) shows the properties of cooling water and water – acetone solution at the absorber.

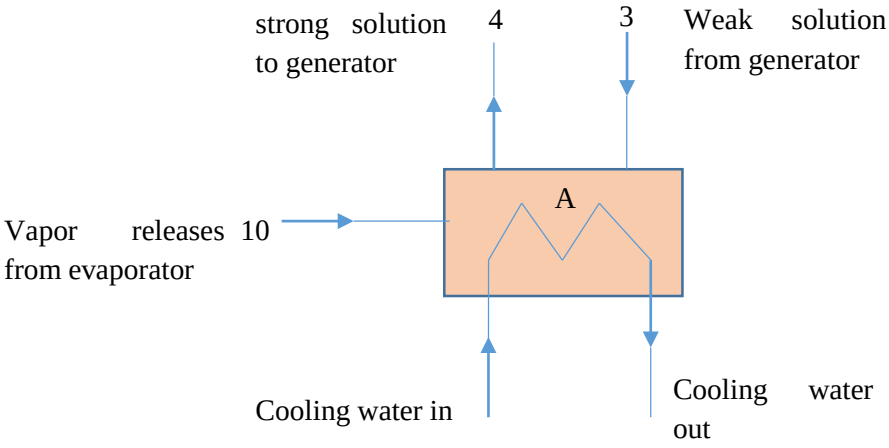

Table (3.8) inlet and outlet data to the absorber.

$\dot{Q}_a$	$T_{cw,i}$	$T_{cw,o}$	T_{ws}	T_{ss}	T_a	$\dot{m}_{ws}$	$\dot{m}_{ss}$	X_{ws}	X_{ss}	T_{av}
kW	°C	°C	°C	°C	°C	kg/s	kg/s	%	%	°C
0.5571	30	35	52.6	40	40	0.009378	0.01	0.467	50	32.5

Table (3.9) the properties of cooling water and acetone- water solution.

Properties of acetone-water solution at 46.7% and 46.3°C, [91].		
ρ	kg/m^3	527.8
μ	kg/m.s	0.0003145

Properties of cold water at 32.5°C, [91].		
ρ_w	kg/m^3	994.9
μ_w	kg/m. s	0.0007571

The mass flow rate of cooling water is:

$$\dot{m}_{cw} = \frac{\dot{Q}_a}{cp*\Delta T} = 0.02664 \ \frac{kg}{s} \quad ...(3.52)$$

The cooling water Reynolds number is:

$$Re = \frac{4\dot{m}_{cw}}{\mu_w \pi d_i} = 3735.42 \quad ...(3.53)$$

The Nusselt number for inner flow for helical coil is, [92]:

$$Nu = 0.021 * Re^{0.85} * Pr^{0.4} \left(\frac{r_i}{R}\right) \quad ...(3.54)$$

$$Nu = \frac{h_i}{k} d_i \quad ...(3.55)$$

$$h_i = 3059.74 \ \frac{W}{m^2 * K}$$

The outside heat transfer coefficient can be found from the following circumstances, [95].

for $\frac{4 * \Gamma}{\mu} < 2100$

$$h_o = 0.5 * \left[\frac{k^2 * \rho^{\frac{4}{3}} * cp * g^{\frac{2}{3}}}{\frac{\pi * d_o}{2} * \mu^{\frac{1}{3}}}\right]^{\frac{1}{3}} * \left[\frac{\mu}{\mu_{wall}}\right]^{\frac{1}{4}} * \left[\frac{4*\Gamma}{\mu}\right]^{\frac{1}{9}} \quad ...(3.56)$$

All properties of strong solution (within the absorber) are evaluated at mean bulk temperature except μ_{wall} at the wall temperature.

for $\frac{4 * \Gamma}{\mu} > 2100$

$$h_o = 0.01 * \left[\frac{k^3 * \rho^2 * g}{\mu^2}\right]^{\frac{1}{3}} * \left[\frac{\mu * cp}{k}\right]^{\frac{1}{3}} * \left[\frac{4 * \Gamma}{\mu}\right]^{\frac{1}{3}} \quad \text{...(3.57)}$$

In this design

$$\Gamma = \frac{\dot{m}}{2 * L_{tube}} = 0.01667 \ \frac{\text{kg}}{\text{m. s}}$$

And

$$\frac{4 * \Gamma}{\mu} = 229.2 < 2100$$

$$\text{h}_\text{o} = 1694.82 \ \frac{\text{W}}{\text{m}^2 * \text{K}}$$

$$\text{U}_\text{o} = 1367.73 \ \frac{\text{W}}{\text{m}^2 * \text{K}}$$

$$\text{LMTD}_c = 7.141$$

$$Q_a = U_o * A_o * LMTD_c \quad \text{…(3.58)}$$

$A_o = \pi * d_o * l$, $l = A_o / \pi d_0$, $l = 1.586$ m

The characteristic of coil;

Length of tube = 2 m

Number of turn = 4

Pitch=15 mm

Coil height=n*d+(n-1)*p …(3.38)

H=4*14.1+3*15=101 mm

H=10.1 cm

3.4.6 Solution heat exchanger design

In the case of low capacity acetone-water cooling systems, solution heat exchanger typically consists of a purely double copper pipe. For this portion, such a heat exchanger is built with a cold-strong solution for indoors and a hot, weak solution in outdoors. Table (3.10) explains the data of inlet and exit of the heat exchanger, while table (3.11) shows the

properties of water- acetone solution for strong and weak solution at the heat exchanger.

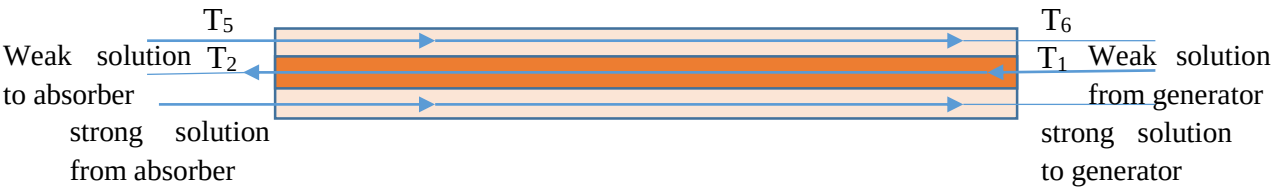

Table (3.10) inlet and exit data to the heat exchanger.

$\dot{Q}_{Hx}$	$T_{ss,i}$	$T_{ss,o}$	$T_{ws,i}$	$T_{ws.o}$	$\dot{m}_{ws}$	$\dot{m}_{ss}$	X_{ws}	X_{ss}	$T_{av,ss}$	$T_{av,ws}$
kw	°C	°C	°C	°C	kg/s	kg/s	%	%	°C	°C
0.3452	40	52.19	75	62.4	0.009378	0.01	46.68	50	46.1	68.7

Table (3.11). the properties acetone- water solution**.**

Properties of solution at 50 % and 46.1 °C, [91].		
ρ_{ss}	kg/m^3	495.5
μ_{ss}	kg/m.s	0.0002965
k_{ss}	w/m.K	0.3194
cp_{ss}	kJ/kg.K	2.826
Pr_{ss}		2.624

Properties of solution at 46.68% and 68.7°C, [91].		
ρ_{ws}	kg/m^3	522.3
μ_{ws}	kg/m.s	0.0002234
k_{ws}	w/m.K	0.3526
cp_{ws}	kJ/kg.K	2.927
Pr_{ws}		1.854

The outer and inner diameters are (9/8 " and 5/8 ") respectively. The coefficients of heat transfer for the inside and outside flow for the heat exchanger can be evaluated as follows:

$$Re = \frac{4\dot{m}}{\pi \mu D} \quad \text{...(3.59)}$$

$$Nu = 0.023\ Re^{0.8}\ Pr^{n} \quad \text{…(5.60)}$$

n= 0.3 for cooling and 0.4 for heating

$$Pr = \frac{\mu\ cp}{k} \quad \text{…(5.61)}$$

For inner strong solution (cold):

Re= 2704 & Nu =18.83

$h_i = 378.9 \frac{W}{m^2 * K}$

For outer weak solution (hot):

Re =4207 & Nu =21.95

$h_o = 609.4 \frac{W}{m^2 * K}$

$U_o = 162.73 \frac{W}{m^2 * K}$

$$LMTD = \frac{(T_{ss,i} - T_{ws,e}) - (T_{ss,e} - T_{ws,i})}{ln\left(\frac{T_{ss,i} - T_{ws,e}}{T_{ss,e} - T_{ws,i}}\right)} = 22.6\ ℃ \quad ...(3.62)$$

$$Q_{HX} = U_o \times A_{HX} \times LMTD_c \quad ...(5.63)$$

$A_o = 0.09479\ m^2$

$L = A_o/(2*0.01531)$

L= 1.9717 m=2m, length of heat exchanger.

3.4.7 Capillary tube design

In fact, the capillary tube wall friction induces the slow pressure drop in the flow of refrigerant, leading to a decrease in the resulting saturation temperature, internal energy and enthalpy, but to an increase in specific volume and kinetic energy with adiabatic vaporization of flash of its own enthalpy. The reduction in pressure and its accompanying rise in specific volume almost hold the term (PV) constant, [98]. Furthermore, the actual pressure decrease does not lead to the recovery of kinetic energy by phase change and therefore the pressure drop share (ΔP_m) losses is negligible. Consequently, the actual drop in total pressure (ΔP) is almost equal to the drop in frictional pressure, ΔP_F. Table (3.12) shows all properties and velocity of the acetone at the capillary tube. Fig.(3.12)

explains the P-h diagram along the isenthalpic expansion line from condenser to evaporator. Fig. (3.13) shows the used capillary tube.

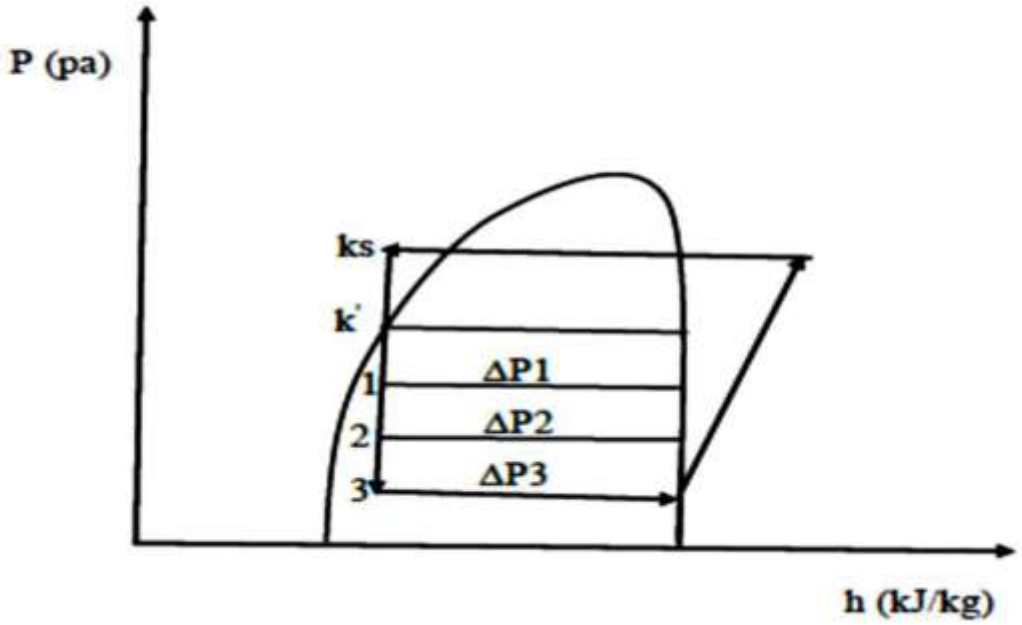

Fig. (3.12) P-h diagram of elementary length along Isenthalpic Line.

The following relationships (Darcy – Weisbach equation 1845) are now used to assess the length of the capillary tube required for each elementary length of the capillary tube between two adjacent temperature nodes:

$$\Delta P_F = \frac{\rho F \Delta L\, u^2}{2d} \qquad \ldots(3.64)$$

L=0. 222 m.

Table (3.12) the results of capillary tube length

node	T_c ˚c	P kpa	h_f kJ/kg	h_{fg} kJ/kg	x	v m^3/kg	u m/s	ΔP kpa	μ kg/m.s	Re	f	ΔL m
k_s	40	56.53	292	508	0	0.001987	1.574	-	0.0002707	2926	0.04351	-
k'	30	38.06	269	521	0.04415	0.07924	62.77	18.47	0.0002946	2689	0.04444	0. 1672
1	20	24.81	246	534	0.08614	0.0003224	192.7	13.25	0.0003224	2457	0.04545	0. 0382

2	10	15.59	223	547	0.12 61	0.4877	386. 3	9.21 9	0.00035 53	2229	0.0465 7	0. 01294
3	6	12.8	213. 8	552. 2	0.14 16	0.6068	480. 7	2.79	0.00037 03	2139	0.0470 5	0. 003115
Total length of capillary tube												0.222

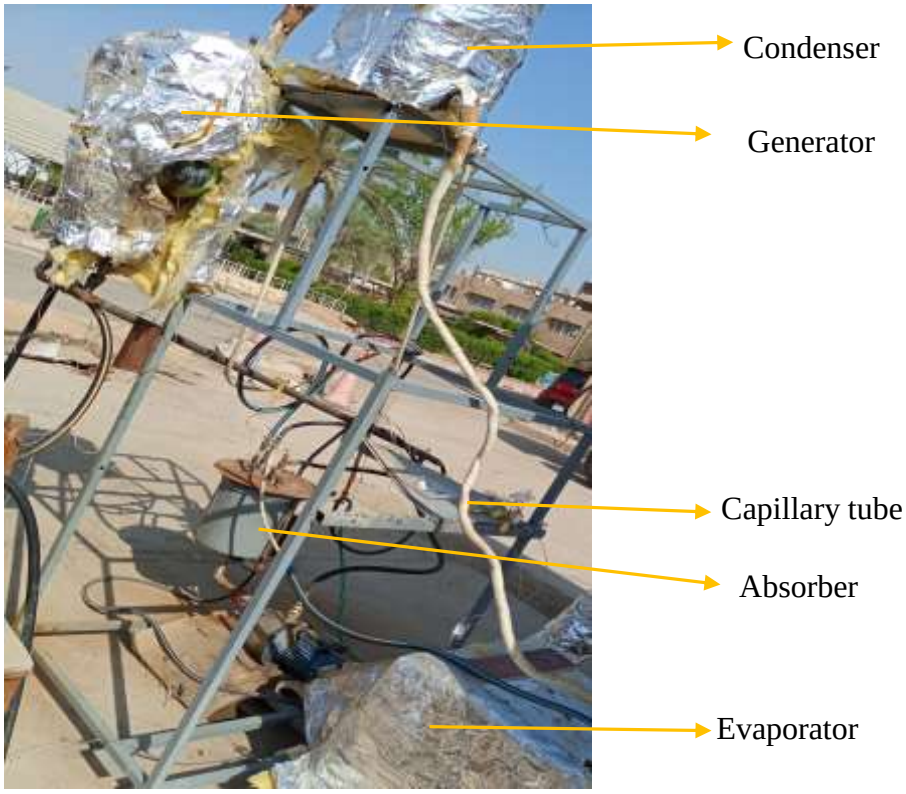

Fig. (3.13) capillary tube.

3.4.8 Working fluid pair

Many different available refrigerant-absorbent pairs which can be used in solar absorption systems. Some of these pairs are (ammonia-water pair, water-lithium bromide pair, water-lithium chloride pair, ethanol-water pair and acetone-water pair…etc.). The selection of the pair solution depends on different parameters such as: heat source temperature, the affinity between the absorbent and refrigerant (chemical, physical and thermodynamic properties of them), the cost, availability and the environmental impact.

The acetone-water pair will be utilized in this study. The acetone is the refrigerant and water is the absorbent. The acetone has been selected because it has several advantages such as: low boiling point at atmospheric pressure, low viscosity, non-toxicity, it is cheap and environmentally friendly. However, the water is selected because it is not-toxic, stable, not-corrosive, available without cost and environmentally friendly. The properties of the solution are mentioned in Appendix-A (table A-1).

Three different concentrations of acetone (by mass) taken in the study are (40%, 50% and 60%) by mass.

3.5 Pumps

The solar assisted absorption cooling consists of two loops: (i) solar collector loop, (ii) absorption cooling loop. A hot water pump is used to circulate a hot water in the solar collector loop. A flow meter is used to measure the hot water flow rate.

A chemical pump is used in the second loop. The chemical pump is utilized to circulate the strong solution, through the heat exchanger to the generator. Another water pump (25 W, 1000L / h, and maximum suction 1.8 m) "circulates the cooling water between condenser and absorber" unit.

3.6 Temperature Measuring Instrument

In this experimental work temperature is the most significant property. The determined temperatures at various locations, together with the corresponding pressure, are used to determine the refrigerant state at any point in the cycle. The Thermocouples are utilized to measure receiver surface temperature, solution acetone vapor outlet, outlet of condenser, environment, and evaporator. These thermocouples are of type (k). The temperatures measured by the thermocouples are recorded via a data logger. The data logger is programmed to keep the temperature recorded

every (15 minutes). The type of data logger used is (Card-12 channels BTM-4208SD) as shown in Fig. (3.14).

Fig. (3.14) data logger of temperature recorder.

3.7 Experimental Procedures for the Absorption system and Ventilated Room Test

The detailed steps of test procedure are as follows:

1. The experimental study is performed during the three months from May to July 2021 at Hilla city.

2. All the (32) point thermocouples of (Type k) are connected to the data logger via plugs and connectors.

3. The exit air from the room is split to (90%) recirculated to room through the evaporator and the (10%) to the outdoor and (10%) fresh air is mixed with the circulated air.

4. For the experiment, the charging valve charges the acetone-water solution (12 liters) to the unit. The acetone concentration is varied in steps as (40%, 50%, 60%) as shown in Fig. (3.15).

5- Preparing the refrigeration pair solution (acetone as a refrigerant and water as an absorbent) with the pre-set refrigerant concentration. This is done by calculating the required volume of acetone for a certain acetone concentration (by mass). Prepare the working fluid pair by adding the acetone to the water. The volume of the required pair to fill the absorption system is 12 kg. The required volume of the pair is charged into the system.

6. Set the collector angles like tilt and azimuth angles to the required values. The tilt angle is selected from the appendix A (Table A-2). The azimuth angle of the module is also measured (30°) from south in summer.

7. The temperature is measured at collector, absorption system and the cooled room every (15 min.) by connecting the thermocouples to the interface data logger. The temperature is measured at collector for the inlet and outlet water to the receiver and at the receiver surface. While the temperature is measure at the absorption system for inside of generator, exit of (generator, condenser, absorber), inlet and exit of (evaporator and heat exchanger) and inlet and outlet for the cooling water for (condenser and absorber). The temperature inside the room is taken for the walls and at two poles. First pole coordinates are (X=1, Z=1 m), while the second pole at (X=1.25 and Z=1.5 m).

8.During the day, the hot water from the collector heats the water-acetone solution in the generator. The acetone is evaporated when the temperature in the generator becomes higher than the boiling temperature of acetone at

generator pressure. Because of the rise in temperature and consequently the pressure of the solution in the generator, the acetone vapor flows into the condenser, where it is condensed by cooling water, and then passes through the capillary tube to the evaporator where the refrigeration effect takes place.

To know the mass of evaporated acetone (refrigerant) two-sight glasses are used, one on the absorber unit, and one on generator unit as explained in Fig. (3.16). The average "refrigerant mass flow rate from the generator" is obtained by measurement of the solution level drop in the generator's sight glass during a period of time. The level drop represents the evaporated acetone by dividing the evaporated acetone on the measured time, the acetone vapor flow rate can be found.

9.After the acetone evaporation, it goes up to the condenser and condensed after the cooling with water in the condenser. The condensed acetone expands in the capillary tube where its temperature and pressure decreases. After that, it passes through the evaporator and gains heat from the air flowing on the surface of the condenser. The saturated acetone has vaporized in the evaporator, then absorbed by the strong solution, the vapor goes to the absorber and was pumped to the generator. The air supplied to the fan is a mixture (90% circulated from the room and 10% is fresh air from the ambient). The fan blows the air to the surface of radiator and it is cooled by the acetone and supplied to the room.

3.8 Instruments Calibration

A- Flowmeter

The flowmeter operating range between (0.06-0.6) m^3/h at 120 ℃. The calibration is performed by using a beaker of determined volume and a stopwatch. The flowmeter is set at different values and determining the time required to fill the beaker. The measured flowrate is calculated by dividing the pre-determined volume on the determined time The flowmeter calibration is shown in Fig. (3.17)

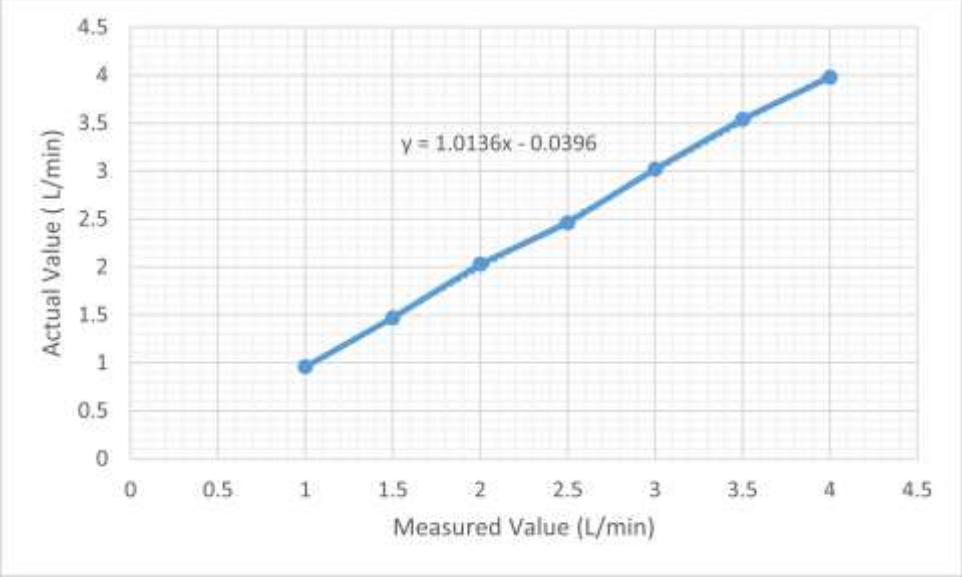

Fig.(3.17) calibration of flow meter.

B-Temperature instrument

In the heat transfer laboratory, the thermocouple calibration is done by comparison of its readings with an already calibrated thermocouple of the same kind (K) as illustrated in Fig. (3.18). Fig. (3.19) explains the equipment of temperature calibration. The uncertainty of thermocouples is explained in Appendix-B.

C-Solar radiation measurement

In the present study, a (WATCHDOG 2000) series weather station is utilized to record the instantaneous solar radiation. The station is installed at the University of Babylon site on the roof of a two-storey building to be sure that no obstacle for measuring the instantaneous solar radiation. Fig.(3.20) shows the photo of watch dog weather station.

Fig. (3.18) photo of thermocouple calibrator.

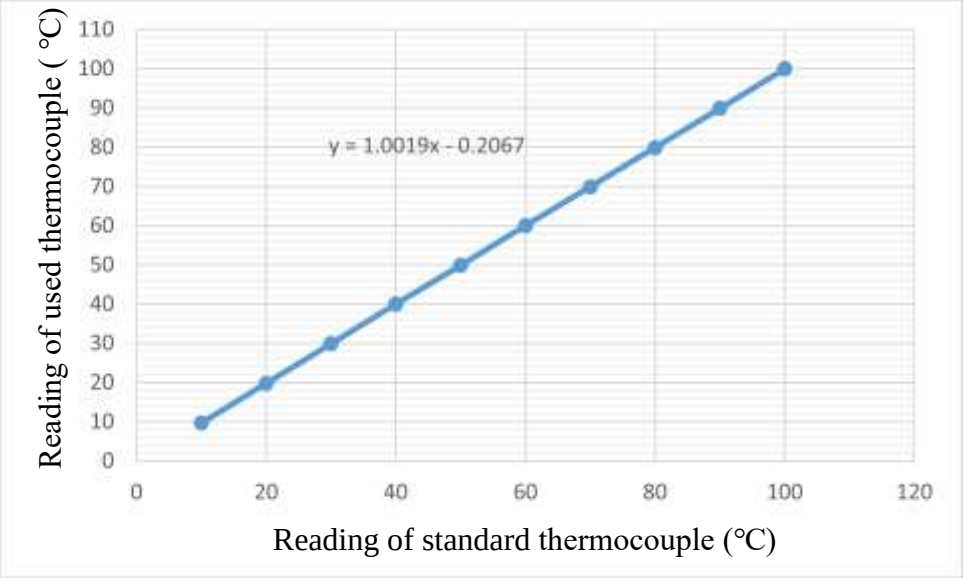

Fig.(3.19) calibration of thermocouple.

CHAPTER TFOUR

THEORETICAL ANALYSIS

CHAPTER FOUR

THEORETICAL ANALYSIS

This chapter presents the theoretical analysis of a solar assisted ventilating system. A solar absorption system built with a non-tracking parabolic trough solar collector (PTSC). The collector thermal efficiency, cooling load, temperature of supplied air and the indoor air quality parameters will be obtained. For the province of Babylon, the total and diffused solar radiation are calculated using theoretical equations. The evaluation and synthesis of the absorption cooling systems needs the implementation of thermodynamics and heat transfer principles, while the indoor air conditions require the equations of conservation of mass and energy as well as the models of turbulence. A parametric study is undertaken on the cycle's steady state model, for which three computer programs are applied. As an outcome, significant insight into the performance of the cycle may be gained.

4.1 Solar Angles

The beam radiation is a ray falling from the sun on earth in a form of beam without spreading or scattering through the atmosphere, so the beam direction does not change through the path in the atmosphere.

The relationships between the direction of any plane relative to the Earth and the direct solar radiation direction coming from sun can be explained with regards to the following angles as explained in Fig.(4.1), [99].

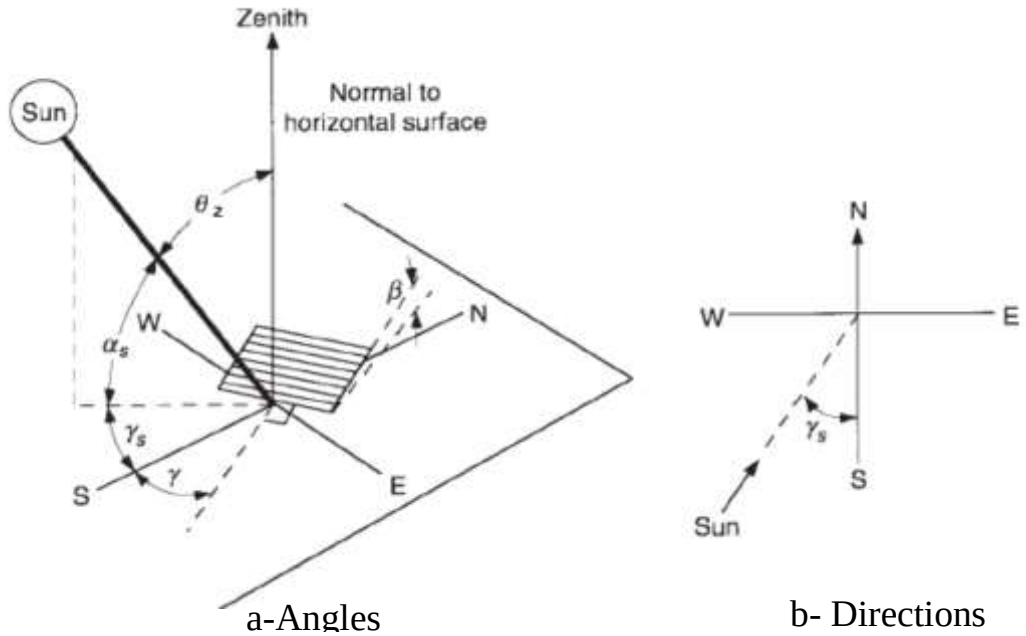

a-Angles b- Directions

Fig. (4.1) zenith angle, title, azimuth angle, and incident angle for a tilted Surface, [99].

4.1.1 Latitude angle (ϕ)

The angular position of surface north or south of the equator. It is positive in the northern hemisphere and negative in the southern part, [100].

4.1.2 Solar declination angle (δ)

Solar declination is the angle between a line connecting the centers of earth and sun and the line projection on the earth equatorial plane, [99]. It changes throughout the year due to earth rotation about its axis. It changes between (+23.45 °) on (21st of June) and (-23.45°) on (21st of December), [101]. It can be evaluated from the equation:

$\delta = 23.45 \sin((N-80)*360/370)$ …(4.1)

Where, N is the day number.

4.1.3 Tilt angle (β)

It is the confined angle between the absorber plate and the horizontal direction ($0° \leq \beta \leq 90°$). The average tilt angle values for months are mentioned in Appendix-A, Table (A-3).

4.1.4 Hour angle (ω)

The hour angle is the angle of position of location away from solar noon due to rotation of earth. It changes through the day. The hour angle has a maximum negative value of (-180°) at sunrise, then it decreases slowly (15°) per hour, until reaches a value of zero at the solar noon. After that, it increases until reaches a maximum value of (180°) at sun set. Its value (in degrees) can be evaluated from the following equation, [100]:

$\omega=15*(ST-12)$ …(4.2)

Where, ST is the solar time. The standard time can be converted to the solar time by using the following two equations:

$ST=\text{standard time}+E/60-(L_{st}-L_{loc})/15$ …(4.3)

Where,

L_{st}: the standard meridian of local time zone for Iraq (it is 45°).

L_{loc}: the longitude location concerned (equal to 44.4° for Hilla city).

Standard time is the local time in hours.

E: the equation of time, which be calculated as, [101] :

$$E=\sum_{k=0}^{k=5}[A_k\cos(\frac{2\times\pi\times k\times N_n}{365.25})+B_k\sin(\frac{2\times\pi\times k\times N_n}{365.25})] \quad \text{... (4.4)}$$

(N_n) is the day number in a 4-year cycle, with N_n =1 being 1st of January of the leap year and (N_n=1461) corresponding to 31th of December of the 4th year of cycle.

A_k, B_k and k are found from appendix: B, (table B-2).

4.1.5 Solar elevation (α)

It is the angle between the solar beam direction and the horizontal direction. It can be evaluated using the following equation, [102]:

$\sin\alpha_s=\cos\omega\cos\Phi\cos\delta+\sin\delta\sin\Phi$ …(4.5)

4.1.6 Solar azimuth angle (γ_s)

It is the angle between the rays of sun and the south direction. The east of south displacement is negative and positive when it is west of south. It is estimated as follows, [102]:

$$\text{Sin } \gamma_s = (\cos \delta \sin \omega)/\cos \alpha \quad \ldots(4.6)$$

4.1.7 Zenith angle(θ_z)

It is the confined angle between the solar radiation and a column standing on a horizontal plane of the surface of earth. It is a complementary angle with the solar elevation angle and can be evaluated as follows:

$$\theta_z = 90-\alpha_s \quad \ldots(4.7)$$

4.1.8 Angle of incidence(θ)

According to Duffie, [133], it can be defined as the angle between the rays of sun and a normal to the surface. It varies throughout the day and year. It is considerably affects the solar energy absorbed by the receiver. It can be found as, [99]:

$$\text{Cos } \theta = \cos \omega \cos (\Phi-\beta) \cos \delta + \sin \delta \sin (\Phi-\beta) \quad \ldots(4.8)$$

4.2 Direct Normal Radiation

The beam radiation outside the atmosphere of earth (solar constant) is influenced when it enters the atmosphere and called direct normal radiation. The direct sunlight intensity through the day can be estimated as, [103]:

$$S_{incident}=1353\times 0.7^{AM^{0.678}} \quad \ldots(4.9)$$

where $S_{incident}$ is the intensity on a plane perpendicular to the sun rays in units of (W/m^2) and (AM) is the air mass. (1353) is the solar constant and (0.7) is the ratio of radiation that reaches the earth. (0.678) is an empirical value to fit with noted data and take into account the non-uniformities in the layers of atmosphere. The mass of air is evaluated as:

$$AM=1/\cos \theta_z \quad \ldots(4.10)$$

The direct irradiation at sea level can be estimated from the equation, [104]:

$$Ho=S_{incident} \times \cos(\theta_z) \quad \ldots(4.11)$$

The direct radiation on tilted collector surface can be determined with regards to the incident angle and the sun altitude by the following equation, [104]:

$$I_{dir}= H_o*\cos(\theta_z)/\cos(\theta) \quad \ldots(4.12)$$

4.3 Diffuse Radiation

It is the solar radiation incident from the sun, spreads, scattered and varies its direction when it enters the atmosphere. It is divided into two parts, the first part is the radiation diffused in the sky and the second part is the radiation reflected from the surface perimeter. The overall diffuse radiation is estimated as follows, [105]:

$$I_{dif}=I_{DN}(C*Y_d+0.5*\rho_g(C+\sin\alpha)) \quad \ldots(4.13)$$

$Y_d=0.45$ if $\cos\theta \leq -0.2$

$Y_d=0.55+0.437*\cos\theta+0.313(\cos\theta)^2$ if $\cos\theta \geq -0.2$

where (ρ_g) is the land reflectivity coefficient with a value of (0.2) for the agricultural or normal land, but it has a value of (0.8) for land covered with snow, [134]. The coefficient of radiation is estimated using the equation:

$$C=0.0965\ (1-0.42\cos(360N/370))-0.0075(1-\cos(1.95N))) \quad \ldots(4.14)$$

Where N is day number.

4.4 Total Radiation

The total radiation components are the direct radiation and the diffused radiation. So, its amount is the sum of the two components. Where, the total radiation is:

$I_{tot}=I_{dir}+I_{dif}$ …(4.15)

The (EES) program software will be used to calculate solar radiation and angles.

4.5 Solar Collector Loop

4.5.1 Parabolic trough solar collector (PTSC)

The (PTSC) collectors have the possibility for reflecting most of the incident radiation to the absorber. The demand for moving the collector for encompassing the changing solar orientation is reduced by utilizing a parabolic section which reflects the incident radiation to the absorber, [106]. Fig.(4.2) shows a schematic representation of the collector loop components.

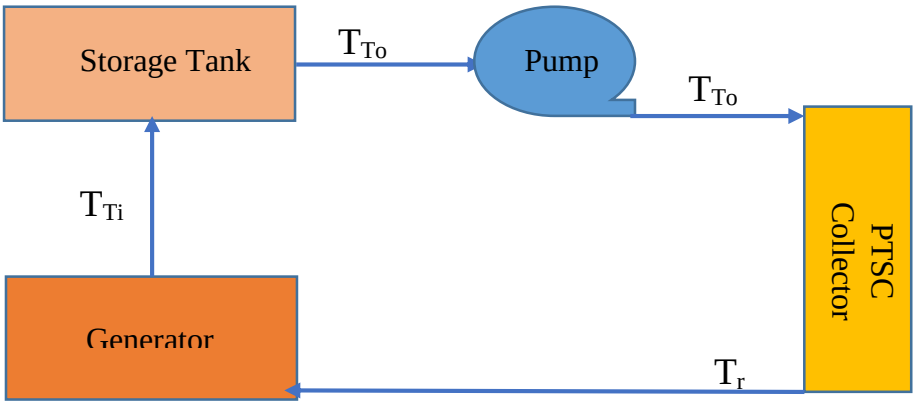

Fig.(4.2) schematic diagram of the collector loop (hot water loop).

4.5.2 Calculation of thermal efficiency

The useful power (Q_u) can be predicted if the intensity of radiation is determined (I_{tot}),(U_L) and (F_R).So, the absorbed power can be set as, [107]:

$I_a = I_{tot} \times \tau_{cover} \times \tau_{PTSC} \times \alpha_r$ …(4.16)

After assuming that the term ($\tau_{cover} \times \tau_{PTSC} \times \alpha_r$) is about 0.8, ($I_a$) can be found. The useful power is found as:

$\dot{Q}_u = F_R.I_a - Q_{loss}$ …(4.17)

$\dot{Q}_{loss} = \dot{Q}_{conv} + \dot{Q}_{rad}$ …(4.18)

$$\dot{Q}_{loss} = F_R \times \left(U_L \times \frac{(T_r - T_a)}{C} + \frac{\sigma A_C (T_r^4 - T_a^4)}{\frac{1}{\varepsilon_c} + \frac{A_c}{A_g}\left(\frac{1}{\varepsilon_g} - 1\right)}\right) \quad \ldots(4.19)$$

$$\dot{Q}_u = F_R \times \left(I_a - \left(U_L \times \frac{(T_r - T_a)}{C} + \frac{\sigma A_C (r - T_a^4)}{\frac{1}{\varepsilon_a} + \frac{A_c}{A_g}\left(\frac{1}{\varepsilon_g} - 1\right)}\right)\right) \quad \ldots(4.20)$$

The emissivity of absorber tube will be taken as 0.27 and glass envelope emissivity is 0.86, [107].

From the above, the thermal efficiency is written as:

$$\zeta = \frac{Q_u}{I_t \times A_c} \quad \ldots(4.21)$$

Heat removal factor is defined as the gained useful energy to the gained energy if the total absorber is at the inlet temperature of heat transfer fluid, [102], and can be written as:

$$F_R = \frac{actual\ output}{output\ of\ collector\ at\ fluid\ inlet\ temperature}$$

$$F_R = \frac{\dot{m} C_p \times (T_{out} - T_{in})}{A_c \times (I_a - U_L \times (T_{in} - T_a))} \quad \ldots(4.22)$$

Where,

T_{out}: temperature of fluid leaving the collector

T_{in}: temperature of fluid entering the collector

A_r: area of absorber

The heat transfer between the glass envelope and the surrounding takes place by natural convection. Churchill and Chu, [108], found a correlation utilized to find the Nusselt number for natural convection over a horizontal cylinder:

$$Nu = \left(0.6 + \frac{0.387 \times Ra_{Dog}^{\frac{1}{6}}}{\left(1 + \left(\frac{0.559}{Pr_{og-a}}\right)^{\frac{9}{16}}\right)^{\frac{8}{27}}}\right)^2 \quad \ldots(4.23)$$

$$Ra_{Dog} = \frac{g\beta(T_{og} - T_a) D_{og}^3 \times Pr_{og-a}}{\nu_{og-a}^2} \quad \ldots(4.24)$$

$$\beta = \frac{1}{T_{og-a}} \quad \ldots(4.25)$$

$Pr_{og\text{-}a} = \frac{\nu_{og-a}}{\alpha_{og-a}}$ …(4.26)

where (Ra_{Dog}) is Rayleigh number evaluated at the outer glass envelope diameter, ($Pr_{og\text{-}a}$) is Prandtl number at (T_{og-a}), (β) is volumetric thermal expansion coefficient, (α_{og-a}) is the thermal diffusivity. The properties; ($Pr_{og\text{-}a}$), (β) are evaluated at the average temperature between the outer glass envelope temperature and the ambient temperature [(T_{og}+T_a)/2]. This correlation is valid for a wide range of Rayleigh numbers ($10^{-3} <$ Ra$<10^{13}$).

$U_L=\frac{Nu\times D_g}{K}$ …(4.27)

4.5.3 Calculation of useful power

The useful power after neglecting the losses from the connecting pipes can be found as:

$\dot{Q}_u = \dot{m}C_p(T_r - T_{To})$ …(4.28)

where $\dot{Q}_u$ is the heat gained by water from the collector, (T_r) is the receiver surface temperature and (T_{To}) is the temperature of water leaving the tank

The useful power is utilized for heating the mixture of water and acetone in the generator. So, the heat transfered to generator after neglecting the heat losses through the connecting pipes is estimated as:

$\dot{Q}_g = \dot{m}C_p(T_r - T_{Ti})$ …(4.29)

Where, $\dot{Q}_g$ is the heat rate given to the mixture by the hot water, (T_{Ti}) is the temperature of fluid leaving the generator and entering the tank.

There are two variables in the equation (4.29) which are $\dot{Q}_g$ and T_{Ti}, so the effectiveness (ε) of the generator with the generator fluid will be assumed to be 0.7 and can be expressed as follows:

$\varepsilon = \frac{T_g - T_{Ti}}{T_r - T_{Ti}}$ (4.30)

4.5.4 Heat balance of the tank

According to the first law of thermodynamics for open systems for segment (i):

$\frac{dE}{dt}=\dot{Q}-\dot{W}+\sum_{inlet}\dot{m}(h+KE+PE)-\sum_{outlet}\dot{m}(h+KE+PE)$…(4.31)

There are many assumptions for this equation:

1- No work and heat transfer to surrounding
2- Kinetic energy (KE) and potential energy (PE) equal to zero
3- The tank is assumed to be adiabatic and well-mixed storage. So the storage heat will be, [109]:

$m\ C_v \frac{dT}{dt} = \dot{Q}_u-\dot{Q}_g$ …(4.32)

$m\ C_v \frac{(T_{Ti}-T_{To})}{\Delta t} = \dot{Q}_u-\dot{Q}_g$ …(4.33)

where T_{Ti} is the fluid temperature entering the tank in the first time and T_{To} is the fluid temperature exiting from the tank in the second time.

4.5.5 Exergy efficiency of the collector cycle

The equation of exergy balance takes the following form, [110]:

$$\dot{E}x_{in}-\dot{E}x_{sto}-\dot{E}x_{out}-\dot{E}x_{dest}=0 \quad \text{…(4.34)}$$

where $\dot{E}x_{in}$ is the rate of inlet exergy, $\dot{E}x_{sto}$ is the rate of stored exergy, $\dot{E}x_{out}$ is the rate of outlet exergy, and $\dot{E}x_{dest}$ is the rate of exergy loss.

The rate of inlet exergy to receiver is the sum of the inlet exergy carried out by fluid flow and the radiation exergy rate from the sun. The inlet exergy rate carried out by fluid flow is, [110]:

$\dot{E}x_{in,r}=\dot{m}c_p(T_{To}-T_o-T_o \ln\frac{T_{To}}{T_o})$ … (4.35)

Where,(ṁ) is the mass flow rate of water with value of (1.5 l/min.). The exergy of radiation from the sun on the collector can be estimated as, [111]:

$$\dot{E}x_s = I_{tot}\, A_c\left(1-\frac{T_o}{T_{sun}}\right) \quad \ldots(4.36)$$

The outlet exergy rate carried out by fluid flow is, [112]:

$$\dot{E}x_{out,r} = \dot{m}\, C_p\left(T_{ro}-T_o-T_o \ln\frac{T_{ro}}{T_o}\right) \quad \ldots(4.37)$$

The rate of useful exergy for receiver is:

$$\dot{E}x_u = \dot{E}x_{out,r} - \dot{E}x_{in,r} \quad \ldots(4.38)$$

$$\dot{E}x_{dest,r} = \dot{E}x_s - \dot{E}x_u \quad \ldots(4.39)$$

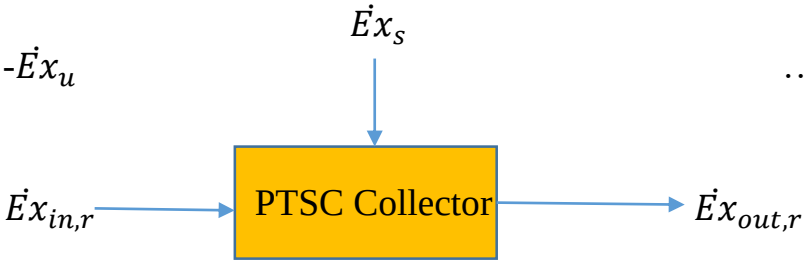

The exergy of the generator heat exchanging is found as:

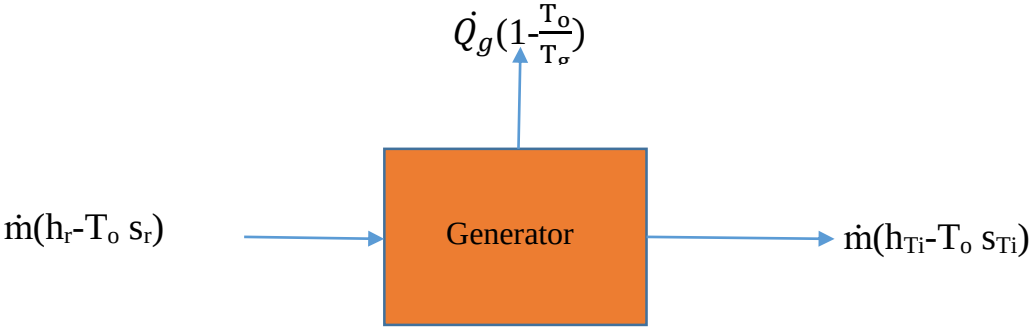

$$\dot{E}x_{in,g} = \dot{m}(h_r-T_o\, s_r) = \dot{m}\, C_p\left(T_r-T_o \ln\frac{T_r}{T_o}\right) \quad \ldots(4.40)$$

$$\dot{E}x_{out,g} = \dot{m}(h_{Ti}-T_o\, s_{Ti}) + \dot{Q}_g\left(1-\frac{T_o}{T_g}\right) = \dot{m}C_p\left(T_{Ti}-T_o \ln\frac{T_{Ti}}{T_o}\right) + \dot{Q}_g\left(1-\frac{T_o}{T_g}\right) \quad \ldots(4.41)$$

$$\dot{E}x_{dest,g} = \dot{m}\, C_p\left[(T_r-T_{Ti})-T_o\left(\ln\frac{T_r}{T_o}-\ln\frac{T_{Ti}}{T_o}\right)\right] - \dot{Q}_g\left(1-\frac{T_o}{T_g}\right) \quad \ldots(4.42)$$

$$\dot{E}x_{dest,g} = \dot{m}\, C_p\left[(T_r-T_{Ti})-T_o \ln\frac{T_r}{T_{Ti}}\right] - \dot{Q}_g\left(1-\frac{T_o}{T_g}\right) \quad \ldots(4.43)$$

While, the storage tank exergy can be found as:

$$\dot{E}x_{dest,st}=(\dot{E}x_{in,st}-\dot{E}x_{out,st})+\dot{Q}_{st}\ (1-\frac{T_o}{T_{st}}) \quad \ldots(4.44)$$

where ($\dot{E}x_{dest,st}$), ($\dot{E}x_{in,st}$) , ($\dot{E}x_{out,st}$) and $\dot{Q}_{st}$) are storage tank exergy, inlet exergy to storage, outlet exergy and the heat entering the storage tank respectively. While (T_{st}) is the storage tank temperature. After substituting the values of ($\dot{E}x_{in,st}$)and ($\dot{E}x_{out,st}$), the exergy can be found as, [113]:

$$\dot{E}x_{dest,st}=\dot{m}(h_{in,f}+T_o\ s_{in,f})-\dot{m}(h_{out,f}+T_o\ s_{out,f})+\dot{Q}_{st}(1-\frac{T_o}{T_{st}}) \quad \ldots(4.45)$$

$$\dot{E}x_{dest,st}=\dot{m}(h_{in,f}-h_{out,f})-\dot{m}T_o(s_{in,f}-s_{out,f})+\dot{Q}_{st}(1-\frac{T_o}{T_s}) \quad \ldots(4.46)$$

$$\dot{Q}_{st}=\frac{m\ C_p\ (T_{Ti}-T_{To})}{t} \quad \ldots(4.47)$$

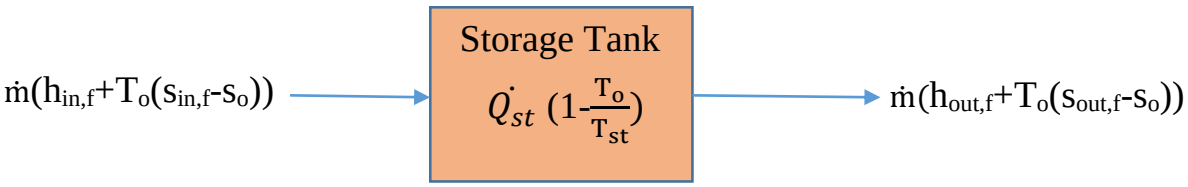

The total exergy destruction of collector loop is the summation of exergy destruction in its components.

$$\dot{E}x_{dest,Cycle}=\dot{E}x_{dest,r}+\dot{E}x_{dest,g}+\dot{E}x_{dest,st} \quad \ldots(4.48)$$

4.6 The Absorption Cycle

The absorption cooling cycle shown in Fig.(4.3) is a closed cycle where the operating fluid flows inside the closed system, and the surrounding interface is at boundaries through which work and heat are transferred. The operating fluid of absorption system is a refrigerant and absorbent solution which has a strong chemical attraction for each other. Fig. (4.4) shows the thermodynamic cycle of the absorption cooling cycle. The solution in the generator is supplied with heat from a high-temperature source hot water from solar collector loop as an outcome, a portion of the refrigerant evaporates from the boiling solution in the generator (point 7),

that becomes less in the absorbent concentration. As the refrigerant vapour is condensed in the condenser, heat is removed from it. The liquid refrigerant then goes through an expansion valve to the evaporator (points 8, 9), [113].

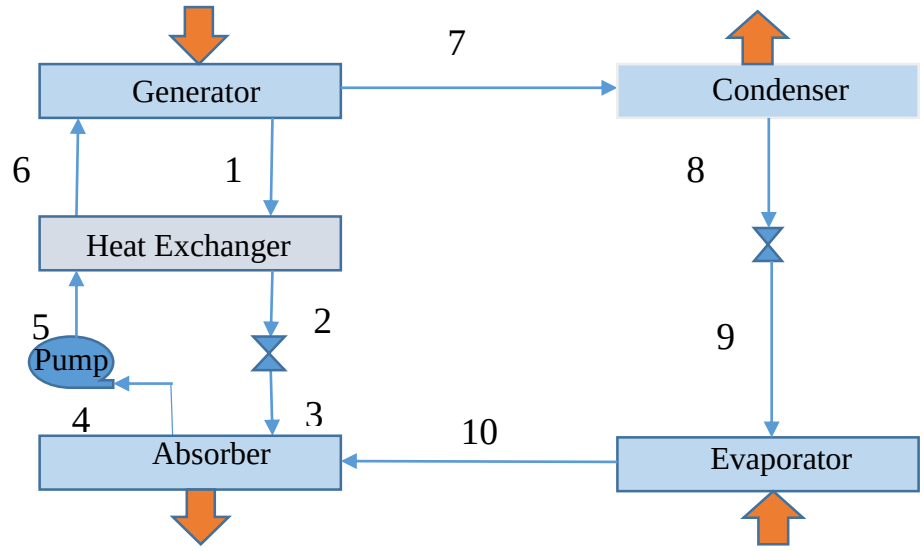

Fig. (4.3) schematic diagram of solar absorption cooling system.

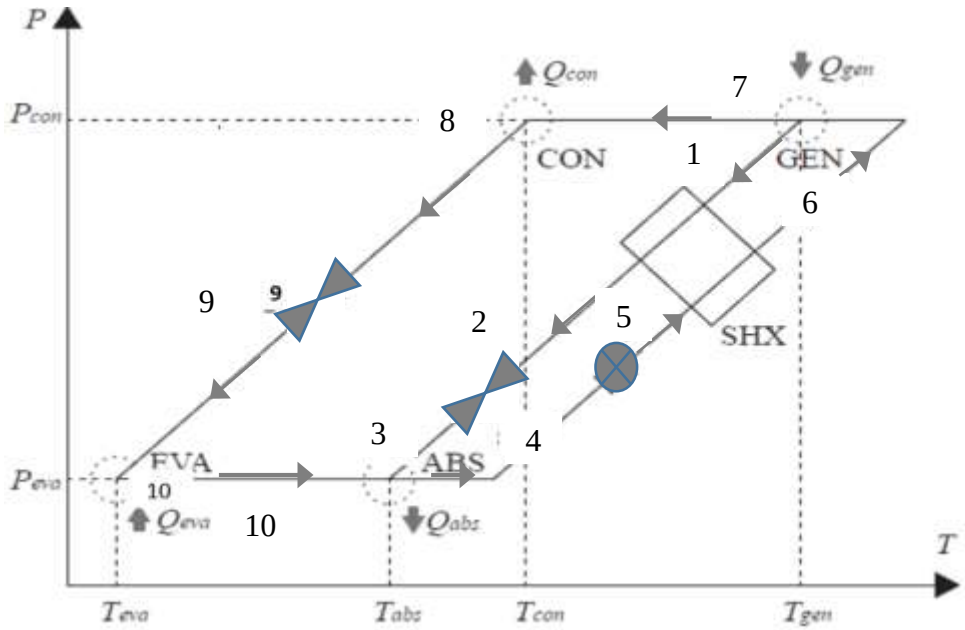

Fig. (4.4) single-effect absorption system cycle on a ln P– (T) diagram, [115].

Evaporation of the liquid refrigerant occurs in the evaporator. The vapor that leaves the evaporator (point 10) is mixed in the absorber with a weak solution (points 1, 2, 3), that arrives from the generator across the heat exchanger and expansion valves. The liquid solution, which is strong is now pumped via the heat exchanger back to the generator, to complete the cycle (points 4, 5, 6). To minimize sensible heat losses, a heat exchanger located between the generator and the absorber in the solution loop is used.

4.7 Quasi Steady State Model

4.7.1 Assumptions

The following assumptions will be taken into consideration:

1- The heat diffusion amount in the direction of flow is negligible.

2- Both generator and evaporator are insulated from the surroundings.

3- The refrigerant at the evaporator exit is assumed as a saturated vapor at evaporator pressure.

4- The refrigerant at the generator exit is assumed to be at the saturated vapor state.

5- The concentration of solutions leaving the absorber and the generator is different from the concentration through the absorber and the generator respectively.

6- The work input to the pump is neglected.

7-There is no loss of pressure in connecting pipes.

8- The temperature of fluid at the exit of each component is the same as the temperature through that component.

4.7.2 Mass and energy analysis

The governing equations used in this analysis are the mass and energy conservation equations. These equations are applied for each component in the cycle.

The governing mass conservation equations utilized in absorber and generator parts are:

$\dot{m}_{ss} = \dot{m}_{ws} + \dot{m}_a$ …(4.49)

For acetone balance

$\dot{m}_{ws}\ X_{ws} + \dot{m}_a = \dot{m}_{ss}\ X_{ss}$ … (4.50)

Where ($\dot{m}_{ss}$), ($\dot{m}_{ws}$) and ($\dot{m}_a$) are the mass flow of the strong solution, weak solution, and acetone refrigerant, and (X_{ss}), (X_{ws}) are the strong and weak solutions of the acetone concentrations.

The concentration is described as the ratio of the acetone mass in a solution to the total mass of acetone and water preserved in the solution.

$$X = \frac{\text{mass of (acetone)}}{\text{mass of (acetone)+mass of (water)}} = \frac{m_a}{m_{ss}} \quad \text{...(4.51)}$$

The steady state, steady flow energy equation is:

$$\sum \dot{Q} + \sum \dot{W} = \dot{m}\left(h_e + \frac{V_e^2}{2} + g\,Z_e\right) - \dot{m}\left(h_i + \frac{V_i^2}{2} + g\,Z_i\right) \ldots(4.52)$$

where $\dot{Q}$ and $\dot{W}$ are the rates of heat transfer and work across the component boundary.

Enthalpy data for the aqueous acetone solution are needed for executing thermal calculations on the absorption refrigeration cycle. The values of enthalpy are based on the constituents choosing the standard state. For each one of the two constituents, water and acetone, the data of enthalpy that will be utilized for calculations in these inquests are focused on a reference state of zero enthalpy at (0 °C).

The steady state steady flow energy equation (4.52) will be adopted to each component using the note in Fig. (4.2), assuming uniform temperatures and equilibrium states inside the component.

(1) Generator: The rate of heat transfer to the solution is

The heat balance can be written as:

Inlet heat=exit heat

$\dot{Q}_G + \dot{m}_6 h_6 = \dot{m}_7 h_7 + \dot{m}_1 h_1$ …(4.53)

$\dot{Q}_G = \dot{m}_7 h_7 + \dot{m}_1 h_1 - \dot{m}_6 h_6$ …(4.54)

But

$\dot{m}_1 = \dot{m}_{ws}$

$\dot{m}_6 = \dot{m}_{ss}$

$\dot{m}_7 = \dot{m}_a$

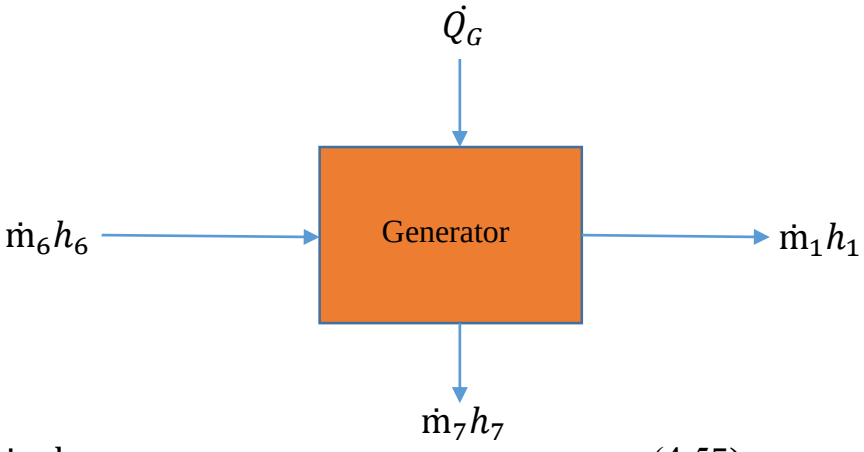

Or,

$\dot{Q}_G = \dot{m}_a h_7 + \dot{m}_{ws} h_1 - \dot{m}_{ss} h_6$ …(4.55)

Where,

h_1=enthalpy of saturated weak solution at (T_1) and (X_{ws})

h_6 =enthalpy of strong solution at (T_6) and (X_{ss})

h_7 =enthalpy of saturated acetone vapor at (T_7)

Generator temperature= $T_1 = T_7 = T_G$

(2) Condenser: The heat transfer across the condenser is:

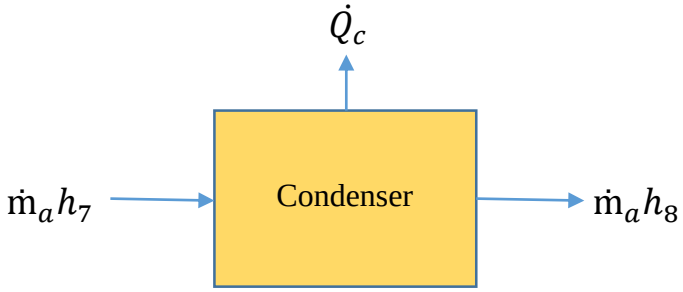

Heat in = heat out

$\dot{Q}_c = \dot{m}_a h_7 - \dot{m}_a h_8$ …(4.56)

$\dot{Q}_c = \dot{m}_a (h_7 - h_8)$ …(4.57)

h_8 =enthalpy of saturated acetone liquid at (T_8)

Condenser temperature=T_8=T_c

(3) Vapor throttling valve (valve 1)

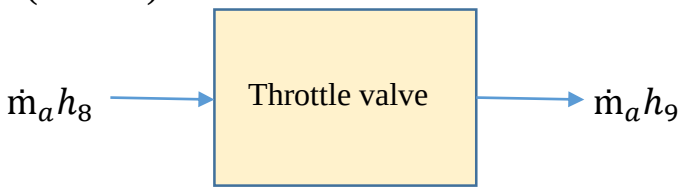

Heat in = heat out

$\dot{m}_a h_8 = \dot{m}_a h_9$ …(4.58)

Hence;

$h_9 = h_8$ …(4.59)

h_9= enthalpy of acetone liquid at (T_9)

(4) Evaporator: The heat balance across the evaporator i.e. (the Cooling effect) is**:**

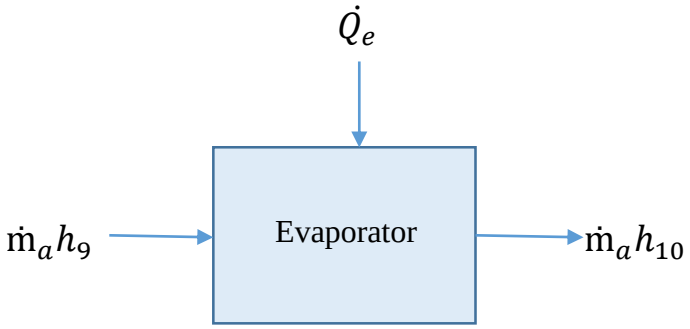

Heat in = heat out

$\dot{m}_a h_9 + \dot{Q}_E = \dot{m}_a h_{10}$ …(4.60)

$\dot{Q}_E = \dot{m}_a (h_{10} - h_9)$ …(4.61)

$\dot{Q}_E = \dot{m}_a (h_{10} - h_8)$ …(4.62)

h_{10}=enthalpy of acetone vapor at T_{10}

Evaporator temperature=T_{10}=T_E

(4) Solution throttling valve (valve 2): the energy balance is:

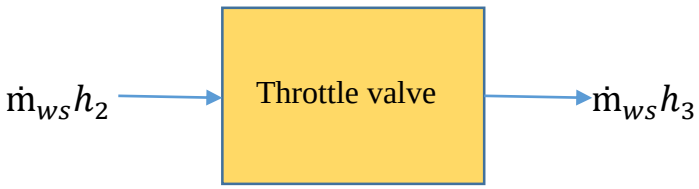

Heat in = heat out

$\dot{m}_{ws} h_2 = \dot{m}_{ws} h_3$ …(5.63)

Hence;

$h_3 = h_2$

h_2 =enthalpy of solution at T_2 and X_{ws}

h_3 =enthalpy of solution at T_3 and X_{ws}

(5) Absorber: The rate of heat transfer from the absorber is:

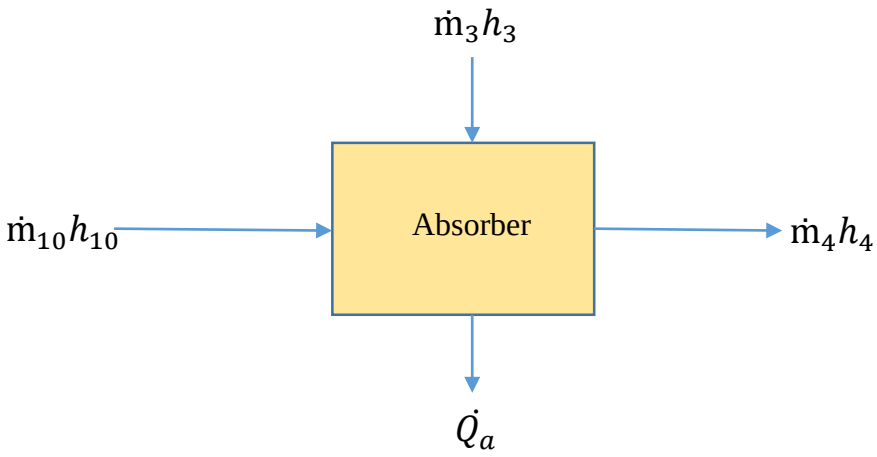

Heat in = heat out

$\dot{m}_3 h_3 + \dot{m}_{10} h_{10} = \dot{Q}_a + \dot{m}_4 h_4$ …(4.64)

$\dot{Q}_a = \dot{m}_3 h_3 + \dot{m}_{10} h_{10} - \dot{m}_4 h_4$ …(4.65)

$\dot{Q}_a = \dot{m}_{ws} h_2 + \dot{m}_a h_{10} - \dot{m}_{ss} h_4$ …(4.66)

h_4 =enthalpy of saturated strong solution at T_4 and X_{ws}

h_{10}=enthalpy of saturated acetone vapor at T_E

T_4=T_a=Absorber temperature

(6) Heat exchanger: Assuming heat losses are neglected for the surroundings, the heat balance between weak and strong solutions is:

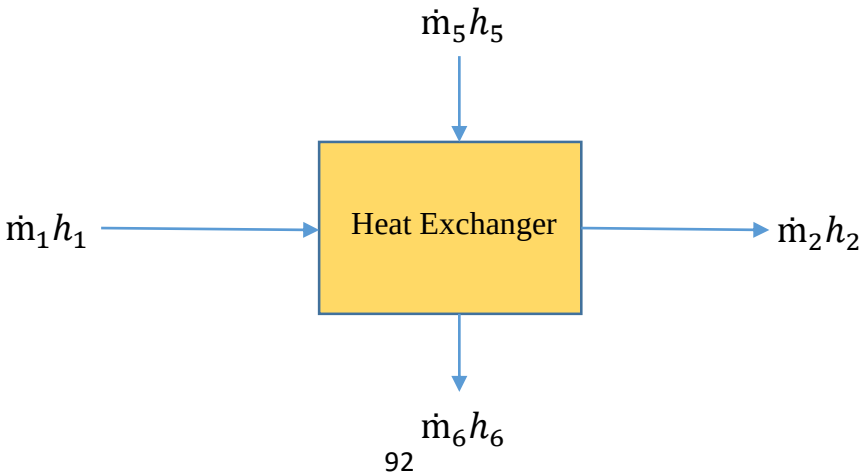

Heat in = heat out

$\dot{m}_5 h_5 + \dot{m}_1 h_1 = \dot{m}_6 h_6 + \dot{m}_2 h_2$ …(4.67)

$\dot{Q_{HX}} = \dot{m}_6 h_6 - \dot{m}_5 h_5 = \dot{m}_1 h_1 - \dot{m}_2 h_2$ …(4.68)

$\dot{Q_{HX}} = \dot{m}_{ws} (h_1 - h_2) = \dot{m}_{ss} (h_6 - h_5)$ ...(4.69)

The effectiveness of the heat exchanger of about 0.7 will be taken in the calculations.

(8) Solution pump: The power input to the pump is

$\dot{W}_P = \dot{m}_{ss} (h_5 - h_4)$ …(4.70)

h_5 =enthalpy of weak solution at T_5 and X_{ws}.

A relation between the evaporated acetone, generator temperature and the concentration of acetone has been obtained from the experimental work in the present study using Statistical Product and Service Solutions (SPSS software) as:

$\dot{m}_a = A*T_g + B*X*T_g + CX^D + E$ …(4.71)

where:

A=0.00000926

B=0.00003846

C= -0.0021263

D=2.333

E= -0.001074252

X=acetone concentration

In Eq. (4.71), the range of T_g between 60 and 85 ℃ and X values from 40-60% with coefficient of determination (R^2 of 0.999) value.

For evaluating the temperature of supplied air from the evaporator, the following equation from chapter three are used:

$\dot{Q}_s = \rho * \dot{V} * cp * (T_m - T_s)$ …(3.13)

Where,

T_m: the mixing temperature, (T_m=31.37 ℃).

$\dot{V}$: air flow rate, ($\dot{V}$ =0.02183 m^3/s).

$\dot{Q}_s=\dot{Q}_e$

$$T_s= T_m-\frac{\dot{Q}_e}{\rho V \dot{C}p} \quad \ldots(4.72)$$

The performance coefficient for the cycle is

$$COP = \frac{\dot{Q}_e}{\dot{Q}_g} = \frac{\dot{m}_a(h_{10}-h_8)}{\dot{m}_a h_7+\dot{m}_{ws} h_1-\dot{m}_{ss} h_6} \quad \ldots(4.73)$$

The daily coefficient of performance can be defined as the mean cooling load for the day to the mean generator heat through the day.

$$COP_{daily} =\frac{\sum_1^n \dot{Q}_e}{\sum_1^n \dot{Q}_g} \quad \ldots(4.74)$$

Where n is the number of operating hours. The circulation ratio (λ) can be defined as the ratio between the acetone vapor ($\dot{m}_a$) produced in the generator to the total mass of solution ($\dot{m}_{ss}$).

$$\lambda = \frac{\dot{m}_a}{\dot{m}_{ss}} \quad \ldots(4.75)$$

The ratio between the obtained cooling effect to the required cooling effect which is (300 W) will be expressed as (ψ).

$$\psi = \frac{\dot{Q}_e}{300} \quad \ldots(4.76)$$

4.8 Exergy Analysis of Solar Absorption Cycle

For the absorption cooling cycle, the main sources of lost work or irreversibility are:

(i) Transfer of heat via a limited variation in the heat exchanging parts.

(ii) Mixing in the absorber. The mixed refrigerant vapor and solution vary in temperature and concentration.

(iii) Free expansion in valves during throttling process.

The exergy of fluid stream can be defined by Arzu Şencan et al. [114]:

$\Phi - \Phi_o = (h - h_o) - T_o (s - s_o)$ …(4.77)

Where Φ is the fluid exergy, h and s are the fluid enthalpy and entropy respectively, h_o and s_o are the enthalpy and entropy of fluid at a reference temperature T_o (298.15 K).

The loss of exergy or loss of availability in each element is expressed by Arzu Şencan et al, [114]:

$$\Delta\Phi = \Sigma \dot{m}_i \Phi_i - \Sigma \dot{m}_o \Phi_o - \Sigma Q\left(1 - \frac{T_o}{T}\right)_i + \Sigma W \quad \ldots(4.78)$$

Where $\Delta\Phi$ is the exergy loss or irreversibility that takes place in the process. The first term is the inlet stream of the control volume and the second term the outlet stream of the control volume. The third and fourth terms are the exergy corresponding to the heat transfer from a source at a temperature of T. The last term is the mechanical work exergy added to the control volume which is negligible for the absorption system due to the very low power needs.

The overall loss of exergy of system is the sum of individual exergy loss of each component and is expressed as:

$$\Delta\Phi = \sum_{n=1}^{m} \Delta\Phi_n \quad \ldots(4.79)$$

The exergy balance equations for each of the components with regard to the second law of thermodynamics can be given as following:

a- Generator

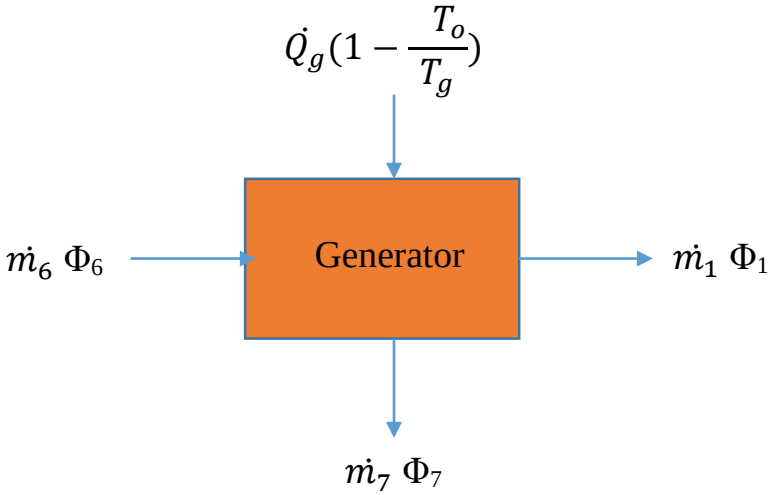

Exergy destruction is the difference between inlet and outlet exergies.

$Ex_{dist,g}= Ex_{in,g}-Ex_{out,g}$ …(4.80)

$Ex_{dist,g}=\dot{m}_6\ \Phi_6+\ \dot{Q}_g(1-\frac{T_o}{T_g})-\dot{m}_7\Phi_7-\dot{m}_1\ \Phi_1$ …(4.81)

b- Condenser

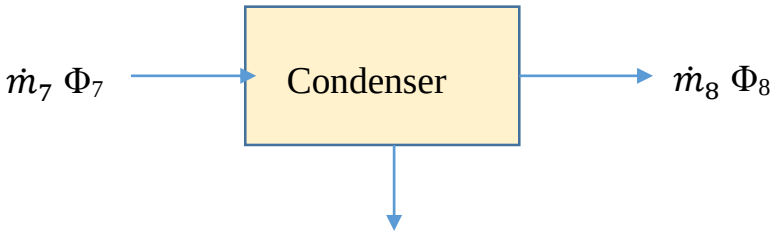

Exergy of inlet fluid($\dot{E}x_{in,c}$)=$\dot{m}_7\Phi_7$ …(4.82)

Exergy of outlet fluid($\dot{E}x_{out,c}$)=$\dot{Q}_c(1-\frac{T_o}{T_c})+\ \dot{m}_8\Phi_8$ …(4.83)

$\dot{E}x_{dest,c}=\dot{m}_7\Phi_7-\dot{m}_8\Phi_8-\dot{Q}_c(1-\frac{T_o}{T_c})$ …(4.84)

c- Refrigerant expansion valve (between condenser and evaporator)

Exergy of inlet fluid($\dot{E}x_{in,v1}$)=$\dot{m}_8\Phi_8$ …(4.85)

Exergy of outlet fluid ($\dot{E}x_{out,v1}$)=$\dot{m}_9\Phi_9$ …(4.86)

$\dot{E}x_{dest,v1}=\dot{m}_8\Phi_8-\dot{m}_9\ \Phi_9$ …(4.87)

d- Evaporator

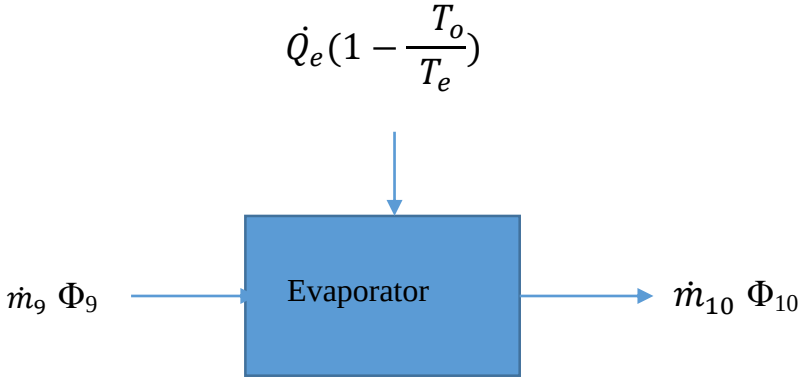

Exergy of inlet fluid($\dot{E}x_{in,e}$)= $\dot{m}_9\ \Phi_9 + \dot{Q}_e(1-\frac{T_e}{T_o})$ …(4.88)

Exergy of outlet fluid ($\dot{E}x_{out,e}$)= $\dot{m}_{10}\Phi_{10}$ …(4.89)

$\dot{E}x_{dest,e}$= $\dot{m}_9\Phi_9 - \dot{m}_{10}\ \Phi_{10} + \dot{Q}_e(1-\frac{T_e}{T_o})$ …(4.90)

e- Absorber

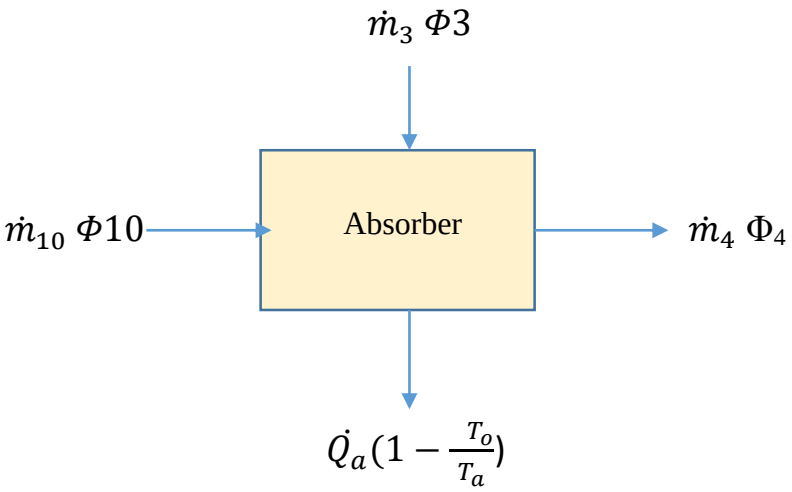

Exergy of inlet fluid ($\dot{E}x_{in,a}$)=$\dot{m}_{10}\Phi_{10}+\dot{m}_3\Phi_3$ …(4.91)

Exergy of outlet fluid ($\dot{E}x_{out,a}$)=$\dot{Q}_a(1-\frac{T_o}{T_a}) + \dot{m}_4\Phi_4$ ...(4.92)

$\dot{E}x_{dest,a}$=$\dot{m}_{10}\Phi_{10}+\dot{m}_3\Phi_3-\dot{m}_4\Phi_4-\dot{Q}_a(1-\frac{T_o}{T_a})$ …(4.93)

f- Heat exchanger

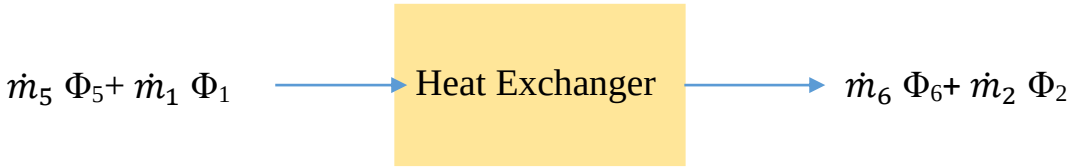

Exergy of inlet fluid ($\dot{E}x_{in,HX}$)= $\dot{m}_5\Phi_5+\dot{m}_1\Phi_1$ …(4.94)

Exergy of outlet fluid($\dot{E}x_{out,HX}$)= $\dot{m}_6\ \Phi_6 + \dot{m}_2\ \Phi_2$ …(4.95)

$\dot{E}x_{dest,HX}= \dot{m}_5\ \Phi_5+ \dot{m}_1\ \Phi_1- \dot{m}_6\ \Phi_6- \dot{m}_2\ \Phi_2$

g- Solution expansion valve (between heat exchanger and absorber)

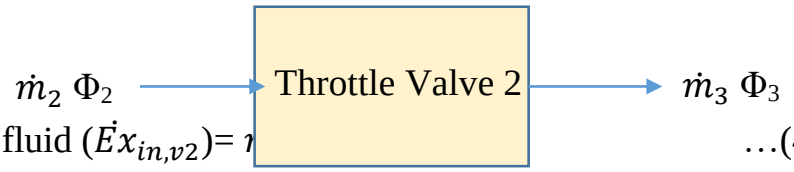

Exergy of inlet fluid ($\dot{E}x_{in,v2}$)= $\dot{m}$ …(4.96)

Exergy of outlet fluid ($\dot{E}x_{out,v2}$)= $\dot{m}_3\Phi_3$ …(4.97)

$\dot{E}x_{dest,v2}= \dot{m}_2\Phi_2-\dot{m}_3\ \Phi_3$ …(4.98)

The total exergy loss of absorption system is the sum of exergy loss in each component and is written as:

$\dot{E}x_{dest,Cucle}=\sum_{i=1}^{n} \dot{E}x_{dest,i}$ …(4.99)

$\dot{E}x_{dest,Cucle}= \dot{E}x_{dest,g} + \dot{E}x_{dest,c} + \dot{E}x_{dest,valv1} + \dot{E}x_{dest,e} + \dot{E}x_{dest,a} + \dot{E}x_{dest,HX} + \dot{E}x_{dest,valve2}$ …(4.100)

4.9 Thermodynamic Efficiency

The ideal absorption cycle is a combination of a Carnot engine operating between (T_H) and (T_o) and a cooling cycle working between (T_r), and (T_o), [73].

For the Carnot engine,

$$\frac{\dot{Q}_g}{\dot{W}} = \frac{T_H}{T_H-T_o} \quad \ldots(4.101)$$

For the refrigeration cycle,

$$COP=\frac{\dot{Q}_e}{\dot{W}} = \frac{T_r}{T_o-T_r} \quad \ldots(4.102)$$

The COP of the ideal cycle is

$$(COP)_{ideal}=\frac{\dot{Q}_e}{\dot{Q}_g} =\frac{T_r(T_H-T_o)}{T_H(T_o-T_r)} \quad \ldots(4.103)$$

The primary task of an absorption refrigeration cycle is to remove heat from the cooled medium. If the input work is small, the second law efficiency is:

efficiency of second law is

$$\eta_{sec} = \frac{(\dot{Q}_e)_{\text{ideal}}}{(\dot{Q}_g)_{\text{actual}}} \quad \ldots(4.104)$$

$$\eta_{sec} = \frac{\frac{\dot{Q}_e}{(\text{COP})_{\text{ideal}}}}{\frac{\dot{Q}_e}{(\text{COP})_{\text{actual}}}} = \frac{\text{COP}}{(\text{COP})_{\text{ideal}}} \quad \ldots(4.105)$$

The ratio of the cooling effect to the total solar energy can be defined as, the overall efficiency, η_{ov}.

$$\eta_{ov} = \frac{\dot{Q}_e}{I_{tot} \times A_c} \times 100\% \quad \ldots(4.106)$$

4.10 The Engineering Equation Solver (EES) Software

The analysis and modeling of this theoretical study is conducted utilizing the Engineering Equation Solver (EES) software, which was established by F-CHART SOFTWARE ®, [115]. (EES) software is a package that merges the (C^{++}) programing structures and (FORTRAN) with a built-in-iteration, thermodynamics and the relations of transport property (of more generally materials like water, air, and most refrigerants) and capacities of graphics.

Numerical integration, solves more sets of equations simultaneously. These capacities made the (EES) software is so helpful device for solving the thermodynamic problems, heat transfer and fluid dynamics. It can be utilized for different engineering applications. It can be utilized to conduct a parametric theoretical studies, where the influence of a specific variable can be easily found as shown in Fig.(4.5).

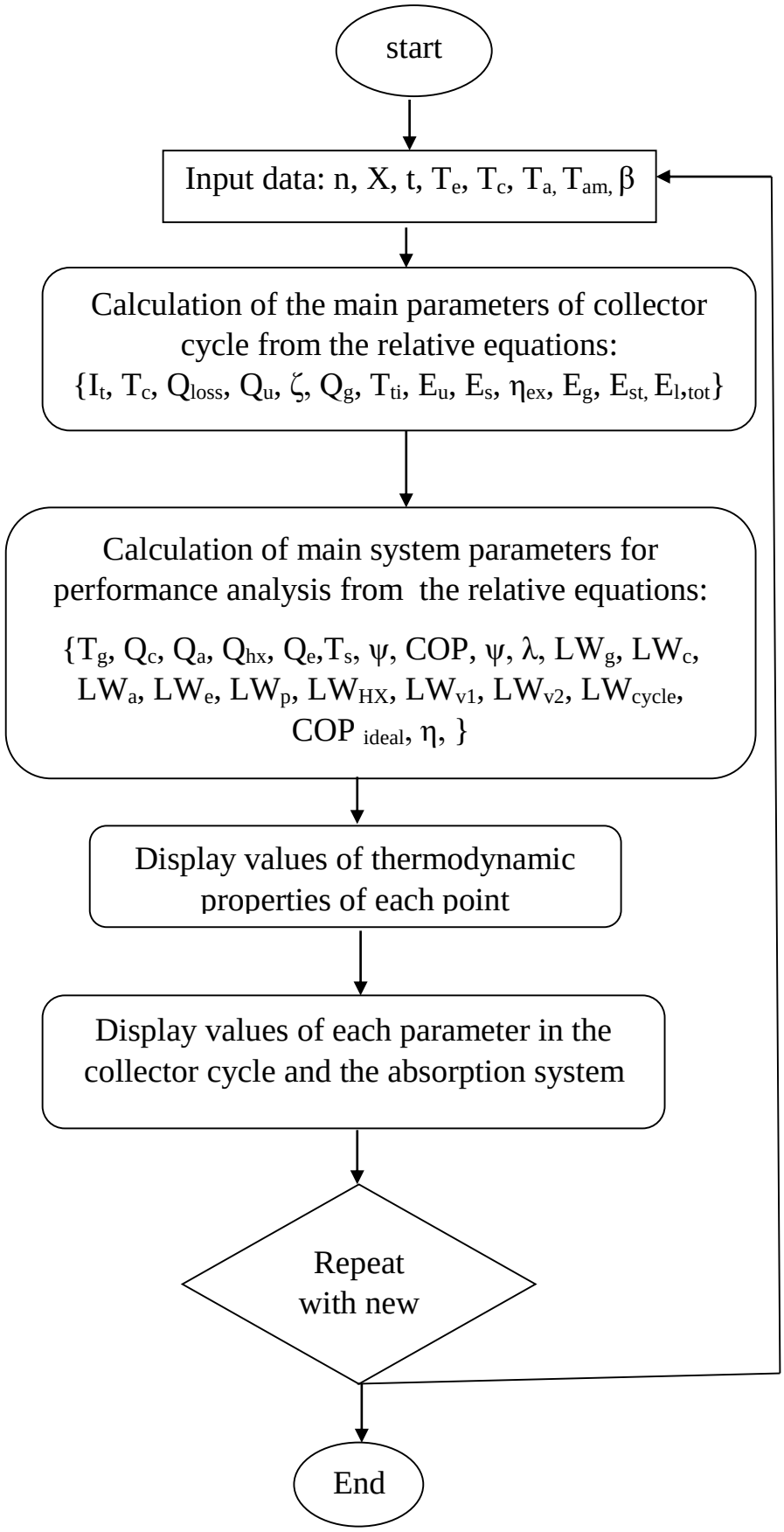

Fig.(4.5) flow chart of the EES program.

4.11 Mathematical Formulation of Ventilation System

The mathematical modeling of a convection problems is governed by the basic laws of fluid dynamics because every movement of fluid is subjected to these laws. The basic laws are named as conservation laws and considered as flow problems principle equations. These conservation equations can be put in form of partial differential equations (PDE's) for laminar or turbulent flow. They will be discussed in form of Cartesian coordinate system (i.e., x, y and z) based on a unit volume of fluid.

4.11.1 General governing conservation equations

Flowing fluid problem may be modeled by combining conservation equation of mass, momentum, energy and transport species. In the present simulation, the motion of air is considered to be three dimensional, incompressible and steady.

Conservation of mass

The mass conservation can be put as follows, [116]:

$$\frac{\partial}{\partial x}(\rho u)+\frac{\partial}{\partial y}(\rho v)+\frac{\partial}{\partial z}(\rho w)=0 \qquad \ldots(4.107)$$

Conservation of momentum (Navier–Stokes Equations)

The resultant forces on a control volume may be found by application of conservation of momentum in each direction to get three components of forces in x, y and z directions in form of differential equations as follows, [116]:

x-direction (U-momentum)

$$\frac{\partial}{\partial \mathrm{x}}(\rho \mathrm{uu})+\frac{\partial}{\partial \mathrm{y}}(\rho \mathrm{uv})+\frac{\partial}{\partial \mathrm{z}}(\rho \mathrm{uw})=-\frac{\partial \mathrm{p}}{\partial \mathrm{x}}+\frac{\delta}{\delta \mathrm{x}}\left(\mu \frac{\partial \mathrm{u}}{\partial \mathrm{x}}\right)+\frac{\delta}{\delta \mathrm{y}}\left(\mu \frac{\partial \mathrm{u}}{\partial \mathrm{y}}\right)+$$

$$\frac{\partial}{\partial \mathrm{z}}\left(\mu \frac{\partial \mathrm{u}}{\partial \mathrm{z}}\right)+\frac{1}{3}\frac{\partial}{\partial \mathrm{x}}\left[\mu\left(\frac{\partial \mathrm{u}}{\partial \mathrm{x}}+\frac{\partial \mathrm{v}}{\partial \mathrm{y}}+\frac{\partial \mathrm{w}}{\partial \mathrm{z}}\right)\right]+\frac{\partial}{\partial \mathrm{x}}\left(-\rho\,\overline{u'u'}\right)+\frac{\partial}{\partial \mathrm{y}}\left(-\rho\,\overline{u'v'}\right)+\frac{\partial}{\partial \mathrm{z}}\left(-\rho\,\overline{u'w'}\right) \qquad \ldots(4.108)$$

y-direction (V-momentum):

$$\frac{\partial}{\partial x}(\rho uv)+\frac{\partial}{\partial y}(\rho vv)+\frac{\partial}{\partial z}(\rho vw)=-\frac{\partial p}{\partial y}+\frac{\partial}{\partial x}\left(\mu\frac{\partial v}{\partial x}\right)+\frac{\partial}{\partial y}\left(\mu\frac{\partial v}{\partial y}\right)+\frac{\partial}{\partial z}\left(\mu\frac{\partial v}{\partial z}\right)+\frac{1}{3}\frac{\partial}{\partial y}\left[\mu\left(\frac{\partial u}{\partial x}+\frac{\partial v}{\partial y}+\frac{\partial w}{\partial z}\right)\right]+\frac{\partial}{\partial x}(-\rho\,\overline{u'v'})+\frac{\partial}{\partial y}(-\rho\,\overline{v'v'})+\frac{\partial}{\partial z}(-\rho\,\overline{v'w'})+\rho g_y \quad \ldots(4.109)$$

z-direction (W-momentum):

$$\frac{\partial}{\partial x}(\rho uw)+\frac{\partial}{\partial y}(\rho vw)+\frac{\partial}{\partial z}(\rho ww)=-\frac{\partial p}{\partial z}+\frac{\partial}{\partial x}\left(\mu\frac{\partial w}{\partial x}\right)+\frac{\partial}{\partial y}\left(\mu\frac{\partial w}{\partial y}\right)+\frac{\partial}{\partial z}\left(\mu\frac{\partial w}{\partial z}\right)+\frac{1}{3}\frac{\partial}{\partial z}\left[\mu\left(\frac{\partial u}{\partial x}+\frac{\partial v}{\partial y}+\frac{\partial w}{\partial z}\right)\right]+\frac{\partial}{\partial x}(-\rho\,\overline{u'w'})+\frac{\partial}{\partial y}(-\rho\,\overline{v'w'})+\frac{\partial}{\partial z}(-\rho\,\overline{w'w'}) \quad \ldots(4.110)$$

Conservation of thermal energy:

Applying balance of heat energy on infinitesimal control volume with differentials of dx, dy and dz sides, which means that the overall variation of stored energy in the control volume equals the net inlet energy flow into the control volume minus the outlet net energy flow outside the control volume. For steady state conditions, the energy conservation equation can be stated as, [117]:

$$\frac{\partial}{\partial x}(\rho ut)+\frac{\partial}{\partial y}(\rho vt)+\frac{\partial}{\partial z}(\rho wt)=\frac{\partial}{\partial x}\left(\Gamma\frac{\partial t}{\partial x}\right)+\frac{\partial}{\partial y}\left(\Gamma\frac{\partial t}{\partial y}\right)+\frac{\partial}{\partial z}\left(\Gamma\frac{\partial t}{\partial z}\right)+\frac{\partial}{\partial x}\left(-\rho\overline{u't'}\right)+\frac{\partial}{\partial y}\left(-\rho\overline{v't'}\right)+\frac{\partial}{\partial z}\left(-\rho\overline{w't'}\right)+S_t \quad \ldots(4.111)$$

Where:

(Γ) is the diffusivity, which is stated by: $\Gamma=\frac{\mu}{\sigma}$

($\sigma=\frac{\mu C_p}{Y}$) is the Prandtl or Schmidt number for the fluid.

The terms ($-\rho\overline{u't'}$, $\rho\overline{v't'}$ *and* $\rho\overline{w't'}$) are turbulent heat fluxes, (S_t) is a source term allowing for the rate of production of thermal energy, [117].

4.12 Turbulence Model

For a better estimation of the movement of indoor air and the dispersion of contaminant, a suitable turbulence model should be chosen. The two-equations renormalized group (RNG K-ε) turbulence model will be utilized for prediction of the turbulent air flow. This model gives an accurate estimation of indoor air flow, temperature and contaminant distribution, [117]. Its form is similar to the (standard k-ε) turbulent model, may be stated as, the turbulent kinetic energy, [118]:

$$\frac{\partial(\rho k u_i)}{\partial x_i} = \frac{\partial}{\partial x_j}\left[\left(\mu + \frac{\mu_t}{\sigma_k}\right)\frac{\partial k}{\partial x_j}\right] + P_k + \rho\varepsilon \qquad \ldots(4.112)$$

Convection Diffusion Generation Dissipation

The dissipation rate equation is:

$$\frac{\partial(\rho \varepsilon u_i)}{\partial x_i} = \frac{\partial}{\partial x_j}\left[\left(\mu + \frac{\mu_t}{\sigma_\varepsilon}\right)\frac{\partial \varepsilon}{\partial x_j}\right] + C_{1\varepsilon}\frac{\varepsilon}{k}p_k + C_{2\varepsilon}^{*}\rho\frac{\varepsilon^2}{k} \qquad \ldots(4.113)$$

Convection Diffusion Generation Destruction

where:

$C_{2\varepsilon}^{*} = C_{2\varepsilon} + (C_\mu \eta^3 (1 - \frac{\eta}{\eta_o}))/(1 + C_\omega \eta^3)\ with\ \eta = \frac{sk}{\varepsilon}\ and\ s = \sqrt{2S_{ij}S_{ij}}$,

The constants in the RNG k- ε turbulence model are:

C_μ=0.0845, σ_k=0.7194, σ_ε=0.7194, $C_{\varepsilon 1}$=1.42, $C_{\varepsilon 2}$=1.68, η_o=4.38 and C_ω=0.012.

4.13 Computational Set and Numerical Scheme

4.13.1 General

The wide spreading of efficient codes of (CFD) during the recently years with grater computer capacities for numerical simulations, made (CFD) computations one of the most important design strategies widely utilized in the studies of flow problems. One of these studies is the study of air movement in (HVAC) problems. (ANSYS AirPak) code is utilized for constructing the geometry of room, generation of a suitable grid and estimation of indoor air quality such as the distribution of temperature and velocity.

(AirPak) software will be utilized due to its accuracy, speed, and the easiness of its utilization as a design tool which simplifies the application of air flow modeling technology for ventilation systems design and analysis, which are needed to deliver indoor air quality(IAQ), thermal comfort and contaminants control. The capacity to quickly create and automatically mesh the ventilation system problems is conjugated with FLUENT's speed, accuracy, and well-proven unstructured solution. Moreover, post processing is necessary for ventilation industry because it gives designers a tool that gives more accurate solution possible in a shortest time in comparison for other airflow modeling tools, [119].

4.13.2 Assumptions

In the present work (CFD) simulation, the following assumptions are made:

1- The flow of air is assumed to be steady.
2- The flow of air is three dimensional.
3- The flow of air is Newtonian and turbulent.
4- The tested room and air ducts are insulated totally from the surrounding(adiabatic).

4.13.3 Room geometry

The present study includes an office room with one heat source above a solid table, a single person, lamp and window as shown in Fig.(4.6). The predicted results are plotted on the planes (P1, P2 and P3) as shown in Fig. (4.7), where the plane (1) at (z=1 m) and the other two planes at elevation of (Y=1.1 and 1.8 m), respectively inside the occupied zone. Plane (1) passes through the diffuser, computer, person and exit, while plane (2) at the breathing level for seated persons, while, plane (3) at the breathing level for standing persons. The comparison between the experimental and theoretical work will be taken at the pole (2).

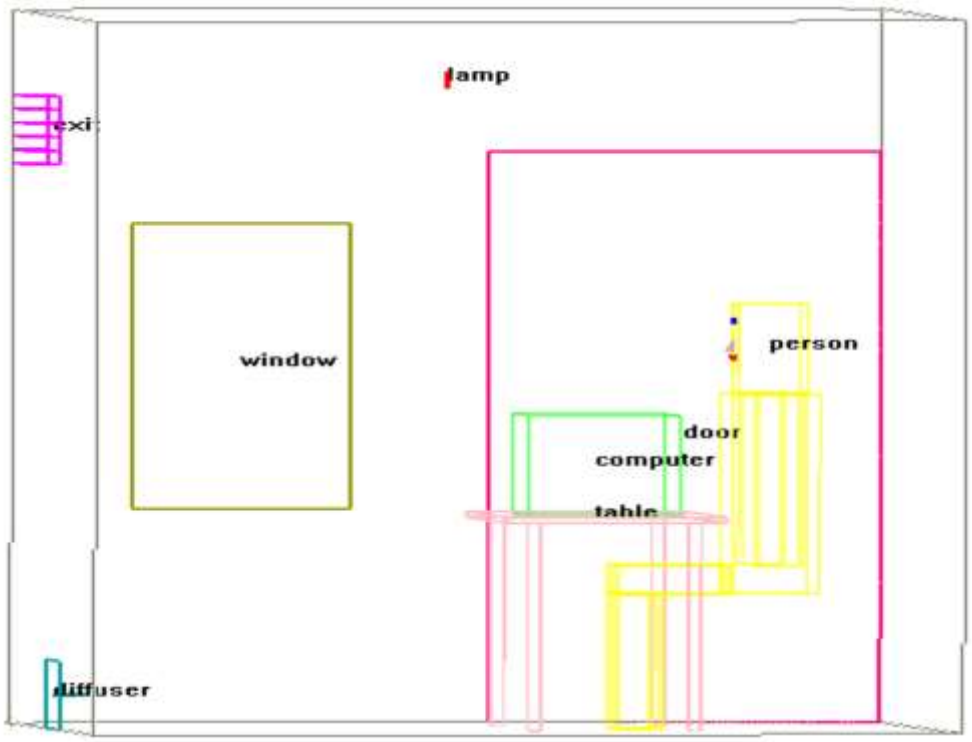

Fig. (4.6) geometry of tested room with its parts.

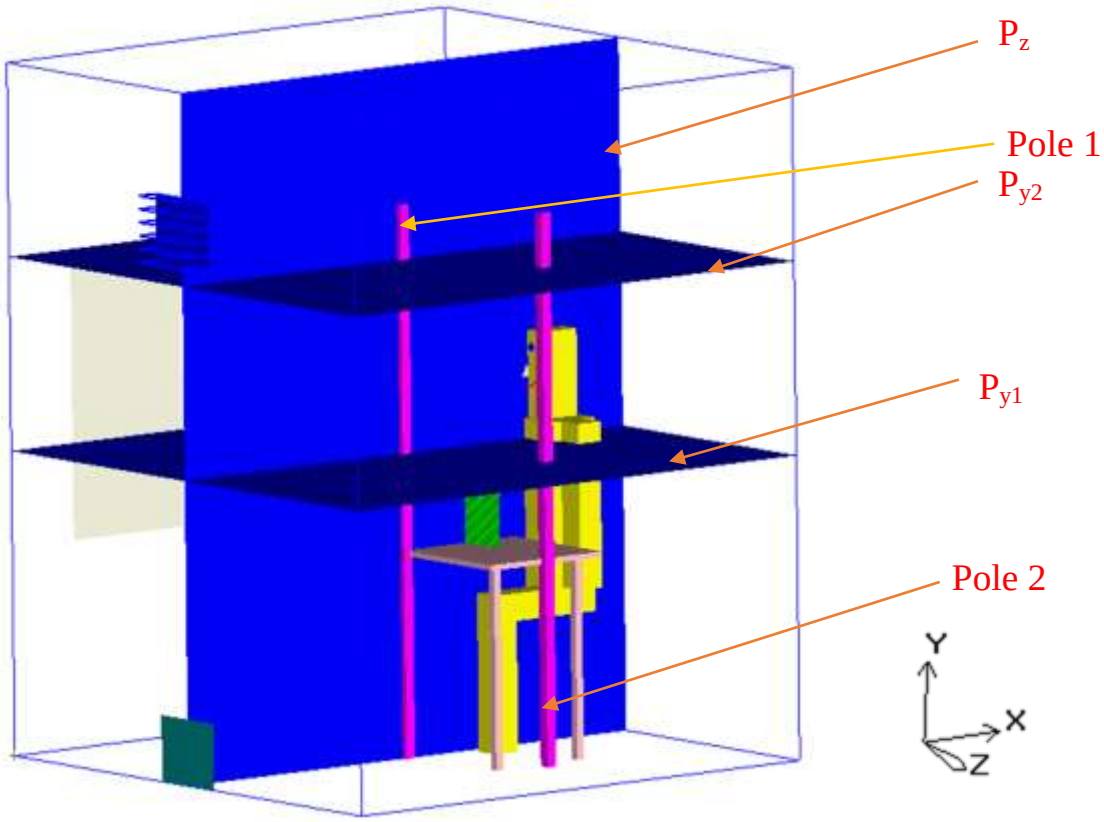

Fig. (4.7) schematic of room geometry stating the plot planes for all types (Plane P_Z at z=1 m, Plane P_{y1} at y=1.1 m, P_{y2} at y=1.8, Pole 1 at x=1 m and z=1 m and Pole 2 at x=1.25m and z=1.5m.

4.13.4 Mesh generation

The solution to flow field problems (temperature, pressure, velocity, etc) is defined at nodes for each cell. The accuracy of (CFD) solution is governed by the number of cells in the grid. In general, the larger the number of cells, the better the solution accuracy, [120]. Eight testing meshes has been considered through the study which are (815335, 922735, 1168771, 1240539, 1427500, 1535560, 1641902 and 1719847 nodes). Four positions where chosen to estimate the temperature and velocity at the selected meshes: p_1(0.5,0.3,1), p_2(1.5,1.2,1), p_3(0.8,1.1,1) and p_4(1.3,1.6,1.4). Figs. (4.8) and (4.9) show the relation between the temperature and local velocity with the number of mesh node, where the

temperature and local velocity remains approximately constants after the mesh of (1427500) nodes. Therefore, this mesh is chosen in the simulation. Table (4.1) shows the parameters of the selected mesh for the simulation. Figs. (4.10)&(4.11) show the mesh of the tested room with all components.

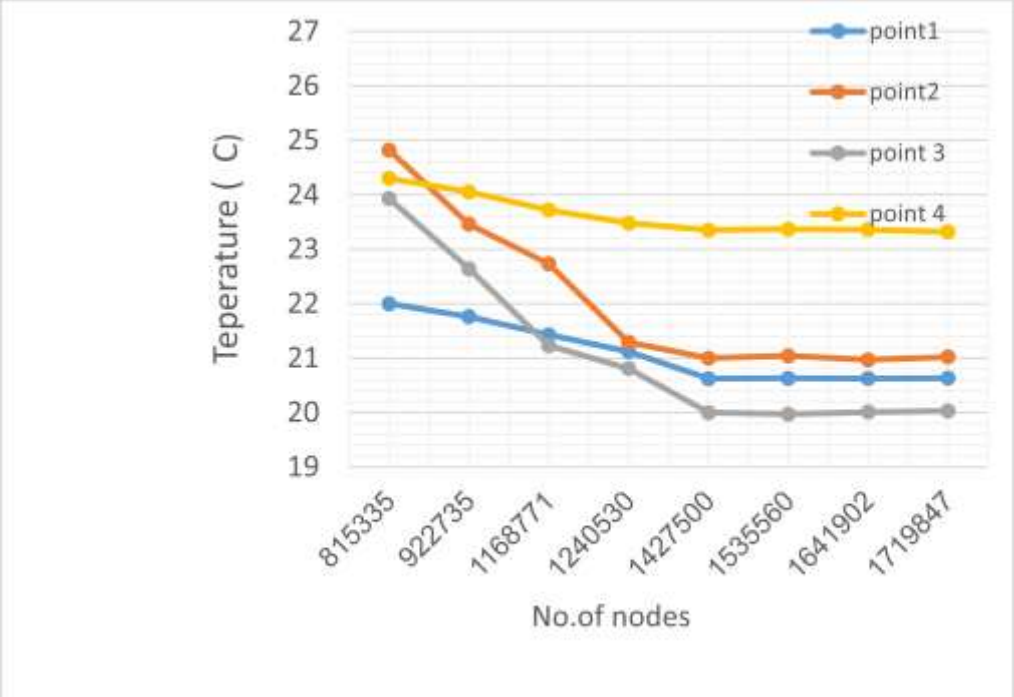

Fig. (4.8) variation of temperature with number of mesh nodes for different points.

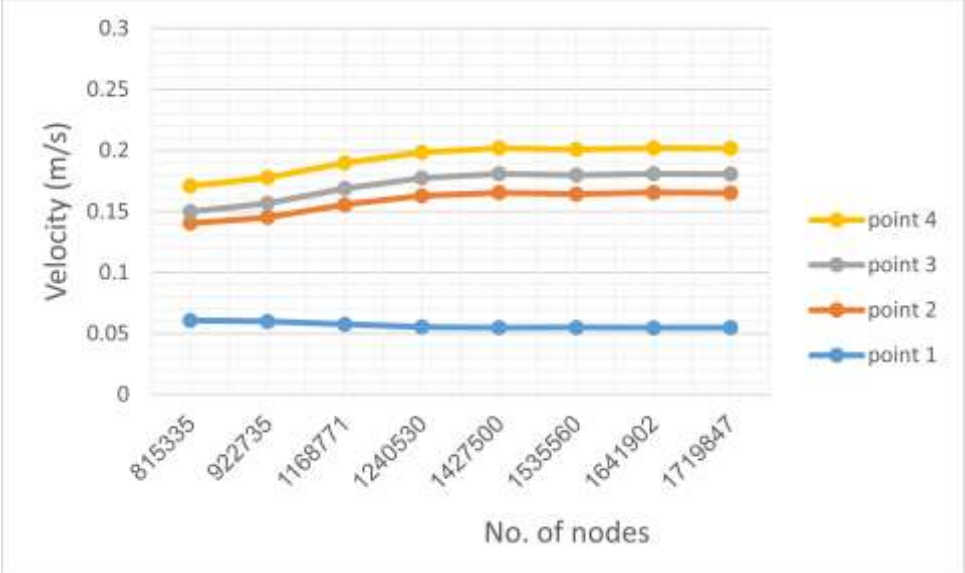

Fig. (4.9) variation of local mean velocity with the number of mesh nodes for different points.

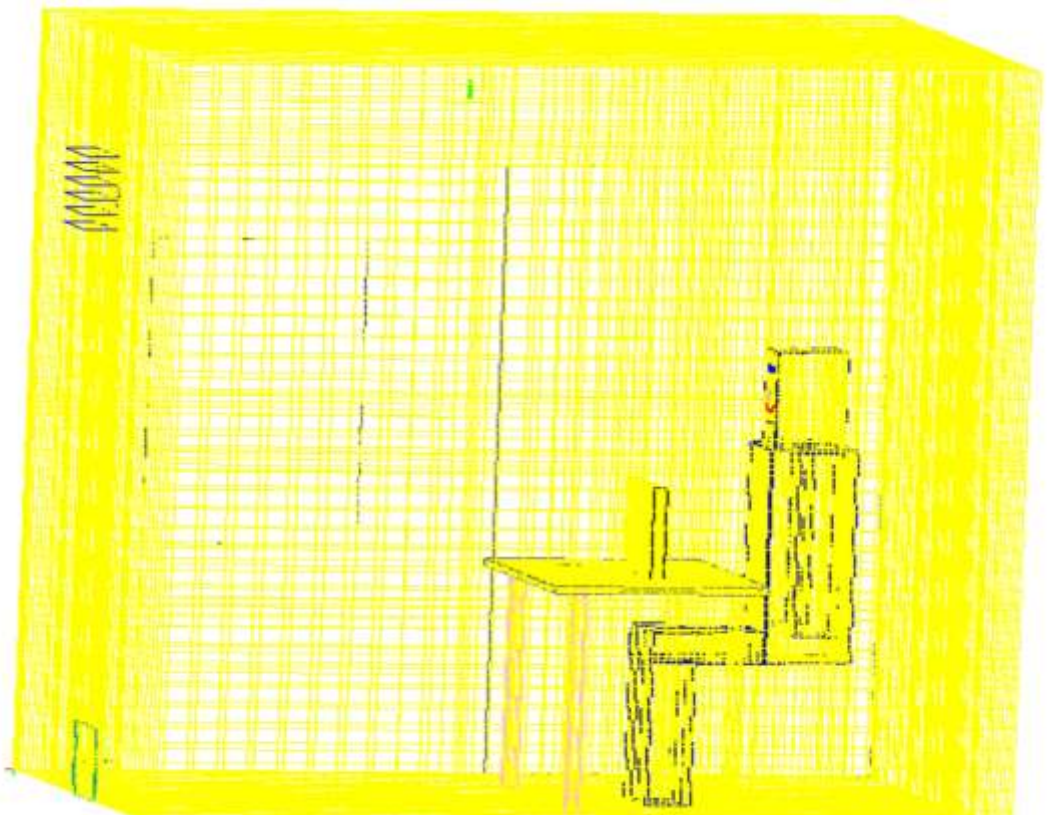

Fig. (4.10) mesh of the tested room.

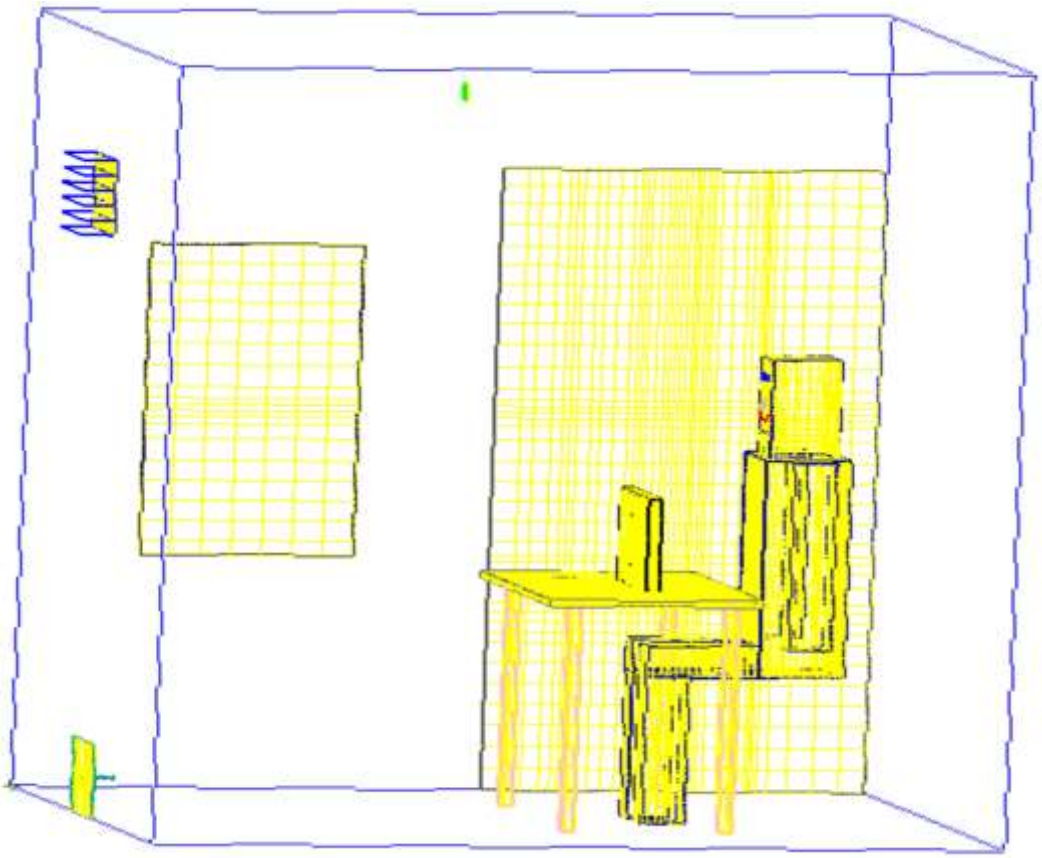

Fig. (4.11) mesh of the room parts.

Table (4.1) the parameters of selected mesh.

Mesh type	Hexa Cartesian	Min. y size	0.001	Max. size ratio	2
No. of elements	1427500	Max. z size	0.02	Min. elems. On cyl. face	3
No. of nodes	1471041	Min. z size	0.001	Min. elems. On tri face	4
Max. x size	0.02	Mesh parameters	normal	Cylinder shrink factor	0.99
Min. x size	0.001	Min. elems. In gap	4		
Max. y size	0.02	Min. elems. On edge	3		

4.14 Verification Case

The present study uses (CFD) technique to investigate the temperature contour for a room with air supply diffuser using displacement ventilation system. It is necessary to validate (ANSYS AirPak) software with another experimental study. The validation is done by comparing the (RNG k-Ɛ) model results with experimental data obtained in an office room with a wall-supply displacement ventilation system, [121]. The present results are simulated using the RNG(k-Ɛ) turbulence model.

Fig. (4.12) shows the relation between the temperature of the simulation work and the temperature of the experimental work of Ref. [121] with the height of the room at the pole (X=3 m, Z=1.95 m) at the room center. The Fig. shows good agreement between the two works. Table (4.2) gives the error percentage between the experimental study from, [121], and the simulation of present study. The maximum percentage

error is about (1.54 %) which is a better result and within the accepted range.

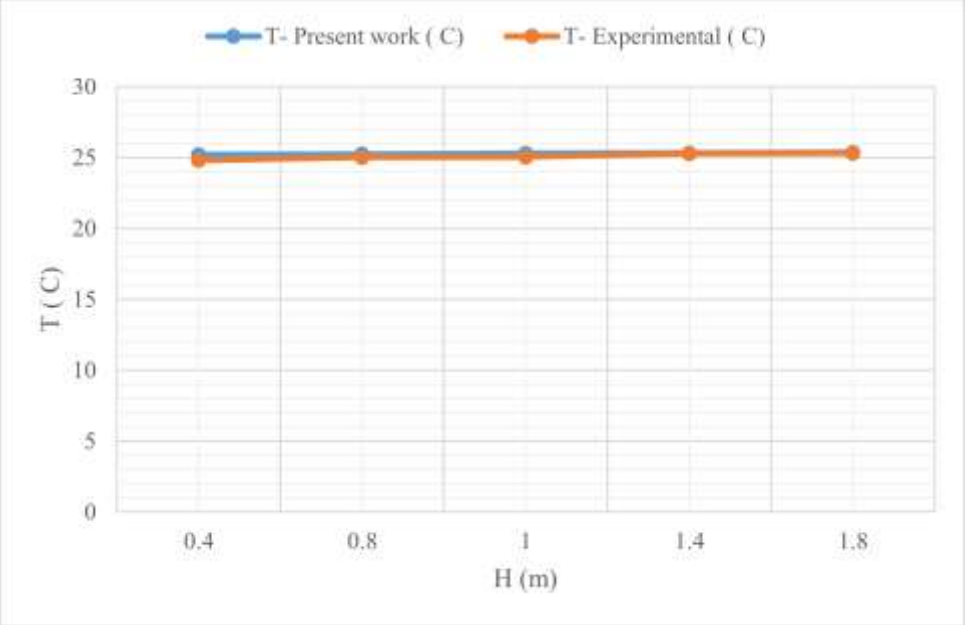

Fig. (4.12) variation of temperature of the present work and of the Ref. [150] with the height at the pole (X=3, Z=1.95).

Table (4.2) temperature distribution of the present work and experimental work of Xu, [121**],** at pole (x=3, z=1.95).

H(m)	T_{ex}, [121] ◦C	T_{th}[121] ◦C	T_{CFD}, (present work) ◦C	Error %
0.4	24.82	23.81	25.21	1.54
0.8	25.03	25.05	25.25	0.87
1	25.05	25.405	25.305	1
1.4	25.3	25.61	25.32	0.08
1.8	25.32	25.78	25.37	0.2

4.15 Numerical setup

The following three steps are used in (AirPak ANSYS(CFD)) program as shown in Figs. (4.13&4.14).

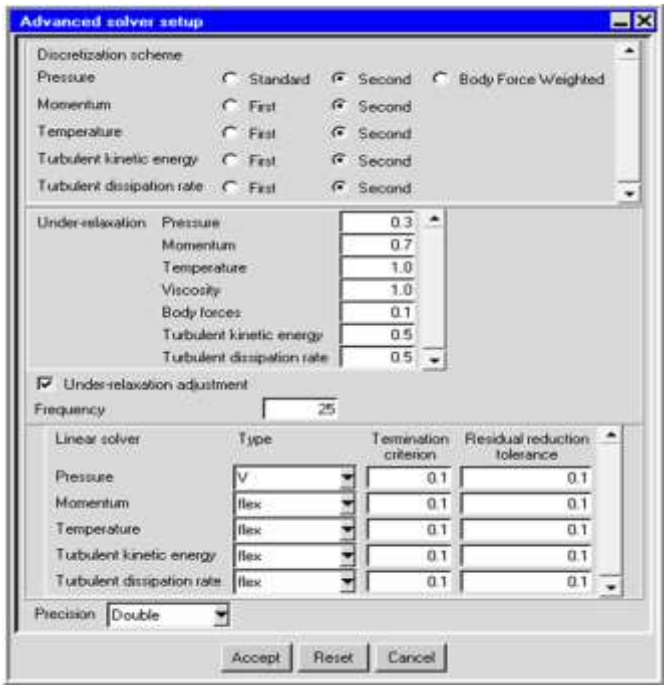

Fig.(4.14) advanced solver setup of the simulation.

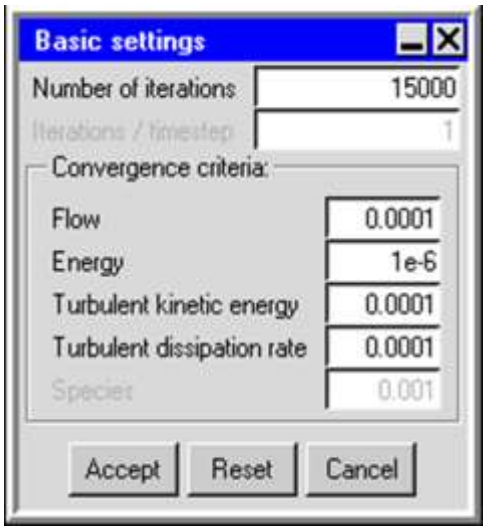

Fig.(4.15) basic settings of the simulation.

4.15.1 Problem setup

The style of problem setup is shown in Fig. (4.14), and the parameters of problem setup is shown in Table (4.3).

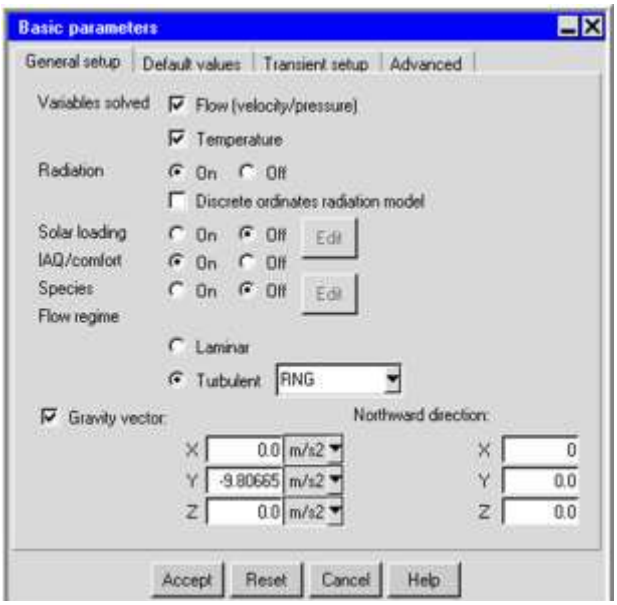

a-general setup

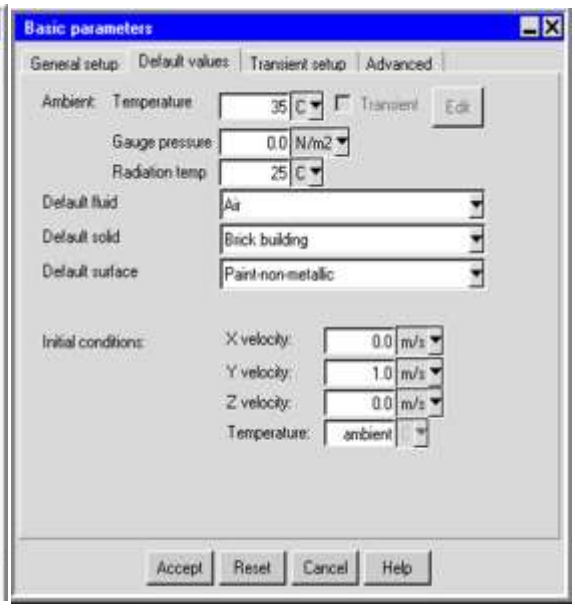

b- default values

Fig (4.13) simulation boundary conditions of the present work.

Table (4.3) the parameters of problem set up.

Flow regime	**Turbulent**	**Radiation Temperature**	**25 °C**
Model	RNG (K- ε)	Default fluid	Air
Temperature	35 °C	Time variation	Steady
Gauge Pressure	0 N/m^2(1 atm)		

4.15.2 Boundary conditions

Selection of appropriate boundary conditions has a significant impact on (CFD) simulation success in giving reliable results for solved problem. The following boundary conditions will be set:

1- The walls with no slip condition.

2- The heat flux of lights and occupants is constant.

3- The door, window and walls heat fluxes are constants.

4- The exit air at atmospheric pressure.

5- The supplied air will be fixed at velocity of inlet.

The following Boundary conditions in (CFD) simulation implemented in this work consist of three types: temperature, velocity of inlet air and exit as shown in table (4.4). Constant heat gain from the internal sources is mentioned in Table (4.5).

Table (4.4) boundary conditions

Boundary	Velocities	Temperature
Inlet	U = u_s , V=0 and W = 0	T=T_s
Exit	$U=u_s \frac{A_{in}}{A_{out}}$	$\frac{\partial T}{\partial X}=0$

Table (4.5) heat gain for different items.

Item	Heat gain (W)
Person	75
Computer	45
Light	15
window	31.26

4.16 Numerical Solution Procedure

4.16.1 Working fluid properties

The working fluid used is air and the flow is assumed to be steady, three-dimensional flow, incompressible fluid and Newtonian and turbulent flow. Its properties are shown in Table (4.6).

Table (4.6) air properties,[151]

Parameter	Value	unit
density, ρ(T)	1.225	kg/m^3
Thermal Conductivity (k)	0.0242	W/m.K
Specific Heat (C_p)	1006.43	J/kg.K
Viscosity (μ)	1.7894e-05	kg/m.s

4.16.2 Solution control

Table (4.7) shows the parameters of discretization scheme. The solution is performed under relaxation factor of (25) as shown in Fig. (4.13) . Table (4.8) shows the flow parameters values at the case of under relaxation.

Table (4.7) the parameters of discretization scheme.

pressure	**Second order**	**Turbulent kinetic energy**	**Second order**
momentum	Second order	Turbulent dissipation rate	Second order

temperature	Second order	precision	double

Table (4.8) the parameters of flow at under relaxation

pressure	**0.3**	**Body forces**	**0.1**
momentum	0.7	Turbulent kinetic energy	0.5
temperature	1	Turbulent dissipation rate	0.5
viscosity	1		

4.16.3 Convergence criteria

When solving problem numerically it is impossible to get an exact solution, so an accepted scaled error residual should be specified for different terms such as continuity, velocity components, energy, turbulent kinetic energy and turbulent dissipation rate as show in Figs. (4.15). Fig. (4.16) shows the error of the flow components with the iteration while, Fig. (4.17) explains the relation between three points with the iteration. The limits of scaled residual error are listed in Table (4.9). Fig.(4.18) explains the flow chart of AirPak 3.0.16 software.

Table (4.9) Residual error for the tested cases

Equations	Residual error
Continuity	0.0001
energy	$1*10^{-6}$
Turbulent kinetic energy	0.0001
Turbulent dissipation rate	0.0001

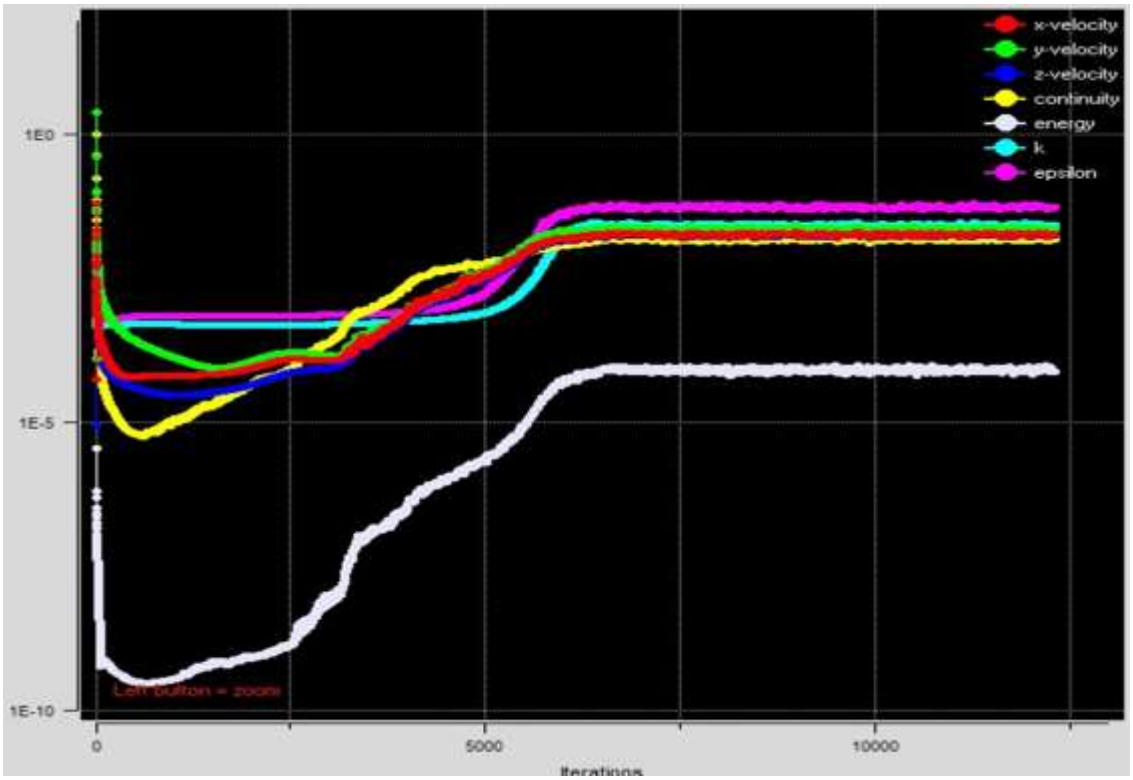

Fig. (4.16) variation of error with iteration

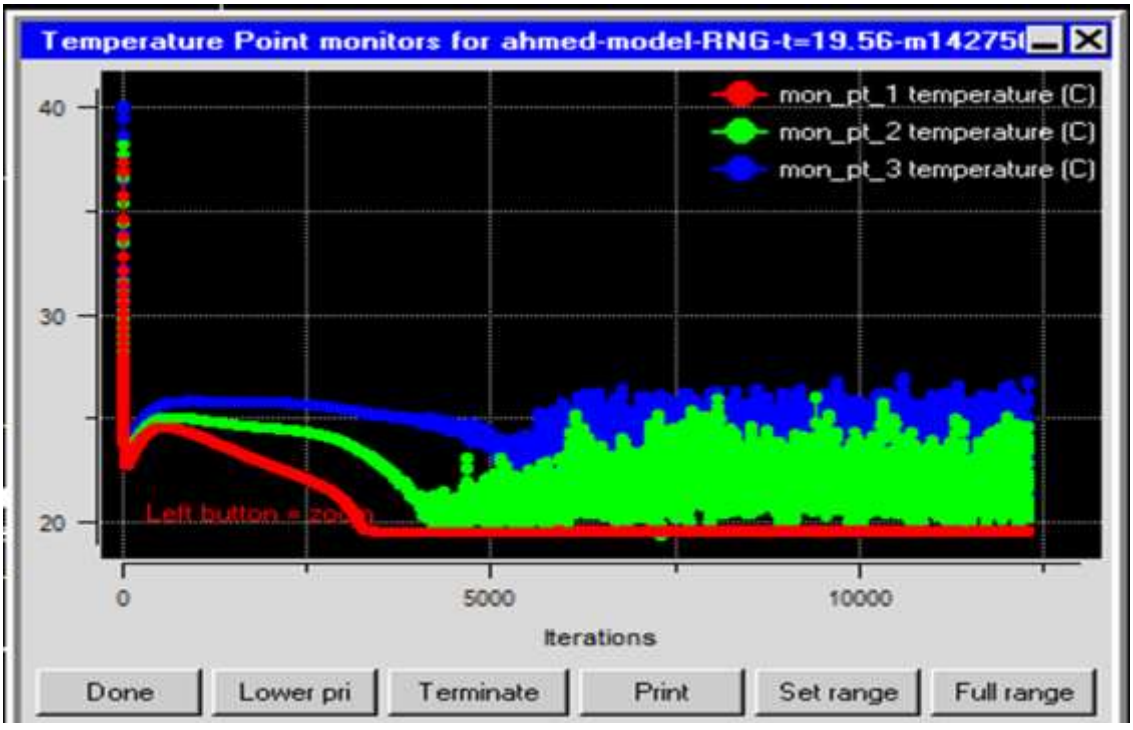

Fig. (4.17) variation of temperature with iteration for three points. P_1(0.5,0.1,1), P_2 (0.5,0.4,1) and P_3 (0.5,1.1,1).

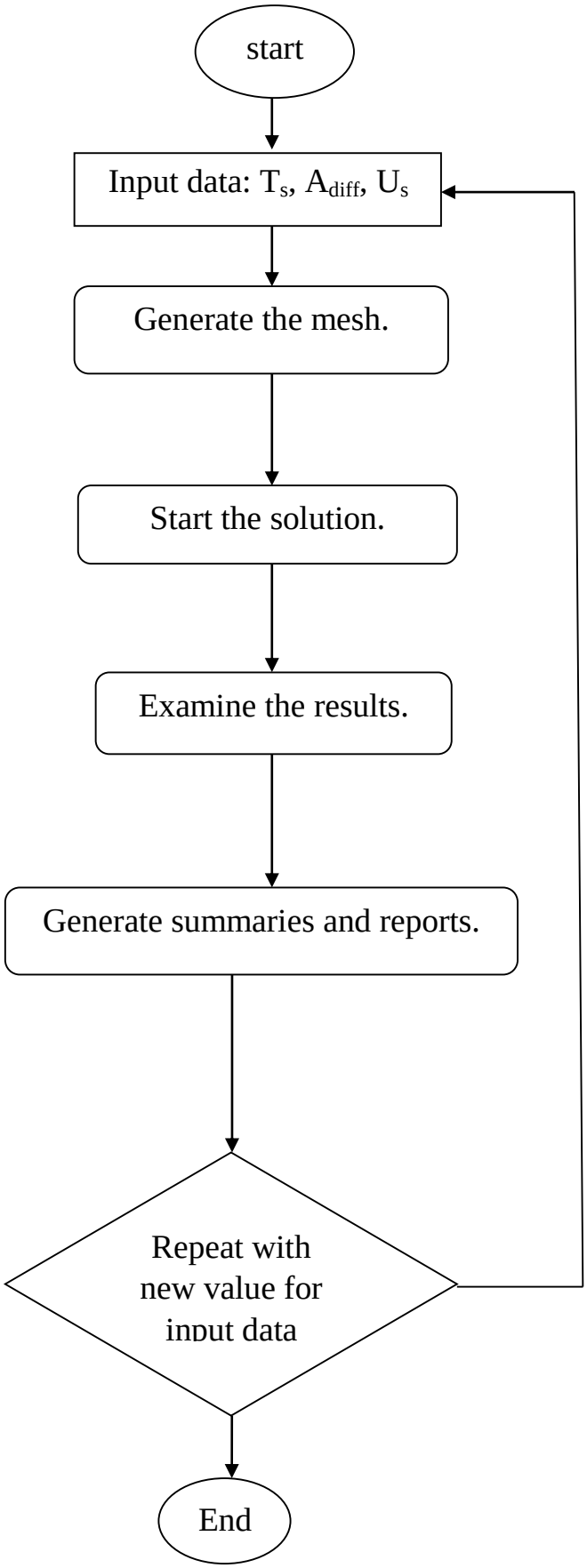

Fig. (4.18) flow chart of the AirPak ANSYS software.

4.17 Prediction of Indoor Air Quality Parameters (IAQ)

The parameters of indoor air quality (IAQ) such as air mean age, the distribution of temperature and velocity of air, predicted mean vote (PMV), predicted percentage dissatisfied, air diffusion performance index (ADPI) and ventilation effectiveness for temperature distribution, are predicted in this work.

4.17.1 Air mean age

The definition of air age is (the ability of ventilation system for exchanging the room old air by new air), [122]. The nominal time constant can be calculated as follows:

$$\tau_n = \frac{V}{Q_{DV}} \quad \ldots(4.114)$$

The time, τ_a, needed for replacing the air presented in the place is double of the room air mean age [123]:

$$\tau_a = 2\times\ \tau \quad \ldots(4.115)$$

4.17.2 Predicted percentage dissatisfied (PPD)

It is the people percentage that feel thermal discomfort of too hot or too cold. It is given as, [22]:

$$PPD=100\text{-}exp\text{-}[0.03353\times PMV^4+0.2179\times PMV^2] \quad \ldots(4.116)$$

The allowable environment PPD limit for common comfort is about 10%, [124],in accordance with $-0.5\leq PMV\leq 0.5$, [125].

4.17.3 Predicted mean vote (PMV)

It is utilized for predicting the thermal comfort and the conditions of human which is calculated as given below, [126]:

$$PMV=[0.303\times \exp(-0.036)+0.028]\times L \quad \ldots(4.117)$$

The PMV value is classified as seven point (from +3 at cold air of indoor to -3 at hot air). Based on (ASHRAE standards), the better range of (PMV) for allowable internal comfort is (-0.3 to +0.3), [125].

4.17.4 Air distribution performance index (ADPI)

One of the most important ventilation design parameters is indoor air movement needed to determine thermal comfort in buildings. Excessive unwanted air movement makes occupants complains because of undesired cooling of some human body parts caused by this air movement 'draft'. For this reason, values of the air speed should be also controlled in design criteria to maintain good index of thermal comfort. Values of air speed are used to find the effective draft temperature (EDT), which is essential to predict the air diffusion (distribution) performance index (ADPI). This parameter is helpful in assessment of diffusion performance of air for diffusers in a ventilated space. The effective draft temperature (EDT) is calculated from equation below, [126]**:**

$$EDT = (Tx - \text{Tav}) - 8 * (Vx - 0.15) \quad \ldots\ldots\ldots\ldots (4.118)$$

Where,

T_x : local temperature (K)

T_{av} : average room temperature (K)

V_x : local air velocity (m/s)

The air diffusion (distribution) performance index (ADPI) is a percentage that is defined by the number of points measured in an occupied zone where (EDT) is within the set limit (> -1.7°C and < 1.1°C) over the total number of points measured, [126]. ADPI at 80% and above is considered as a good air distribution. The (ADPI) rating of an air diffusion system depends on a number of factors:

1. Outlet type
2. Room load
3. Room dimensions and diffuser layout
4. Outlet throw

When these factors are properly selected, most outlets can achieve an acceptable (ADPI) rating. The higher the (ADPI) rating is the higher the

quality of room air diffusion is within the space. Generally, an (ADPI of 80 %) is considered acceptable.

4.17.5 Thermal ventilation effectiveness

Effectiveness temperature is another parameter in the present study used to confirm the results obtained from (ADPI). The effectiveness temperature is calculated by using the following equation, [126]:

$$\varepsilon_t = \frac{T_{ex}-T_i}{T_m-T_i} \quad \ldots(4.119)$$

Where,

ε_t = Effectiveness temperature

T_{ex} =temperature at return grille

T_i = temperature at supply air diffuser

T_m = temperature at occupied zone in tested room

CHAPTER FIVE

RESULTS AND DISCUSSIONS

CHAPTER FIVE

RESULTS AND DISCUSSIONS

The obtained experimental and theoretical results are presented, discussed and compared in this chapter. The experiments are carried out under outdoor exposure within the climate middle of Iraq, Hilla city (latitude of 32.46 °N and longitude of 44.42°E). Water-acetone pair solution is used in this work with different acetone concentrations (40%,50% and 60%) by mass. The test duration is from (9:00 AM) to (03:00 PM) for the days (22-May,31-May, 14-June, 28-June, 1-July and 7-July). The inlet air to the evaporator is a mixture of (90% recirculated air and 10% fresh air from the outdoor). The flow rate of supplied air to cooled room from the diffuser is 0.022 m^3/s that passes across the evaporator. The temperature in the cooled room is measured at two poles. The first pole is placed at line of air supply at (X=1 m and Z=1 m), while the second pole near the person at (X=1.25 m and Z=1.5m). the temperature is measured at four levels (Y=0, 0.5, 1.1 and 1.6 m).

5.1 Experimental Results

The experimental results are divided into two parts:

1- Temperature measurement results which include temperature in all components of collector and absorption system as well as the overall coefficient of performance.

2- Temperature measurement in the ventilated space at two poles. The first pole is placed at (X=1m, Z=1m) and the second pole is placed at (X=1.25, Z=1.5). The temperature of supplied air is also measured.

The experimental results are obtained for the three concentrations of acetone.

5.1.1 Collector loop and absorption loop results

5.1.1.1 Results of collector loop

Figs.(5.1-5.3) show the variation of received radiation with time for (22-May,31-May, 14-June, 28-June, 1-July and 7-July). The data is recorded between (6:00 AM) and (6:00 PM). It is seen that the received radiation increases with time to reach maximum at time between (11:30 AM) and (12:20 PM) at maximum elevation angle and then decreases due to the earth rotation around the sun until the sun become behind the collector. The maximum recorded instantaneous solar radiation is (846 W/m^2) for (28-June) and ambient temperature of (49 ℃).

Figs.(5.4-5.6) explain the variation of useful power with time. The data is recorded between (8:45 AM) and (3:00 PM). It is noted that the useful power at start of operation is zero because there is no water heating and then increases with a faster rate to reaches the regular behavior through a time of (30 minutes). Then, the useful power increases with time due to increasing the received solar radiation to reaches maximum at solar noon as shown in Fig.(5.1) and then decreases with decreasing received solar radiation and increasing the losses to surroundings. The useful power for (28-June) is higher than other days with maximum useful power of (1157 W) at (12:00 PM).

Figs.(5.7-5.9) display the variation of the receiver surface temperature with time. It is noticed that the receiver surface temperature increases with time due to increasing the instantaneous solar radiation as shown in Fig. (5.1) to reach maximum at peak radiation and then decreases with decreasing solar radiation and increasing the losses to surroundings. The receiver temperature at 28-June higher than the other days because the radiation is higher with a maximum value of (87.1℃) at (12:00).

Figs.(5.10-5.12) show the variation of inlet and outlet temperatures with time for the receiver for (28-June, 1-July and 7-July). It is noted that

the temperature increases with time due to increase the instantaneous solar radiation to reach maximum at peak radiation as shown in Fig.(5.1). With maximum inlet and outlet temperature of (78.2 ℃) and (85.7 ℃) respectively at (12:00) for (28-June) then decreases due to decrease the solar radiation and increase the losses to the surroundings.

Figs.(5.13-5.15) explain the variation of storage temperature with time. It is noticed that the storage temperature increases with time due to increase the solar radiation to reach maximum value at about 30 minutes after the peak instantaneous solar radiation. After that it decreases with decreasing solar radiation and increasing the losses to surroundings. This is because the storage remains receives solar radiation and the storage temperature increases until the losses to surroundings becomes higher than the received radiation. The peak storage temperature at (28-June) is higher than the other days because the instantaneous solar radiation is higher with a maximum value of (78.5◦C) at (12:30 PM).

Figs. (5.16-5.18) display the variation of collector efficiency with time. It is seen that the collector efficiency at starting is zero then it increases with time with a faster rate due to the faster rate of useful power until reaches the regular behavior after a duration of about (30 minutes). Then, it decreases with time due to the increase of liquid temperature in the receiver due to the power received and so the loses to surroundings increases. The collector efficiency at (28-June) higher than the other days because the radiation is higher. With a maximum collector efficiency of (0.731) at (09:30 AM).

Fig. (5.19) shows the maximum instantaneous recorded generator temperature for the days (22-May, 28-June and 7-July). It is noted that the maximum instantaneous generator temperature is recorded on 28 of June. Since the received radiation for that day is the maximum with a value of (81.2 ℃).

Fig.(5.20) shows the maximum achieved instantaneous collector efficiency for the days (22-May, 28-June and 7-July). It is noted that the maximum efficiency is achieved for the day 28-June with a value of (0.731). Since the received solar radiation for that day is the maximum.

Fig.(5.21) shows the optical collector efficiency curve. The maximum optical collector efficiency is (0.739).

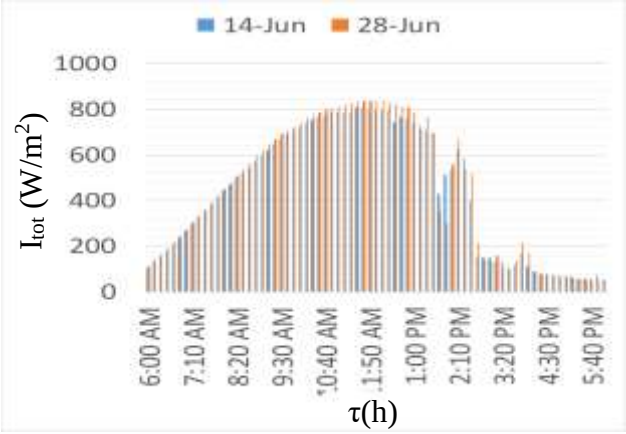

Fig.(5.1) variation of received radiation with time for 14 and 28 of June.

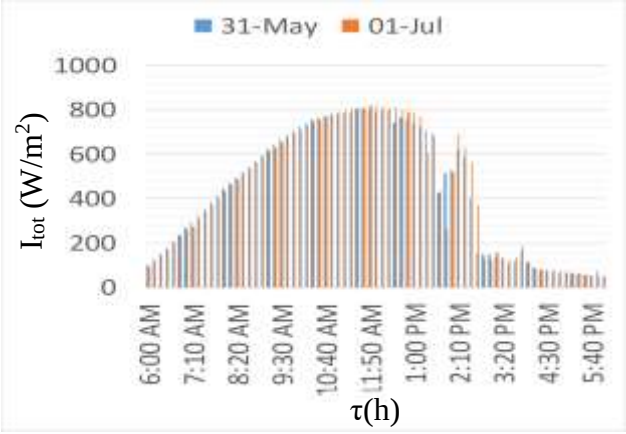

Fig.(5.2) variation of received radiation with time for 31-May and 1-July.

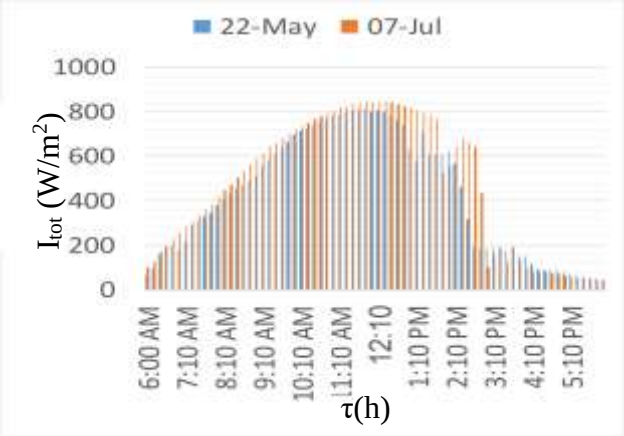

Fig.(5.3) variation of received radiation with time for 22-May and 7-July.

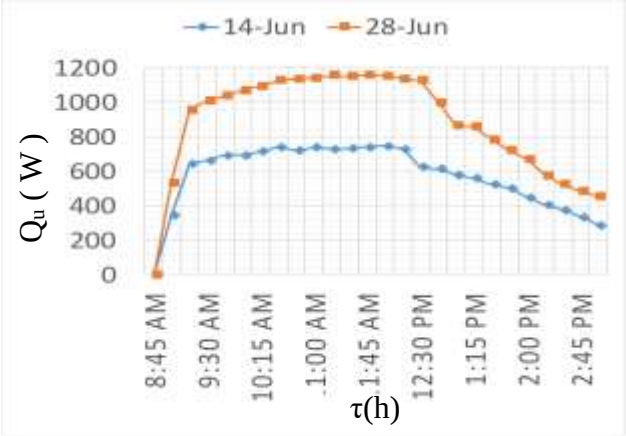

Fig.(5.4) variation of useful power with time for 14 and 28 of June.

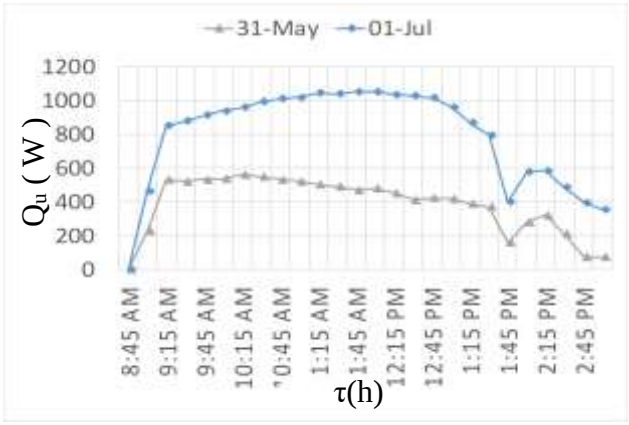

Fig.(5.5) variation of useful power with time for 31-May and 1-July.

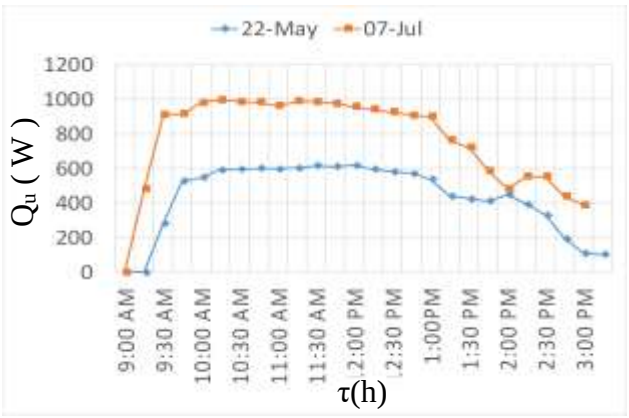

Fig.(5.6) variation of useful power with time for 22-May and 7-July.

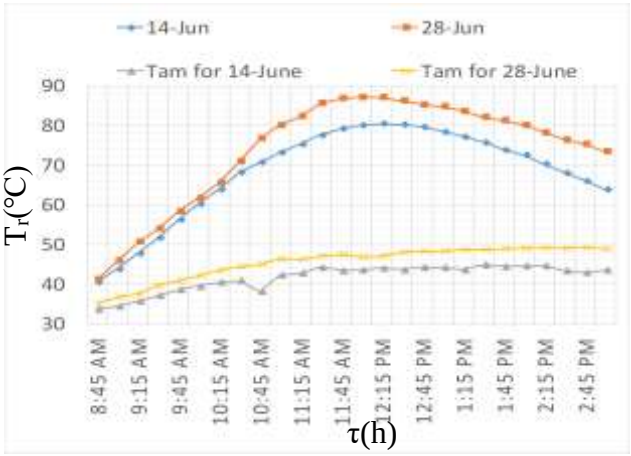

Fig.(5.7) variation of receiver surface temperature with time for 14 and 28 of June.

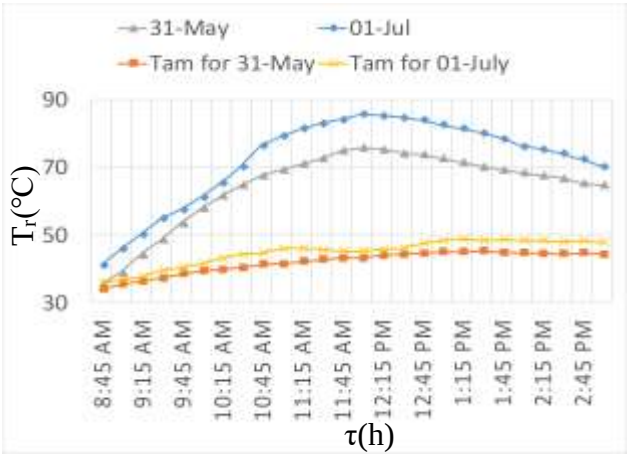

Fig.(5.8) variation of receiver surface temperature with time for 31-May and 1-July.

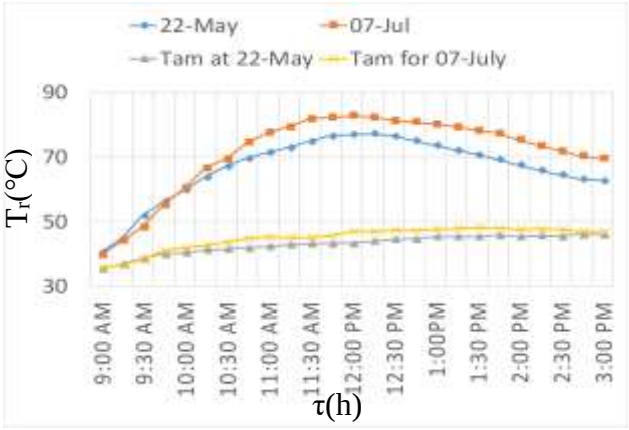

Fig.(5.9) variation of receiver surface temperature with time for 22-May and 7-July.

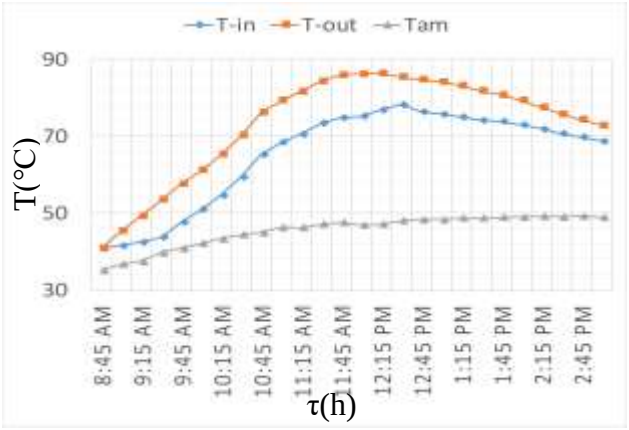

Fig.(5.10) variation of inlet and outlet temperatures with time for the collector for 28-June.

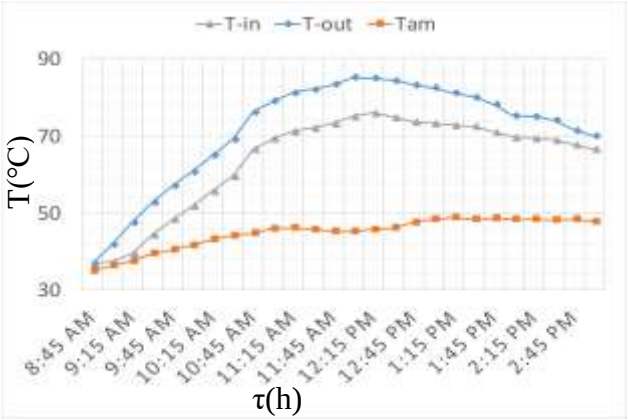

Fig.(5.11) variation of inlet and outlet temperatures with time for the collector for 1-July.

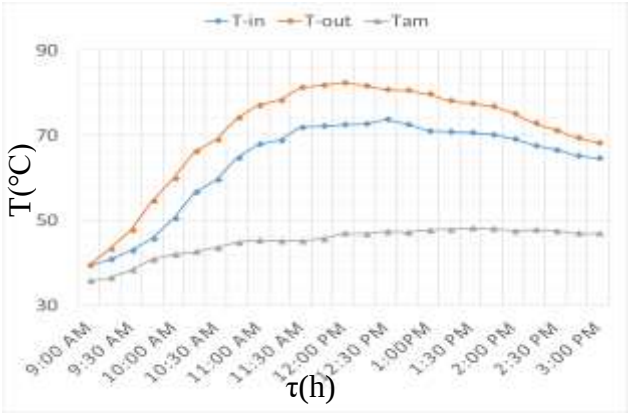

Fig.(5.12) variation of inlet and outlet temperatures with time for the collector for 7-July.

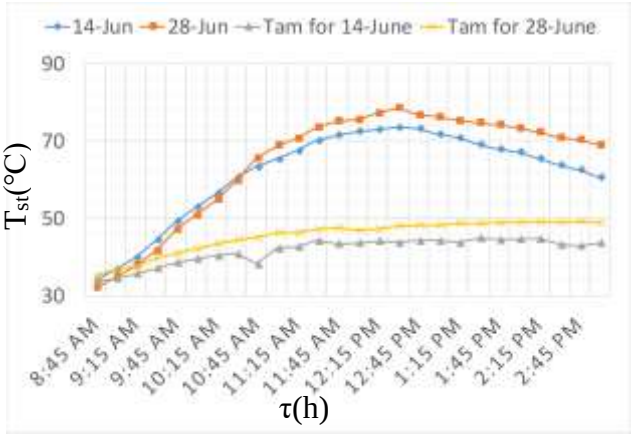

Fig.(5.13) variation of storage temperature with time for 14 and 28 of June.

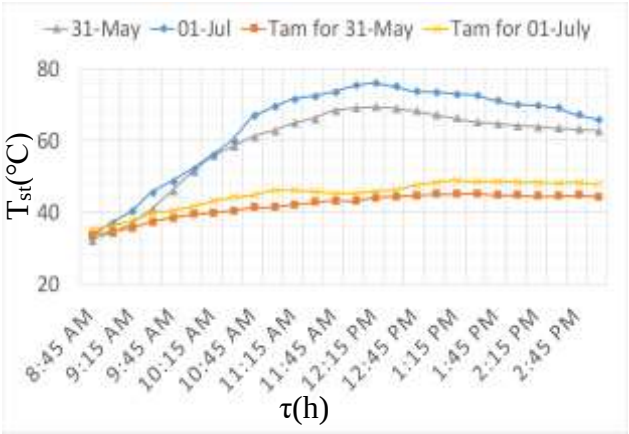

Fig.(5.14) variation of storage temperature with time for 31-May and 1-July.

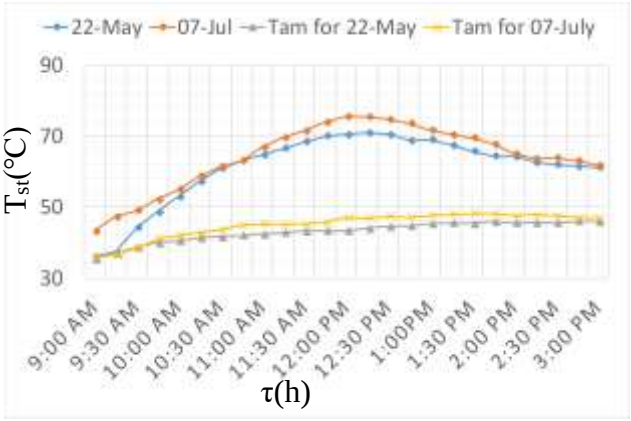

Fig.(5.15) variation of storage temperature with time for 22-May and 7-July.

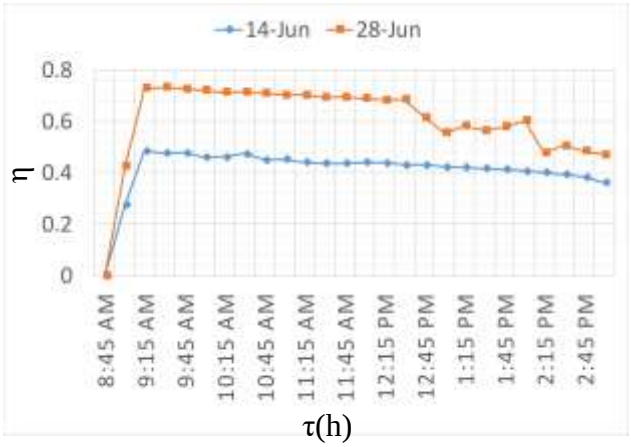

Fig.(5.16) variation of collector efficiency with time for 14 and 28 of June.

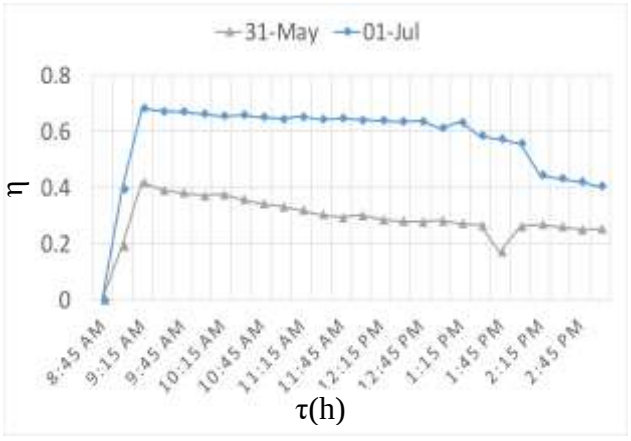

Fig.(5.17) variation of collector efficiency with time for 31-May and 1-July.

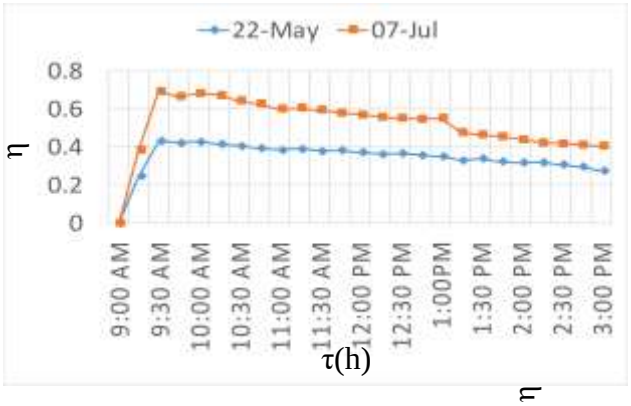

Fig.(5.18) variation of collector efficiency with time for 22-May and 7-July.

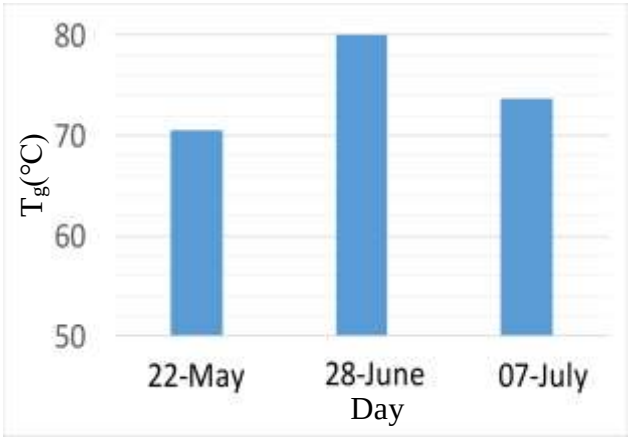

Fig.(5.19) variation of generator temperature with days (22-May, 28-June and 7-July).

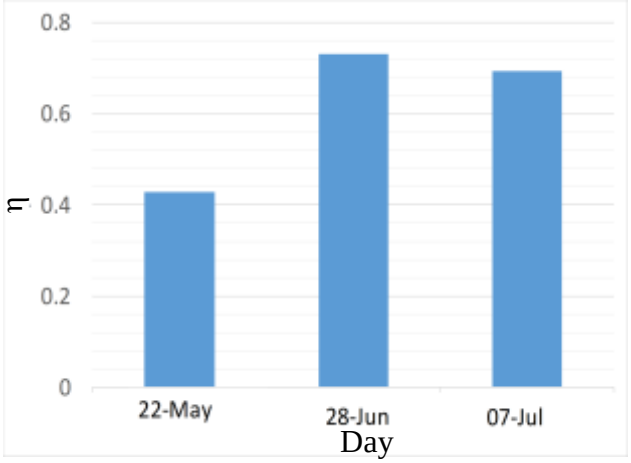

Fig.(5.20) variation of collector efficiency with days (22-May, 28-June and 7-July).

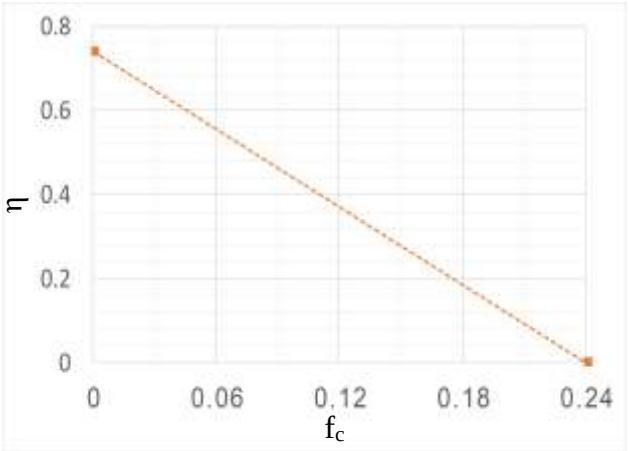

Fig.(5.21) variation of optical collector efficiency with efficiency function for 7-July.

5.1.1.2 Results of solar absorption system

Figs.(5.22-5.24) show the variation of generator temperature throughout the day for the (14 &28) of June. The temperature increases gradually until reaching a maximum value of (81.2 ℃) at (12:30 hr.). This is due to the increase in solar radiation fallen on the collector. It is noticed that there is a (30 min.) a late of phase between maximum solar radiation and maximum generator temperature. It is noticed that the maximum generator temperature is obtained on the 28 of June which is about 81.2 ℃) at (12:30 PM).

Fig.(5.25) shows the variation of condenser temperature and temperature of acetone at condenser exit with time during the day for (22-May) and (7-July). The temperature is measured during the period between (8:45 AM) and (3:00 PM). It is noticed that the condenser temperature rises through the day due to the rise in cooling medium temperature during the day. The maximum condenser temperature for the (22-May) is (38.6℃) at (2:00 PM) and (42.5℃) for (7-July). The condenser temperature must be as low as possible for better system performance.

Fig.(5.26) shows the variation of instantaneous temperature difference across the evaporator with time for (14 and 28 of June) for acetone concentration of (40%). The time of measuring is between (10:30 AM and 3:00 PM). It is seen that the instantaneous evaporator temperature difference increases with time due to increase the generator temperature as shown in Fig.(5.22) which increases the evaporation of acetone in the generator. The maximum instantaneous temperature difference for (14-June) occurs between (01:00 PM to 01:15 PM). After that it decreases due to decrease solar radiation and increase the losses to the surroundings. The instantaneous evaporator temperature difference for (28-June) is higher than that for (14-June) because the radiation is higher and so the

evaporation of acetone is higher. The maximum instantaneous air temperature difference is (6.7 ℃ and 10.3 ℃) for (14 and 28-June) respectively at (01:00 PM). Moreover, it is noticed that the maximum instantaneous air temperature difference occurs after the time of peak radiation. This is because the acetone vapor needs a period of time (about 30 minutes) to be condensed in the condenser and expands in the capillary tube and after that reaches the evaporator to cools the air supplied to the cooled room. The period between the operation start and the starting of decreasing the temperature of supplied air is about (1:30 hr).

Fig.(5.27) explains the variation of instantaneous air temperature difference across the evaporator with time for different acetone concentrations in the generator. It is noted that the instantaneous air temperature difference increases with increasing the acetone concentration due to increase of evaporated acetone at the generator that cools the air at the evaporator and so the temperature of the air decreases. The maximum instantaneous air temperature difference across the evaporator occurs at acetone concentration of 60% with a value of 14.1℃ at time of 01:00 PM.

Fig.(5.28) shows the variation of instantaneous evaporator cooling effect with time for (14 and 28 of June) with acetone concentration of (40%). It is seen that the evaporator instantaneous cooling effect increases with time due to increase the generator temperature as shown in Fig.(5.22) which increases the vaporized acetone at the generator. The maximum cooling effect occurs at (01:00 PM) and then decreases due to decrease the generator temperature and increase the losses to the surroundings. The evaporator cooling effect for (28-June) is higher than that of (14-June) because the generator temperature is higher. The maximum evaporator instantaneous cooling effects are (169.2 W) and (260.1 W) for (14 and 28-June) respectively at time of (12:45 PM and 01:15 PM). Moreover, it is

noticed that the maximum evaporator instantaneous cooling effect occurs after the time of peak radiation as discussed in Fig. (5.26).

Fig.(5.29) explains the variation of evaporator instantaneous cooling effect with time for different acetone concentrations. It is noticed that the instantaneous cooling effect increases with increasing acetone concentration due to increase the evaporated acetone at the generator as discussed previously. The peak instantaneous cooling effect occurs at about (01:00 PM) for all acetone concentrations. The peak value for cooling effect at 60% acetone concentration is 365.1 W.

Fig.(5.30) shows the variation of the instantaneous temperature of supplied air to the room with time for (14 and 28 of June) at acetone concentration of (40%). It is noticed that the instantaneous temperature of supplied air for (28-June) is higher than its value for (14-June) because the air temperature entered to the evaporator is higher than the (14-June). It is seen that the instantaneous temperature of supplied air decreases with time since larger amount of acetone enters the evaporator and more cooling effect occurs although the initial instantaneous air temperature is higher. The minimum temperature occurs between (01:00 PM and 01:15 PM) and then increases with decreasing generator temperature and increasing the losses to the surroundings. The minimum instantaneous temperature of supplied air is (31 ℃ and 32.5 ℃) for (14 and 28-June) respectively. Moreover, it is noticed that the minimum instantaneous temperature of supplied air occurs after the time of peak radiation as discussed in Fig.(5.26).

Fig.(5.31) explains the effect of acetone concentration on the temperature of supplied air. It is noticed that the instantaneous temperature of supplied air decreases with increasing the acetone concentration due to increase the evaporated acetone at the generator that produces more cooling effect. Therefore, the minimum instantaneous temperature of

supplied air to the room at the concentration of 60% and time of 01:00 PM with a value of 27.5°C for 7-July.

Fig.(5.32) shows the variation of instantaneous COP with time for (14 and 28 of June) at acetone concentration of (40%). It is seen that the instantaneous COP increases with time due to increase the cooling effect as discussed previously to reach a maximum value at (01:00 PM) and then decreases with decreasing the cooling effect and increasing the losses to the surroundings. It is noticed that the instantaneous COP at (28-June) is higher than that of (14-June) because the cooling effect is higher. The maximum instantaneous COP is (0.382 and 0.423) for (14 and 28-June) respectively at (01:00 PM). Moreover, it is noted that the maximum instantaneous COP occurs after the time of peak generator temperature as discussed in Fig. (5.26).

Fig.(5.33) explains the variation of instantaneous COP with time at different acetone concentrations. It is noted that the instantaneous COP increases with increasing the acetone concentration due to increase the evaporation of acetone at the generator that cools the supplied air to the tested room. The maximum instantaneous COP for (60%) acetone concentration occurs at time of (01:00 PM) which is (0.76).

Fig.(5.34) shows the variation of mass flow rate of acetone vapor with time for different acetone concentrations. It is seen that the amount of acetone vapor increases gradually with time, due to increase of generator temperature, for all concentrations. As the acetone concentration increases the acetone vapor increases. For 60% concentration, the maximum mass flow rate of acetone vapor occurs at about 12:00 noon is about 0.00071 kg/s.

Fig.(5.35) explains the variation of mass flow rate of acetone vapor per kilogram of acetone with time for different acetone concentrations. It is noted that it increases with increasing acetone concentration due to

increase the mass of acetone at the generator, so the evaporation of acetone increases. The maximum mass flow rate of acetone vapor per kilogram of acetone for (60%) acetone concentration occurs at time of (12:00) which is ($9.86*10^{-5}$ kg/s/kilogram of acetone).

Fig.(5.36) displays the variation of the circulation ratio (λ) with time for different acetone concentrations. It is noted that the circulation ratio increases with increasing acetone concentration due to increase the mass of acetone at the generator, so the evaporation of acetone increases. The maximum circulation ratio for (60%) acetone concentration occurs at time of (12:00) which is (7.1%).

Fig.(5.37) Fig.(5.37) variation of cooling effect per liter of acetone with generator temperature for acetone concentration of 40% at (28-June). It is noted that the cooling effect per liter of acetone increases with generator temperature as discussed in Fig. (5.28). The maximum cooling effect per liter of acetone occurs at generator temperature of (76 ℃) which is (54.19 W/liter of acetone).

Fig.(5.38) displays the variation of maximum instantaneous temperature difference across the evaporator with acetone concentration for the days (28-June, 1-July and 7-July). It is noticed that the instantaneous temperature difference across the evaporator increases with acetone concentration due to increase the evaporated acetone that cools the air. The maximum instantaneous temperature difference is achieved for acetone concentration of (60%) with a value of (14.1℃).

Fig.(5.39) shows the maximum instantaneous cooling effect across the evaporator with acetone concentration. It is noted that the instantaneous cooling effect increases with acetone concentration due to increase the evaporated acetone that cools the air. The maximum instantaneous cooling effect at acetone concentration of (60%) is (356 W).

Fig.(5.40) shows the maximum achieved instantaneous COP with acetone concentration. It is noticed that the COP increases with acetone concentration due to increase the evaporation of acetone. The maximum COP at acetone concentration of (60%) is (0.76).

Fig.(5.41) shows the variation of daily COP with acetone concentration. It is noticed that the daily COP increases with acetone concentration due to increase the evaporated acetone that cools the air. The maximum daily COP at acetone concentration of (60%) is (0.4856).

Fig.(5.42) explains the variation of the overall COP with time for (22-May and 7-July) at acetone concentration of (60%). It is noticed that the overall COP for 7-July higher than that of (22-May) because the cooling effect is higher as discussed previously. The overall COP increases with time due to increase the cooling effect. The maximum overall COP occurs at (01:00 PM) with value of (0.2174).

Fig.(5.43) shows the achieved overall efficiency with acetone concentration. It is noticed that the overall efficiency increases with acetone concentration due to increase the evaporated acetone that increases the cooling effect. The maximum overall efficiency at acetone concentration of (60%) is (0.2174).

Fig.(5.44) explains the variation of the instantaneous COP and the overall efficiency with generator temperature for (7-July) at acetone concentration of (60%). It is noticed that both (COP and η_{ov}) increase with increasing the generator temperature due to increase the evaporated acetone and so increasing the cooling effect. The maximum (COP and η_{ov}) occur at the maximum generator temperature as discussed in Fig.(5.26). The maximum (COP and η_{ov}) occur at generator temperature between (71°C and 69.8°C) with values of (0.76 and 0.2174).

Fig.(5.45) shows a comparison between the maximum achieved temperature difference across the evaporator for the present work and other

researchers for different working pairs. However, the cooled fluid is air for present work, while for other researchers, it was water. The comparison shows that the water-lithium bromide pair gave the maximum temperature difference followed by the methanol-water pair and finally the acetone-water pair used in the present work. This is attributed the lowest latent heat of vaporization of acetone compared to other two refrigerants.

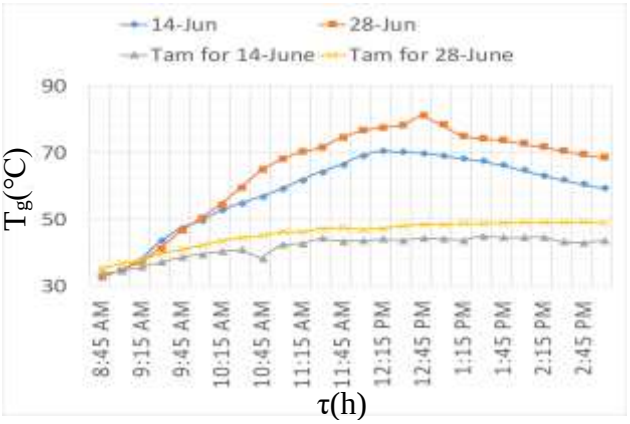

Fig.(5.22) variation of generator temperature with time for 14 and 28 of June.

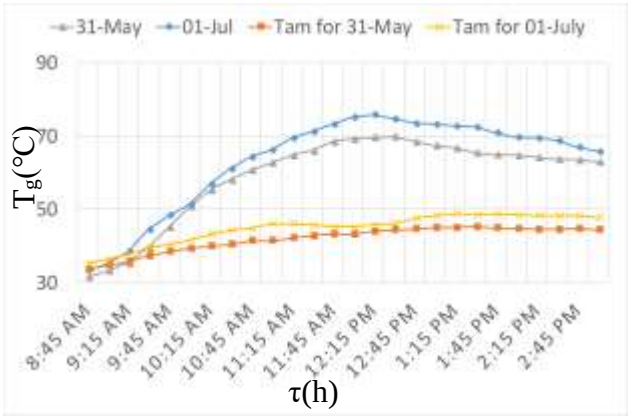

Fig.(5.23) variation of generator temperature with time for 31-May and 1-July.

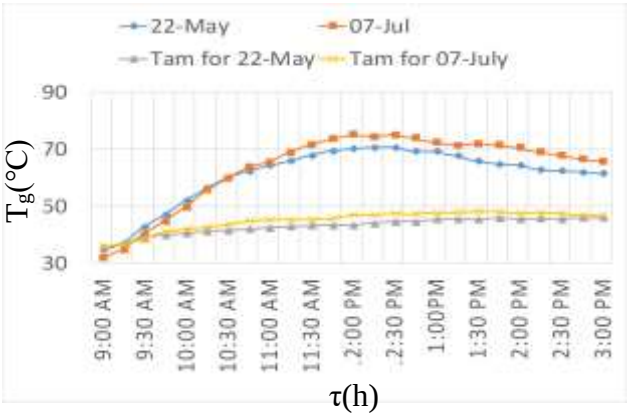

Fig.(5.24) variation of generator temperature with time for 22-May and 7-July.

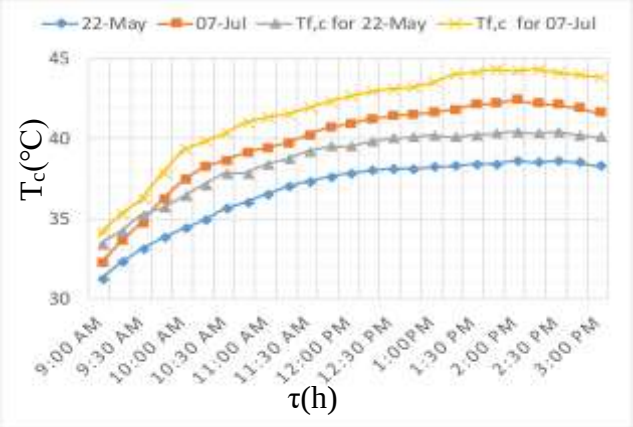

Fig.(5.25) variation of condenser temperature and temperature of acetone at condenser exit with time for 29-May and 7-July.

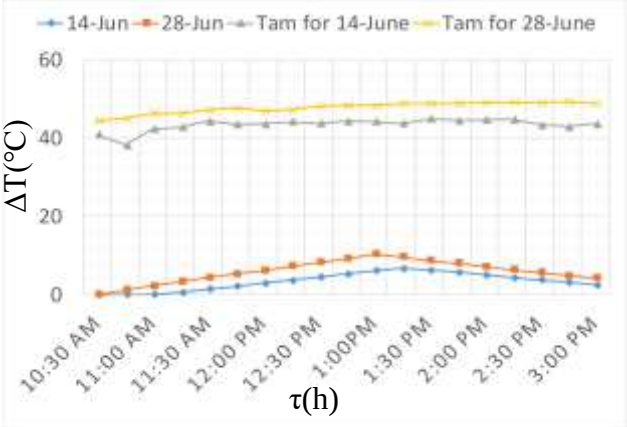

Fig.(5.26) variation of temperature difference across the evaporator and ambient temperature with time for 14 and 28 of June at acetone concentration of 40%.

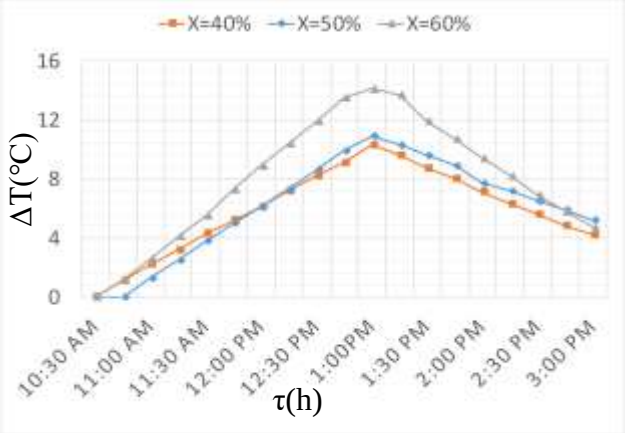

Fig.(5.27) variation of instantaneous temperature difference at the evaporator with time for different acetone concentrations.

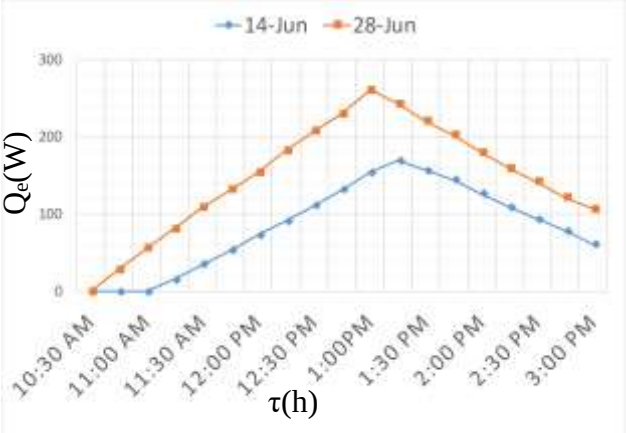

Fig.(5.28) variation of instantaneous evaporator cooling effect with time for 14 and 28 of June at acetone concentration of 40%.

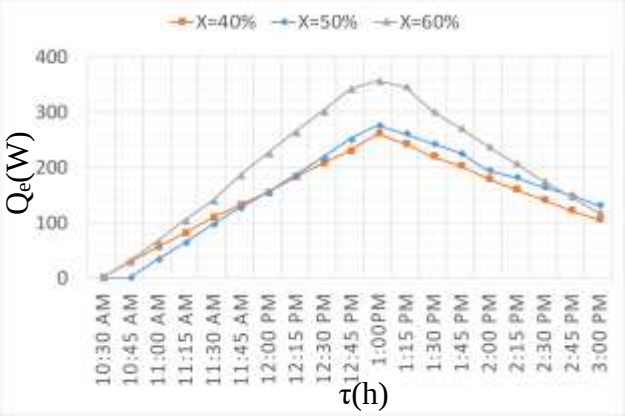

Fig.(5.29) variation of evaporator instantaneous cooling effect with time for different acetone concentrations.

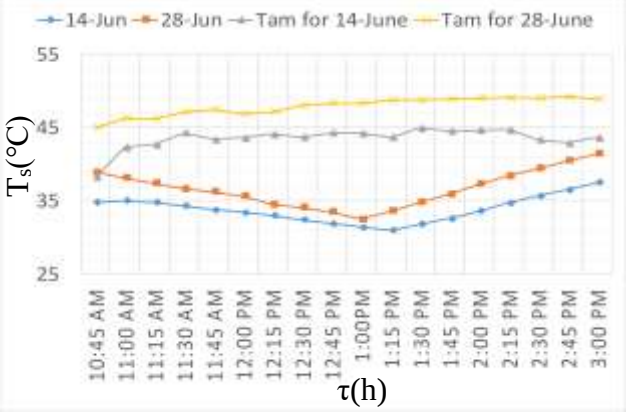

Fig.(5.30) variation of instantaneous temperature of supplied air with ambient temperature to the room with time for 14 and 28 of June at acetone concentration of 40%.

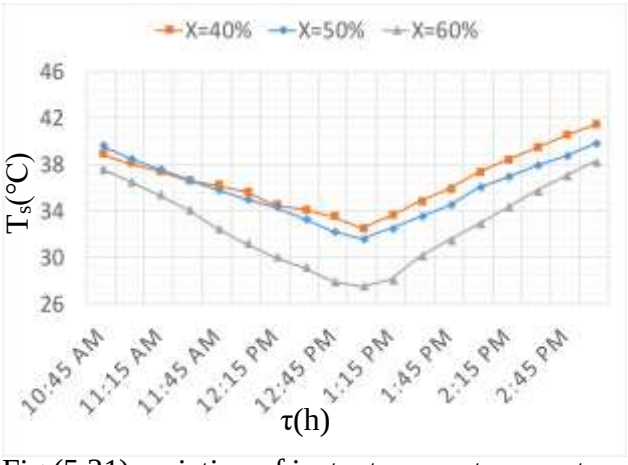

Fig.(5.31) variation of instantaneous temperature of supplied air to the room with time at different acetone concentrations.

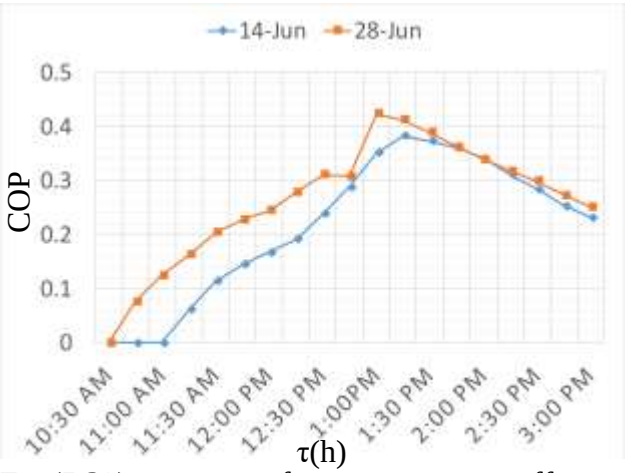

Fig.(5.32) variation of instantaneous coefficient of performance with time for 14 and 28 of June at acetone concentration of 40%.

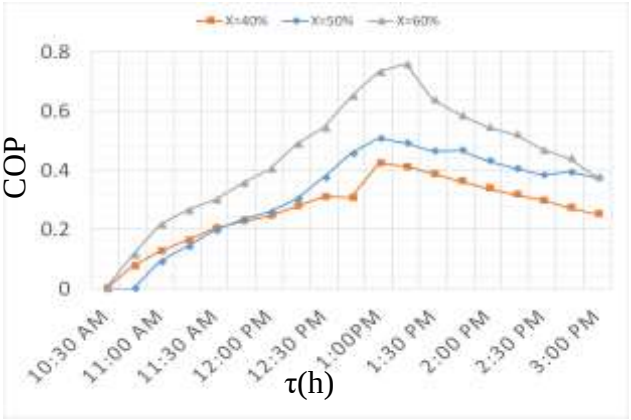

Fig.(5.33) variation of instantaneous coefficient of performance with time at different acetone concentrations.

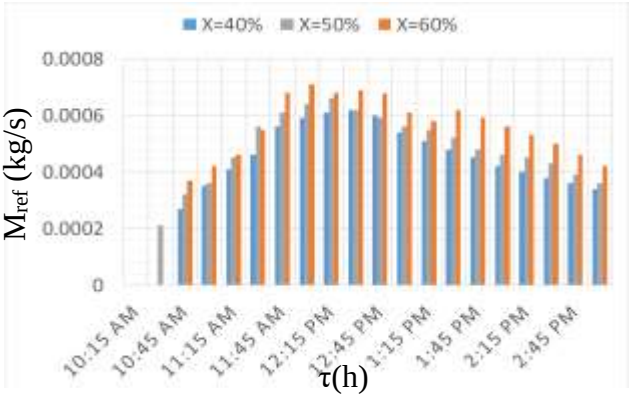

Fig.(5.34) variation of mass flow rate of acetone vapor with time for different acetone concentrations.

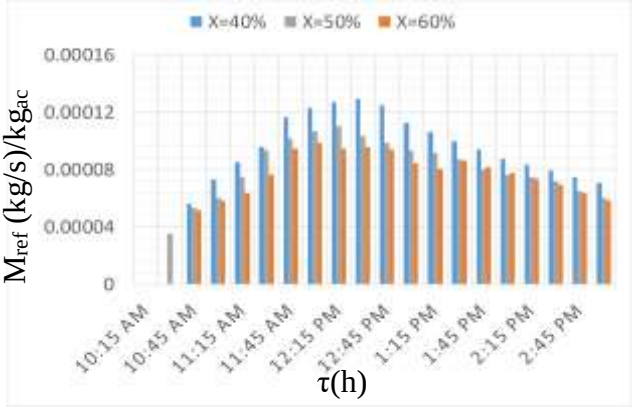

Fig.(5.35) variation of mass flow rate of acetone vapor per kilogram of acetone with time for different acetone concentrations.

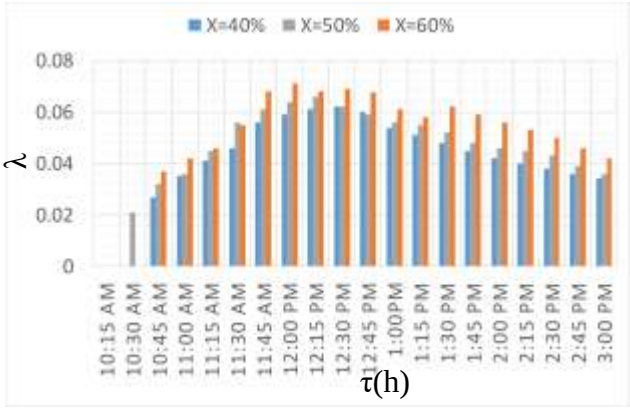

Fig.(5.36) variation of circulation ratio (λ) with time for different acetone concentrations.

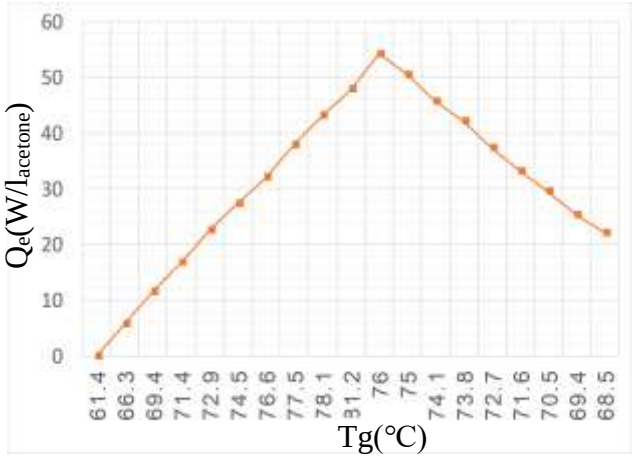

Fig.(5.37) variation of cooling effect per liter of acetone with generator temperature for acetone concentration of 40% at (28-June).

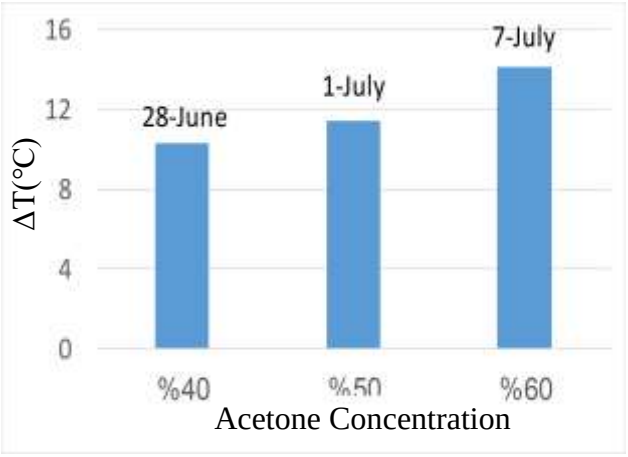

Fig.(5.38) variation of maximum temperature difference across the evaporator with acetone concentration.

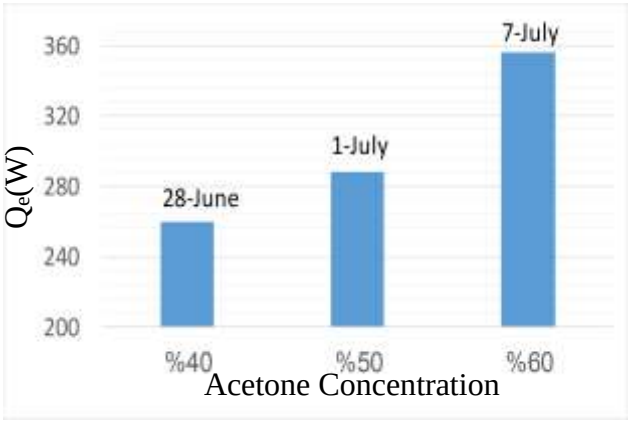

Fig.(5.39) variation of maximum cooling effect across the evaporator with acetone concentration.

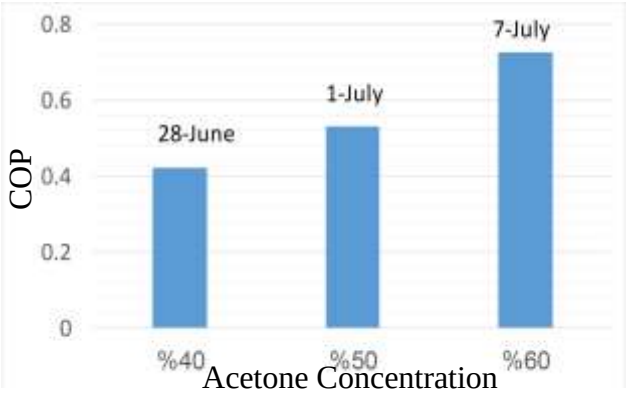

Fig.(5.40) variation of maximum coefficient of performance with acetone concentration.

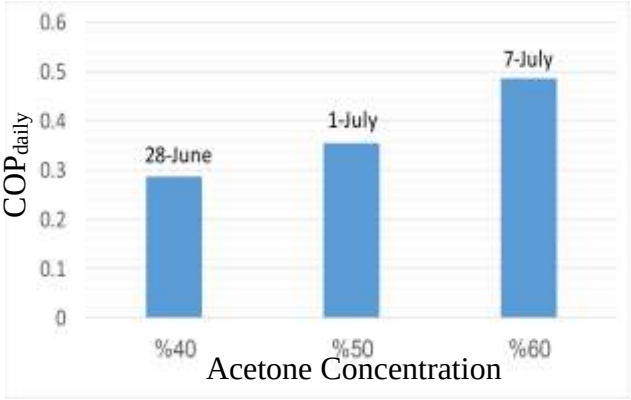

Fig.(5.41) variation of daily coefficient of performance with acetone concentration.

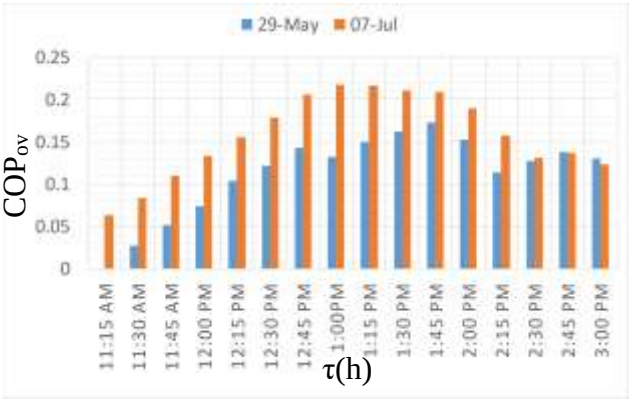

Fig.(5.42) variation of overall coefficient of performance with time at two different days that are 29-May and 7-July at acetone concentration of 60%.

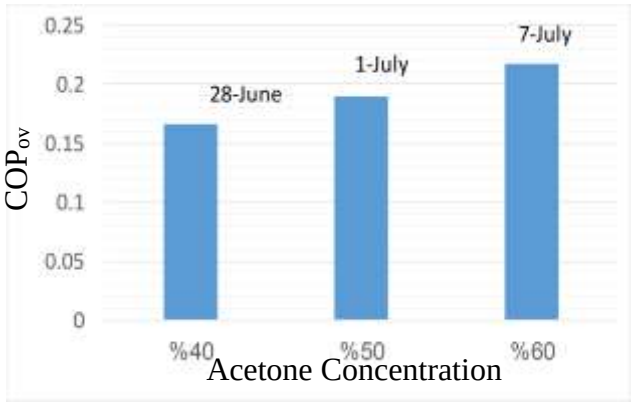

Fig.(5.43) variation of overall coefficient of performance with acetone concentration.

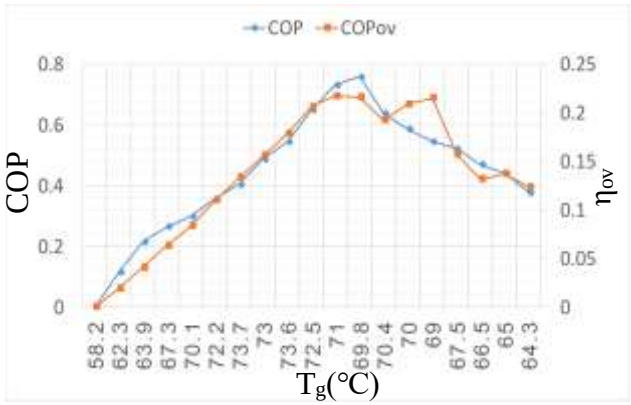

Fig.(5.44) variation of coefficient of performance and overall efficiency with generator temperature for 7-July at acetone concentration of 60%.

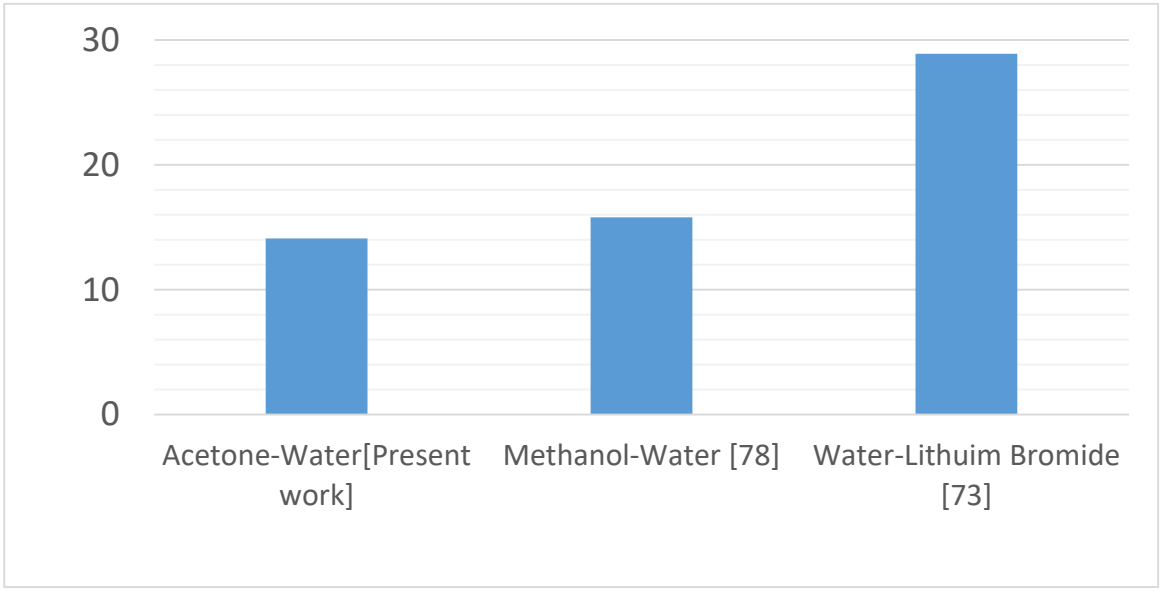

Fig.(5.45) effect of pair type on the temperature difference across the evaporator.

5.1.2 Acetone Vapor mass flow rate empirical equation

An empirical equation relates the acetone vapor mass flow rate with generator temperature and acetone concentration has been obtained from the experimental work using (SPSS software). The maximum mass acetone vapor mass flow rate obtained at generator temperature of 85°C at acetone concentration of 60% with a value of 0.000924 kg/s.

The results showed that there is a better agreement between the empirical equation data and the experimental data and so it can be considered in the theoretical work.

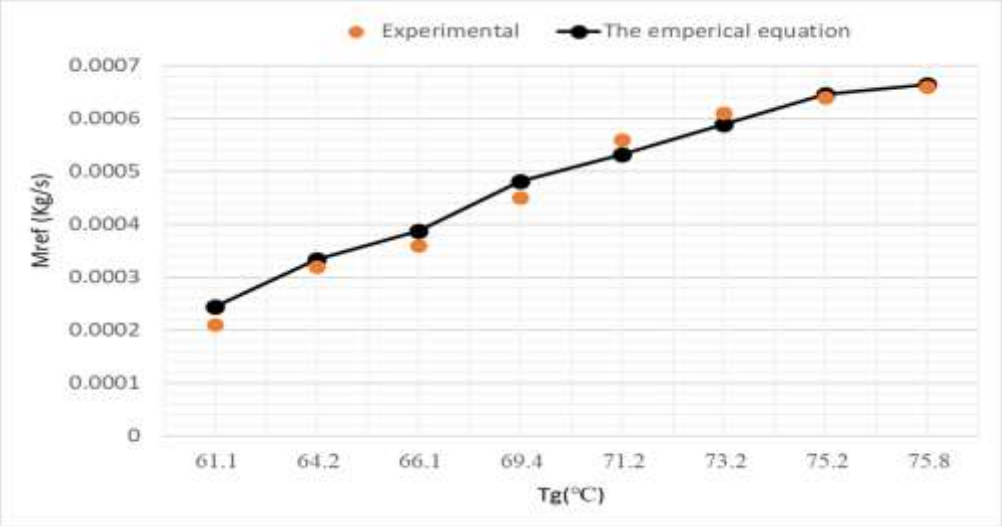

Fig.(5.46) the empirical equation data and the experimental data of acetone vapor mass flow rate for (1-July) at acetone concentration of 50%.

5.1.3 Results of the cooled space

The temperature in the cooled space is measured at the walls and two poles. The first pole is placed at (X=1,Z=1) at the line of air supply, while the second pole is placed near the person at (X=1.25, Z=1.5).

Figs.(5.47-5.49) show the variation of the local temperature with height at different hours for days (28-June, 1-July and 7-July) at the first pole with different acetone concentrations of (40%, 50% and 60%). It is noted that the local temperature increases with height for all hours because the supplied air is at floor level and the cold air with high density stays at lower levels while the hot air with lower density moves up to higher levels. The local temperature increases with time for all heights due to increase the gained heat from the outside and increase the outside ambient air temperature and the heat gain from walls which are not perfectly insulated.

The optimum local temperature is at floor level and time of (11:00 AM) with a value of (34.4 ℃) for (7-July).

Figs.(5.50-5.52) explain the variation of the local temperature with height at different hours for days (28-June, 1-July and 7-July) at the second pole with acetone concentrations of (40%, 50% and 60%). It is noticed that the temperature at the second pole showed same behavior as the first pole. The optimum local temperature is at floor level and time of (11:00 AM) with value of (35.7 ℃) for (7-July).

Fig.(5.53-5.55) show the variation of the local temperature with time at the breathing level for the days (28-June, 1-July and 7-July) with different acetone concentration of (40%, 50% and 60%). It is noticed that the first and second poles show approximately the same temperature. It is also noticed that at (11:00 AM), the 60% acetone concentration gives the optimum temperature for both poles with a value of (35.6 ℃).

Fig.(5.56) shows the variation of temperature difference between head and foot with time for seated person for (7-July). It can be noted that the temperature difference is less than the accepted difference (2 ℃ for seated person) due to the variation of cooling effect with time and the error in measuring devices. The temperature gradient increases with time due to the difference in elevation between head and foot which is taken as 1.1m, [7].

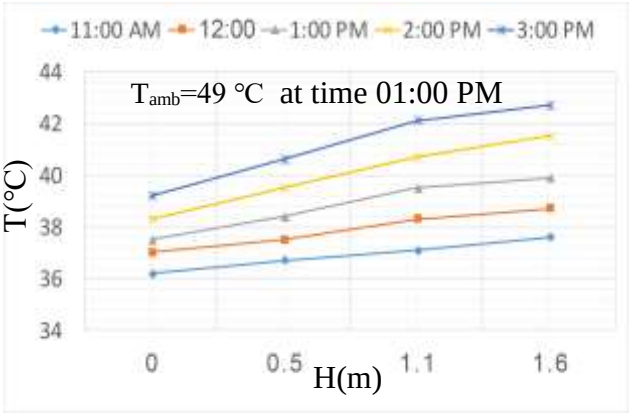

Fig.(5.47) variation of local temperature with height at different hours for 28-June at the first pole at acetone concentration of 40%.

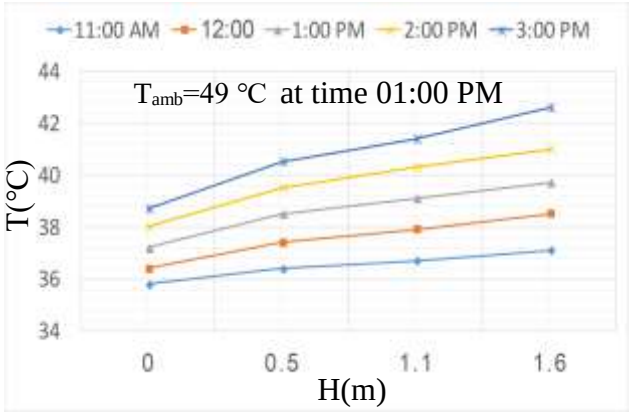

Fig.(5.48) variation of local temperature with height at different hours for 1-July for the first pole at acetone concentration of 50%.

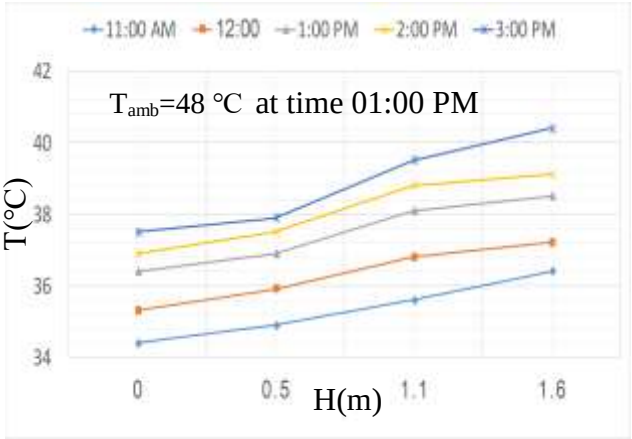

Fig.(5.49) variation of local temperature with height at different hours for 7-July at the first pole at acetone concentration of 60%.

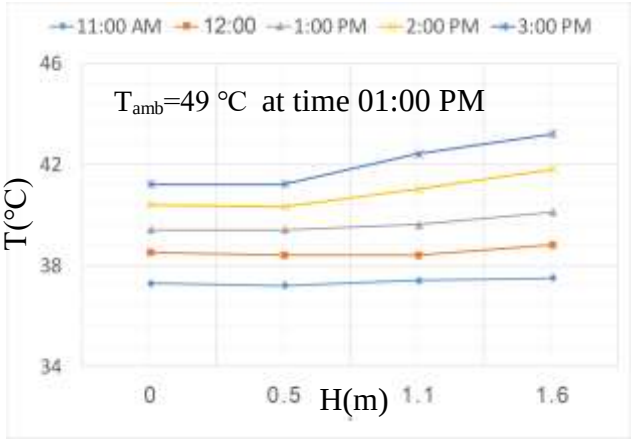

Fig.(5.50) variation of local temperature with height at different hours for 28-June at the second pole at acetone concentration of 40%.

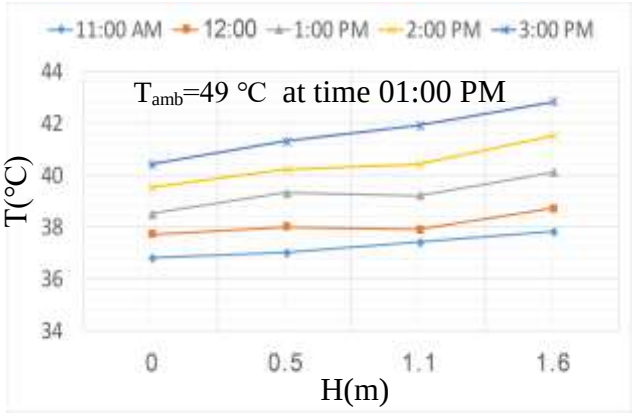

Fig.(5.51) variation of local temperature with height at different hours for 1-July at the second pole at acetone concentration of 50%.

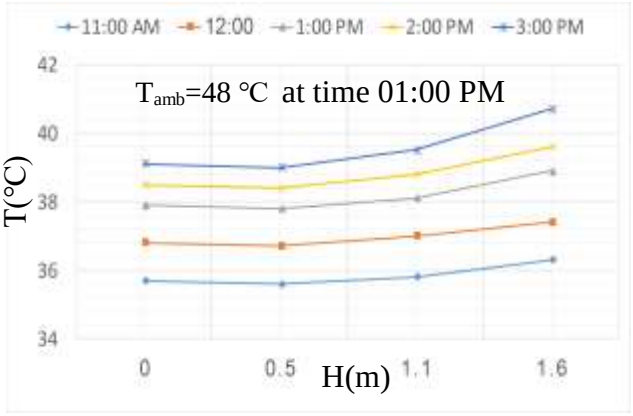

Fig.(5.52) variation of local temperature with height at different hours for 7-July at the second pole at acetone concentration of 60%.

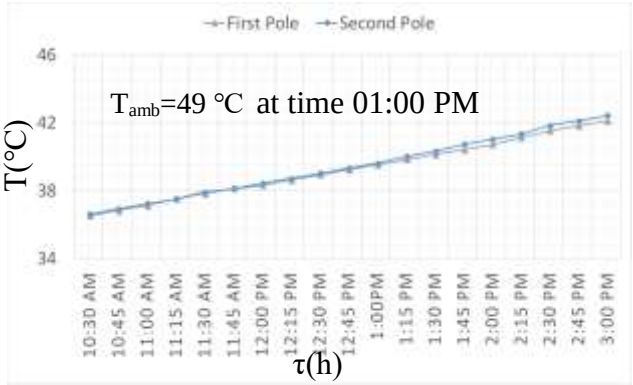

Fig.(5.53) variation of local temperature with time for the breathing level for 28-June at acetone concentration of 40%.

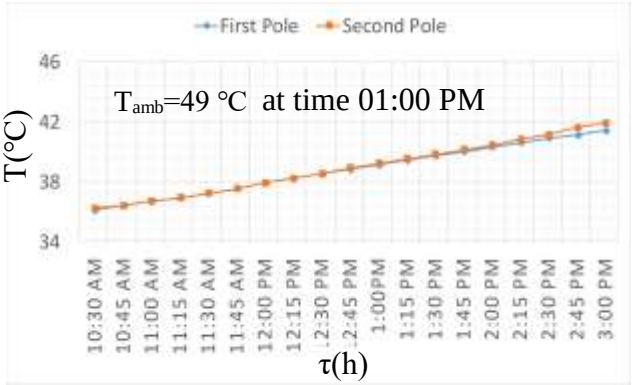

Fig.(5.54) variation of the local temperature with time for the breathing level for 1-July at acetone concentration of 50%.

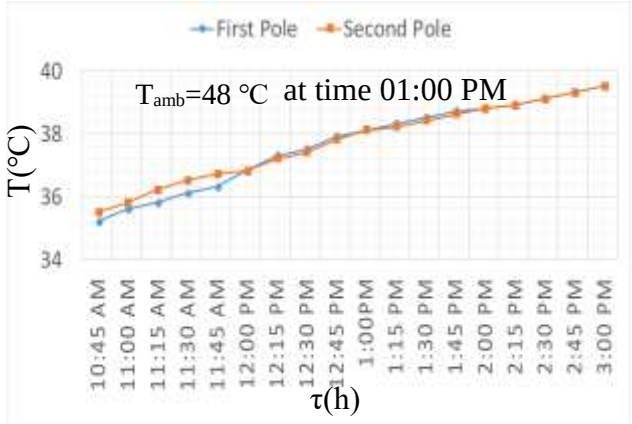

Fig.(5.55) variation of local temperature with time for the breathing level for 7-July at acetone concentration of 60%.

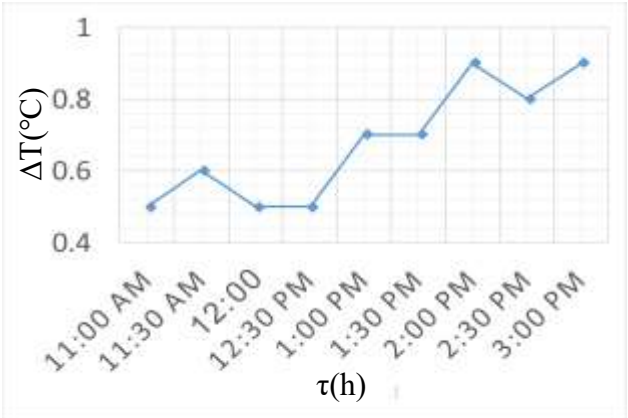

Fig.(5.56) variation of temperature difference between head and foot with time for seated person for 21-July.

5.2 Theoretical Results

The theoretical results are divided into two parts:

1- The solar energy analysis obtained from (EES) program that includes:
   a- Results of collector.
   b- Results of the absorption cooling system.
   c- The exergy analysis of the PTSC collector.
   d- The exergy analysis of the absorption cooling.
   e- The systematic efficiency.
2- Ventilation analysis obtained using the (ANSYS Fluent AIRPAK3.0.16) using the turbulent model (RNG K- ε).

5.2.1 Solar energy analysis

5.2.1.1 Results of solar collector

The collector loop consists of the PTSC with helical coil receiver, tank and pump. The studied performance of the collector includes received solar radiation, useful energy, receiver surface temperature, inlet and outlet water temperatures, storage tank temperature and collector efficiency. All results are performed for the day 21st of each of months (May, June, July and August).

Fig.(5.57) explains the variation of the solar radiation with time for the days, (21st of May, June, July and August) as a sample of theoretical data. It can be noted that the solar radiation increases with time and reaches maximum value at (12:00) due to higher elevation angle at solar noon and then decreases due to earth rotation and the sun being behind the collector. The solar radiation at (21-July) is higher than other days with a maximum value of (1126 W/m^2) at (12:00).

Fig.(5.58) shows the variation of the useful power with time. It can be noted that the useful power starts with zero value and increases sharply for the first (30 min.) and remains almost constant for rest of test time until noon and decreases later due to decrease in received radiation and increase in losses to the surroundings. It is seen that the maximum useful energy occurs before the maximum radiation due to the increase in the heat loss to the surroundings by convection and radiation. Moreover, the maximum useful power at (21-July) higher than other days with a maximum value of (1585 W) at (12:00 PM).

Fig.(5.59) shows the variation of the receiver temperature with time. It can be noted that the receiver temperature increases fastly before time (12:00) due to increase the instantaneous solar radiation as discussed in Fig.(5.56) to reach about (86.21°C) for the (21^{st} of July) and then increases in a slower rate after that due to decrease in the instantaneous solar radiation and increase of the losses to environment to reach (96.32°C) for the (21^{st} of July) at (02:30 PM). It is noted that the temperature at (21^{st} of July) is the higher in comparison to other days due to higher received radiation.

Fig.(5.60) explains the variation of the inlet and outlet water temperatures for the receiver with time for (21-July). It can be noted that the inlet and outlet temperatures increase rapidly before time (12:00 PM) to reach about (78.63°C and 85.74°C) for inlet and outlet respectively due to increase in the instantaneous solar radiation as discussed in Fig.(5.57) and then increases slowly after that due to decrease in the solar radiation and increase of the losses to environment to reach (91 °C and 96.32°C) at (02:30 PM).

Fig.(5.61) presents the variation of storage tank temperature with time. It can be noted that the storage temperature increases sharply with

time until reaches (78.63 °C) at (12:00) of (21st of July) due to the increase in the solar radiation as discussed in Fig.(5.56) and then increases slowly due to decrease the solar radiation and increase the losses in heat to the surrounding to reach (91°C) at (02:30 PM) for (21st July). Storage tank temperature at (21-June) is higher than the other days because the solar radiation is higher.

Fig.(5.62) shows the variation of collector efficiency with time. It can be noted that the collector efficiency increases sharply from zero due to the faster increase in the useful power and reached a maximum value after about (30 min.) from start of test and then decreases with time due to the increase in the liquid temperature in the receiver and that increases the losses to the surroundings. The maximum value of the efficiency at (09:25 AM) is (0.792) for (21st of August) because the instantaneous radiation is higher at this time and the minimum efficiency value is at (02:30 PM) for (21st of May) with value of (0.6473).

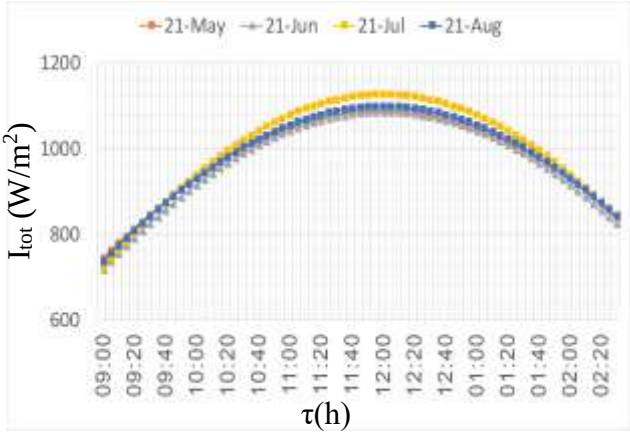

Fig.(5.57) variation of solar radiation with time for the days, 21st of May, June, July and August

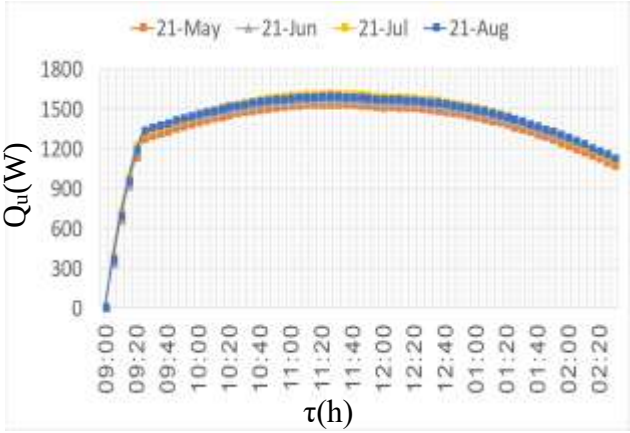

Fig.(5.58) variation of useful power with time for the days, 21st of May, June, July and August.

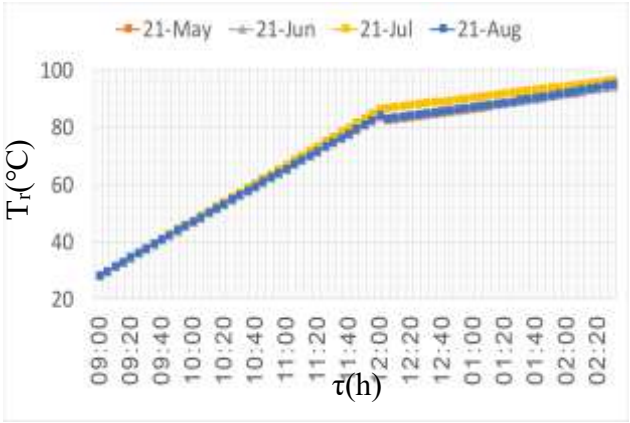

Fig.(5.59) variation of receiver temperature with time for the days, 21st of May, June, July and August.

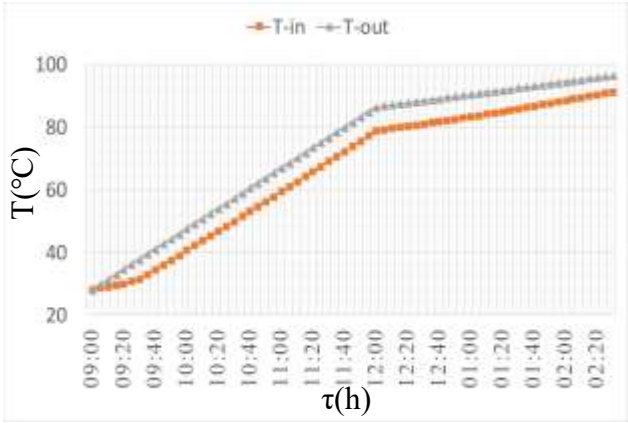

Fig.(5.60) variation of inlet and outlet temperatures with time for the collector for 21-July.

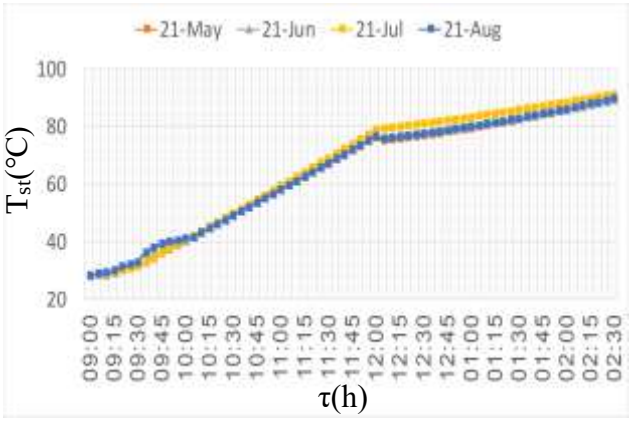

Fig.(5.61) variation of tank temperature with time for the days, 21st of May, June, July and August.

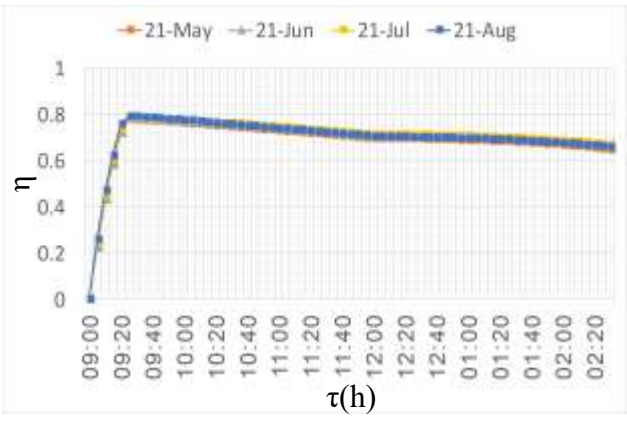

Fig.(5.62) variation of collector efficiency with time for the days, 21st of May, June, July and August.

5.2.1.2 Results of solar absorption cooling system

Fig.(5.63) shows the variation of generator temperature with time for the days, (21st of May, June, July and August) from (9:00 AM) to (02:30 PM). It is noted that the generator temperature increases fastly with time until reaches (12:00) with value of (78.1 °C) for (21-July) because of increasing the solar radiation with time as discussed in Fig.(5.57) and then increases slowly due to decrease in the solar radiation and increase of the losses to reach (91°C) for (21-July).

Fig.(5.64) shows the variation of temperature difference of air across the evaporator with time. It can be noticed that the temperature difference increases fastly with time before (12:00) with a value of (13.43 °C) for (21-July) due to increase the generator temperature as discussed in Fig.(5.63). The increase in generator temperature increases the mass of acetone vapor that cools the supplied air. After (12:00 PM), the temperature difference increases slowly due to decrease the generator temperature to reach (21 °C) for (21-July). It is seen that the temperature difference at (21-July) is higher than other days due to the higher solar radiation.

Fig.(5.65) explains the variation of the evaporator cooling effect with time. It can be noticed that the cooling effect increases with time due to increase the generator temperature that increases the mass of acetone vapor that cools the supplied air. It can be noticed that the cooling effect increases fastly before (12:00 PM) due to the sharp increase in the generator temperature as shown in Fig.(5.63) to reach (351 W) for(21-July) and then increases slowly after that due to slow increase in the generator temperature to reach (549 W) for the (21-July) at (02:30 PM). The cooling effect for July is larger than other days because of higher generator temperature.

Fig.(5.66) shows the variation of (COP) with time. It can be noticed that the coefficient of performance increases with time due to increase the cooling effect. The (COP) increases sharply before (12:00 PM) due to the sharp increase in the cooling effect to reach (0.3164) for (21-July) and then increases slowly after that due to the slow increase in the cooling effect as discussed in Fig.(5.65) to reach (0.71) for (21-July) at (02:30 PM). The (COP) for July is higher than other days because the cooling effect is higher.

Fig.(5.67) shows the variation of the supplied air temperature with time. It can be noticed that the temperature of supplied air decreases sharply with time before (12:00) due to increase the cooling effect to reach (18.04 °C) for (21-July) and then decreases in a slow rate with time due to accumulated heat gain from outside and slow rate of increase in the cooling effect as discussed in Fig.(5.65) to reach (10.53 °C) at (02:30 PM). Moreover, the temperature of supplied air for (21-July) is less than others because the cooling effect is higher.

Fig.(5.68) illustrates variation of temperature difference across the evaporator with time for different acetone concentrations at 21-July. It can be noticed that the temperature difference increases with time as discussed in Fig.(5.64). The temperature difference increases with acetone concentration due to increase the mass of acetone vapor that cools the supplied air. Therefore, the maximum temperature difference for (60%) acetone concentration at (2:30 PM) with a value of (23 °C).

Fig.(5.69) presents the variation of cooling effect with time for different acetone concentrations. It can be noticed that the cooling effect increases with acetone concentration due to increase the mass of acetone vapor that cools the supplied air. Therefore, the maximum value occurs at

(60%) acetone concentration and time of (2:30 PM) with value of (612.2 W).

Fig.(5.70) presents the variation of instantaneous (COP) with time for different acetone concentrations. It can be noticed that the (COP) increases with acetone concentration due to increase the mass of evaporated acetone that cools the supplied air and so increases the coefficient of performance with a maximum value of (0.791) at (60%) acetone concentration.

Fig.(5.71) presents the variation of circulation ratio (λ) with time for different acetone concentrations. It can be noted that the circulation ratio increases with time due to increase the generator temperature that increases the acetone vapor. It increases with acetone concentration due to increase the mass of acetone vapor so increases the circulation ratio with a maximum value of (0.127) at (60%) acetone concentration.

Fig. (5.72) shows the variation of the ratio of obtained cooling load to the required cooling load (ψ) with time for different acetone concentrations. It can be noticed that (ψ) increases with time due to increase the cooling effect as discussed in Fig.(5.65). It increases with acetone concentration due to increase the acetone vapor which cools the air with a peak value of (2.041) at (60%) acetone concentration.

Fig.(5.73) explains the variation of the temperature of supplied air with time for different acetone concentrations. It can be noticed that the temperature of supplied air decreases with acetone concentration due to increasing the mass of acetone vapor that cools the air and so decreases the air temperature. Therefore, the maximum value occurs at (60%) acetone concentration with a value of (8.13°C) and time of (2:30 PM).

Fig.(5.74) presents the variation of the mass flow rate of acetone vapor with time for different acetone concentrations. It can be noted that the mass of acetone vapor increases with time due to increase the generator temperature as discussed in Fig.(5.63) which increases the acetone vapor. It increases with acetone concentration. So, the maximum value occurs at (2:30 PM) and (60%) acetone concentration with a value of (0.00127 kg/s).

Fig.(5.75) shows the variation of cooling effect with condenser temperature at time of (01:00 PM). It can be noticed that the cooling effect decreases with increasing condenser temperature due to decrease the acetone vapor condensation which reduces the cooling effect across the evaporator. The cooling effect at (21-July) is higher than other days as discussed in Fig.(5.65) with a maximum value of (542.5W) at a condenser temperature of (25°C).

Fig.(5.76) explains the variation of cooling effect with the evaporator exit temperature at time of (01:00 PM) at (40 °C) condenser temperature. It can be noted that the cooling effect increases with increasing evaporator temperature due to increase the temperature at evaporator exit which means that the acetone vapor gains more heat from the cooled air across the evaporator. This leads to increase the cooling effect. The cooling effect at (21-July) is higher than other days as discussed previously with a maximum value of (470 W) at an evaporator exit temperature of (10°C).

Figs.(5.77 and 5.78) explains the daily COP . It can be noted that the daily COP at (21-July) is higher than other days due to higher generator temperature that leads to larger amount of acetone vapor. The daily COP increases with acetone concentration due to increase the acetone vapor at generator. Therefore, the maximum value of (COP_{daily}) is at (21-July) and acetone concentration of (60%) which is (0.392).

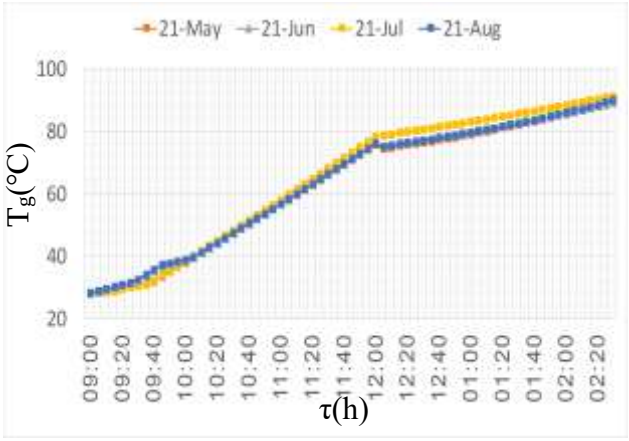

Fig.(5.63) variation of generator temperature with time for the days, 21st of May, June, July and August.

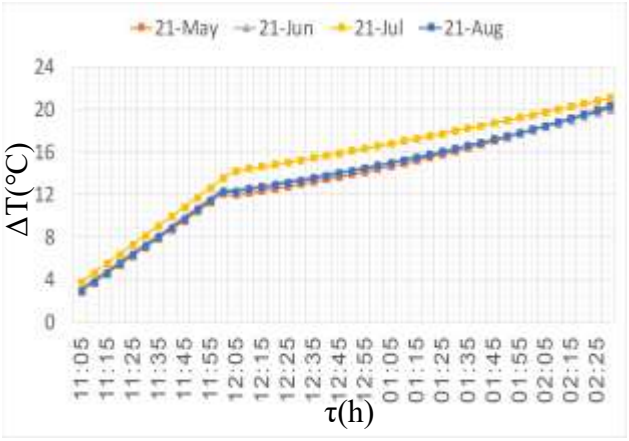

Fig.(5.64) variation of temperature difference at the evaporator with time for the days, 21st of May, June, July and August.

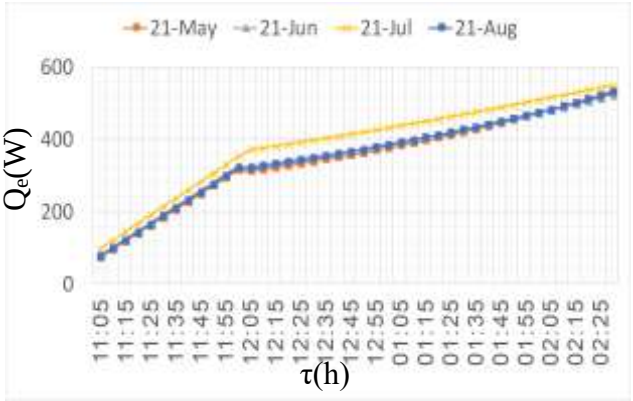

Fig.(5.65) variation of evaporator cooling effect with time for the 21st of May, June, July and August.

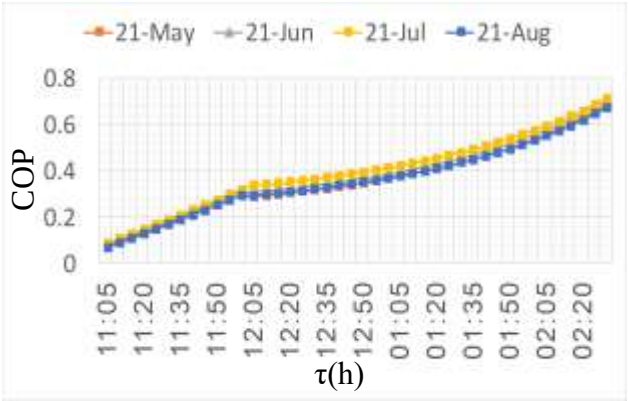

Fig.(5.66) variation of instantaneous COP with time for the 21st of May, June, July and August.

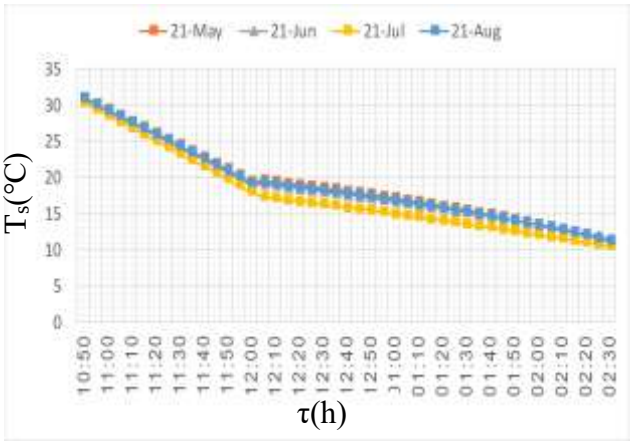

Fig.(5.67) variation of temperature of supplied air with time for different acetone concentrations at 21-July.

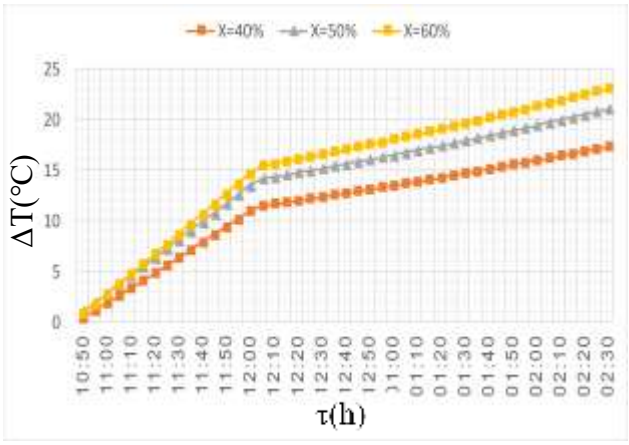

Fig.(5.68) variation of evaporator temperature difference with time for different acetone concentrations at 21-July.

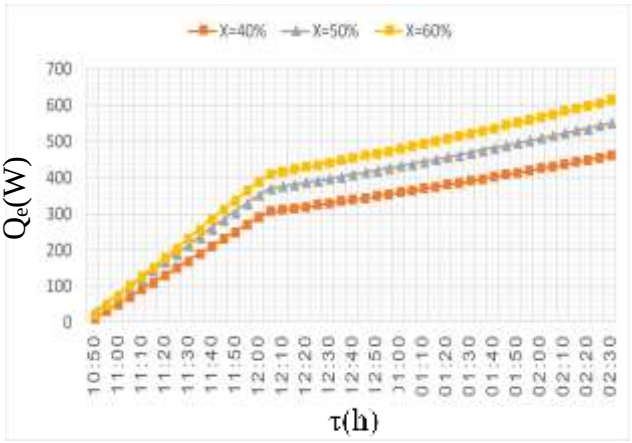

Fig.(5.69) variation of cooling effect with time for different acetone concentrations at 21-July.

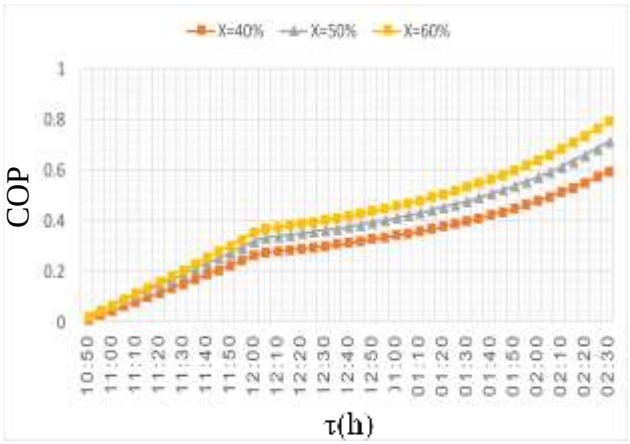

Fig.(5.70) variation of COP with time for different acetone concentrations at 21-July.

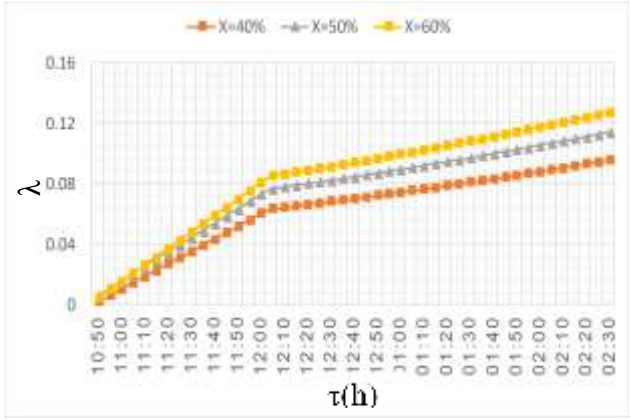

Fig.(5.71) variation of circulation ratio (λ) with time for different acetone concentrations at 21-July.

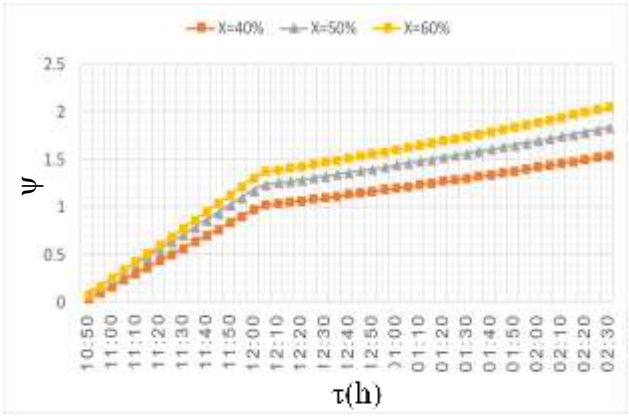

Fig.(5.72) variation of ratio (ψ) with time for different acetone concentrations at 21-July.

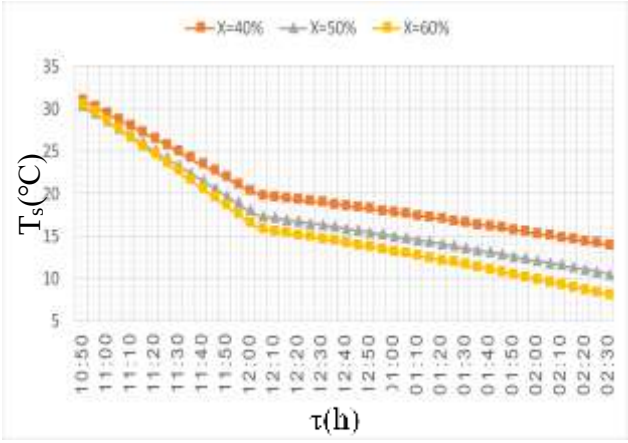

Fig.(5.73) variation of temperature of supplied air with time for different acetone concentrations at 21-July.

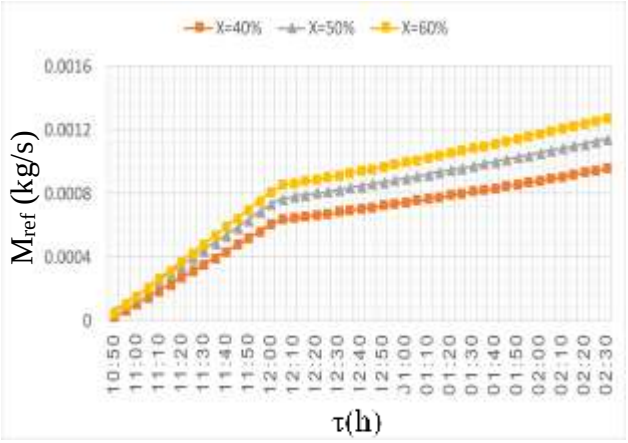

Fig.(5.74) variation of M_{ref} with time for different acetone concentrations at 21-July.

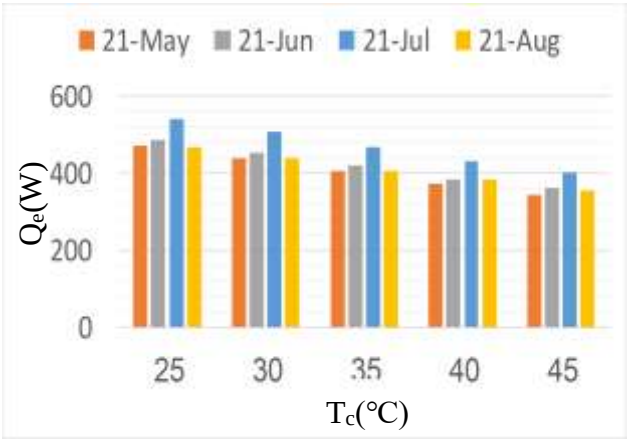

Fig.(5.75) variation of cooling effect with condenser temperature at time 01:00 PM.

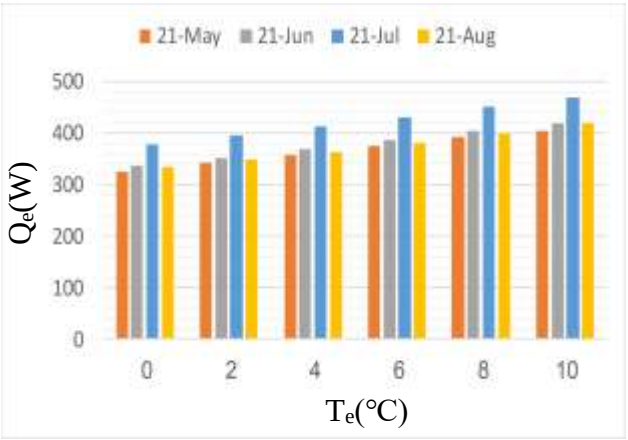

Fig.(5.76) variation of cooling effect with evaporator temperature at time 01:00 PM.

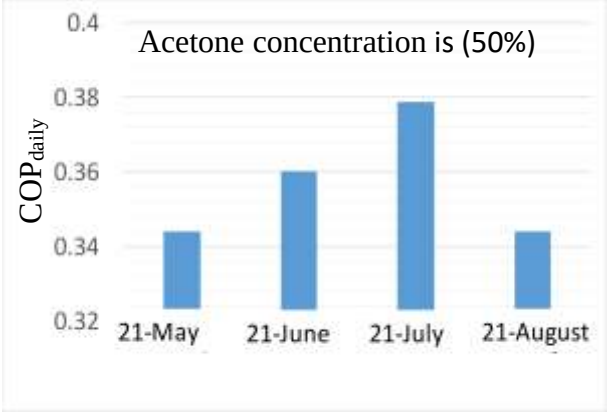

Fig.(5.77) daily coefficient of performance.

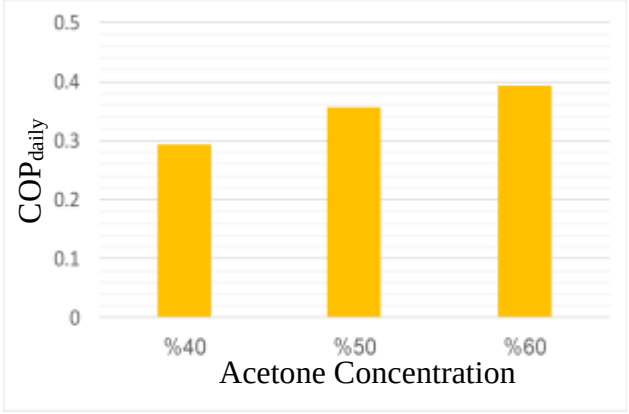

Fig.(5.78) variation of daily coefficient of performance with concentration for (21-July).

5.2.1.3 Exergy analysis of collector loop

Fig.(5.79) shows the variation of exergy destruction in collector with time for the (21st of May, June, July and August). It can be noted that the exergy destruction in collector increases with time due to increase the received solar radiation and increase the losses to the surroundings to reach maximum at (11:30 AM) and then decreases due to decrease the received solar radiation as discussed in Fig.(5.56) with maximum value of (1412.7 W) at (12:00) at (21-July).

Fig. (5.80) presents the variation of the exergy destruction of storage tank with time. It can be noted that the exergy destruction increases fastly with time to reach (233.84 W) at (12:00) noon for (21-July) due to the sharp increase in the solar radiation and then increases at a slower rate to reach a maximum value of (237.1 W) at (12:30 PM) and then decreases due to decrease the obtained useful energy. The exergy of storage tank of (21-July) higher than other days because the water temperature is higher.

Fig.(5.81) shows the variation of the exergetic efficiency of collector with time. It is noted that the exergetic efficiency increases fastly and reaches a maximum value for the first (30 min.) of operation due to the high heat rate of water. It is then decreases slowly for the rest of running time, due to smaller difference between receiver temperature and water. The maximum collector exergetic efficiency is at (09:25 AM) of (21-July) with a value of (0.4054) and its minimum value at (21-May) at (2:30 PM) with a value of (0.332).

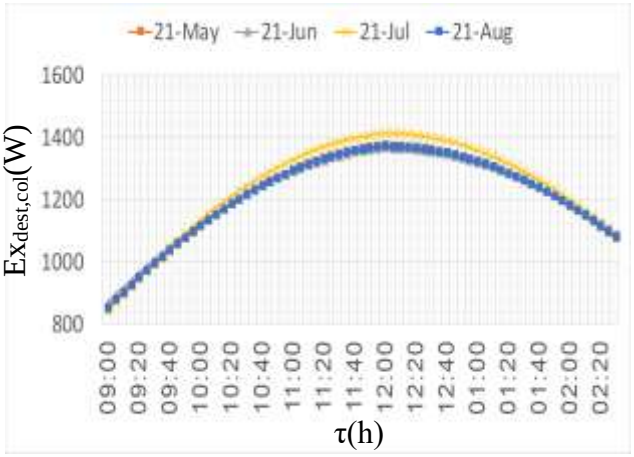

Fig.(5.79) variation of exergy destruction in collector with time.

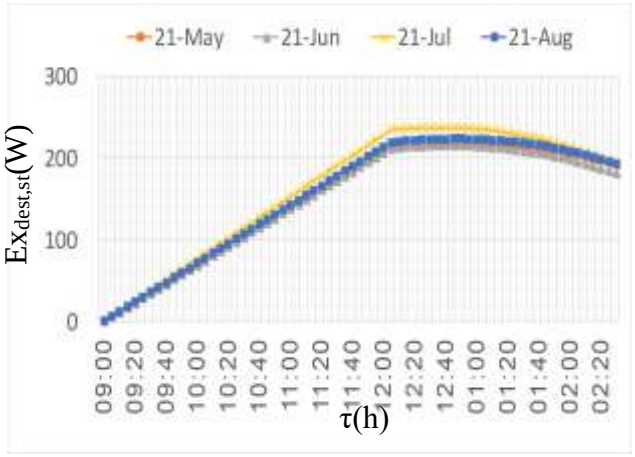

Fig.(5.80) variation of exergy of storage tank with time.

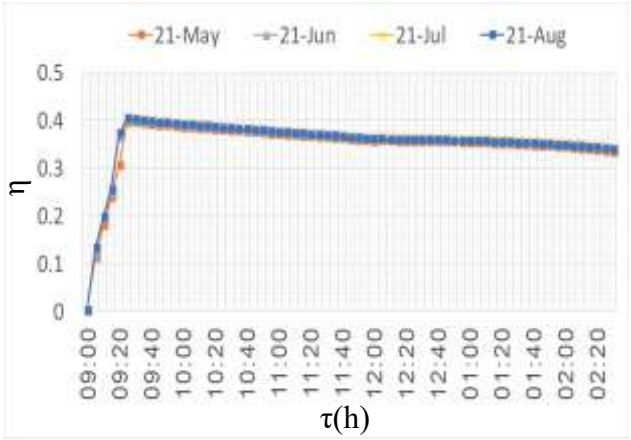

Fig.(5.81) variation of exergetic efficiency of collector with time for the 21st of May, June, July and August.

5.2.1.4 Exergy analysis of absorption system

Figs. (5.82-5.89) show the variation of the exergy destruction in solar absorption system components and overall destruction in the system with time for the (21st of May, June, July and August). It can be noted that, the exergy destruction increases sharply in the beginning due to more heat transfer between the system components as well as the heat transfer from the system components to the surroundings due to high temperature difference between the system and the ambient. After that, the increase of destruction becomes slow with time since the temperature difference

between the system components decreases, so the heat transfer decreases, also, the temperature of ambient increases and the temperature difference between the system components and the surroundings decreases so the heat transfer rate decreases. The exergy destruction increases with time due to increase the generator temperature. Also, the exergy destruction at (21-July) is higher than other days since the generator temperature is higher due to higher solar radiation with maximum values of (732, 167, 36, 140, 511, 650, 762 and 2998 W) for (generator, condenser, valve 1, evaporator, absorber, heat exchanger, valve 2 and overall absorption system) respectively at 02:30 PM. The maximum exergy destruction occurs at the solution expansion valve because the greater pressure drop that causes high entropy difference. The maximum exergy destruction for the main components occurs at the generator because the high heat exchange between the hot water of collector loop and the mixture within it. While the minimum value for the primary components at the evaporator because the least value of acetone vapor mass flow rate inside it.

Fig.(5.90) shows the exergy destruction of system components for 21-July at 01:00 PM. It can be noted that, the maximum exergy destruction occurs at the solution expansion valve with a value of 769 W while the minimum value at the acetone vapor expansion valve with a value of 30 W. The maximum exergy destruction for the main components is at the generator with a value of 738 W because the maximum heat exchange occurs at it while the evaporator has a minimum destruction with a value 116 W because the mas flow rate of acetone vapor is very small.

Fig.(5.91) explains the variation of second law efficiency with time. It can be noted that second law efficiency increases with time due to increase the coefficient of performance as discussed in Fig.(5.65) and

reaches the maximum at (02:30 PM) with a value of (0.976) for (21st of July).

Fig.(5.92) shows the variation of ideal COP with time. It can be noticed that the ideal COP increases fastly before (12:00) to reach (0.861) for (21-July) and then increases so slowly with time due to increase the loses to the surroundings to reach (0.906) for (21-July) at (02:30 PM). The ideal COP for July higher than others because the generator temperature is higher.

Fig.(5.93) shows the variation of second law efficiency with acetone concentration. It can be noted that the second law efficiency increases with concentration due to increase the acetone vapor and so increase the cooling effect and the COP. The second law efficiency at (21-July) higher than the other days because the higher cooling effect. Therefore, the maximum second law efficiency at (21-July) and (60%) acetone concentration with a value of (0.6717).

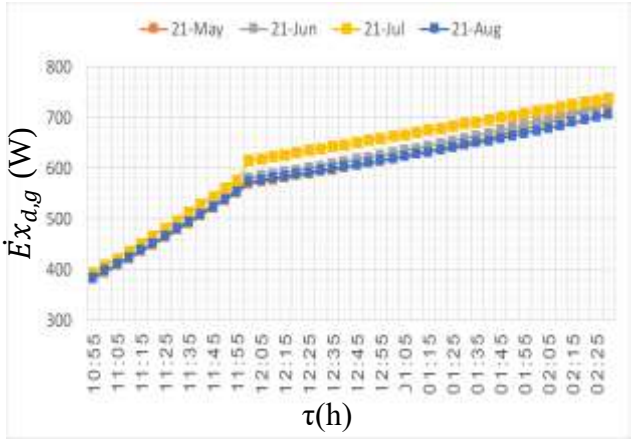

Fig.(5.82) variation of the exergy destruction in generator with time.

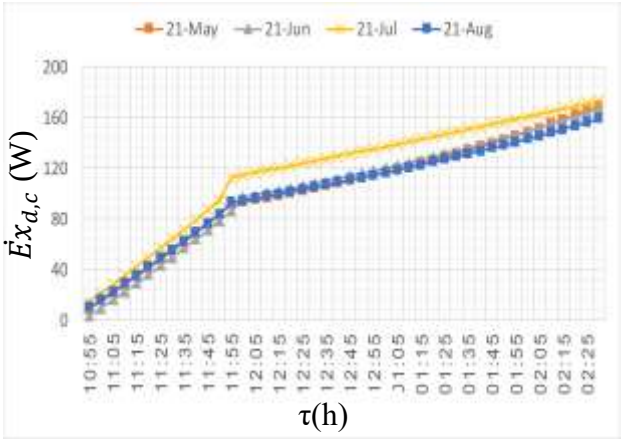

Fig.(5.83) variation of the exergy destruction in condenser with time.

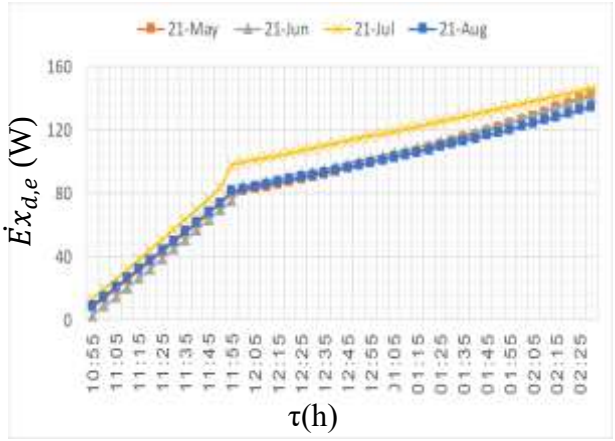

Fig.(5.84) variation of the exergy destruction in evaporator with time.

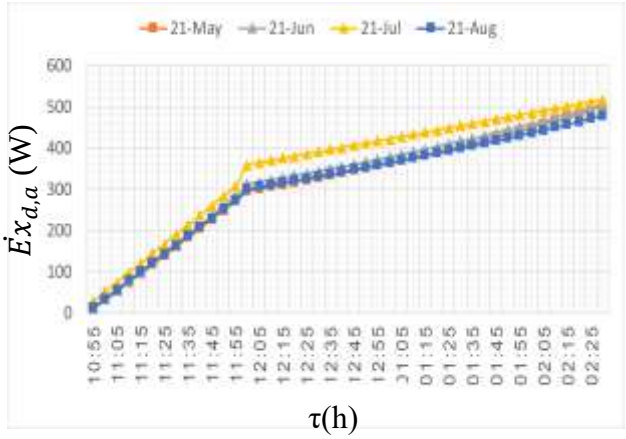

Fig.(5.85) variation of the exergy destruction in absorber with time.

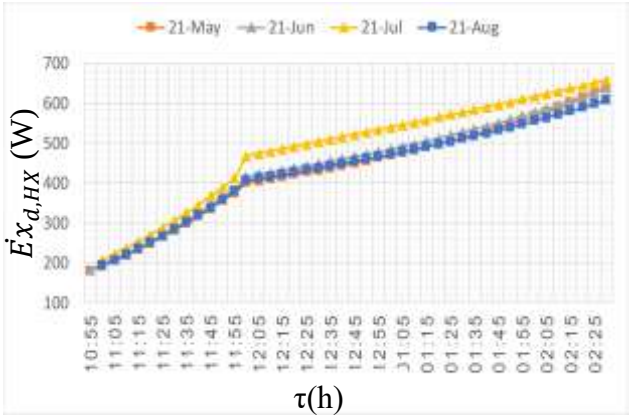

Fig.(5.86) variation of the exergy destruction in heat exchanger with time.

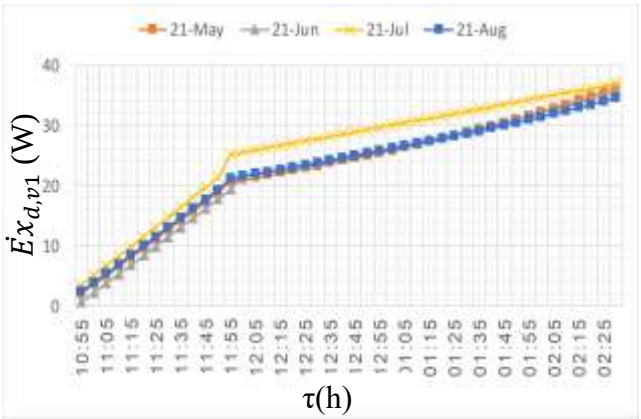

Fig.(5.87) variation of the exergy destruction in first capillary tube with time.

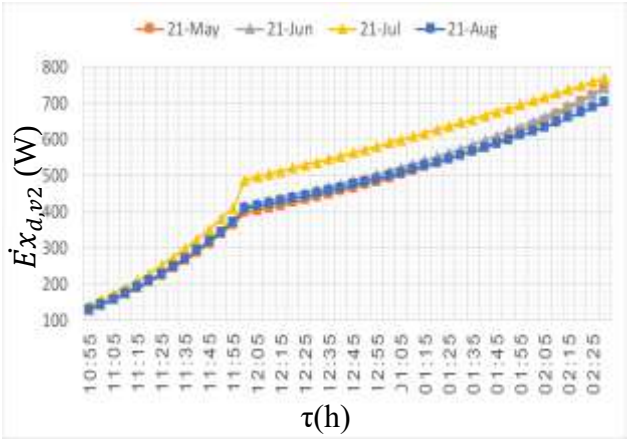

Fig.(5.88) variation of the exergy destruction in second capillary tube with time.

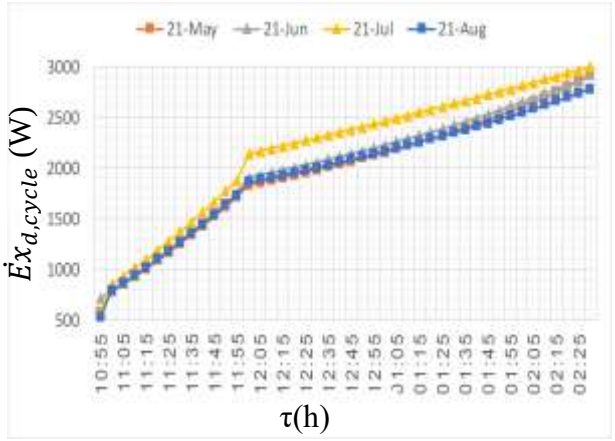

Fig.(5.89) variation of the exergy destruction in overall solar absorption system with time.

Fig.(5.90) the exergy destruction of system components for 21-July at 01:00 PM.

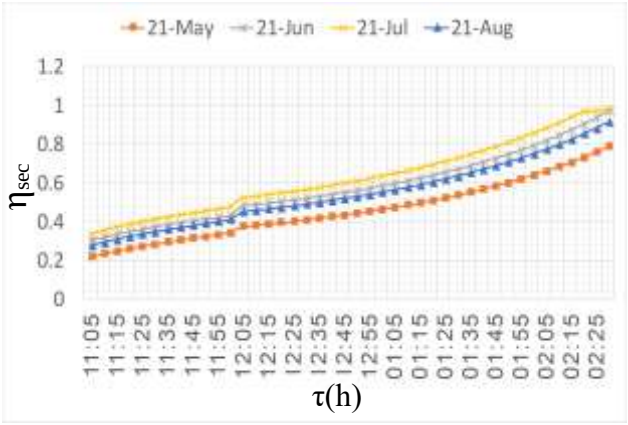

Fig.(5.91) variation of the second law efficiency with time.

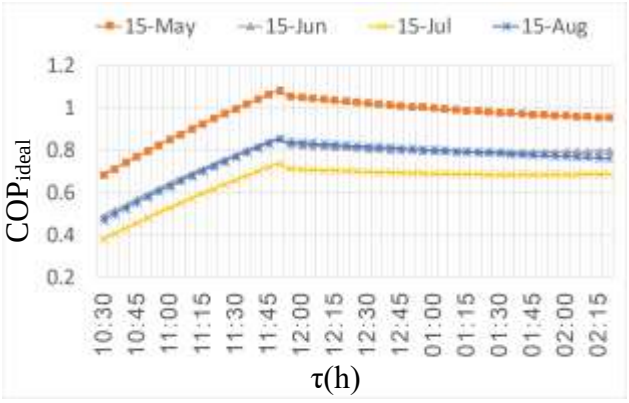

Fig.(5.92) variation of COP_{ideal} with time.

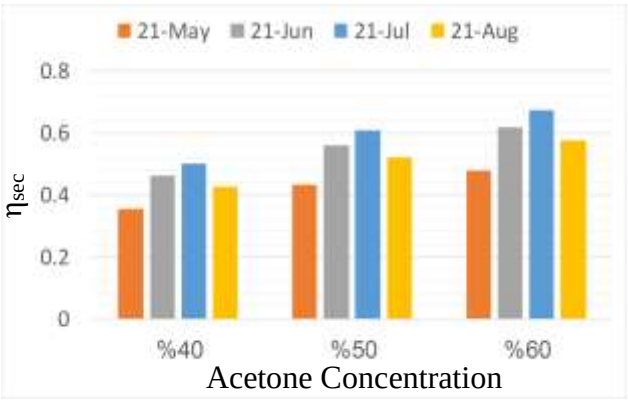

Fig.(5.93) variation of second law efficiency with acetone concentration.

5.2.1.5 Overall efficiency

Fig.(5.94) shows the variation of overall efficiency (η_{ov}) with time. It can be noted that (η_{ov}) increases with time due to increase the generator temperature which increases the evaporated acetone and so increases the cooling effect until reach the maximum at (02:30 PM). The systematic efficiency at (21-July) is higher than others because the generator temperature is higher with a value of (0.3273).

Fig.(5.95) explains the variation of overall efficiency with time for different acetone concentrations for 21-July. It can be noted that the overall efficiency increases with increasing the acetone concentration due to increase the acetone vapor that increases the cooling effect as discussed in Fig.(5.65). The overall efficiency increases with time. Therefore, the maximum overall efficiency occurs at (60%) acetone concentration with a value of (0.2218).

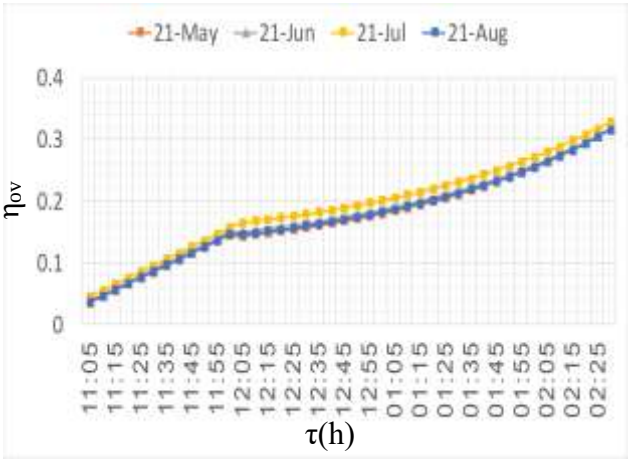

Fig.(5.94) variation of (η_{ov})with time for the 21st of May, June, July and August.

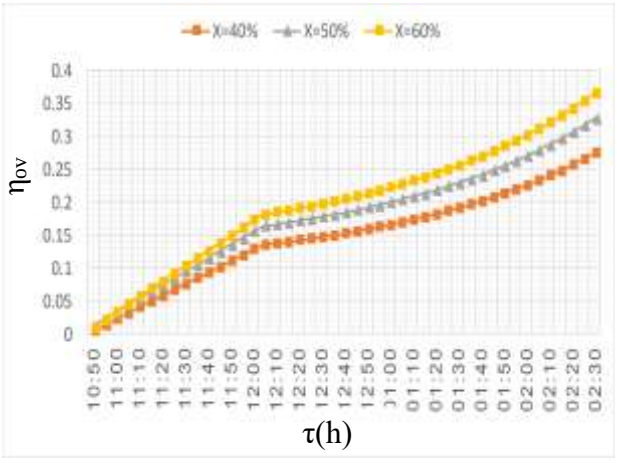

Fig.(5.95) variation of (η_{ov}) with time for different acetone concentrations for 21-July.

5.2.2 Indoor air quality parameters

5.2.2.1 Air diffusion performance index (ADPI)

Figs.(5.96 and 5.97) show the variation of air diffusion performance index (ADPI) with time for the (21st of May, June, July and August) at mean velocity of supplied air of (0.3 m/s and 0.25 m/s) value using displacement ventilation (DV). The volume flow rate is (0.022 m^3/s) and the required cooling effect is (300 W). It can be noted that (ADPI) for both cases increases with time at starting because the space is hot and so it is far from comfort and then increases with time because the space is cooled and so it becomes nearer to the comfortable zone and so the (ADPI) increases to reach maximum value at the temperature of supplied air of (20°C) because the room approaches to the condition of thermal comfort at the design temperature of (20 °C) at air flow rate of (0.02183 m^3/s). When the temperature of supplied air becomes less than (20 °C), (ADPI) decreases because the space becomes cold and uncomfortable. Therefore, the maximum (ADPI) is (70.92%) and (69.17 %) for the two cases respectively at (T_s) of (19.46°C) for (21-May) at (12:00) which is near the design temperature. (ADPI) increases with the velocity of supplied air so the velocity of (0.3 m/s) has been considered at design. The accepted (ADPI) for displacement ventilation is greater than (70%), [127].

Fig.(5.98) explains a comparison between the (ADPI) for exit location at the same side of diffuser and opposite side with time between (11:30 AM) and (02:00 PM) for (21st of July). It can be noted that (ADPI) for the same side of exit at all times and at all the temperatures of supplied air is higher than the (ADPI) for the case of opposite side because in the first case the air moves from the diffuser to the exit with a semi-circular path that passes most room zones so the space approaches the comfortable zone. While in the second case the air moves from the diffuser to the exit

in a short path and so the air passes through less volume of the space and so it becomes far from the comfort. The maximum (ADPI) for same side at time (12:00) is (68.83 %) while for the opposite side is (52.91%).

Fig.(5.99) explains the variation of (ADPI) with acetone concentration for (21-July) at time of (12:00). It can be noted that (ADPI) at concentration of (40%) is less than its value at (50%) because the temperature of supplied air at (40%) is higher than (20 ℃), so the space is hot and the (ADPI) is low. While at the concentration of (50%), the temperature of supplied air is closer to (20℃), so the space is comfortable and the (ADPI) is at highest value. However, at the concentration of (60%), the temperature of supplied air is less than (20 ℃), so the space becomes cold and uncomfortable. This leads to a lower value of (ADPI). The maximum (ADPI) at acetone concentration of (50%) with a value of (68.83%).

Fig.(5.100-5.101) explain the variation of (ADPI) with evaporator exit temperature for (21-July) at times of (11:30 AM and 01:00 PM). It can be noted that (ADPI) at (11:00 AM) increases with increase of evaporator exit temperature due to the increase in cooling effect and decrease of the temperature of supplied air as discussed in Fig.(5.76). So, the temperature of supplied air decreases to approaches to the design temperature of (20 ℃) that satisfy the thermal comfort and highest (ADPI). So, the maximum (ADPI) at evaporator exit temperature of (10 ℃) with a value of (62.41 %). While for the time of (01:30 PM), the temperature of supplied air less than (20 ℃) and the (ADPI) decreases with decreasing the temperature of supplied air. The increase in evaporator exit temperature decreases the temperature of supplied air, so decreases the (ADPI) value because the space becomes colder and uncomfortable. Therefore, the (ADPI) decreases

with increase of evaporator exit temperature with maximum (ADPI) at evaporator exit temperature of (0 ℃) and a value of (56.62%).

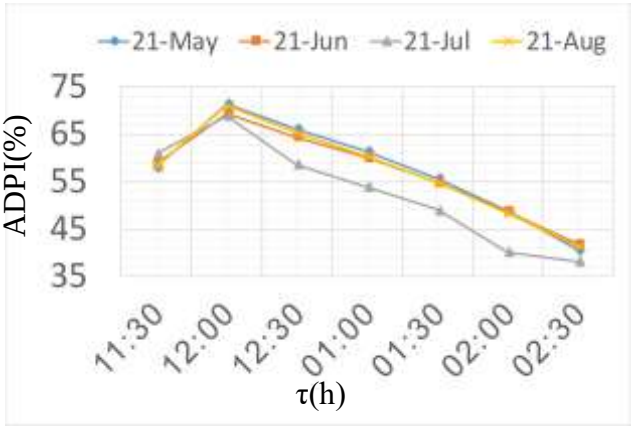

Fig.(5.96) variation of (ADPI) with time for 21st of May, June, July and August at velocity of 0.3 m/s.

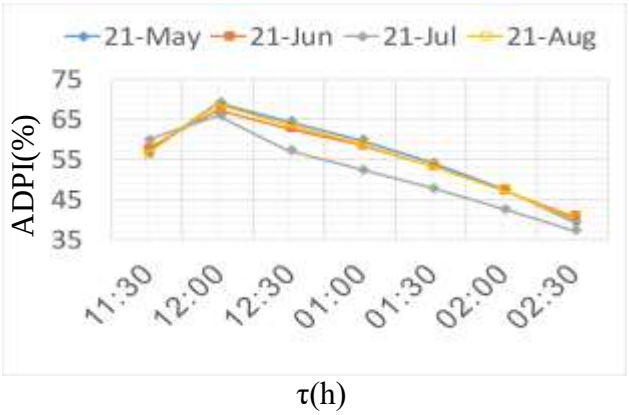

Fig.(5.97) variation of (ADPI) with time for 21st of May, June, July and August at velocity of 0.25 m/s.

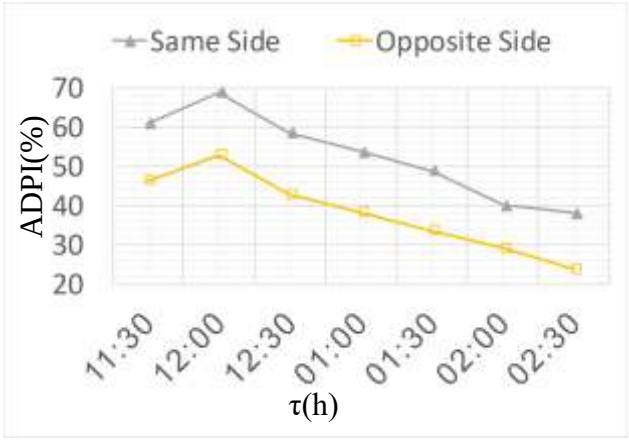

Fig.(5.98) comparison between the ADPI for exit location at the same side of diffuser and opposite side with time for 21st of July.

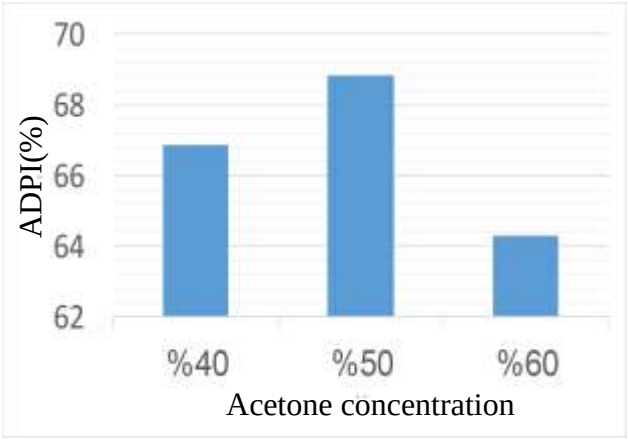

Fig.(5.99) variation of ADPI with acetone concentration for 21-July at time of 12:00.

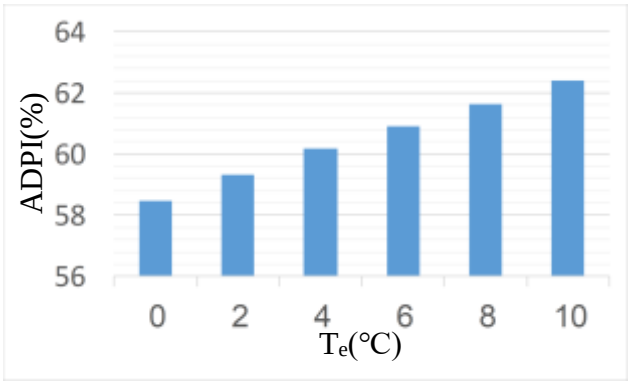

Fig.(5.100) variation of ADPI with evaporator temperature for 21-July at time of 11:30 PM for 50% acetone concentration.

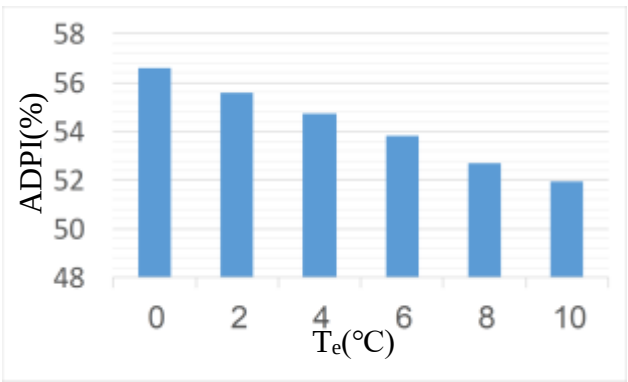

Fig.(5.101) variation of ADPI with evaporator temperature for 21-July at time of 01:00 PM for 50% acetone concentration.

5.2.2.2 Thermal ventilation effectiveness (ε_t)

Fig.(5.102 and 5.103) present the variation of thermal ventilation effectiveness (ε_t) with time for (21^{st} of May, June, July and August) at mean velocity of supplied air of (0.3 m/s and 0.25 m/s) respectively using displacement ventilation(DV). The volume flow rate is (0.022 m^3/s) and the required cooling effect is (300 W). It can be noted that (ε_t) increases with time as the room temperature approaches the design environment temperature of (25°C) that satisfies the thermal comfort with a value of (1.402 and 1.346) at (12:00 AM) for (21^{st} of May). Then (ε_t) decreases since the room temperature drops below (25 °C) and the space becomes cold and uncomfortable. The thermal ventilation effectiveness increases with increase of velocity of supplied air. The accepted (ε_t) for displacement ventilation is greater than (1), [127].

Fig.(5.104) explains the variation of thermal ventilation effectiveness (ε_t) with acetone concentration for (21-July) at time of (12:00 PM). It can be noted that thermal ventilation effectiveness (ε_t) increases as the room temperature decreases and approaches (25 °C) which is the comfortable temperature with acetone concentration of 50%. Further increase in acetone concentration produces more acetone vapor and larger cooling effect and the room temperature drops below (25 °C) and becomes uncomfortable. `The maximum (ε_t) is obtained at acetone concentration of (50%) at (21-July) at time of (12:00) with value of (1.393).

Fig.(5.105-5.106) explain the variation of (ε_t) with the evaporator exit temperature for (21-July) at times of (11:30 AM) and (01:00 PM). It can be noted that (ε_t) at (11:30 AM) increases with increase of evaporator exit temperature due to the increase in cooling effect and decrease of the temperature of supplied air as discussed in Fig.(5.76). So, the temperature of supplied air decreases to approach the design temperature of (20 °C)

that satisfy the thermal comfort and highest (ε_t) . Therefore, the maximum (ε_t) at evaporator exit temperature of (10 °C) with a value of (0.967). At the time of (01:30 PM), the temperature of supplied air becomes less than (20 °C) and the (ADPI) decreases with decrease the temperature of supplied air. The increase in evaporator temperature reduces the temperature of supplied air, so decreases the (ε_t) value because the space becomes colder and uncomfortable. Therefore, the (ε_t) decreases with increase of evaporator temperature. The maximum (ε_t) at evaporator temperature of (0 °C) with value of (1.198).

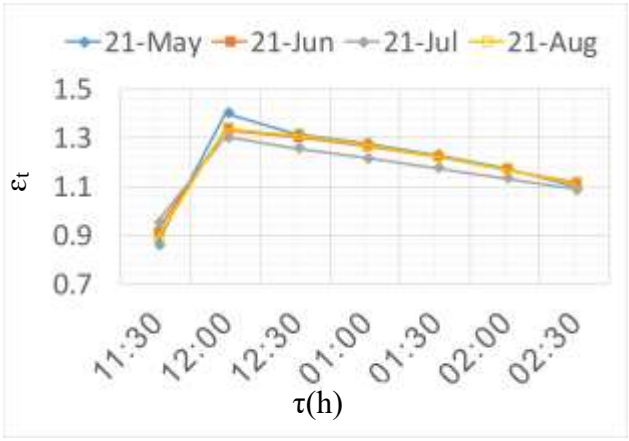

Fig.(5.102) variation of (ε_t) with time for the 21st of May, June, July and August at mean velocity of supplied air of 0.3 m/s.

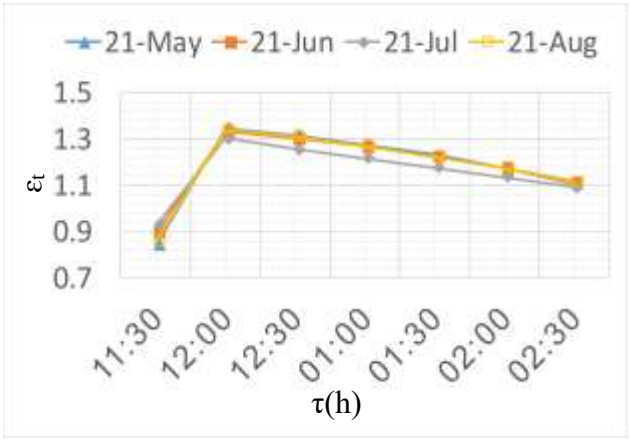

Fig.(5.103) variation of (ε_t) with time for the 21st of May, June, July and August at mean velocity of supplied air of 0.25 m/s.

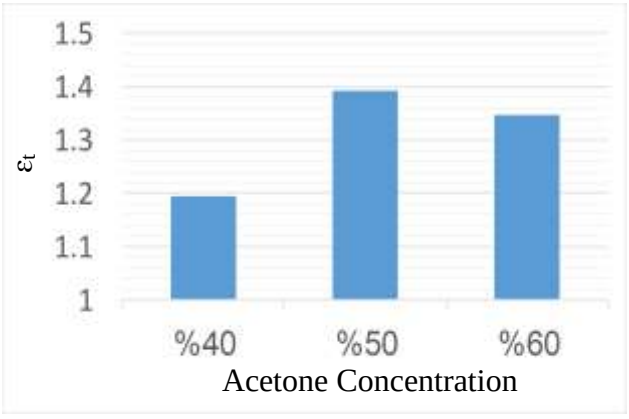

Fig.(5.104) variation of (ε_t) with acetone concentration for 21-July at time of 12:00.

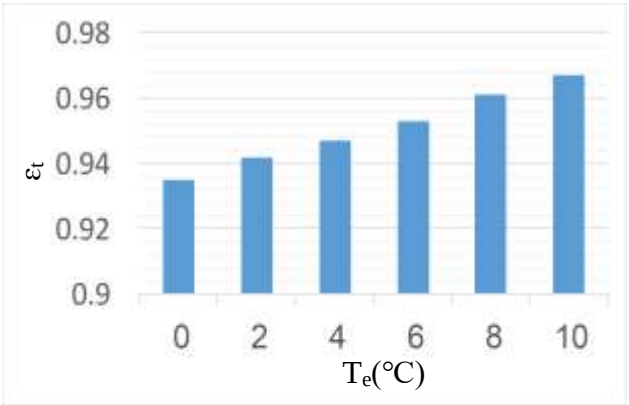

Fig.(5.105) variation of (ε_t) with evaporator temperature for 21-July at time of 11:30 AM.

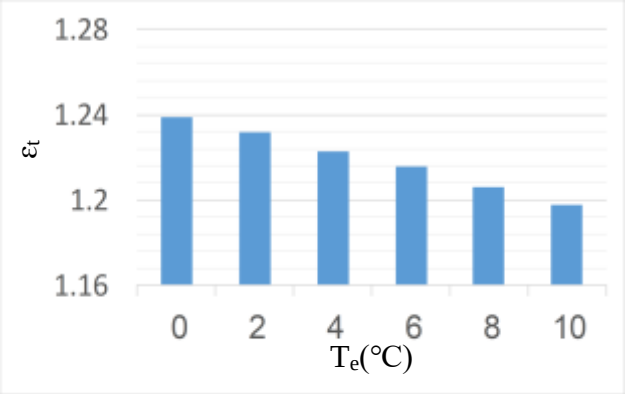

Fig.(5.106) variation of (ε_t) with evaporator temperature for 21-July at time of 01:00 PM.

5.2.2.3 Temperature distribution

The temperature distribution has been taken at two poles. The first pole is located at coordinates of (X=1 m and Z=1 m) forward to diffuser, while the second pole has been located at (X=1.25 m, Z=1.5 m) near the person as shown in Fig.(5.107).

Figs. (5.108-5.109) show the variation of local temperature with height for (21st of May, June, July and August) at time of (12:00) for first pole at (X=1 m and Z=1 m) and second pole at (X=1.25 m and Z=1.5m) using displacement ventilation(DV). The volume flow rate is (0.022 m^3/s) and the required cooling effect is (300 W). It can be remarked that for the two poles the temperature increases with height for all days because the difference in air density, where the cold air remains at lower levels while the hot air moves to higher levels as well as the supplied air is at lower levels. The minimum value of local temperature at 21st July is at floor level with values of (18.04 °C) and (18.34 °C) for the first and second poles respectively due to the higher cooling effect as discussed in Fig. (5.64), while the maximum values of temperature at 21st May and height of 2.5 m are (28.2 °C) and (26.55 °C). So, the space within the occupied zone is comfortable.

Figs.(5.110-5.111) explain the variation of local temperature with height for (21st July) at different times for first and second poles respectively. It can be noticed that the temperature increases with height for all times, but its value decreases with time due to the lower supplied air temperature. The minimum values of local temperatures at (01:00 PM) at floor level are (15.02 °C) and (15.23 °C) for the two poles respectively, while the maximum values of temperature at (11:30 AM) and height of (2.5 m) are (30.4 °C) and (30.74 °C) respectively, but the space within the occupied zone is comfortable and the mean temperature less than 25 °C.

Figs.(5.112-5.113) present the variation of local temperature with height for the (21st of July) at time of (12:00) at different mean velocities of supplied air for first and second poles. It can be noted that the temperature increases with height for the two mean air velocities, but it decreases with increasing the mean air velocity. The minimum values of local temperatures at mean velocity of (0.3 m/s) at floor level has values of (18.04 °C) and (18.34 °C) for the two poles respectively. However, the maximum values of temperatures at mean air velocity of (0.25 m/s) and height of (2.5 m) with values of (26.54 °C) and (26.21°C).

Fig.(5.114) explains the variation of local temperature and acetone concentration for the (21st of July) at time of (12:00) for the two poles. It can be noticed that the local temperature decreases with increase the acetone concentration due to decrease the temperature of supplied air to the cooled room. The minimum local temperatures at acetone concentration of (60%) with values of (19.58 °C) and (22.81 °C) for the first and second poles respectively.

Fig.(5.115) shows the variation of temperature difference between head and foot with time for the seated and standing persons for (21-July). It can be noted that the temperature difference increases with time due to

increasing the cooling effect with time where the lower levels are cooled faster than the upper levels since it is closer to cold air supply. The temperature difference for standing person is higher than seated person because the difference in level is higher with maximum values of (2.73 °C) and (3.82 °C) for the seated and standing persons respectively. The accepted value of temperature difference is (2 °C) and (3°C) for the seated and standing persons respectively, [128].

Fig.(5.116) shows the contours of distribution of air temperature inside the cooled room for plane (P_z) at (Z=1 m) for (21-July) at (12:00). It can be noted that the minimum temperature is at the floor level near the diffuser exit that is installed at bottom of room in the west direction at (Z=1 m). It increases in all directions with height until reaches a maximum local value of (44.88 °C) near the computer and the sitting person. The temperature of air begins from the temperature of supplied air which is (15.79 °C) at the diffuser exit that is installed at bottom of room in the west direction at (Z=1 m). The maximum temperature is obtained near the computer and the head of person since they are both heat sources.

Fig.(5.117) display the contours of distribution of air temperature inside the cooled room for plane (P_{y1}) at (Y=1.1 m) (breathing level) for seated persons for (21-July) at (12:00). The air temperature starts from (23.37 °C) and increases towards the persons and computer (the source of heat) and reaches a maximum value of (44.88 °C).

Fig.(5.118) explains the contours of distribution of air temperature inside the cooled room for plane (P_{y2}) at (Y=1.8 m) that is called breathing level for standing persons for (21-July) at (12:00). The temperature of air starts from (26.93 °C) then increases gradually in the direction of X-axis until reaches (34.92 °C) at dead zones. It is noticed that the temperature

distribution is more uniform in this level because it is far from any heat source.

Fig.(5.119) displays the contours of distribution of air temperature inside the cooled room for plane (P_z) at (Z=1 m) at (21-July) at (12:00) for acetone concentration of (X=40%, 50% and 60%). The temperature of air begins from the temperature of supplied air which is (21.4 °C), (18.04 °C) and (17.05 °C) for the three concentrations at the diffuser exit. Then the temperature increases gradually with height and in all directions in the room until reaches to (43.99 °C), (42.75 °C) and (42.23 °C) for the three concentrations. The maximum temperature at the person and the computer which are the sources of heat and at the corners. Moreover, it can be remarked that the temperature decreases with acetone concentration due to decrease the temperature of supplied air and so, the maximum temperature decreases with concentration.

Fig.(5.120) shows the contours of distribution of air temperature inside the tested room for plane (P_{y1}) at (Y=1.1 m) at (21-July) at (12:00 PM) for acetone concentration of (X=40% and 50%). It is seen that the temperature increases gradually towards the source of heat and the corners until reaches to (43.99 °C and 42.75°C) for the two concentrations. The temperature decreases with acetone concentration due to decrease the temperature of supplied air and therefore, the maximum temperature decreases with concentration.

Fig.(5.121) explains the contours of distribution of air temperature inside the tested room for plane (P_{y2}) at (21-July) at (12:00 PM) for acetone concentration of (X=40%, 50% and 60%). It is seen that the temperature increases gradually towards the room walls which are called dead zones until reaches to (43.65 °C, 39.25 °C and 39.89 °C) for the three concentrations respectively. It can be noted that the temperature decreases

with acetone concentration due to decrease the temperature of supplied air and therefore, the maximum temperature decreases with concentration.

Fig.(5.122) shows the contours of distribution of air temperature inside the tested room for plane (P_z) for (21-July) at (12:00) for different locations of air exit. In the first case, the exit at the same side of diffuser, while at the second case, the air exits at the opposite side of the diffuser position. The temperature of air starts from the temperature of supplied air that is (18.04 °C) at the diffuser exit. Then the temperature increases gradually with height and other directions in the room. It can be noted that the maximum temperature at the first case is less than the other because there are a smaller dead zones, where the air moves with a semi-circular path that reaches most room zones and then exits. However, at the second case, the air enters from the diffuser and goes across the space directly to the exit with little circulation (short path). The dead zone is larger in this case, so the temperature is higher. The maximum temperatures are (42.75 °C and 44.63 °C) for the two cases respectively, but the mean temperature less than 25°C.

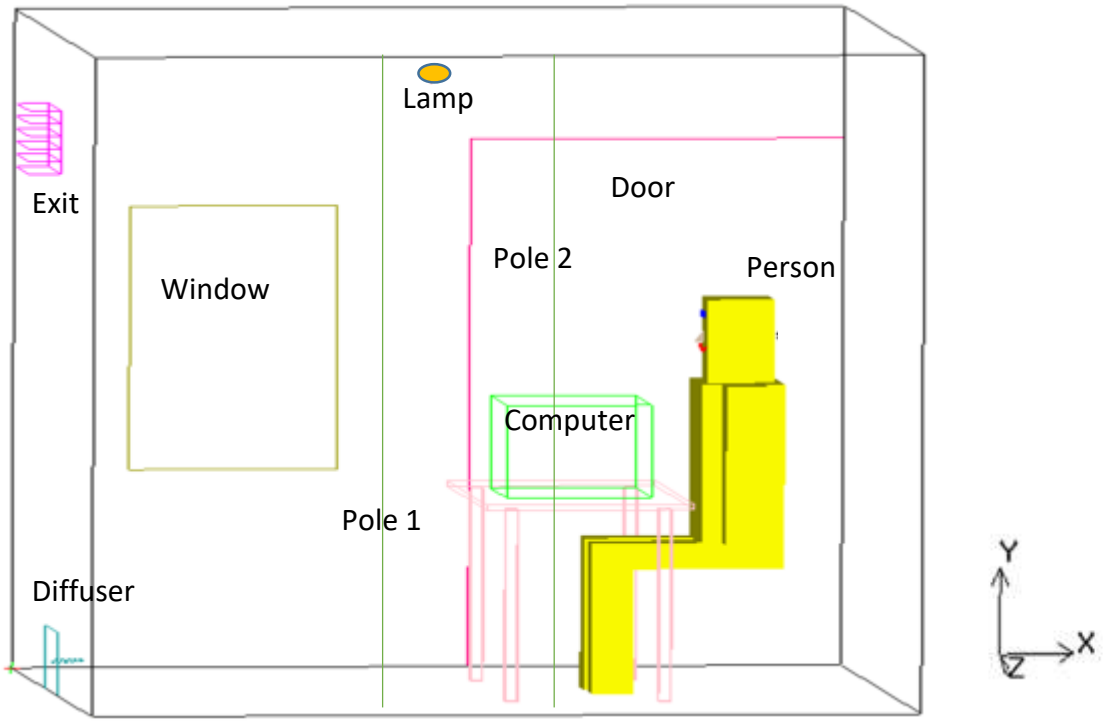

Fig.(5.107) tested room with the poles. First pole is at (X=1m,Z=1m) and the second pole is at (X=1.25m, Z=1.5m).

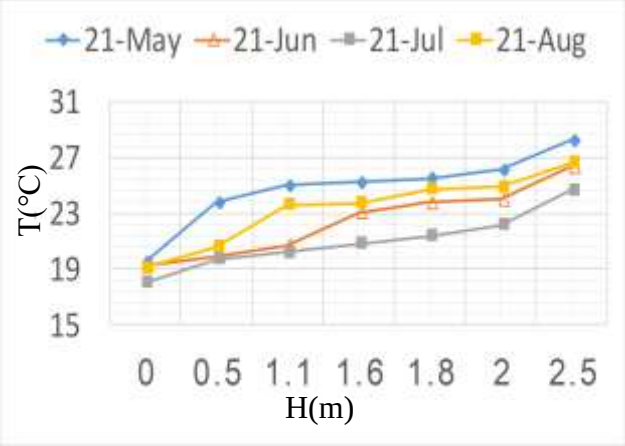

Fig.(5.108) variation of local temperature with height for the 21st of May, June, July and August at time of 12:00 for first pole.

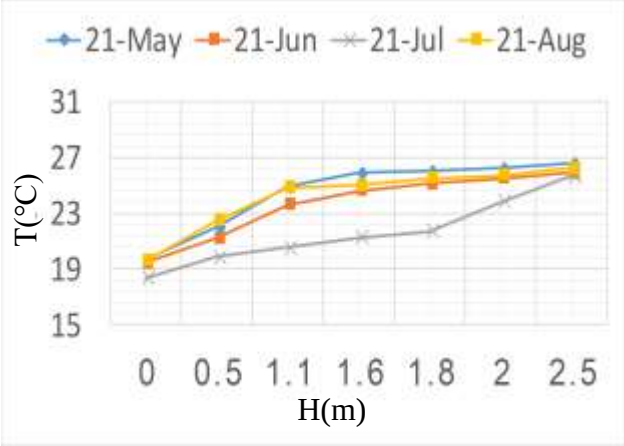

Fig.(5.109) variation of local temperature with height for the 21st of May, June, July and August at time of 12:00 for second pole.

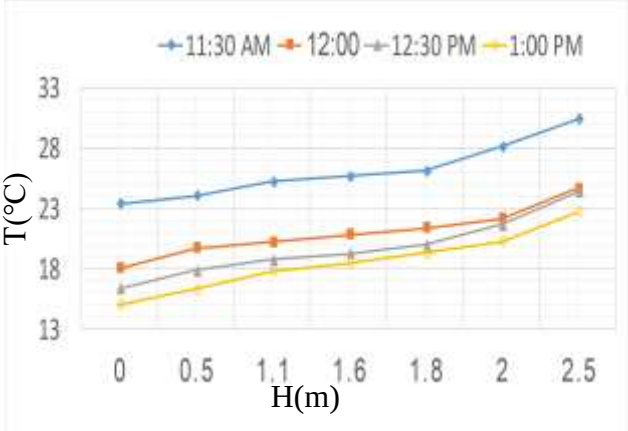

Fig.(5.110) variation of local temperature with height for 21st July at different times for first pole.

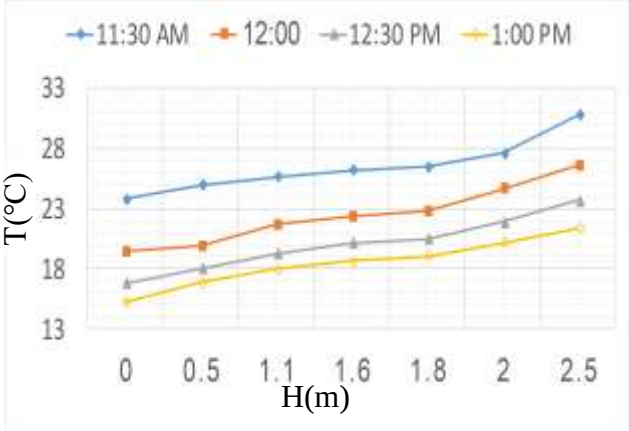

Fig.(5.111) variation of local temperature with height for 21st July at different times for second pole.

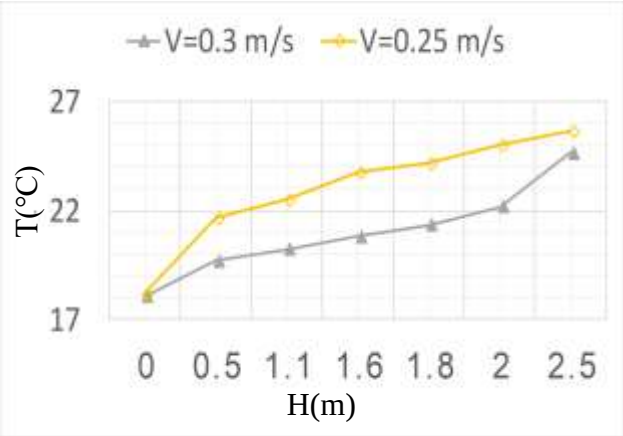

Fig.(5.112) variation of local temperature with height for the 21st of July at time of 12:00 at different mean velocities of supplied air for first pole.

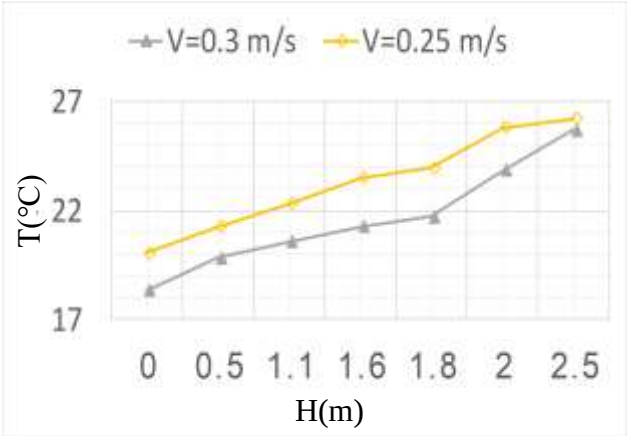

Fig.(5.113) variation of local temperature with height for the 21st of July at time of 12:00 at different mean velocities of supplied air for second pole.

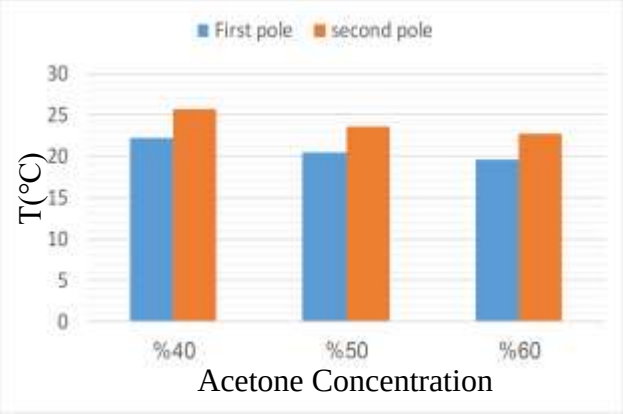

Fig.(5.114) variation of local temperature with acetone concentration for the 21st of July at time of 12:00 at for the two pole.

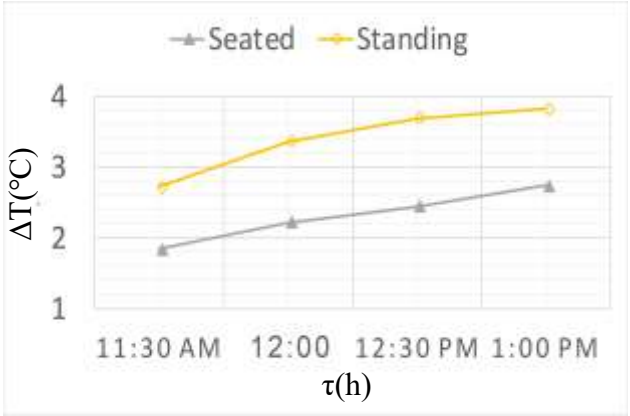

Fig.(5.115) variation of temperature difference between head and foot with time for seated and standing person.

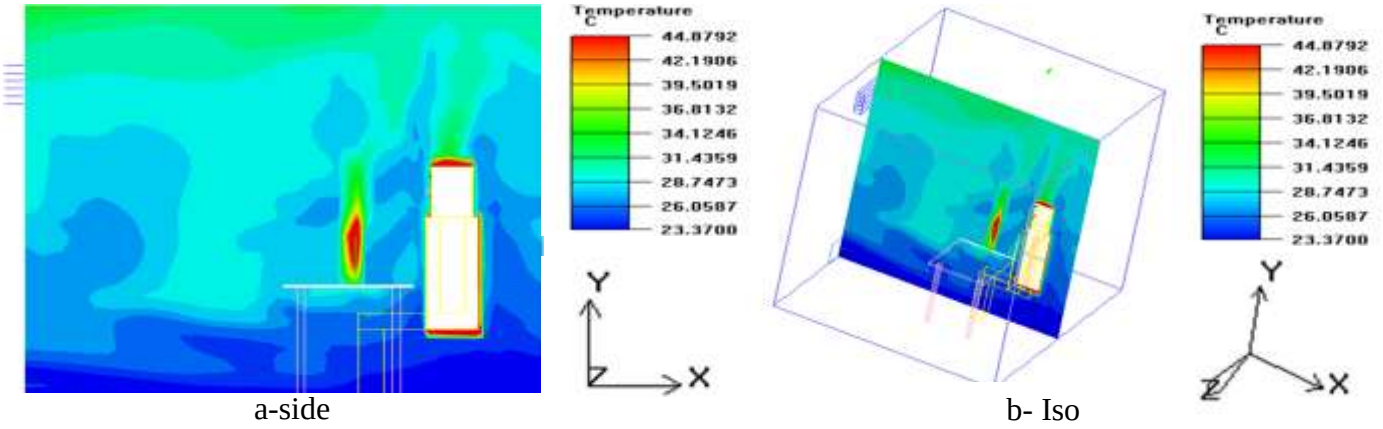

a-side b- Iso

Fig.(5.116) contours of distribution of air temperature inside the tested room for plane (P_z) at Z=1 m at 21-July at 11:30 AM.

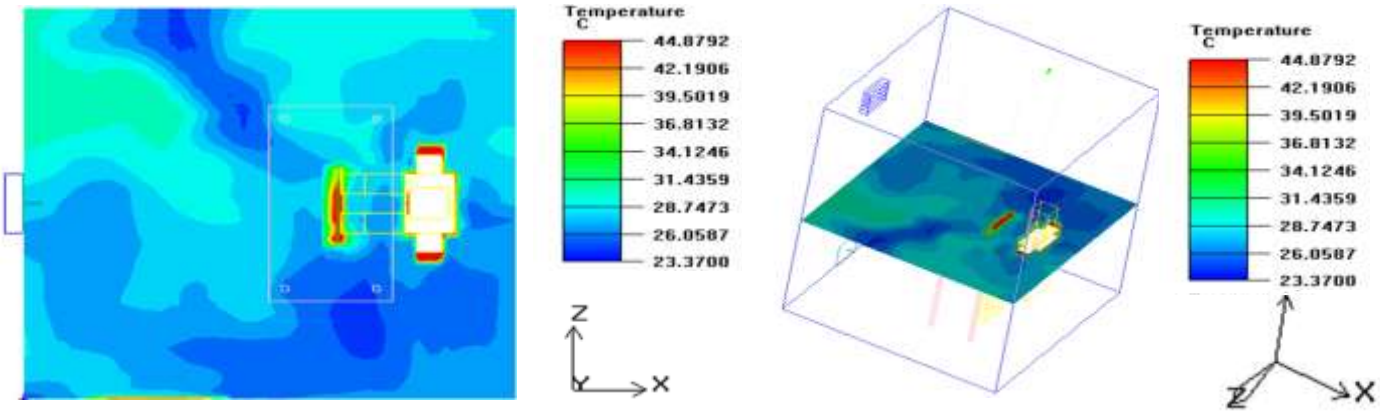

a-side b- Iso

Fig.(5.117) contours of distribution of air temperature inside the tested room for plane (P_{y1}) at Y=1.1 m at 21-July at 11:30 AM.

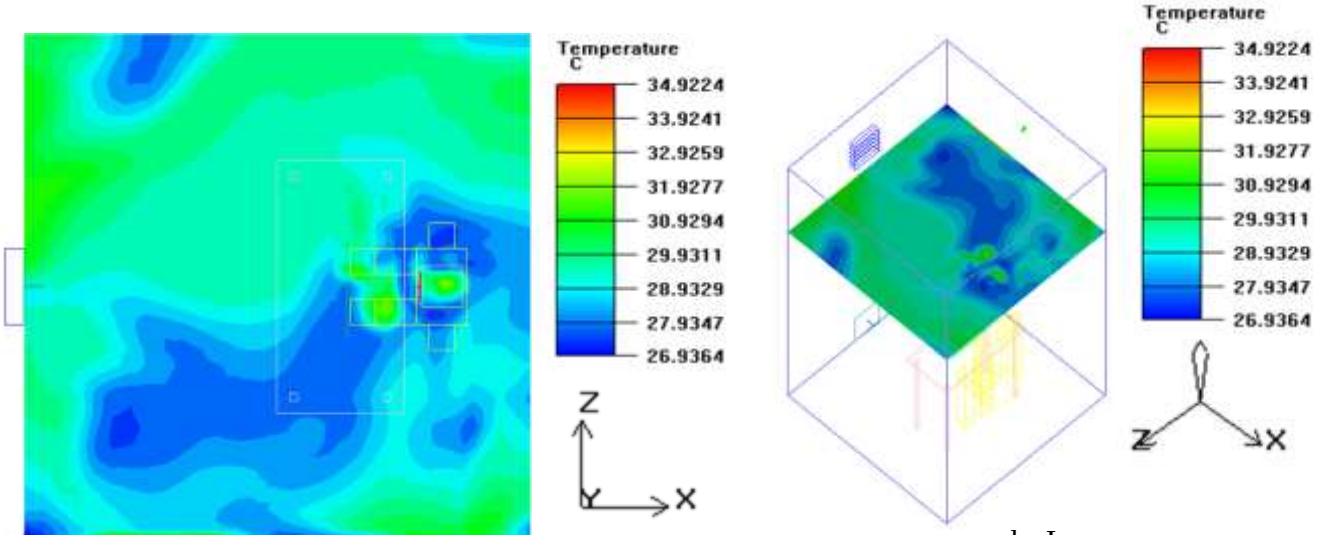

a-side b- Iso

Fig.(5.118) contours of distribution of air temperature inside the tested room for plane (P_{y2}) at Y=1.8 m at 21-July at 11:30 AM.

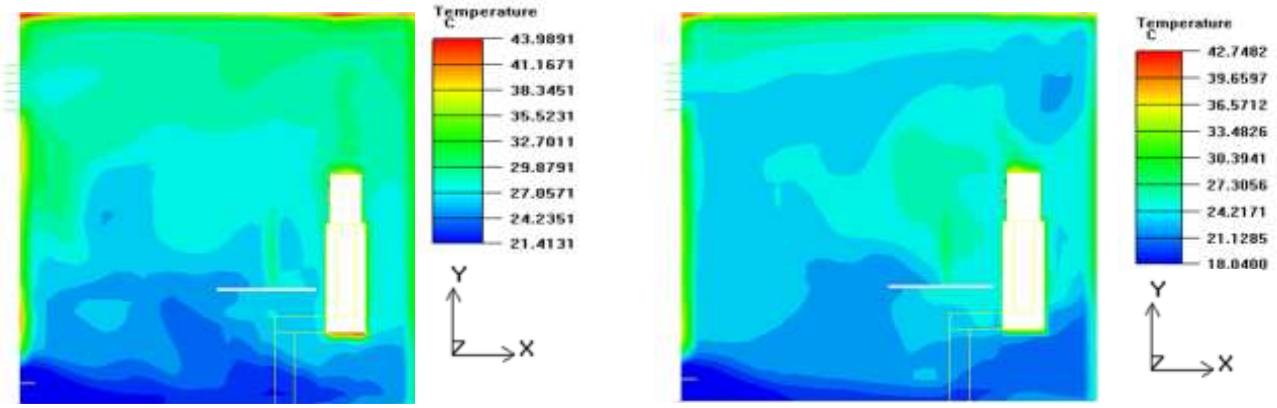

a-X=40% b- X=50%

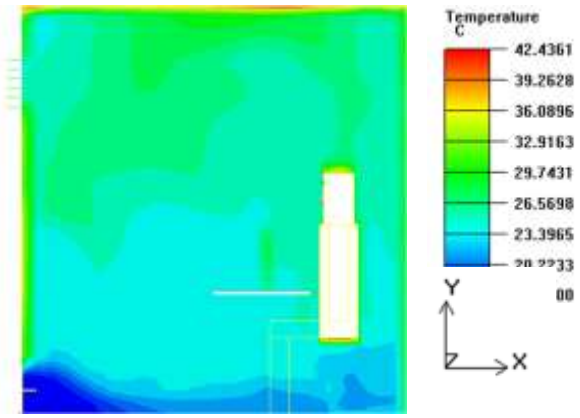

c-X=60%

Fig.(5.119) contours of temperature distribution inside the tested room for the plane (P_z) for 21-July at 12:00 at the three acetone concentrations.

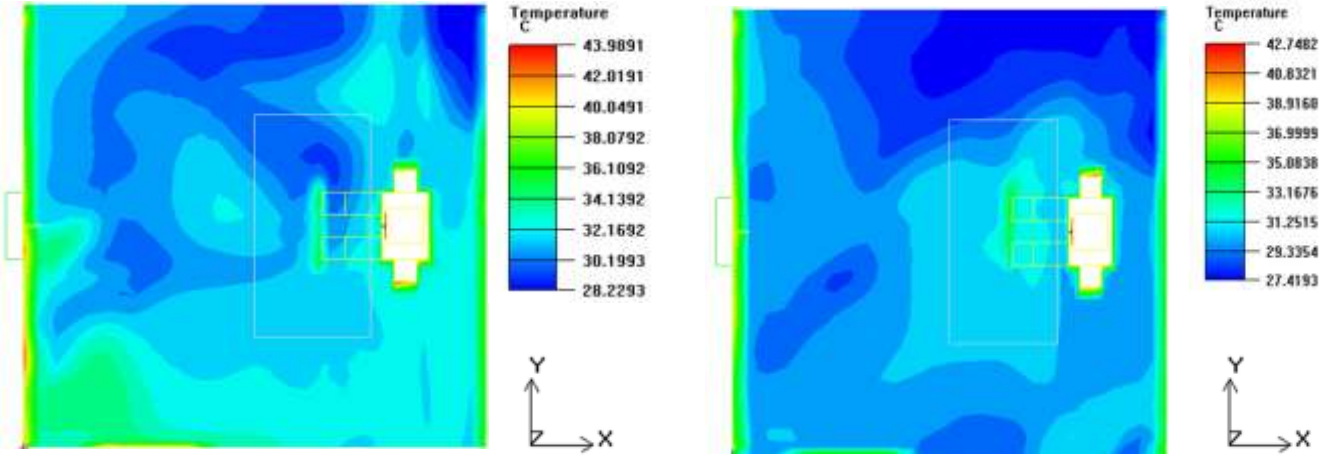

a-X=40% b- X=50%

Fig.(5.120) contours of temperature distribution inside the tested room for plane (P_{y1}) for 21-July at 12:00 at two acetone concentrations.

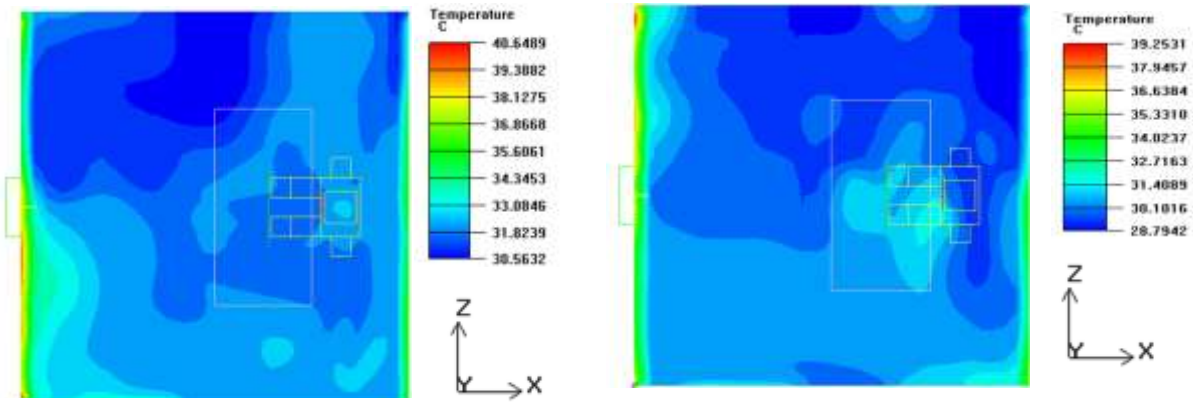

a-X=40% b- X=50%

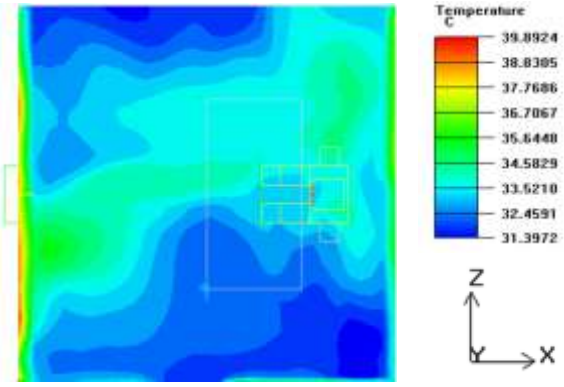

c-X=60%

Fig.(5.121) contours of temperature distribution inside the tested room for plane (P_{y2}) for 21-July at 12:00 at the three acetone concentrations.

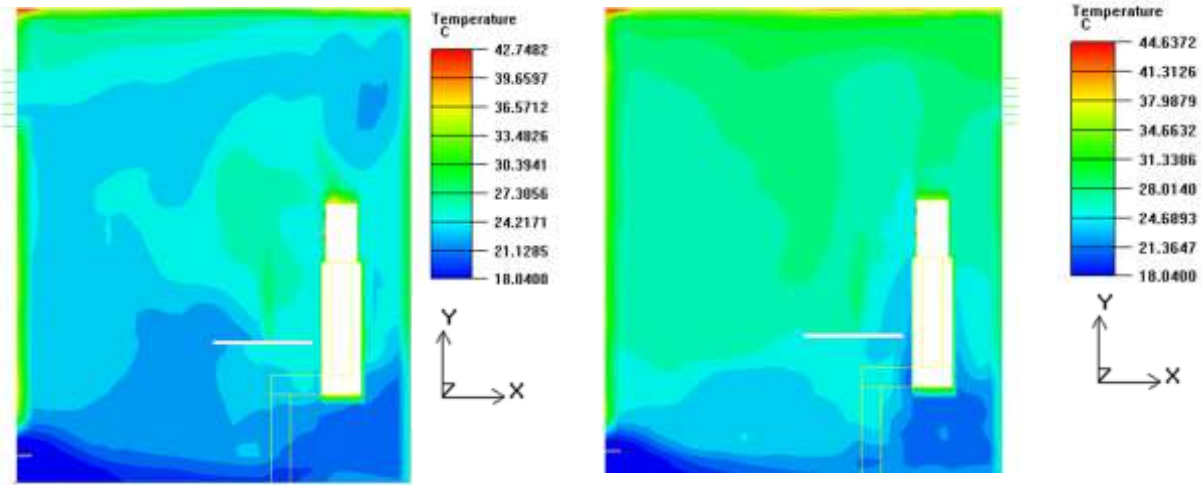

a-Same Side b- Opposite Side

Fig.(5.122) contours of temperature distribution inside the tested room for plane (P_z) for 21-July at 12:00 for different locations of air exit.

5.2.2.4 Velocity distribution

Fig.(5.123) shows the velocity contours of air inside the cooled room for two different mean velocities of supplied air (V=0.3 m/s and V=0.25 m/s) using displacement ventilation (DV) at (21-July) at (12:00) for plane (P_z). It is noted that the maximum velocity of air occurs at the exit where the area less than the inlet area and at the top of the computer and person due to natural convection, where the temperature is higher therefore, there will be vortices due to density deference, so the velocity will increase due to vortices formation with values of (0.4631 and 0.4189 m/s) for the two cases respectively.

Fig.(5.124) explains the contours of velocity of air inside the tested room for two different mean velocities of supplied air to room which are (V=0.3 m/s and V=0.25 m/s) at (21-July) at (12:00) for plane (P_{y1}). It can be noted that the maximum velocity for both cases occurs at the computer and person head with values of (0.448 and 0.384 m/s) respectively as discussed in Fig. (5.123).

Fig. (5.125) explains the contours of velocity of air inside the tested room for two different mean velocities of supplied air to room that are (V=0.3 m/s and V=0.25 m/s) for (21-July) at (12:00) for plane (P_{y2}). The maximum velocity for both cases occurs at the computer and person head as discussed previously with values of (0.54 and 0.4372 m/s) respectively.

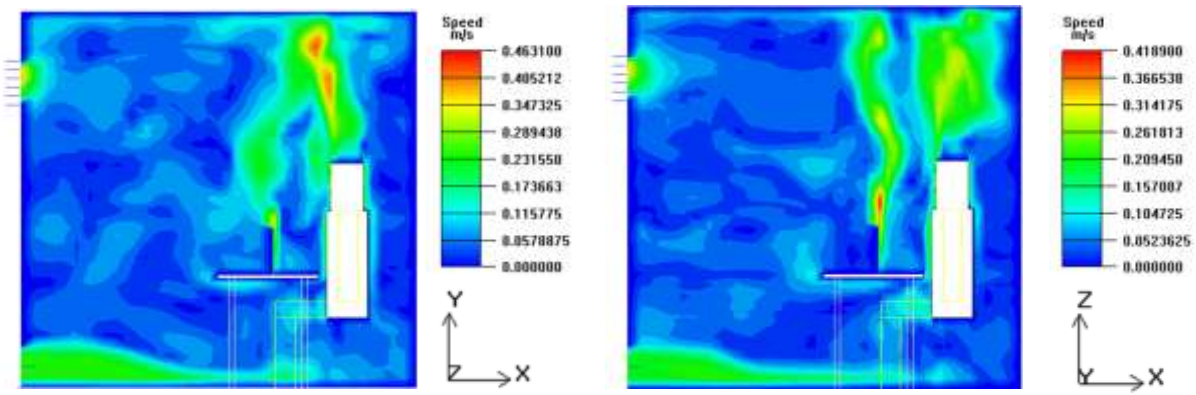

a-V=0.3 m/s b-V=0.25 m/s

Fig.(5.123) contours of air velocity inside the tested room for plane (P_z) for 21-July at 12:00.

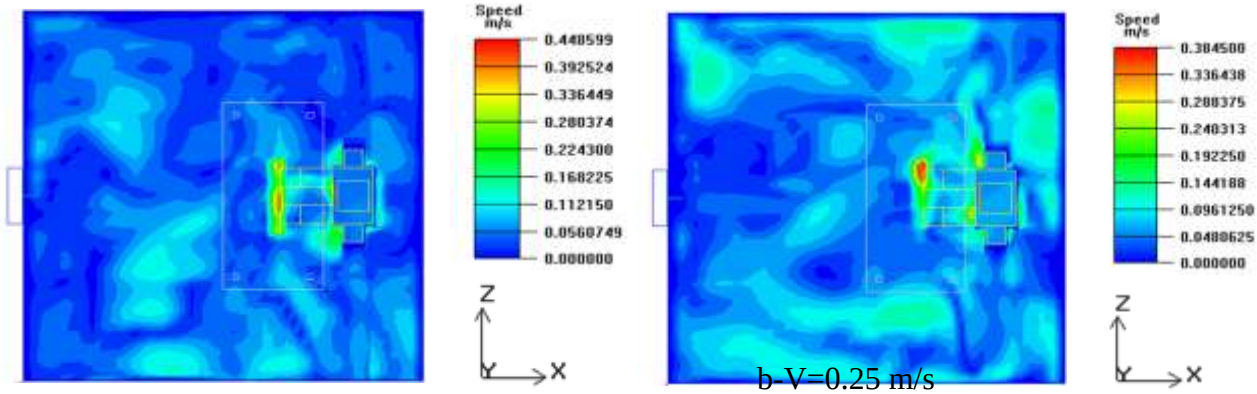

a-V=0.3 m/s b-V=0.25 m/s

Fig.(5.124) contours of air velocity inside the tested room for plane (P_{y1}) for 21-July at 12:00.

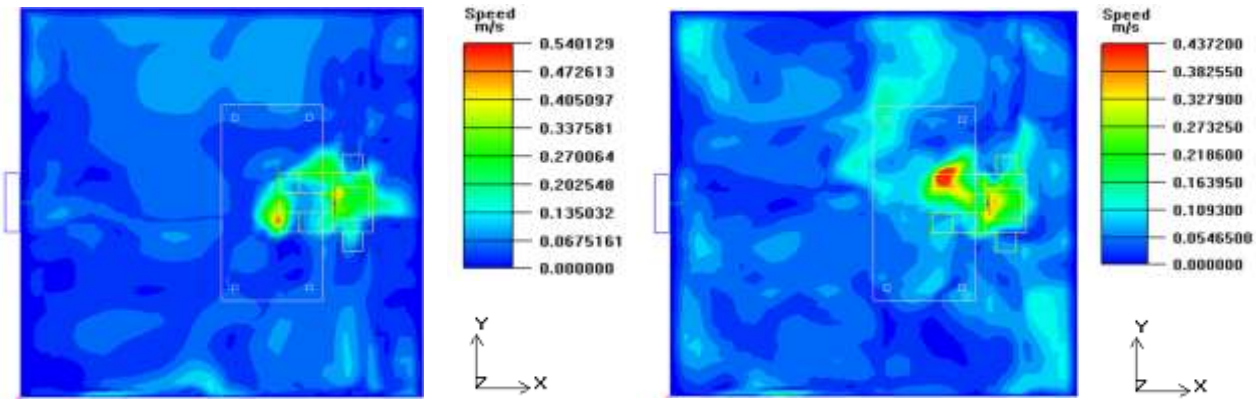

a-V=0.3 m/s b-V=0.25 m/s

Fig.(5.125) contours of air velocity inside the tested room for plane (P_{y2}) for 21-July at 12:00.

5.2.2.5 Mean age of air distribution

Fig.(5.126-5.127) explain the variation of mean age of air with height at (21st of May, June, July and August) at time (12:00) for the first and second poles respectively. It can be noted that mean age of air increases with height due to the long distance from the air supply where many dead zones will be formed. Therefore, little air reaches it and therefore, the air will not change for long time in these zones. When air is cooled, its density will be increased therefore it will become heavy. The heavy air takes more time than hot air to reach the same zone, so its mean age will be higher than the hot air. Where the maximum mean age of air is (503 s) at height of (1.1 m) for (21st July) for first pole which has the minimum temperature of supplied air, while for second pole the maximum mean age of air at height of (2.5 m) with a value of (549 s). The value of mean age at second pole greater than first pole because the first pole is located closer to diffuser and hence shorter travel distance. The minimum mean age of air is (120.5 s) at floor level for (21st of May) for first pole and (274 s) at floor level for (21st of June). Moreover, it is noted that the gradient in air mean age is very large at 0.5 m height from the floor level because the higher effect of cooling at this level after that the effect of cooling decreases and so the mean age after that approximately constant.

Fig.(5.128) shows the contours of mean age of air inside the tested room for plane (P_z) at (Z=1 m) for (21-July) at (12:00) at acetone concentrations of (X=40%, 50% and 60%). It can be noted that the mean age of air increases with height due to the longer distance from the diffuser and the air needs longer time to reach it. The maximum mean age is at the higher corner opposite to the diffuser with maximum values of (371.3 s), (381 s) and (406.3 s) for the three concentrations respectively. The mean age increases with concentration increase, where the increase of

concentration reduces the temperature of supplied air and its density will increase so it will take more time to reach the space and so the mean age of air will increase. The preferred concentration gives less mean age of air and supplies temperature close to (20 ℃).

Fig.(5.129) shows the contours of distribution of mean age of air inside the cooled room for plane (P_z) at (Z=1 m) for (21-July) at (12:00) for two air exit locations. At the first case, the exit at the same side of diffuser, while at the second case, the air exits at the opposite side of the diffuser position. The mean age of air increases gradually for all directions. It can be noted that the maximum mean age of air for the first case less than the other case because there will be a smaller dead zones, where the air moves with a semi-circular path to reach exit. However, for the second case, the air enters from the diffuser and goes up directly to the exit and so the air path is shorter and the air does not pass through most room zones. Therefore, there will be larger dead zones so the mean age of air will be higher. The maximum mean ages of air are (381 and 449 s) for the two cases respectively.

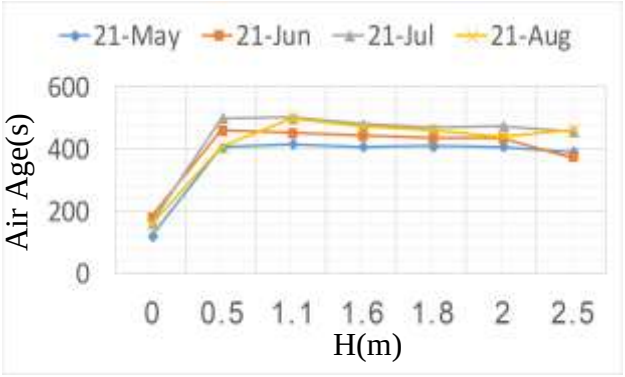

Fig.(5.126) variation of mean age of air with height at 21st of May, June, July and August at time 12:00 for pole 1.

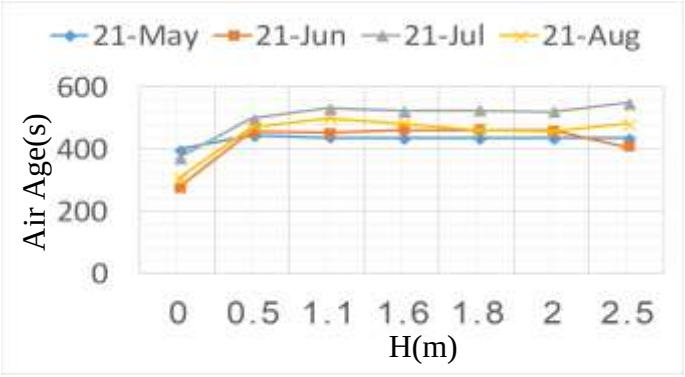

Fig.(5.127) variation of mean age of air with height at 21st of May, June, July and August at time 12:00 for pole 2.

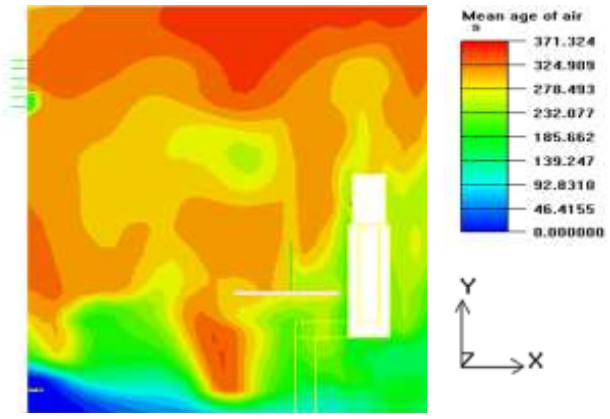

a-X=40%

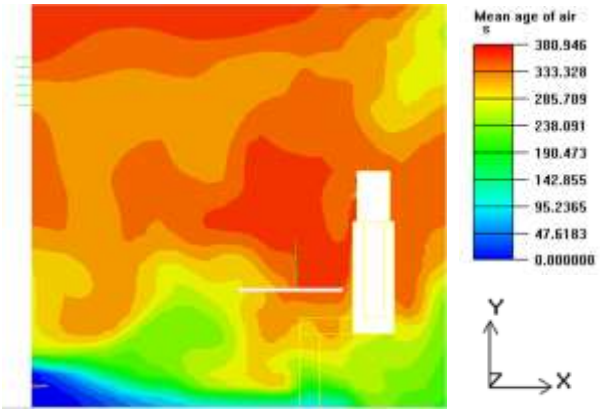

b- X=50%

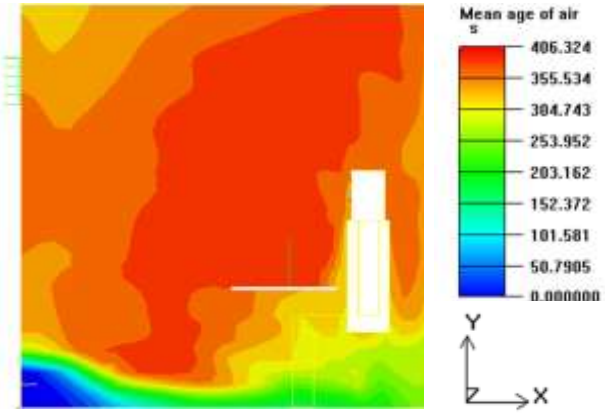

c-X=60%

Fig.(5.128) contours of mean age of air inside the tested room for plane (P_z) for 21-July at 12:00.

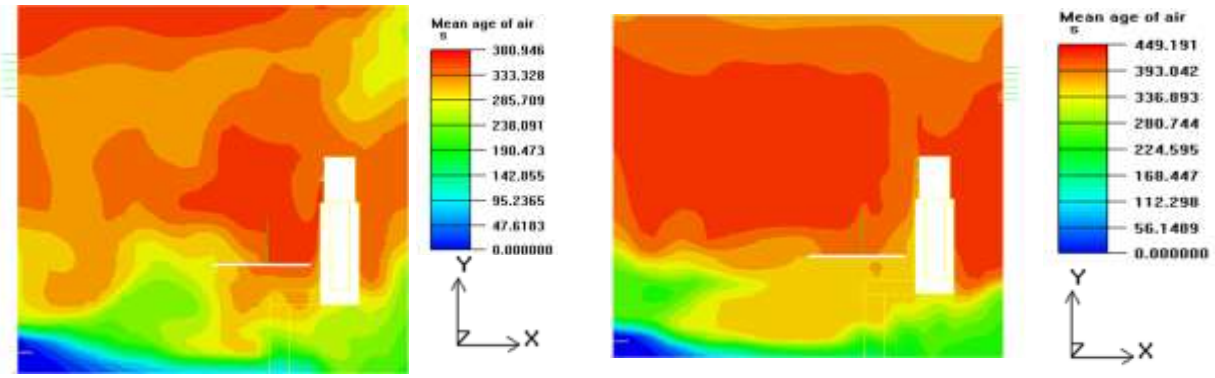

a- Same Side b- Opposite Side

Fig.(5.129) contours of mean age of air inside the tested room for plane (P_z) for 21-July at 12:00 for different location of air exit.

5.2.2.6 Predicted percentage dissatisfied (PPD) and predicted mean vote (PMV) distribution

The maximum value of (PPD) is (100) far from comfortable zone for heating and cooling and decreases when the space approaches the comfortable zone until reaches the minimum value of (5) at the comfortable zone, while (PMV) has seven levels. (+3 is hot, +2 is warm, +1 is slightly warm, 0 is the comfortable zone, -1 is slightly cool, -2 is cool and -3 is cold). The accepted value for displacement ventilation of (PPD) is less than (10), while for (PMV) is between (-0.3 and +0.3), [127].

Figs.(5.130-5.131) present the variation of the (PPD) with height for (21^{st} of May, June, July and August) at time (12:00 PM) for first and second poles. It can be noted that (PPD) decreases with height due to increase the air temperature and approach the comfortable level at about 0.5 m height. The temperature near floor level is low and the zone is cold therefore, it is not comfortable. The minimum value of PPD is (7) at (21-June) at height (2.5 m) for first pole and (PPD) value of (4) at (21-May), while the maximum values are at (21^{st} of July) at height of (2.5 m) with (38.32 and

41.62) values for the two poles respectively where the area is hot and not comfortable.

Figs.(5.132-5.133) shows the variation of (PMV) with height at (21st of May, June, July and August) at time (12:00) for first and second poles. It can be noted that (PMV) near the floor level is low which means that the zone is cold and not comfortable. The (PMV) increases with height due to increase the air temperature and approach from the comfortable zone, where the minimum value of (PMV) is (-1.252) at (21-June) at floor level for first pole and a value of (-1.2) at (21st of May) where the space is cold. The maximum values are (1.43 and 1.62) at (21st of July) for the two poles respectively, this means that (21st July) hotter than other days.

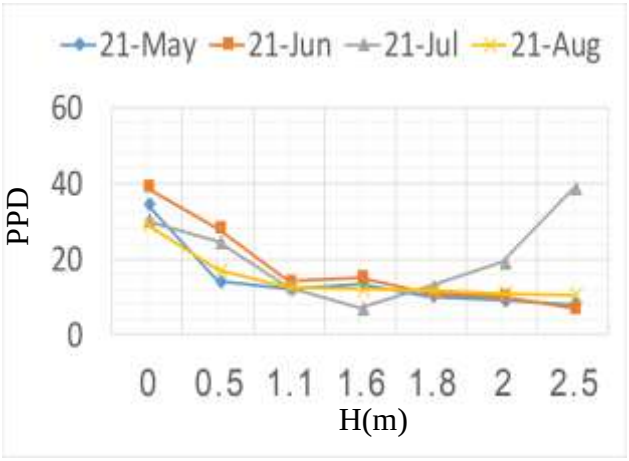

Fig.(5.130) variation of PPD with height at 21st of May, June, July and August at time 12:00 for pole 1.

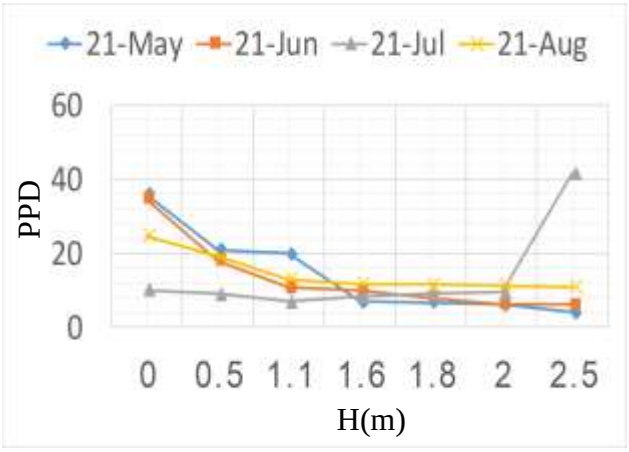

Fig.(5.131) variation of PPD with height at 21st of May, June, July and August at time 12:00 for pole 2.

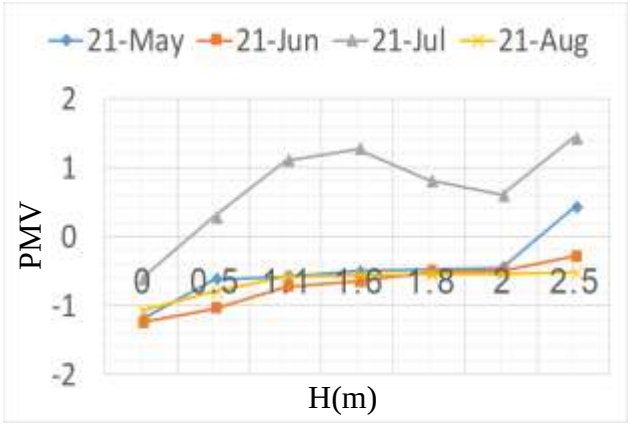

Fig.(5.132) variation of PMV with height at 21st of May, June, July and August at time 12:00 for pole 1.

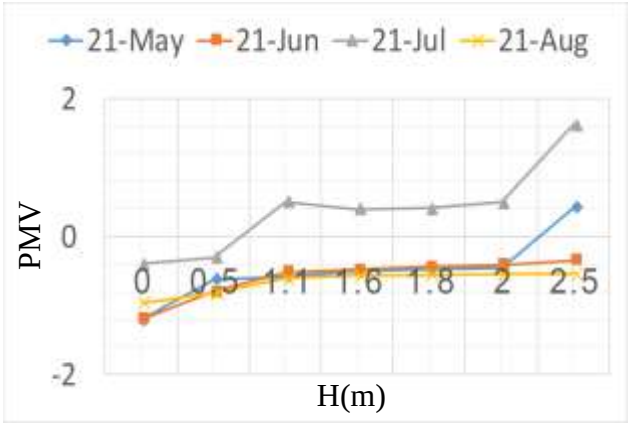

Fig.(5.133) variation of PMV with height at 21st of May, June, July and August at time 12:00 for pole 2.

5.3 Comparison Between the Experimental and Theoretical Results

The comparison between the experimental and theoretical results has been done by considering the experimental results of (7-July) with that of the theoretical results for same day, at (1:00 PM). The theoretical results of the cooled room included both adiabatic and non-adiabatic cases. The non-adiabatic case is more realistic. A balance has been considered between the heat gain as a function of mean room temperature with the obtained cooling effect at (01:00 PM) and evaluating the mean room temperature from the heat balance as shown in appendix (C).

The evaluated mean room temperature from the heat balance based on non-adiabatic assumption is about (37.48 ℃) which is close with the experimental results for this day. The temperature of the supplied air has been calculated from the mean room temperature with a value of (24.91 ℃) which is convergent with the temperature of supplied air obtained from the experimental results that has a value of (27.5 ℃) at (01:00 PM), while the temperature of supplied air for the adiabatic case is (17.27 ℃). The obtained temperature of supplied air (24.91℃) has been used in the AirPak software to obtain the temperature distribution in the room based on non-adiabatic assumption.

Fig.(5.134) shows a comparison between the experimental and theoretical collector receiver temperature. It is seen that the experimental and theoretical receiver temperatures converge with values of (80.1 ℃ and 82.12 ℃) respectively. The difference between the experimental and theoretical results comes from several reasons. First is the assumption that the storage tank and generator are insulated, while the second reason is the

constant error existed in the measuring thermocouples. The third reason is the round error and error in the theoretical results.

Fig.(5.135) explains the experimental and theoretical generator temperature. It is noticed that the experimental and theoretical generator temperatures converge with values of (71 ℃ and 76.47 ℃) respectively. The difference between the experimental and theoretical results is due to the above mentioned errors.

Fig.(5.136) explains the experimental and theoretical temperature difference across the evaporator. It is noted that the experimental and theoretical temperature differences converge with values of (14.1 ℃ and 15.53 ℃) respectively.

Fig.(5.137) displays the experimental and theoretical evaporator cooling effect. It is seen that the experimental and theoretical cooling effect values are (356 W and 413 W) respectively. The difference between values due to the errors in measuring devices and the errors in the theoretical work comes from neglecting the terms with small values and the higher order derivatives.

Fig.(5.138) explains the experimental and theoretical overall efficiency. It is noted that the experimental and theoretical systematic efficiency converge with values of (21.74 and 22.18%) respectively.

Fig.(5.139) shows the experimental, non-adiabatic theoretical and adiabatic theoretical temperature of supplied air to the tested room. It is noted that the experimental and non-adiabatic theoretical temperatures of supplied air converge with values of (24.91 ℃) and (27.5 ℃) respectively, while for the adiabatic theoretical case it is (17.27 ℃). The non-adiabatic case results are closer to the experimental results which is better assumption than the adiabatic. The difference between the experimental

and adiabatic theoretical results due to the neglected heat transfer through walls that increases the inside room temperature which is recirculated to the evaporator, so the supplied temperature will be higher.

Fig.(5.140) displays a comparison between the experimental, non-adiabatic theoretical and adiabatic theoretical local temperatures of the tested room at (pole 2). It is seen that there is a difference between the experimental and theoretical non-adiabatic local temperatures due to the reasons mentioned above especially at floor level where the experimental reading is (37.6 ℃) while the theoretical reading is (33.26 ℃). But at the height of (1.6 m) the error is small where the experimental result is 38.6℃, while the theoretical result is (37.9 ℃). Moreover, the adiabatic theoretical results are far from other cases and is considered unrealistic, because the higher heat transfer through the cooled room walls.

Table (5.1) shows the experimental, theoretical local temperatures for the non-adiabatic case and the error value for second pole at 01:00 PM for 7-July. The maximum value of error is 10.83% at floor level. The error is explained in another way in Appendix-D.

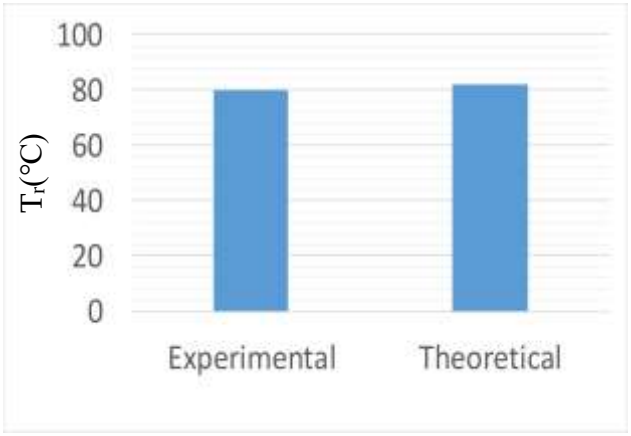

Fig.(5.134) experimental and theoretical collector receiver temperature for 7-July at 01:00 PM.

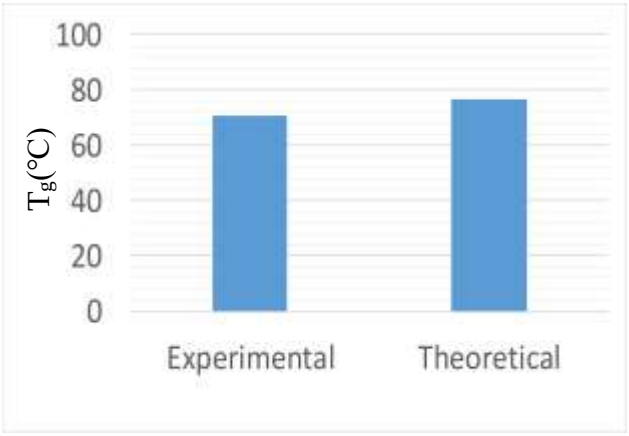

Fig.(5.135) experimental and theoretical generator temperature for 7-July at 01:00 PM.

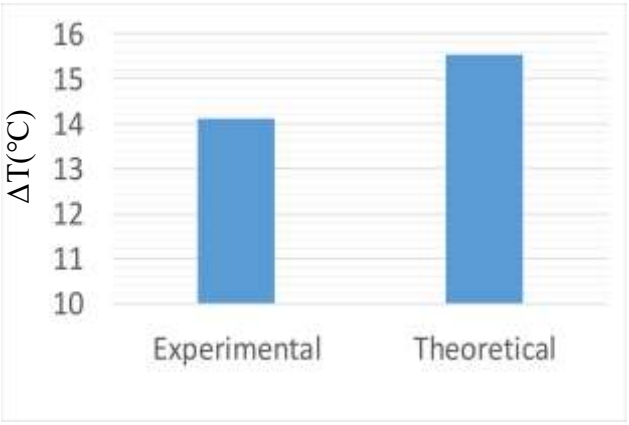

Fig.(5.136) experimental and theoretical temperature difference at the evaporator for 7-July at 01:00 PM.

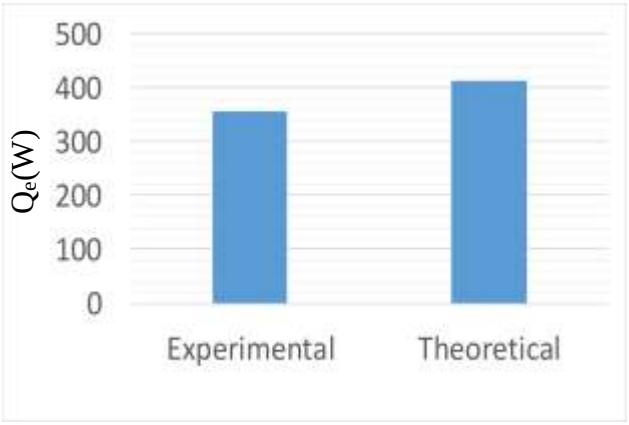

Fig.(5.137) experimental and theoretical evaporator cooling effect for 7-July at 01:00 PM.

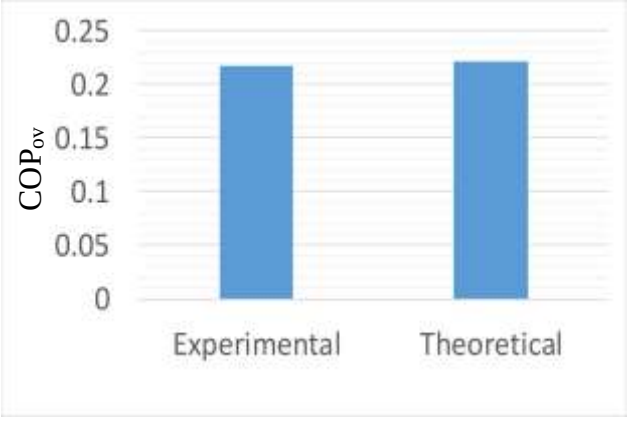

Fig.(5.138) experimental and theoretical overall coefficient of performance for 7-July at 01:00 PM.

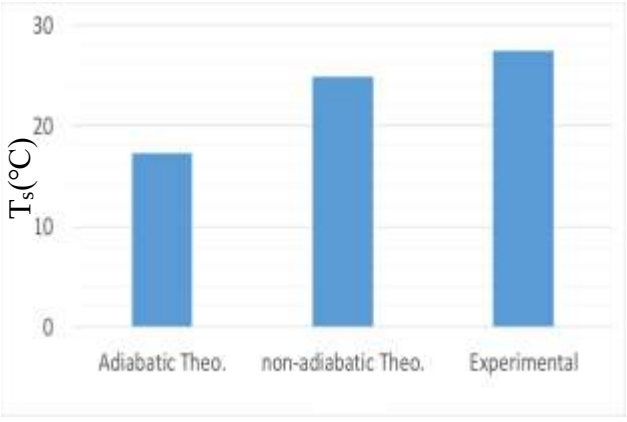

Fig.(5.139) experimental, non-adiabatic theoretical and adiabatic theoretical temperature of supplied air to the tested room.

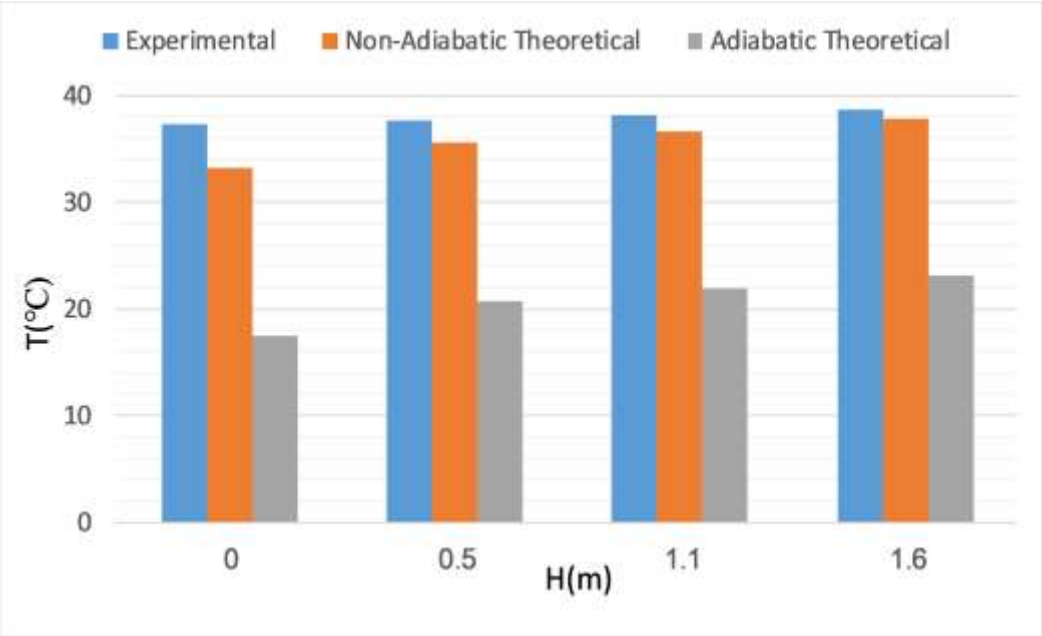

Fig.(5.140) variation of experimental, non-adiabatic theoretical and adiabatic theoretical local temperature of the tested room with height at pole 2 for 7-July at 01:00 PM.

Table (5.1) shows the experimental and theoretical local temperatures at the non-adiabatic analysis for second pole at 01:00 PM for 7-July.

H(m)	T_{ex}(°C)	T_{th}(°C)	Error(%)
0	37.3	33.26	10.8311
0.5	37.7	35.6	5.570292
1.1	38.2	36.7	3.926702
1.6	38.6	37.9	1.813472

CHAPTER SIX

CONCLUSIONS AND SUGGESTIONS FOR FUTURE WORKS

CHAPTER SIX

CONCLUSIONS AND SUGGESTIONS FOR FUTURE WORKS

6.1 Conclusions

After presenting and discussing the results of the present work, the following conclusions may be drawn:

1- The system operates efficiently at generator temperature between 60 ℃ and 85℃.
2- The increase in acetone concentration increases the acetone vapor at the generator and so increases COP and the obtained cooling effect.
3- The increase in condenser temperature decreases COP and the cooling effect because it decreases the condensation rate of the refrigerant.
4- The increase in the evaporator temperature increases COP and the obtained cooling effect.
5- The increase in generator temperature increases COP and the obtained cooling effect.
6- The maximum temperature difference at the evaporator is at 7-July with value of 14.1℃ at acetone concentration of 60%.
7- The maximum experimental cooling effect obtained is 365 W at 7-July at 01:00 PM and acetone concentration of 60%.
8- The obtained maximum overall efficiency` at 01:00 PM for experimental work is 0.2174 while the theoretical value is 0.2218.
9- The maximum exergy destruction for the system occurs at the solution expansion valve with a value of 762 W while the minimum

value occurs at the acetone vapor expansion valve with value of 36 W for 21-July at 2:30 PM.

10- The maximum exergy destruction for the main components is at the generator of 732 W value, while the minimum value is at the evaporator with a value of 146 W at 2:30 PM.

11- The maximum exergetic efficiency of the collector is 0.4416.

12- The maximum cooling effect per liter of acetone occurs at 60% acetone concentration with value of 25.62 $W/l_{acetone}$.

13-The value of ADPI at the case of the diffuser and exit location at the same side is better than its value at the case when they are at opposite location.

14-The maximum thermal ventilation effectiveness(ε) is 1.402 at the design room temperature that is 20 ℃.

15-The theoretical temperature distribution based on adiabatic assumption shows that the temperature decreases with time but this is not obtained experimentally due to the heat gain from outside across the insulation. It is noted that the temperature increases with time.

16-The maximum room mean age of air at the case of the diffuser and exit at the same side is less than at the case when they are at opposite locations.

17-The mean age of air increases with solar radiation and acetone concentration.

18-The non-adiabatic assumption gives more acceptable results than the adiabatic assumption. It is more realistic.

6.2 Suggestions for Future Works

The following recommendations are suggested to the future works:

1- Using the nanoparticles with the (PTSC) collector to increase heat absorption by the collector fluid.
2- Testing solar absorption cooling systems with double and triple effect using other energy sources in addition to the solar energy like hot gasses and hot oils.
3- Testing solar absorption systems with other operating pairs (refrigerants and absorbents) like:
   a- H_2O- LiCl, $LiClO_3$, $ZnCl_2$ and $CaCl_2$.
   b- Ethanol- LiBr, LiCl, LiI, $ZnBr_2$ and $ZnCl_2$.
   c- Methanol- LiCl, LiI and $ZnCl_2$.
4- Setup a tracking system to increase the received solar radiation and increase the obtained cooling load.
5- Using hybrid cooling by adding an air conditioner with low capacity for obtaining the required cooling load because the cooling effect of solar absorption is small and cannot investigate the required cooling load.
6- Using a solar system with a greater capacity to investigate the required cooling load for the cooled space.

REFERENCES

References

[1] Hawlader, M. N. A. & Brinkworth, B. "An analysis of the non-convecting solar pond". *Solar Energy*, 27(3)**,** 195-204, 1981.

[2] "Iraq-Climate. Iraq Index". Available at: http://data.mongabay.com/history/iraq/iraq-climate.html, (Accessed: 27 July 2015), 1988.

[3] "Surface meteorology and solar energy" Available at: https://eosweb.larc.nasa.gov/sse/ (Accessed: 26 October 2016), 2014.

[4] Malek M. S.," Designing an adsorption based air condition system for family housed in iraq" , Thesis. University of Szent Istvan, Hungary, 2016.

[5] Faisal S. H. ," Performance study of LiBr-Water pump less absorption refrigeration system ", PhD. Thesis. University of Basra, 2011.

[6] Kalogirou S., "The potential of solar industrial process heat applications". Appl Energy, 76, 2003.

[7] Calise F. and Vanoli L., "Parabolic trough photovoltaic/thermal collectors: design and simulation model", Energies, 5 (10), pp.4186–4208, 2012.

[8] Kalogirou A. S., "Solar thermal collectors and applications, progress in energy and combustion science", 30, pp. 231–295, 2004.

[9] Balghouthi, M., Chahbani, M., & Guizani, A. ,"Solar Powered air conditioning as a solution to reduce environmental pollution in Tunisia". *Desalination* , pp. 105-110, 2005.

[10] Henning, H. M. , "Solar assisted air conditioning of buildings – an overview", *Applied Thermal Engineering* , pp. 1734-1749, 2007.

[11] Abass K. I. , " Is Iraq Ready to Use Solar Energy Applications: A Review", International Journal of Engineering Science Invention, 6(10), pp. 27-42, 2017.

References

[12] Fulloy L., "Study of a Solar Cooling Plant using Absorption Chiller", Institute National des Sciences Appliquées de Lyon (INSA de Lyon), 2010.

[13] Nicol F. and Wilson M., "An overview of the European Standard EN15251", London Metropolitan University, UK. Proceedings of Conference: Adapting to Change: New Thinking on Comfort Cumberland Lodge, Windsor, UK, 9-11 April 2010.

[14] Tarish H. *A. S.*, "Study the Indoor Air Quality by using Mixing and Personal Ventilation Systems in Iraq", M. Sc. Thesis, College of Engineering, University of Babylon, 2021.

[15] Xu Y., "Modeling and Evaluation of Personal Displacement Ventilation System for Improving Indoor Air Quality", Master of Science, University of Miami, Coral Gables, Florida, 2007.

[16] Yuan X, Chen Q and LR. G.,"A critical review of displacement ventilation", ASHRAE Transactions, 104(1A), 1998.

[17] Riffat S, Zhao X and Doherty P., "Review of research into and application of chilled ceilings and displacement ventilation systems in Europe", International Journal of Energy Research, 28:257-86, 2004.

[18] Livchak A. and Nall D., "Displacement ventilation–application for hot and humid climate", Proceedings of Clima, 2000.

[19] Yang, X. and Srebric, J., CLIMA 2000 Conference, Napoli, Italy, September 15-18, 2001.

[20] Özdamar M. and Umaroğullari F., "Thermal Comfort and Indoor Air Quality", International Journal of Scientific Research and Innovative Technology, 5 (3), pp. 90-109, 2018.

[21] Atmaca, İ. and Yiğit, A., "Isıl Konfor ile İlgili Mevcut Standartlar ve Konfor Parametrelerinin Çeşitli Modeller ile İncelenmesi", IX. Ulusal Tesisat Mühendisliği Kongresi, İzmir, pp. 543-555, 2009.

[22] Pijush K, Ira M and David R., "Fluid mechanics", *Elsevier*,5, 2012.

References

[23] ASHRAE. Standard 55-2004, "Thermal environmental conditions for human occupancy", Atlanta, GA: American Society for heating, refrigerating and air conditioning engineers, 2004.

[24] Boonnasa and Namprakai, P., "The chilled water storage analysis for a university building cooling system", Applied Thermal Engineering, 30, pp.1396-1408, 2010.

[25] Haroun. A.K. Shahad, and Hamzah D. A., "Investigation on an Intermittent Absorption Refrigeration Prototype Powered by Solar Irradiation", Al-Qadisiyah Journal for Engineering Sciences, 8(4), pp. 513-525, 2015.

[26] Mezher, W.M., Awadh ,A.A. and Mohammed, A.A., "Solar Powered Air-Conditioning Using Absorption Refrigeration Technique", Journal of Engineering, 20(10), pp. 47-59,2014.

[27] Widiharto A. , Pamuji,D.S., Laila, A.N., Salis, F.R., Zharif,L., Zakariy, Fikriyadi,A., Falaq,A.M. and Pranadi,A.D., "System Design of Solar Absorption Cooling: A Case Study in Building of Engineering", Physics Department UGM, New, Renewable Energy and Energy Conservation Conference and Exhibition,The 3rd Indonesia EBTKE-ConEx, 2014 , 2, pp. 22-29, 2015.

[28] Ahmad S. A., Muneer U., Saifullah, M. J. and Abdullah H. S., "Design and Fabrication of Solar Powered Hydrogen Ammonia Absorption Refrigeration System", Pakistan European Journal of Advances in Engineering and Technology, 3(11), pp. 37-41, 2016.

[29] Osman E. A., and Abdalla K. N., "Design and Construction of an Absorption Cooling System Driven by Solar Energy", Department of Mechanical Engineering, Faculty of Engineering-University of Khartoum, Scientific Research and Innovation for Sustainable Development in Africa 20-23 February 2016**,** Friendship Hall, Khartoum, Sudan, 2016.

References

[30] Gandhi, A. and Arakerimath R.R., " Solar Vapour Absorption Cooling System Using parabolic dish Collector", Journal of Mechanical and Civil Engineering, 13 (2), pp 09-13, 2016.

[31] Bux S. & Ansari E. A. , "Performance Analysis Vapor Absorption Refrigeration Chiller Run by Solar Thermal Energy", International Journal of Advanced Engineering Research and Science, 4(10), pp.89-96, 2017.

[32] Chen J. F., Dai Y. J. and Wang R. Z.," Experimental and analytical study on an air-cooled single effect LiBr-H2O absorption chiller driven by evacuated glass tube solar collector for cooling application in residential buildings", Solar Energy, 151,110–118, 2017.

[33] Reddy G. C. M., Rao G. A., Prasad V.V.S. H. and Vardhan M. V., " Design of Concentrated Parabolic Dish Collector for Vapor Absorption Refrigeration System", International Journal of Civil Engineering and Technology (IJCIET) , 8(7), pp. 714-724, 2017.

[34] Huang L. , Zheng R. and Piontek U.," Installation and Operation of a Solar Cooling and Heating System Incorporated with Air-Source Heat Pumps", Energies, 12,pp. 1-17, 2019.

[35] Rahman S., Said Z. and Issa S., "Performance evaluation and life cycle analysis of new solar thermal absorption air conditioning system", The 6th International Conference on Power and Energy Systems Engineering, CPESE 2019, 20–23 September 2019, Okinawa, Japan, 6, pp. 673–679, 2020.

[36] Grosu L., " Energy and exergy analyses of a solar-driven absorption cooling system", Mécanique et Electromagnétisme, Université Paris Ouest Nanterre La Défense, International Journal of Exergy, 15(3), pp. 308-327, 2014.

[37] Fakhraldin S. M., "Design of a solar cooling system for Iraq climate, PhD dissertation, Mechanical Engineering, School of Marine Science and Engineering", Plymouth University, July 2016.

References

[38] Cascetta, F., Cirillo, L., Corte, A. D. and Nardini, S., "Comparison between different solar cooling thermally driven system solutions for an office building in Mediterranean Area", International Journal of Heat and Technology, 35(1), pp. 130-138, 2017.

[39] Shirazi A., Feasibility of Solar-Assisted Absorption Chillers for Air-Conditioning Applications, Doctoral of philosophy, School of Mechanical and Manufacturing Engineering, University of New South Wales, July 2017.

[40] Hui X., Hao Q., Yan G., and Wang Q., "The Collector Matching Analysis of Solar Cooling System Based on Three Kinds of Working Medium", pp. 19- 22, 2017.

[41] Hussein, H.A., "Modeling and Simulation of an Absorption Solar Cooling System Under Iraqi Weather Conditions", Engineering and Technology Journal, 35(4), pp.356-364, 2017.

[42] Narayanan M.," Techno-Economic Analysis of Solar Absorption Cooling for Commercial Buildings in India", International Journal of Renewable Energy Development, 6 (3), pp. 253-262, 2017.

[43] Petela K., Manfrida G., and Szlek A., "*Advantages of variable driving temperature in solar absorption chiller*", pp 1-30, 2017.

[44] Bellos E. , and Tzivanidis C.,"Energetic and financial sustainability of solar cooling systems with 1 single effect absorption chiller in various climates". Applied Thermal Engineering, 2017.

[45] Xu, Z.Y. and Wang, R.Z., "Comparison of CPC driven solar absorption cooling systems with single, double and variable effect absorption chillers", Solar Energy, 158, 511–519, 2017.

[46] T. Adibi," Evaluation of using solar ammonia absorption cooling system for major cities of the Middle East", International Journal of Heat and Technology, 36(3), pp.840-846,2018, Iran.

References

[47] Jing Y., Li Z. , Liu L. and Lu S., "Exergoeconomic Assessment of Solar Absorption and Absorption–Compression Hybrid Refrigeration in Building Cooling", Entropy, 20, 130, pp. 1-22, 2018.

[48] Dwivedi, A. and Mishra, R. S. , "Study of Performance Enhancement of Half Effect Vapor Absorption System Using Loop Heat Pipes", International Journal for Research in Applied Science and Engineering Technology, 6(1), pp.3260-3172, 2018.

[49] Kumar V., Pandya B., Patel J. and Matawala V.," Vapour Absorption System Powered by Different Solar Collectors Types: Cooling Performance, Optimization and Economic Comparison", Science and Technology for the Built Environment, pp. 1-47, 2018.

[50] Arabkoohsar A. and Andresen G. B., " A smart combination of a solar assisted absorption chiller and a power productive gas expansion unit for cogeneration of power and cooling", Renewable Energy, 115, pp.489-500, 2018.

[51] Uçkan, I. and Yousif, A. A., "Simulation of a solar absorption cooling system in Dohuk city of the Northern Iraq", Energy Sources, Part A: Recovery, Utilization, and Environmental Effects, pp.1-17, 2019.

[52] Pandya B., Modi N., Upadhyai R., and Patel J., "Thermodynamic performance and comparison of solar assisted double effect absorption cooling system with LiCl-H_2O and LiBr-H_2O working fluid", 2019.

[53] Abdulateef J., Ali S.D. and Mahdi M. S., "Thermodynamic Analysis of Solar Absorption Cooling System, Journal of Advanced Research in Fluid Mechanics and Thermal Sciences", Iraq, 60(2), pp. 233-246, 2019.

[54] Nandi P., Mahalingesh B., Mariappan V., "Design and Analysis of Solar Vapour Absorption Cooling System, Journal of Emerging Technologies and Innovative Research", India, 6(5),pp. 57-62, 2019.

References

[55] Toprak K., Ouedraogo K. E., "Effect of storage tanks on solar-powered absorption chiller cooling system performance", International Journal of Energy Research, Turkey , pp. 1-10, 2020.

[56] Abusaibaa G. Y., Al-Aasam A. B., Al-Waeli A. H A, Al-Fatlawi A. W. A., Sopian K. B., "Performance Analysis of Solar Absorption Cooling Systems in Iraq", International Journal of Renewable Energy Research, Iraq, 10(1), 2020.

[57] Al-Falahi A., Alobaid F.and Epple B., "A New Design of an Integrated Solar Absorption Cooling System Driven by an Evacuated Tube Collector: A Case Study for Baghdad", Iraq, Applied Sciences, 10, Iraq, pp. 3622 1-23, 2020.

[58] Lamine C. M. and Said Z., "Exergy and energy analysis of solar absorption cooling system in hot regions with NH_3-H_2O and NH_3-$LiNO_3$ refrigerant solutions", International Journal of Innovation and Applied Studies, Algeria, 30 (1), pp. 186-198, 2020.

[59] Chekir N., Snoussi A. and Brahim A. B., "Alternative Refrigerants for Solar Absorption Air-Conditioning", International Journal of Air-Conditioning and Refrigeration, Tunisia, 28 (1), pp. 2050001-11, 2020.

[60] Tawalbeh M., Salameh T., Albawab M. , "Al-Othman A. , M. E.Assad, A. H. Alami, "Parametric Study of a Single Effect Lithium Bromide-Water Absorption Chiller Powered by a Renewable Heat Source", Journal of Sustainable Development of Energy, Water and Environment Systems, U. A. E., 8(3), pp. 464-475, 2020.

[61] Souri K., Kashyzadeh K R, Naghdali A S and Mesbah M., "Performance of a single effect absorbing chiller lithium bromide-water coupled to a solar collector", International Conference on Engineering Systems 2020, Journal of Physics: Conference Series , Russia, 1687 (2020) 0120261-8, 2020.

References

[62] Rosiek S. and Batlles F. J., "Performance study of solar-assisted air conditioning system provided with storage tanks using artificial neural networks", International Journal of Refrigeration, 34, pp.1446-1454, 2011.

[63] Gonzalez-Gil, A., Izquierdo, M., Marcos, J. D. & Palacios, E. , "New flat-fan sheets adiabatic absorber for direct air-cooled LiBr/H_2O absorption machines: simulation, parametric study and experimental results", Applied Energy, 98, pp.162–173, 2012.

[64] Marc O., Anies G., Lucas F., and Castaing-Lasvignottes J., Assessing performance and controlling operating conditions of a solar driven absorption chiller using simplified numerical models, Solar Energy, 86, 2231-2239, 2012.

[65] Azhar, M. & Siddiqui, M. A., "Thermodynamic Analysis of a Gas Operated Triple Effect Absorption Cycle", International Journal of Innovative Research in Science, Engineering and Technology, 2(5), pp.1610-1616, 2013.

[66] Schwerdt P. and Ali A. H. H. ," German/Egyptian demonstration project on solar cooling in a hot arid climate" ,Energy Procedia, 48, pp.991 – 996, 2014.

[67] Aman, J., Ting, D.S.K. and Henshaw,P., "Residential solar air conditioning: Energy and exergy analyses of an ammonia water absorption cooling system", Applied Thermal Engineering, 62 , pp. 424-432, 2014.

[68] Sun H. Q., Xu Z.Y., Wang H. B. and Wang R. Z.," A solar/gas fired absorption system for cooling and heating in a commercial building", China, International Conference on Solar Heating and Cooling for Buildings and Industry, 2015.

[69] Zhai X., Li Y., Cheng X., and Wang R., "Experimental investigation on a solar-powered absorption radiant cooling system", International Conference on Solar Heating and Cooling for Buildings and Industry, 2015.

References

[71] Soussi, M., Balghouthi,M., Guizani ,A. & Bouden,C., "Model performance assessment and experimental analysis of a solar assisted cooling system", Solar Energy, 143, pp. 43–62, 2017.

[71] Wang J., Yan R., Wang Z., Zhang X. and Shi G., "Thermal Performance Analysis of an Absorption Cooling System Based on Parabolic Trough Solar Collectors", Energies, 11, pp. 1-17, 2018.

[72] Abdul Ameer, S. A. & Shahad, H. A. K., "Analysis of the Experimental and Theoretical Performance of the Two-dimension Concentrating Solar Collector", Indian Journal of Science and Technology, 11(12), pp.1-13, 2018.

[73] Abdul Ameer, S. A., "Experimental and Theoretical Study of Absorption Cooling System Integrated with Solar Concentrated Collector", PhD dissertation, Department of Mechanical Engineering, College of Engineering, University of Babylon, 2018.

[74] Nasruddin, N.Aisyah, M.I. Alhamid, B. B. Saha, S. Sholahudin and A. Lubis, "Solar absorption chiller performance prediction based on the selection of principal component analysis", Case Studies in Thermal Engineering, Indonesia, 13, pp. 100391 1-9,2019.

[75] Boero A. and Agyenim F., "Modeling and simulation of a small-scale solar-powered absorption cooling system in three cities with a tropical climate", International Journal of Low-Carbon Technologies, Ghana, 15, pp. 1-16, 2020.

[76] Qadeer A., Hussain S., Ali M. and Khan M., "Experimental investigations of a small-scale solar-assisted absorption cooling system", Heat Transfer, Pakistan, pp. 1-23, 2020.

[77] Huirem B. and Sahoo P. K., "Thermodynamic Modeling and Performance Optimization of a Solar-Assisted Vapor Absorption Refrigeration System (SAVARS)", International Journal of Air-Conditioning and Refrigeration, India, 28(1), pp. 2050006 1-18,2020.

References

[78] Ghyadh N. A.H., "Experimental and Theoretical Study of a Parabolic Trough Solar Absorption Cooling System with Continuous Flow Mode", Ph. D dissertation, Department of Mechanical Engineering, College of Engineering, University of Basrah, 2020.

[79] Shbeeb A. A., Mahdi A. A. and Hussein A. K.," Effects of supply Diffuser Shape on Air Age and Human Comfort in an Office with Displacement Ventilation and Chilled Ceiling System in Hot and Dry climate", 4th International Conference on Engineering Sciences (ICES 2020), IOP Conf. Series: Materials Science and Engineering, 2021.

[80] Saheb H. A. , Mahdi A. A. and Al-amir Q. R.," A Comparative Study of Performance Between Two Combined Ventilation Systems and Their Effect on Indoor Air Quality and Thermal Comfort Inside Office Rooms",IOP Conf. Series: Materials Science and Engineering, International Workshop on Nanotechnology (IWN 2020), 2021.

[81] Muna, "Experimental and Numerical Investigation on Air Flow and Temperture Distribution Under Different Geometries of Displacement Ventilation Devices in an Office Room", M.Sc. thesis, Department of MechanicsCollege of Engineering, University of Babylon, 2017.

[82] Lastovets N , Kosonen, R , Jokisalo J. and Kilpeläinen S., "Dynamic design model of displacement ventilation", E3S Web of Conferences 111 0 4049 CLIMA, 2019.

[83] Shi Z., Lu Z. and Chen Q., "Indoor Airflow and Contaminant Transport in a Room with Coupled Displacement Ventilation and Passive-chilled-beam Systems", Building and Environment, 161:106244, 2019.

[84] Cetin Y. E., Avci M. and Aydin O., "Particle Dispersion and Deposition in Displacement Ventilation Systems Combined with Floor Heating", Science and Technology for the Built Environment,2021.

References

[85] Mahdi, A. A., Al-amir Q. R. and Yakoob, A. K., "Air Distribution Performance Inside Office Room with Combined Displacement and Personal Ventilation", 3rd International Conference on Recent Innovations in Engineering (ICRIE 2020),2021.

[86] Shbeeb, A. A., " Experimental and Numerical Investigation of Displacement Ventilation System with Assessment of Four Turbulence Models", M. Sc. Thesis, University of Babylon, College of Engineering, Department of Mechanical Engineering, 2016.

[87] Iraqi cooling cod, 2012.

[88] Bhatia A. B.E.," HVAC Made Easy: A Guide to Heating & Cooling Load Estimation", PDH Course M196, 2012.

[89] Chen, Q. and Glicksman, L. "system performance evaluation and design guidelines for displacement ventilation", ASHRAE, Atlanta, p. 112,2003.

[90] Singh H., "Basic Fundamentals of Parabolic Trough Collector, Department of Mechanical Engineering", University Institute of Engineering and Technology, Panjab University, 2019.

[91] Energy Equation Solver (EES) software.

[92] Noori H. M., " Experimental study of free convection in coiled tube heat exchanger with vertical orientation ", Tikrit Journal of Engineering Sciences, 18(4), pp. 80 – 87, 2011.

[93] Lorenz J.J. and Yung D., "A note on combined boiling and evaporation of liquid films on horizontal tubes", Journal heat transfer, 101, pp. 178-180, 1979.

[94] Patil R.K., Shende B.W. and Ghosh P.K., "Designing a helical coil heat exchanger", Chemical Engineering, 13, pp. 85 – 8, 1982.

[95] J.P.Holman, "Heat Transfer", McGraw hill Kogakusha , 4th edition, 1976.

References

[96] "ASHRAE handbook and product directory", Fundamentals volume, 1977.

[97] Incropera F. P., Dewitt D. P. Bergman T. L. and Lavine A. S. " Fundamentals of Heat and Mass Transfer", Sixth Edition.

[98] Asim, M., " Simulation of Solar Powered Absorption Cooling System for Buildings in Pakistan", Ph. D. dissertation, University of Manchester, School of Mechanical, Aerospace and Civil Engineering, 2016.

[99] Sukhatme S P. and J K. Nayak, "Solar energy: principles of thermal collection and Storage", McGraw-Hill, 3rd, New Delhi, 2008.

[100] Yogi G. D., Kreith F. and Kreider J. F., "Principles of solar engineering", Taylor & Francis, 2nd, Philadelphia, 1999.

[101] Yassen T. A., " Experimental and Theoretical Study of a Parabolic Trough Solar Collector", Anbar Journal for Engineering Sciences, 5(1), pp. 109-125, 2012.

[102] Kalogirou and Soteris A., "Solar energy engineering: Processes and Systems", Elsevier, USA, 2009.

[103] Duffie, Jouh A. and Beckman W. A., "Solar engineering of thermal processes", John Wiley & Sons, 3rd, New Jersey, 2006.

[104] Lunde, P.J., "Solar thermal engineering – space heating and hot water system", John wily and sons, New york, 1980.

[105] Dhadan N. S., " Application of a solar Assisted Heating ans desiccant cooling systems for a Domestic building in Baghdad", M.Sc. Thesis. University of Baghdad, 1999.

[106] Gary H. P. and Prakash J. "Solar Energy Fundamentals and Applications", New Delhi, www.Tata McGraw-Hill. Com, 2005.

[107] Tijani A. S. and Roslan A. M.S., "Simulation analysis of thermal losses of parabolic trough solar collector in Malaysia using computational fluid dynamics", Procedia Technology, 15, pp. 841 – 848, 2014.

References

[108] Rathore, M.M., Raul J. and Kapuno R.A.. "Engineering Heat Transfer", USA: Jones & Bartlett Learning, LLC, 2011.

[109] Sukhatme, S. P. and Nayak J. K., "Solar energy: principles of thermal collection and storage", India: McGraw-Hill Education; 2009.

[110] Farzad, J. and Emad A., "Energetic and exergetic evaluation of flat plate solar collectors", Renewable Energy, 56, pp.55–63, 2013.

[111] Torres-Reyes, E., Cervantes de Gortari, J.G.; Ibarra-Salazar B.A. and Picon-Nunez M.A., "design method of flat-plate solar collectors based on minimum entropy generation", Exergy, 1, 46–52, 2001.

[112] Wang M., Carlos A. and Ferreira I., "Absorption heat pump cycles with NH3 – ionic liquid working pairs", Applied Energy, 204, pp. 819–830, 2017.

[113] Ucar A. and Inalli M., "Exergoeconomic analysis and optimization of a solar-assisted heating system for residential buildings", Building and Environment, 41, pp. 1551–1556, 2006.

[114] Şencan, A., Kemal, A., Yakut, S. and Kalogirou A., Exergy Analysis of Lithium Bromide/Water Absorption Systems, Renewable Energy , 30, 645-657, 2005.

[115] Klein S.A and Alvarado F.L, "Engineering equation solver-EES software", F-Chart Software, Professional-Ver.7.124, 2004.

[116] Awbi H., "Ventilation - Systems Design and performance", Taylor & Francis e-Library, 2008.

[117] Abdul-Jabar M. A., "Regional Airflow Characteristics in Mechanically Ventilated Rooms", M.Sc. Thesis, University of Technology, 2004.

[118] Horikiri K, Yao Y and Yao J., "Numerical study of unsteady airflow phenomena in a ventilated room", Ichmt Digital Library Online, 2012.

[119] Airpak 3.0 User's Guide, Fluent Inc. Centerra Resource Park 10 Cavendish Court Lebanon, NH 03766, 2007.

References

[120] Qasim H. , "Numerical Study of Air Velocity and Temperature Distribution by Displacement Ventilation", M.Sc. thesis, Department of Mechanical Engineering , University of Technology,2010.

[121] Xu Y., Yang X. , Yang C. and Srebric J., "Contaminant dispersion with personal displacement ventilation Part I: Base case study", Building and Environment, 44, pp. 2121-2128, 2009.

[122] Cao G, Awbi H, Yao R, Fan Y, Sirén K, Kosonen R and Zhang J J, "A review of the performance of different ventilation and airflow distribution systems in buildings", *Build. and Environ.* 73 171-186, 2014.

[123] Sandberg M. and Sjoberg M., "The Use of Moments for Assessing Air Quality in Ventilated Rooms", *Building and Environment* 18(4), pp. 181-197, 1983.

[124] Awbi, H. B., "Ventilation of Buildings", Spon Press, 2003.

[125] ASHRAE Fundamentals Handbook 2013.

[126] Sandberg M., "The multi-chamber theory reconsidered from the viewpoint of air quality studies", Building and Environment,19, pp. 221-233, 1984.

[127] ASHRAE Fundamentals Handbook 2013.

[128] Cao G, Awbi H, Yao R, Fan Y, Sirén K, Kosonen R and Zhang J J, "A review of the performance of different ventilation and airflow distribution systems in buildings", *Build. and Environ.* 73 171-186, 2014.

[129] Almousawi Z. J. D. K., "Investigation the performance analysis of combined photovoltaic thermal solar system and their potential in middle of iraq", M.SC. Thesis, University of Kerbala, 2018.

[130] Khaled.A.Joode, "Air condition and refrigeration engineering", first edition, p.216, 1984.

[131] Chen, Yixing, Raphael B., and Sekhar S. C. ,"Individual control of a personalized ventilation system integrated with an ambient mixing ventilation system." HVAC and Research, 18(6),2012.

APPENDICES

Appendix (A): Tables

Table (A-1 Physical properties of Acetone and Water.

	Acetone	water
Formula	C_3H_6O	H_2O
Molar mass	58.08 g/mol	18.015 g/mol
Density	0.791 g/cm^3	0.999 g/cm^3
Normal boiling point	56.5 ℃	99.98 ℃
Normal melting point	-94.7 ℃	0 ℃
Enthalpy change of vaporization	539 J/g	2257 J/g

Table (A-2) Optimal Tilt Angle for each Month of Location with Latitude of 32.47°N. [129].

January	February	March	April	May	June	Year
53.32	45.8	34.86	22.98	13.66	9.39	
July	August	September	October	November	December	32.47
11.37	19.17	30.48	42.32	51.4	55.53	

Table (A-3) A_k and B_k coefficients for equation (4.4), [101].

K	A_K	B_K
0	$2.0870*10^{-4}$	0
1	$9.2869*10^{-3}$	$-1.2229 * 10^{-1}$
2	$-5.2258 * 10^{-2}$	$-1.2698*10^{-1}$
3	$-2.1867*10^{-3}$	$-2.9823 * 10^{-3}$
4	$-2.1867 * 10^{-3}$	$-2.9823 * 10^{-3}$
5	$-1.51 * 10$	$-2.3463 * 10^{-4}$

Appendix (B): Uncertainty Calculation of Temperature

Thermocouple error = +-0.2 ºC

Thermometer error = +- (0.004T+0.5) …(B-1)

$U_T = [(0.25)^2 + (0.004T+0.5)^2]^{0.5}$ …(B-2)

Uncertainty for room temperatures at 7-July

Time:11:00 AM				Time:11:30 AM			
Temperature		Uncertainty		Temperature		Uncertainty	
T_1	34.4	U_{T1}	0.6732	T_1	34.9	U_{T1}	0.6755
T_2	34.9	U_{T2}	0.6728	T_2	35.5	U_{T2}	0.6747
T_3	35.6	U_{T3}	0.6736	T_3	36.1	U_{T3}	0.6762
T_4	36.4	U_{T4}	0.6755	T_4	36.7	U_{T4}	0.6778
T_5	35.7	U_{T5}	0.6682	T_5	36.3	U_{T5}	0.6701
T_6	35.6	U_{T6}	0.6701	T_6	36.1	U_{T6}	0.6724
T_7	35.8	U_{T7}	0.6728	T_7	36.5	U_{T7}	0.6747
T_8	36.3	U_{T8}	0.6759	T_8	36.9	U_{T8}	0.6770

Time:12:00				Time:12:30 PM			
Temperature		Uncertainty		Temperature		Uncertainty	
T_1	35.3	U_{T1}	0.6774	T_1	35.8	U_{T1}	0.6793
T_2	35.9	U_{T2}	0.6758	T_2	36.4	U_{T2}	0.6785
T_3	36.8	U_{T3}	0.6774	T_3	37.5	U_{T3}	0.6797
T_4	37.2	U_{T4}	0.6797	T_4	37.9	U_{T4}	0.6827
T_5	36.8	U_{T5}	0.6717	T_5	37.3	U_{T5}	0.6736
T_6	36.4	U_{T6}	0.6739	T_6	37.1	U_{T6}	0.6759
T_7	36.8	U_{T7}	0.6774	T_7	37.4	U_{T7}	0.6800
T_8	37.4	U_{T8}	0.6789	T_8	38.2	U_{T8}	0.6816

Time:01:00 PM				Time:01:30 PM			
Temperature		Uncertainty		Temperature		Uncertainty	
T_1	36.4	U_{T1}	0.6816	T_1	36.7	U_{T1}	0.6831
T_2	36.9	U_{T2}	0.6812	T_2	37.3	U_{T2}	0.6823
T_3	38.1	U_{T3}	0.6823	T_3	38.5	U_{T3}	0.6835
T_4	38.5	U_{T4}	0.6854	T_4	38.9	U_{T4}	0.6869
T_5	37.9	U_{T5}	0.6758	T_5	38.3	U_{T5}	0.6770
T_6	37.8	U_{T6}	0.6778	T_6	38.1	U_{T6}	0.6793
T_7	38.1	U_{T7}	0.6823	T_7	38.4	U_{T7}	0.6839
T_8	38.9	U_{T8}	0.6839	T_8	39.3	U_{T8}	0.6854

Time:02:00 PM				Time:02:30 PM			
Temperature		Uncertainty		Temperature		Uncertainty	
T_1	36.9	U_{T1}	0.6839	T_1	37.2	U_{T1}	0.6847
T_2	37.5	U_{T2}	0.6835	T_2	37.6	U_{T2}	0.6847
T_3	38.8	U_{T3}	0.6850	T_3	39.1	U_{T3}	0.6862
T_4	39.1	U_{T4}	0.6881	T_4	39.5	U_{T4}	0.6896
T_5	38.5	U_{T5}	0.6778	T_5	38.7	U_{T5}	0.6789
T_6	38.4	U_{T6}	0.6800	T_6	38.7	U_{T6}	0.6804
T_7	38.8	U_{T7}	0.6850	T_7	39.1	U_{T7}	0.6862
T_8	39.6	U_{T8}	0.6862	T_8	40	U_{T8}	0.6877

Time:03:00 PM			
Temperature		Uncertainty	
T_1	37.5	U_{T1}	0.6862
T_2	37.9	U_{T2}	0.6858
T_3	39.5	U_{T3}	0.6877
T_4	40.4	U_{T4}	0.6908
T_5	39.1	U_{T5}	0.6800
T_6	39	U_{T6}	0.6816
T_7	39.5	U_{T7}	0.6877
T_8	40.3	U_{T8}	0.6911

Appendix(C): Comparison Between Experimental and Theoretical work

The comparison between theoretical and experimental works was found at 7-July by calculating the total cooling load required as a function of room temperature and equating it with the obtained cooling effect using (EES) software as following:

1- Heat gain from walls

$Q=U*A*\Delta T$

$$\frac{1}{U}=\frac{1}{h_{out}}+\frac{x_{sand}}{K_{sand}}+\frac{x_{gw}}{K_{gw}}+\frac{1}{h_{in}} \quad \ldots(C\text{-}1)$$

$$\frac{1}{U_e}=\frac{1}{h_{out}}+\frac{x_{sand}}{K_{sand}}+\frac{x_{gw}}{K_{gw}}+\frac{1}{h_{in}} \quad \ldots(C\text{-}2)$$

X_{sand}=0.05 m

K_{sand}=0.14 W/m.K

h_{in}=9.37 W/m^2.°C

h_{out}=22.7 W/m^2.°C

K_{gw}=0.038 W/m.K, [130].

X_{gw}=0.02 m

U_e=0.9669 W/m.K

$U_s = U_w = U_n = U_e = U_{ceil}$ =0.9669 W/m.K

$A_s=A_e=A_w=2*2.5=5$ m^2

$A_n=2*2.5-2*0.9-0.5*1= 2.7$ m^2

$CLTD_{c,n}=(CLTD_n+LM_n)*K+(25.5-T_r)+(T_o-29.4)$ …(C-3)

$CLTD_{c,e}=(CLTD_e+LM_e)*K+(25.5-T_r)+(T_o-29.4)$ …(C-4)

$CLTD_{c,s}=(CLTD_s+LM_s)*K+(25.5-T_r)+(T_o-29.4)$ …(C-5)

$CLTD_{c,w}=(CLTD_w+LM_w)*K+(25.5-T_r)+(T_o-29.4)$ …(C-6)

$CLTD_{c,ceil}=(CLTD_{ceil}+LM_{ceil})*K+(25.5-T_r)+(T_o-29.4)$ …(C-7)

From Ref.,[130],table 6-4:

K=0.65

T_{out}=48 ℃

DR=18 ℃

$T_o=T_{out}$-DR/2

$CLTD_n$=6 ℃

$CLTD_e$=13 ℃

$CLTD_s$=8 ℃

$CLTD_w$=10 ℃

$CLTD_{ceil}$=18℃

LM_n=-1.1 ℃

LM_e=0 ℃

LM_w=0 ℃

LM_s=0.5 ℃

LM_{ceil}=0.5 ℃

$Q_n=CLTD_{c,n}*A_n*U_n$

$Q_e=CLTD_{c,e}*A_e*U_e$

$Q_s=CLTD_{c,s}*A_s*U_s$

$Q_w=CLTD_{c,w}*A_w*U_w$

2- Heat gain from floor

$$\frac{1}{U_{fl}}=\frac{1}{h_{out}}+\frac{x_w}{K_w}+\frac{1}{h_{in}} \quad \text{…(C-8)}$$

K_w=0.17 W/m.K, [85].

X_w=0.03 m

U_{fl}=3.056 W/m.K

$Q_{fl}= U_{fl}*A_{fl}*(T_{out}-T_r)$ …(C-9)

$A_{fl}=2*2=4m^2$

3- Heat gain from door

$$\frac{1}{U_{gl,do}} = \frac{1}{h_{out}} + \frac{x_{gl}}{K_{gl}} + \frac{x_{gw}}{K_{gw}} + \frac{1}{h_{in}} \quad \text{…(C-10)}$$

$$\frac{1}{U_{door}} = \frac{1}{h_{out}} + \frac{x_{pvc}}{K_{pvc}} + \frac{x_{gw}}{K_{gw}} + \frac{1}{h_{in}} \quad \text{…(C-11)}$$

K_{gl}=0.78 W/m.K

K_{pvc}=0.19 W/m^2.°C

X_{pvc}=0.02 m

X_{gl}=0.005 m

U_{door}=1.278 W/m.K

$U_{gl,do}$=1.463 W/m.K

Q_{door}=(U_{door}*A_{door}+ $U_{gl,do}$*$A_{gl,do}$)*$CLTD_{c,n}$ …(C-12)

A_{door}=2*0.9-0.48*0.63=1.4976 m^2

$A_{gl,do}$= 0.48*0.63=0.3042 m^2

4- Heat gain from window

$$\frac{1}{U_{win}} = \frac{1}{h_{out}} + \frac{x_1}{K_1} + \frac{x_{air}}{K_{air}} + \frac{x_2}{K_2} + \frac{1}{h_{in}} \quad \text{…(C-13)}$$

The window consists of two layer of reflective glass of 6 mm thickness with conductivity of (0.83 Btu/h.ft^2 °F),[88], and a cavity of air with 8 mm thickness.

K_1=K_2=0.83 Btu/h.ft^2 °F=1.436 W/m. ^{o}C.

X1=X2=0.006 mm

K_{air}=0.025 W/m. ^{o}C

X_{air}=0.008 mm

U_{win}=2.1484 W/m^2. ^{o}C

A=1*0.5=0.5

U_{win}=2.148 W/m.K

A_{win}=1*0.5=0.5 m^2

$Q_{win}=U_{win}*A_{win}*CLTD_{c,win}$ …(C-14)

5- Heat gain from infiltration

$Q_{inf}=1.22*V_{inf}*(T_o-T_r)$ …(C-15)

$V_{inf}=\frac{0.5\times v}{3600}=\frac{0.5\times2\times2\times2.5}{3600}=1.555\ l/s$ …(C-16)

V_{inf}=0.51.555

$Q_{ex}=Q_n+Q_e+Q_s+Q_w+Q_{win}+Q_{inf}+Q_{ceil}+Q_{fl}+Q_{door}$ …(C-17)

6- Internal heat gain

a- Heat gain from person

Q_p=75 W

b- Heat gain from computer

Qc=45 W

c- Heat gain from light

Q_l=15 W

$Q_{int}=Q_p+Q_c+Q_l$= 135 W

$Q_{tot}=Q_{ex}+Q_{int}$ …(C-18)

From the solar absorption cooling system, the cooling effect at 01:00PM is 356 W.

Q_{tot}=356 W

T_r=37.48 ℃

$T_m=T_r*0.9+T_{out}*0.1$ …(C-19)

$T_s=T_m-Q_{tot}/(\rho_{air}*Cp_a*\dot{V})$ ...(C-20)

$T_s=T_m-Q_{tot}/(1.18*1007*0.022)$

T_s=24.91℃

Appendix (D): Error Calculation

Calculating the percentage error between the measured data (air temperature at vertical line) of experimental data and that of the non-adiabatic numerical model by using the equation (E-1), [131]:

$$Err=\frac{1}{n}\sum_{i=1}^{n}\frac{[X_{CFD}^{i}-X_{EXP}^{i}]}{[X_{EXP}^{i}]}\times 100\% \quad \ldots(D\text{-}1)$$

$$Err=\frac{|33.26-37.3|+|35.6-37.7|+|36.7-38.2|+|37.9-38.6|}{37.3+37.7+38.2+38.6}=\frac{8.34}{151.8}\times 100\%$$

$$Err=5.49\%$$

Appendix (E): The Published Papers

1-The paper entitled "**Overview of Solar Assisted Cooling Technologies**" published in International Journal of Applied Engineering Research".

International Journal of Applied Engineering Research ISSN 0973-4562 Volume 15, Number 8 (2020) pp. 843-863
© Research India Publications. http://www.ripublication.com

Overview of Solar Assisted Cooling Technologies

Ahmed Abbas SHAHHATH*, Haroun SHAHAD, Alaa Abbas MAHDI

Department of Mechanical Engineering, Babylon University, Babylon, Iraq.

Abstract

Traditional air conditioning devices or vapor compression devices are the major consumers of power in epochal buildings. Public environment problems arise from the vapor compression device, like greenhouse gases emissions and also heat waste. The adaptation of solar energy elements to the vapor compression device will reduce these problems. The buildings sectors account for 30-40 % of the consumption of energy of world and the manufacturing sector is the most energy-intensive sector. Solar energy is the most appropriate clean energy source which is utilized in cooling, heating and electricity generation in the building sector. Solar refrigeration is a cleaner and price-effective technology, solar chilling provides environmental advantages, including decreasing major grid request and shifting load during maximum usage and reducing the emissions of greenhouse gases. The paper discusses the various solar technologies of refrigeration that can be used to provide the necessary cooling and cooling effect of solar energy.

Keywords: absorption system; solar cooling; solar absorption;

EV: Expansion Valve

FPC: Flat Plate Collector

G. A.: Genetic Algorithm

GAX: Generator Absorption Exchange

GHI: Global Horizontal Irradiance

HGAX: Hybrid Generator Absorption Exchange

HGETSC: Water-In-Glass Evacuated-Tube Solar Collector

HPA: Heat Pipe Array

HPG: High Pressure Generator

HX: Heat Exchangers

IFPC: Improved Flat-Plate Collector

IRR: Internal Rate of Return

LCOR: Levelized Cost of Refrigeration

LFR: Linear Fresnel Reflector

2-The paper entitled "**Parametric Theoretical Study of Solar Assisted Cooling System Using Lithium Bromide-Water Pair**" Published in 7th International Conference on Renewable Energy and Material Technology (ICOREMT 2021). IOP Conference Series: Earth and Environmental Science.

ICOREMT 2021 IOP Publishing
IOP Conf. Series: Earth and Environmental Science **877** (2021) 012020 doi:10.1088/1755-1315/877/1/012020

Parametric Theoretical Study of Solar Assisted Cooling System Using Lithium Bromide- Water Pair

Ahmed A Shahhath*, Haroun A K Shahad and Alaa A Mahdi
Department of Mechanical engineering, College of Engineering, University of Babylon, Babylon, Iraq.

*Corresponding E-mail: Eng.haroun.abdul@uobabylon.edu.iq

Abstract: In this paper, the effect of parameters of solar absorption system such as evaporator, absorber, condenser, generator temperatures and the mass of the solution on the evaporator cooling load and the coefficient of performance has been explained theoretically. The results show that, increasing of evaporator and condenser temperatures increase the evaporator cooling load, performance coefficient and the Ratio of Circulation while increasing the temperature of condenser and absorber decreases the evaporator cooling load, performance coefficient and the Circulation Ratio. In addition, increasing the solution mass increases the refrigeration power while the performance coefficient and the Circulation Ratio was constant at increasing the solution mass. The reached maximum cooling load was (1.932 kW) at 15 kg solution mass and 100 °C generator temperature, the maximum COP was 0.774 at (10 °C) temperature of evaporator and the peak Circulation Ratio was 0.3066 at (30 °C) temperature of absorber and (100 °C) temperature of generator.

Keywords: Water; Lithium Bromide; Generator Temperature; Evaporator Cooling Load; Coefficient of Performance

1. Introduction

Solar power is one of the most major renewable energy resources. In Comparison to other sources, solar power can be described by the reality that it is obtainable, almost, anywhere. Moreover, it is neat and has no poor impacts on the atmosphere. It could be used in one of the next two methods: by converting irradiance directly to electric power, by utilizing photovoltaic cells, or by converting irradiance into frontal thermal power utilizing collectors. Climatic conditions decrease the level of solar irradiance that hits the Earth's surface before dissipating about 20% to 30% of the incident light and adjusting its spectrum. After crossing meantime, the atmosphere of Earth, about one half of the solar radiation is in the visible electromagnetic spectrum with the other half is mostly in the infrared and ultraviolet spectrum [1].

Gonzalez-Gil et al. [2] assessed the efficiency of an absorption cooler cooled directly by air in summer 2010, centered on test outcomes of many days in Madrid. The system was working effectively,

3-The paper entitled" **Simulation of Ventilation parameters for an Office Room with Displacement Ventilation**" Published in International Journal of Mechanical Engineering.

ISSN: 0974-5823 Vol. 7 No. 2 February, 2022

International Journal of Mechanical Engineering

Simulation of Ventilation Parameters for an Office Room with Displacement Ventilation

A A Shahhath[1,*], H A K Shahad[1] and A A Mahdi[2]

(1) Department of Mechanical engineering, College of Engineering, University of Babylon, Babylon, Iraq.

Abstract: This study will investigate the local mean age of air, temperature and velocity gradient, predicted mean vote, predicted percentage dissatisfied, air diffusion performance index (ADPI) and ventilation effectiveness. The effect of turbulence model, the number of points of mesh, the number of taken points from the room on ADPI also will be studied. The AIRPAK software will be utilized for the simulation of theoretical study. The flow rate is constant at 0.1425 m^3/s, while the velocity of supplied air studied is (0.25, 0.275, 0.3, 0.325 and 0.35 m/s). The temperature of supplied air studied is (18, 19, 20 and 21 °C). Three models of turbulence will be used that are RNG K-ε model, two equations model and Spalart-Allmaras model. The results showed that, the mean local age of air increase with height and decreases with increase the supply air velocity. So the maximum mean air age was 317.9 s at height of 2.5 m and mean velocity of air supply 0.25 m/s, predicted mean vote, predicted percentage dissatisfied are zero, the local velocity increases with height. So, the maximum local velocity for pole (1) was about 0.138 m/s at mean velocity of 0.3 m/s and height of 2.5 m/s, the RNG K-ε model is the best between the turbulence models, the maximum value of ADPI for the RNG model at 0.3 m/s is about 61.84%, Ventilation effectiveness increases with the mean air supply temperature. so the maximum value of effectiveness is 1.488 at velocity of 0.35 m/s. This is caused by the decrease in local temperature with velocity increasing of supplied air and the ADPI increases with the number of mesh and the number of points.

Keywords: *Displacement Ventilation; Thermal Comfort; Air Diffusion Performance Index; Temperature; Velocity; Mean Age of Air; Ventilation Effectiveness.*

1. Introduction

In the air distribution systems design, the occupants thermal comfort might not be the first request in comparison to others main parameters like the room heat loads offseting, fresh air supplying and performance of power related to the HVAC system choice. Only it is stringent in assuring the well-being and output of the room conquerings.

displacement ventilation was used for the past little decades in commercial and industrial constructions. Due to its high efficiency of ventilation, displacement ventilation has been utilized in countries the United Kingdom and The Netherlands for factories and workshops ventilation due to existing a higher grade of dissipation of heat or contamination of air. For some utilizations, displacement ventilation is a suitable technique. So, the displacement ventilation will be used for ventilating an office room to get best indoor air quality, [1].

Lastovets et al., [2] presented a model for the dynamic temperature gradient for DV and evaluated the thermal mass effect on the stratification of temperature. The model was proved with the output of experimental works of the lecture room using displacement ventilation. The results showed that, the model gave better robustness for predicting the thermal output at various working circumstances by picking up the building system dynamic characteristics accurately. Furthermore, the model took into account the heat loads time schedules. Moreover, the two-capacity prototype could estimate the temperature gradient of indoor air in dynamic circumstances by picking up the building system dynamic characteristics accurately. The model could be used at design of DV at different dynamic circumstances.

Patrick Daffin, [3] investigated the circumstances at which it might be possible for implementing a displacement ventilation device in a residential construction. An experimental analysis of the effect on a mechanical air cooling system of a vertical location of the inlet and outlet vents was achieved. It might have been found that, for higher high heat loads, the low inlet high outlet setup might have been fit will uphold give or take the same temperature in the taken zone with respect to a less heat load, same time creating a strong two layers stratification inside the room such-and-such those outlet temperature might have been altogether higher over those encompassing temperature in the being down possessed area of the room.

Yakoob et al., [4] checked a modern ventilation concept: displacement ventilation (DV) helped for customize ventilation (PV) which might have been evaluated to enhance indoor air quality. That approach might move forward ventilation system plan that might much furnish single person domination about indoor microclimate. RNG, k-ε turbulence models were assessed to show how the shape and site of ventilation systems and occupants might influence the air quality and thermal environment in the space. For DV supply temperature of 18°C and PV air supply temperature extend for 18°C to 22°C, it might have been found that PV toward stream rate 10 L/s (21. 19 cfm) furthermore of the circulation about occupants could enhance inhaled air quality in the breathing area. And that these sets up towards an office room for these air supply diffuser DV and PV joined together provided for human thermal comfort agreeable contingent upon that extent from claiming air appropriation execution list (ADPI) and effectiveness of temperature (ε_t) which were progressed over 71% and around 1. 8 separately.

Copyrights @Kalahari

4-The paper entitled "**Testing of a Solar Assisted Absorption-Ventilation System Under Mid-IRAQ Weather Conditions**" (under review) at Journal of Engineering and Technological Sciences.

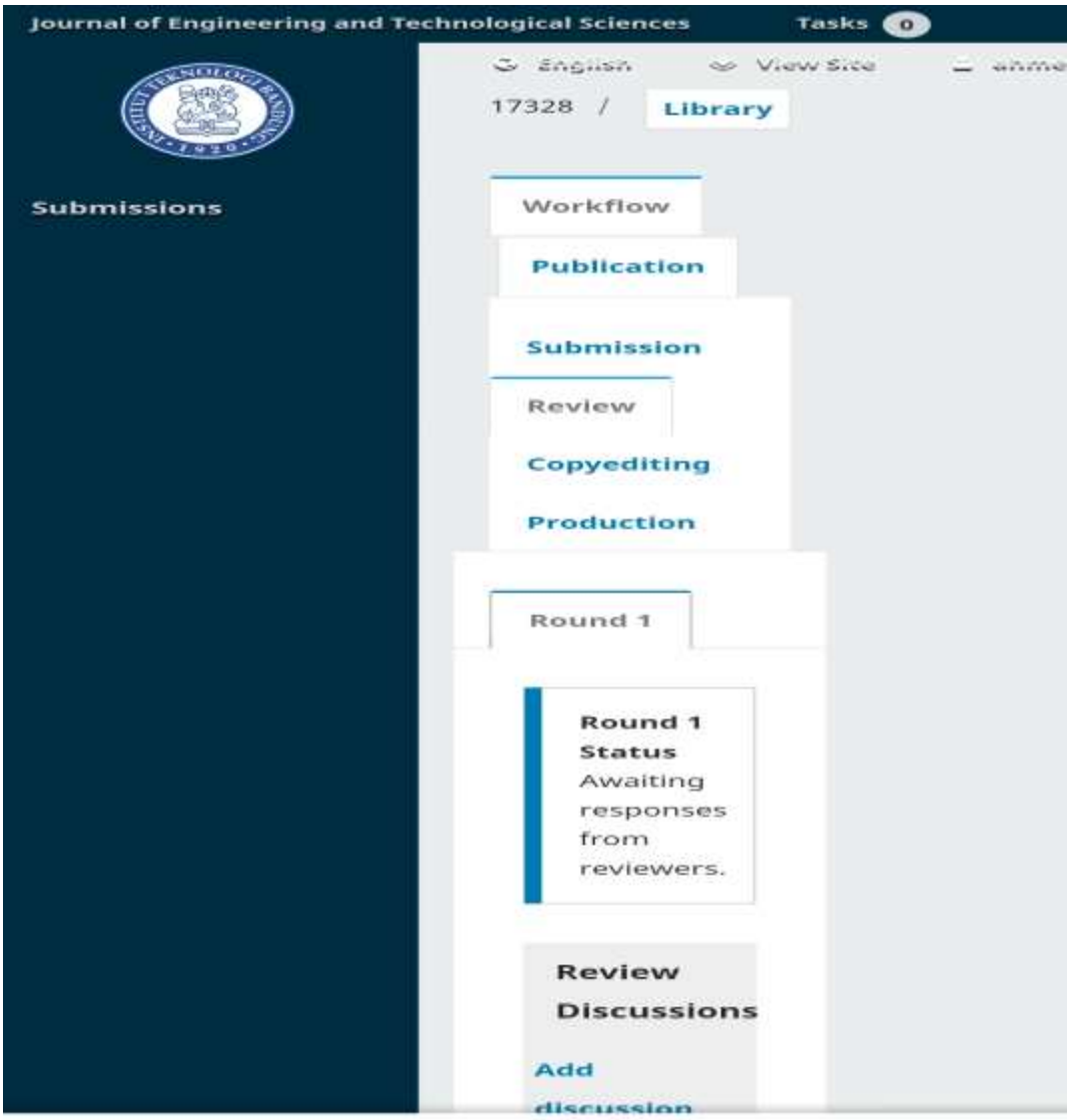

5-The paper entitled " **Simulation of a Solar Absorption Assisted Ventilation System Under IRAQ Weather Conditions"**
(under review) at FME Transactions.

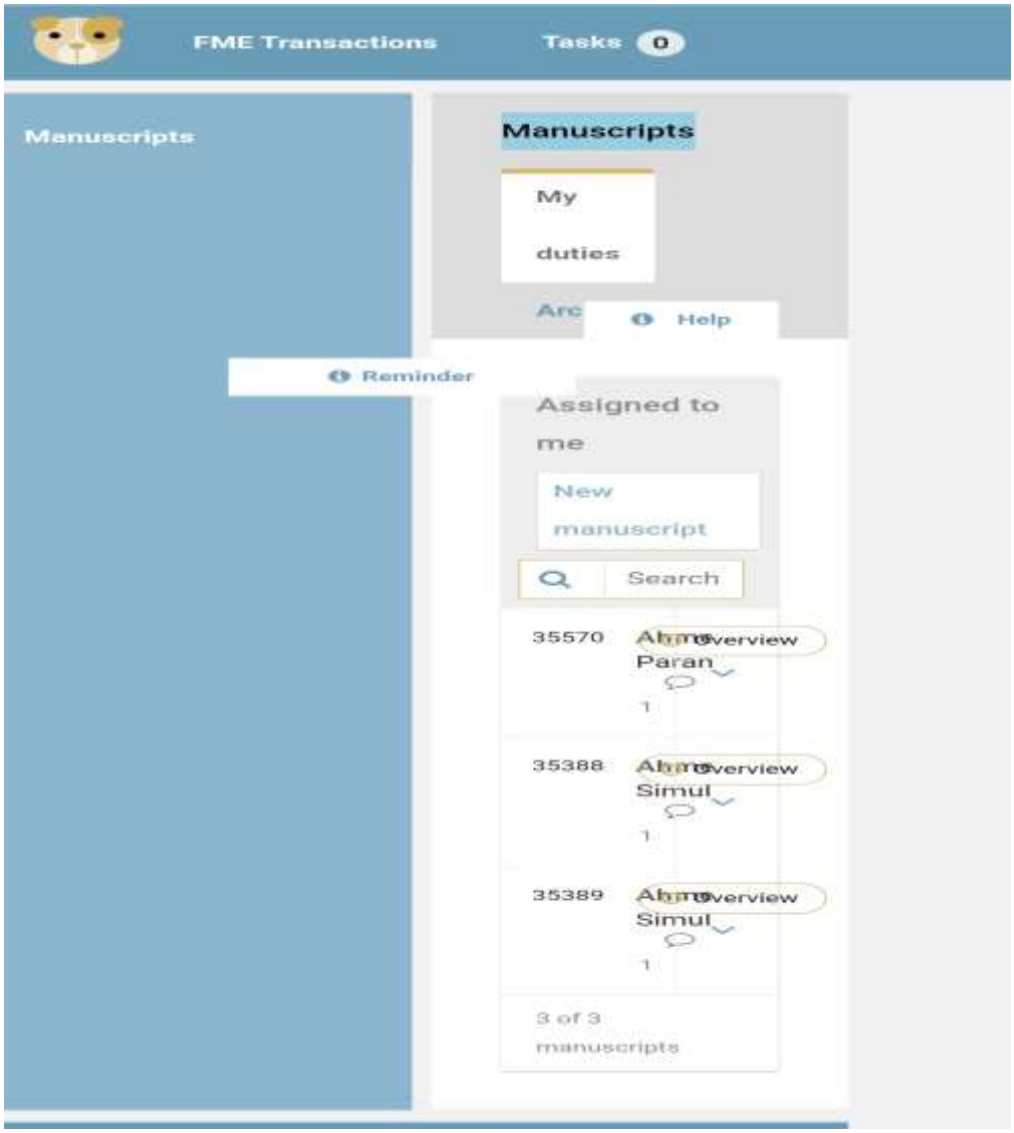

الخلاصة

ان الهدف من الدراسة هو تصميم وبناء واختبار نظام تهوية مع نظام التبريد بالامتصاص في مناخ العراق (مدينة الحلة) ب(خط عرض ٣٢,٤° و خط طول ٤٤,٤°) في وسط العراق لتهوية غرفة مكتبية معزولة باستخدام التهوية الازاحية. وكذلك تم تجهيز موديل رياضي لدورة المجمع الشمسي و نظام التبريد الامتصاصي بالإضافة الى محاكاة للغرفة ذات التهوية.

يتكون نظام التبريد الامتصاصي من مجمع ذو شكل قطع مكافيء و خزان ماء و مولد و مكثف و انبوبين شعريين و مبخر وماص و مضخة ماء كيميائية ومبادل حراري. ان الغرفة المراد تهويتها ذات ابعاد (٢* ٢ * ٢,٥ م ارتفاع) ومصنوعة من الواح الساندويج ذو ٠,١٤ W/m.°C موصلية حرارية وتحتوي على دمية حرارية ذات حرارة ٧٥W وكومبيوتر ذو حرارة ٤٥W ومصباح ذو حرارة ١٥W. هنالك شباك في الحائط الشمالي للغرفة ذو اعلى كسب حراري ٣١,٢٦W. يتسرب الهواء للغرفة بمعدل ٠,٥/h بحرارة كلية ٤٧,٤٣W. ان الحمل الحراري الكلي المطلوب لتبريد الغرفة هو ٣٠٠W و المجمع الشمسي ذو مساحة ٢m^2. تصنع مرايا المجمع الشمسي من ستينلس ستيل لتركيز الاشعاع الشمسي على المستقبل. يكون المستقبل عبارة عن ملف من أنبوب النحاس في أنبوب ناقل مفرغ من الهواء. قطر الملف ٦٣,٤mm وطوله ١,٥١٥m. يغطى ملف المستقبل بطبقة من الطلاء الأسود لتعزيز الامتصاصية للمستقبل. قطر الانبوب النحاسي ١٢,٧mm و سمكه ١mm.

الاسيتون–ماء استخدم كمزدوج مثلج–ماص. استخدمت ثلاث تراكيز للاسيتون في العمل المنجز (٤٠٪, ٥٠٪ and 60%). تم استخدام عمودين داخل الغرفة المبردة. العمود الأول عند (X=1m and Z=1m) والعمود الثاني عند (X=1.25m and Z=1.5m).

أنجزت التهوية الازاحية باستخدام ناشر هواء بابعاد (عرض ٠,٣m و ارتفاع ٠,٢٤m) وسرعة الهواء المجهز هي ٠,٣m/s وبمعدل تدفق حجمي للهواء ٠,٠٢٢m^3/s. يتكون الهواء المجهز للمبخر من مزيج من ٩٠٪ هواء راجع من الغرفة من مخرج الهواء و١٠٪ من الهواء الخارجي كهواء نقي. انجز الجانب العملي في الفترة بين أيار وحزيران للعام ٢٠٢١ في الوقت بين٩:٠٠ AM و ٣:٠٠ PM.

انجز الجانب النظري باستخدام ثلاثة برامج. انجز الموديل الرياضي للنظام الامتصاصي باستخدام برنامج حل المعادلات الهندسية (برنامج EES) باستخدام مبدا اتزان الطاقة لكل أجزاء النظام. استخدم برنامج (الناتج الاحصائي وحلول الخدمة(برنامج SPSS) للحصول على علاقة رياضية تربط كمية البخار الناتج بدرجة حرارة المولد وتركيز الاسيتون في المحلول. بينما تم استخدام برنامج AirPak 3.0.16 لمحاكاة الغرفة المبردة باستخدام الموديل الرياضي RNG. K-εتم استخدام (١٤٢٧٥٠٠) عقدة في نظام الشبكة لانه اعطى نتائج مقبولة.

النتائج العملية بينت بان اعلى اشعاع شمسي عند ٢٨-حزيران لسنة ٢٠٢١ بقيمة ٨٤٦ W/m^2 وقيم اعلى طاقة و درجة حرارة سطح المستقبل و درجة حرارة خزان الماء و درجة حرارة المولد وكفائة المجمع الشمسي هي ٨١,٢ °C, ٧٨,٥ °C, ٨٧,١°C, ١١٥٧W و٠,٧٣١ بالتتابع. بينما تم الحصول على اعلى نتائج للنظام الامتصاصي عند ٧-تموز وتركيز ٦٠% للاسيتون. كانت قيم فرق درجات الحرارة عبر المبخر و تاثير التبريد و معامل الأداء و درجة حرارة الهواء المجهز للغرفة و معامل الأداء الإجمالي ومعامل الأداء اليومي هي ١٤,١ °C, ٠,٢١٧٤, ٠,٧٦, ٢٧,٥٠C, ٣٥٦w و ٠,٤٨٥٦.

بينت النتائج النظرية ليوم ٢١ من الأشهر (أيار, حزيران, تموز و اب) بان اعلى نتائج عند ٢١–تموز. كانت قيمة كل من الاشعاع الشمسي و الطاقة المستفاد منها و درجة حرارة سطح المستقبل و درجة حرارة المولد وكفائة المجمع هي W/m^2 ١١٢٦, W ١٥٨٥, °C ٩٦,٣٢, °C ٩١ و % ٧٩,٢ . بينت النتائج النظرية لنظام الامتصاص الشمسي ليوم ٢١- تموز في الساعة الواحدة ضهرا وتركيز ٦٠% للاسيتون بان قيم الفرق بدرجة حرارة الهواء عند المبخر و تأثير التبريد و معامل الأداء و درجة حرارة الهواء المجهز و معامل الأداء اليومي ومعامل الأداء الإجمالي هي°C ١٧,٩٨ , W٤٧٠, ٠,٤٥٥٢, °C ١٣,٢٢ , ٠,٣٣٨٧, ٠,٢٢١٨ بالتتابع. بالإضافة الى ذلك, بينت النتائج بأن قيم خسائر الطاقة في الساعة الواحدة ضهرا عند المجمع و خزان الماء و المولد و المكثف و الصمام الخانق للبخار و المبخر و الماص و المبادل الحراري و الصمام الخانق للمحلول هي ١٣٥٨, ٢٤٠ , ٦٦٣, ١٣٥, ٣٠, ١١٦, ٥١٧ , ٦٥٧, ٧٦٩ W بالتتابع.

بينت النتائج النظرية للنظام المتصاصي بان اعلى قيم عند ٢١-تموز و٦٠٪ تركيز للاسيتون. كانت قيم كل من فرق درجة الحرارة عبر المبخر و تاثير التبريد و معامل الأداء و درجة حرارة الهواء المجهز و معامل الأداء اليومي ومعامل الأداء الإجمالي هي °C ١٧,٩٨, W ٤٧٠, ٠,٤٥٥٢ °C, ١٣,٢٢ °C, ٠,٣٣٨٧ و ٠,٢٢١٨ عند الواحدة ضهراً. بينما بينت النتائج النظرية للغرفة المبردة بان اعلى قيم لمعامل انتشار الهواء و الفعالية الحرارية للتبريد عند°C ٢٠ درجة حرارة (درجة حرارة التصميم) هي ٧٠,٩٢٪ و١,٤٠٢ بالتتابع .

تمت المقارنة بين النتائج العملية والنظرية في يوم ٧–تموز باعتبار الكسب الحراري من الخارج. بينت النتائج بان هنالك تطابق مقبول بين النتائج العملية والنتائج للنظرية باعتبار الغرفة غير معزولة.

جمهورية العراق

وزارة التعليم العالي و البحث العلمي

جامعة بابل/كلية الهندسة

قسم الهندسة الميكانيكية

محاكاة واختبار نظام تهوية معزز بمنظومة تبريد امتصاصية شمسية تحت ضروف العراق

أطروحه مقدمة الى قسم الهندسة الميكانيكة-كليه الهندسة- جامعة بابل
كجزء من متطلبات نيل درجة الدكتوراه فلسفة في الهندسة/ الهندسة الميكانيكية/
قدرة

اعدت من قبل

أحمد عباس شحاث ضعين

ماجستير هندسة ميكانيكية(٢٠١٥)

باشراف

الأستاذ الدكتور هارون عبد الكاظم شهد الأستاذ الدكتور علاء عباس مهدي

١٤٤٣هـ ٢٠٢٢ م